Electronic and Optoelectronic Devices Using Grown 2-Dimensional Materials

Linlin Hou

Department of Materials

Wolfson College

University of Oxford

Supervised by Professor Jamie Warner

A thesis submitted for the degree of Doctor of Philosophy

November 2021

Declaration

The material contained within this thesis has not previously been submitted for a degree at the University of Oxford or any other university. The research reported within this thesis has been conducted by the author unless indicated otherwise.

Copyright Notice

The copyright of this thesis rests with the author. No quotation from it should be published without the prior written consent of the author, and any information derived from it should be acknowledged.

Abstract

Electronic and Optoelectronic Devices Using Grown 2-Dimensional Materials

Linlin Hou
Wolfson College, University of Oxford
In pursuit of DPhil Degree

Two-dimensional (2D) materials are a category of layered materials with atomic-level thickness. This thesis focuses on electronic and optoelectronic devices with both vertical and lateral configurations by using grown 2D materials, including graphene, tungsten disulfide (WS_2), hexagonal boron nitride (h-BN), and platinum diselenide ($PtSe_2$). Most of the 2D materials used in the project were synthesized by chemical vapor deposition (CVD).

Chapter 4 demonstrates an asymmetrical vertical structure of graphene/WS_2/h-BN/graphene (Gr_B/WS_2/h-BN/Gr_T) using all CVD-grown 2D materials. The device arrays were fabricated by vertically stacking graphene electrodes, h-BN continuous film, and WS_2 single-crystal domains via DI water/ IPA-based wet transfer techniques. The photovoltaic effect of the asymmetrical vertical structure is around 7 times improved than that of the symmetrical structure without the h-BN layer. By changing the sequence of the h-BN layer in the vertical stack, the electron flow direction can be delicately controlled.

Chapter 5 focuses on high-performance electroluminescence (EL) devices with a vertical heterostructure of Gr/h-BN/WS_2/h-BN/Gr by using all CVD-grown 2D materials. Long-lived persistent EL is demonstrated for more than 2 hours without significant degradation of the WS_2. In the cycling test, the EL signal peak position and the intensity stay almost the same after several ON/OFF cycles under high bias, demonstrating good stability and durability when pulsed. Further investigation shows that the limiting factor for EL devices is not the degradation of the WS_2 but the electroburning of the topmost graphene electrode exposed to the air.

Chapter 6 explores a photodetector with a lateral structure of $PtSe_2$-WS_2-$PtSe_2$, where semimetal multi-layered $PtSe_2$ thin film acts as electrodes and monolayer WS_2 acts as the photoactive material. $PtSe_2$ thin film was synthesized by thermally assisted selenization. Direct laser patterning was applied for the device fabrication. As-fabricated devices exhibit a satisfactory ON/OFF ratio and fair photoresponse. A comparison study shows that the device with shorter channel width has better photoresponsivity. The back-to-back Schottky diodes model well estimates the barrier height of $PtSe_2$-WS_2 heterojunction. The device exhibits the lowering of barrier height with the increasing laser power, arising from the photogating effect.

Acknowledgement

First and foremost, I would like to express my sincere gratitude to Professor Jamie H. Warner for providing me with the great opportunity to carry out my DPhil research in the field of 2D materials. He constantly supported and kindly supervised me throughout my DPhil study. His keen observations and broad knowledge always enlightened me whenever I encountered problems. He spared no effort to give me advice and cultivate my independent thinking. I would like to show my deepest respect for him.

I would also like to express my appreciation for the assistance and support from all my colleagues in Jamie's group. Special thanks go to Dr. Yingqiu Zhou, Dr. Hefu Huang, Dr. Martin Tweedie, Dr. Viktoryia Shautsova, and Dr. Wenshuo Xu for generously sharing their knowledge and experience. I could not have made it this far without their patient training in each technique and their valuable discussions about my project. My peers, Qianyang Zhang, Yi Wen, and Dr. Jun Chen, have always accompanied and encouraged me during my time in Oxford. They have left me with many unforgettable memories. We have witnessed each other's growth from freshman to independent researchers.

I would like to acknowledge Mr. Paul Pattinson from the Department of Physics. He provided me with a well-organized cleanroom environment with all the best equipment for my device fabrication, which made my lab time enjoyable. His extreme enthusiasm for his work has always been an inspiration to me.

I would like to sincerely thank all my friends who constantly gave me emotional support and companionship throughout this journey, both in person and remotely. Without their friendship, this journey would not have been as colourful and enjoyable.

Additionally, Mao Mao and Jie Yuan helped me with proofreading my publications and thesis. Dr. Jiasheng Shi provided significant support in mathematics.

In the end, I dedicate this thesis to my family. The support and understanding from my dearest parents gave me the courage to overcome every obstacle. I could not have achieved so much without their unconditional love and endless care.

To my Parents and Grandparents.

Publication List

First author:

Chapter 4

- **Hou, L.**; Zhang, Q.; Tweedie, M.; Shautsova, V.; Sheng, Y.; Zhou, Y.; Huang, H.; Chen, T.; Warner, J. H. Photocurrent Direction Control and Increased Photovoltaic Effects in All-2D Ultrathin Vertical Heterostructures using Asymmetric h-BN Tunnelling Barriers, *ACS Appl. Mater. Interfaces* **2019**, *11*, 40274-40282.

Chapter 5

- **Hou, L.**; Zhang, Q.; Shautsova, V.; Warner, J. H. Operational Limits and Failure Mechanisms in All 2D van der Waals Vertical Heterostructure Devices with Long-Lived Persistent Electroluminescence. *ACS Nano* **2020**, *14*, 15533-15543.

Chapter 6

- **Hou, L.**; Xu, W.; Zhang, Q.; Shautsova, V.; Chen, J; Shu, Y; Li, X; Bhaskaran, H; Warner, J. H. Ultrathin 2D Photodetectors using Transition Metal Dichalcogenides $PtSe_2$-WS_2-$PtSe_2$. *ACS Appl. Electron. Mater.* **2022**, *4*, 1029–1038.

Co-author:

2023

- Wen, Y., Coupin, M. J., **Hou, L.**, & Warner, J. H. Moiré Superlattice Structure of Pleated Trilayer Graphene Imaged by 4D Scanning Transmission Electron Microscopy. *ACS Nano* **2023**, *17*, 19600–19612.

- Zhang, Q., **Hou, L.**, Shautsova, V., & Warner, J. H. (2023). Ultrathin All-2D Lateral Diodes Using Top and Bottom Contacted Laterally Spaced Graphene Electrodes to WS2 Semiconductor Monolayers. *ACS Appl. Mater. Interfaces* **2023**, *15*, 18012–18021.

2021

- Zhang, Q.; **Hou, L.**; Lu, Y.; Chen, J.; Zhou, Y.; Shautsova, V.; Warner, J. H. Large-

Scale Uniform-Patterned Arrays of Ultrathin All-2D Vertical Stacked Photodetector Devices. ACS Appl. Mater. Interfaces **2021**, *13*, 34696–34704.

2020

- Tweedie, M. E. P.; Lau, C. S.; **Hou, L.**; Wang, X.; Sheng, Y.; Warner, J. H. Transparent Ultrathin All-Two-Dimensional Lateral Gr:WS_2:Gr Photodetector Arrays on Flexible Substrates and Their Strain Induced Failure Mechanisms. Mater. Today Adv. **2020**, *6*, 100067.

2019

- Shautsova, V.; Sinha, S.; **Hou, L.**; Zhang, Q.; Tweedie, M.; Lu, Y.; Sheng, Y.; Porter, B. F.; Bhaskaran, H.; Warner, J. H. Direct Laser Patterning and Phase Transformation of 2D $PdSe_2$ Films for On-Demand Device Fabrication. *ACS Nano* **2019**, *13*, 14162–14171.

- Zhou, Y.; Xu, W.; Sheng, Y.; Huang, H.; Zhang, Q.; **Hou, L.**; Shautsova, V.; Warner, J. H. Symmetry-Controlled Reversible Photovoltaic Current Flow in Ultrathin All 2D Vertically Stacked Graphene/MoS_2/WS_2/Graphene Devices. *ACS Appl. Mater. Interfaces* **2019**, *11*, 2234–2242.

- Chen, T.; Sheng, Y.; Zhou, Y.; Chang, R. J.; Wang, X.; Huang, H.; Zhang, Q.; **Hou, L.**; Warner, J. H. High Photoresponsivity in Ultrathin 2D Lateral Graphene:WS_2:Graphene Photodetectors Using Direct CVD Growth. *ACS Appl. Mater. Interfaces* **2019**, *11*, 6421–6430.

2018

- Huang, H.; Xu, W.; Chen, T.; Chang, R. J.; Sheng, Y.; Zhang, Q.; **Hou, L.**; Warner, J. H. High Performance Two-Dimensional Schottky Diodes Utilizing Chemical Vapour Deposition Grown Graphene-MoS_2 Heterojunctions. *ACS Appl. Mater. Interfaces* **2018**, *10*, 37258–37266.

- Huang, H.; Sheng, Y.; Zhou, Y.; Zhang, Q.; **Hou, L.**; Chen, T.; Chang, R.-J.; Warner, J. H. 2D Layer Dependent Behaviour in Lateral Au/WS_2/Graphene Photodiode Devices with Optical Modulation of Schottky Barriers. *ACS Appl. Nano Mater.* **2018**, *1*, 6874–6881.

Contents

Chapter 1 Introduction ***1***

1.1 Project Aim 1

1.2 Layout of this Thesis 1

Chapter 2 Literature Review ***3***

2.1. Introduction 3

2.2 Fundamentals of 2D Materials 4

2.2.1 Graphene 5
2.2.2 TMDs 8
2.2.3 h-BN 14

2.3 Synthesis of 2D Materials 15

2.3.1 Top-down Route 15
2.3.2 Bottom-up Route 17

2.4 Fundamentals of heterojunction 23

2.4.1 Van der Waals Heterostructures 23
Twisted stacks 23
2.4.2 Metal-semiconductor Junction 31
2.4.3 Heterostructure Assembly 33

2.5 Device Applications of 2D materials 36

2.5.1 TMDs-based Field-effect Transistor 36
2.5.2 TMDs-based Light Emitting Device (LED) 43
2.5.3 TMD-based Photodetector 49

Chapter 3: Methodology ***54***

3.1 Introduction 54

3.2 2D Material Synthesis 54

3.2.1 CVD Growth of WS_2 54
3.2.2 CVD Growth of Graphene 55
3.2.3 CVD Grown of h-BN 56
3.2.4 Direct Selenization of $PtSe_2$ 57

3.3 Material Characterizations 58

3.3.1 Optical Microscopy 58
3.3.2 Scanning Electron Microscopy (SEM) 59
3.3.4 The Raman & Photoluminescence (PL) Spectroscopy 60
3.3.5 Atomic Force Microscopy (AFM) 68

3.4 Device Fabrication 70

3.4.1 Transfer Methods: DI Water/IPA/Aligned Transfer 70
3.4.2 E-Beam Lithography (EBL) and Photolithography 73

3.4.3 Thermal Evaporation ... 77
3.4.4 Patterning ... 78

3.5 Electrical and Optoelectrical Measurements ... 80

Chapter 4 Photocurrent Direction Control and Increased Photovoltaic Effects in All-2D Ultrathin Vertical Heterostructures Using Asymmetric h-BN Tunneling Barriers ... 82

4.1 Introduction ... 82

4.2 Results and Discussion ... 83
4.2.1 Characterizations of CVD-grown 2D Materials ... 83
4.2.2 Fabrication of the Gr_B/h-BN/WS_2/Gr_T Asymmetrical Vertical Heterostructure ... 87
4.2.2 Comparison Study on the Symmetrical and Asymmetrical Vertical Heterostructures ... 89

4.3 Conclusion ... 95

4.4 Contribution Statement ... 96

Chapter 5 Operational Limits and Failure Mechanisms in All-2D van der Waals Vertical Heterostructure Devices with Long-Lived Persistent Electroluminescence ... 97

5.1 Introduction ... 97

5.2 Result and Discussion ... 98
5.2.1 Fabrication of VLH EL Devices ... 98
5.2.2 Characterizations of 2D Materials and VHL EL Devices ... 101
5.2.3 EL of the Gr_B/h-BN/WS_2/h-BN/Gr_T VLH ... 103
5.2.4 The Red Shift on the EL Mapping ... 107
5.2.4 Study on the Mechanism of the Failure and Operation Limits for the VLH EL ... 109

5.3 Conclusion ... 116

5.4 Contribution Statement ... 117

Chapter 6 Ultrathin 2D Photodetectors using Transition Metal Dichalcogenides $PtSe_2$–WS_2–$PtSe_2$ by Direct Laser Patterning ... 118

6.1 Introduction ... 118

6.2 Results and discussion ... 119
6.2.1 Synthesis and Characterizations of $PtSe_2$ Thin Film ... 119
6.2.2 Device Fabrication of $PtSe_2$-WS_2-$PtSe_2$ Photodetector ... 123
6.2.3 Optoelectronic Characterization $Ptse_2$-WS_2-$Ptse_2$ Photodetector ... 126

6.3 Conclusion ... 133

6.4 Contribution Statement 134
Chapter 7 Conclusion and Future outlook.. 135
7.1 Thesis Summary.. 135
7.2 Future Outlook 137
Appendix A: Fitting procedures for PL and Raman spectra............. 139
References.. 145

Chapter 1 Introduction

1.1 Project Aim

The aim of this doctoral project is to explore the applications of chemical vapor deposition (CVD)-grown 2-dimensional (2D) materials in electronic and optoelectronic devices, with a particular focus on heterostructures in both vertical and lateral configurations. The building blocks utilized for device fabrication include graphene, WS_2, h-BN, and $PtSe_2$. CVD was chosen for the growth of 2D materials due to its suitability for large-scale synthesis and its ability to provide a sufficient number of devices for reproducibility.

1.2 Layout of this Thesis

This thesis presents the research conducted during my DPhil study at the Department of Materials, University of Oxford. It begins with a concise literature review in Chapter 2, which covers the fundamentals of 2D materials and heterojunctions, as well as the advancements in electronic and optoelectronic devices based on 2D materials. Chapter 3 outlines the comprehensive methodology employed throughout the project, including v2D-material synthesis, characterization techniques, device fabrication, and electrical/optoelectrical measurements.

Chapter 4 summarizes my work on an asymmetrical vertical heterostructure of graphene/WS_2/h-BN/graphene using all CVD-grown 2D materials. Layer-by-layer controlled assembly techniques were employed to create a crossbar geometry with

graphene electrodes at the top and bottom. The structure incorporates a continuous multi-layered h-BN film as a tunnel barrier and a layer of WS_2 single-crystal domains as the photoactive material. The introduction of the h-BN layer significantly enhances the photovoltaic effect compared to a symmetrical structure without the h-BN layer. Chapter 5 focuses on the high-performance ultrathin all-2D light-emitting devices with a vertical heterostructure of graphene/h-BN/WS_2/h-BN/graphene. These devices exhibit strong red electroluminescence (EL) and demonstrate continuous operation for over 2 hours under atmospheric conditions. The success rate of EL emission in these devices is over 90%. The breakdown mechanism in these devices is attributed to the oxidation of the top graphene contact when exposed to air under high bias voltages. Chapter 6 investigates the optoelectronic properties of a metal–semiconductor–metal (MSM) photodetector with a lateral heterostructure of $PtSe_2$–WS_2–$PtSe_2$. The multi-layered $PtSe_2$ thin film was synthesized by thermally assisted selenization of Pt thin film, and the device channel was fabricated using direct laser patterning.

Chapter 7 summarizes the results of my DPhil study and discusses the prospects for future research.

Chapter 2 Literature Review

2.1. Introduction

Graphene has attracted people's attention for decades since it was first isolated from graphite by Geim and Novoselov in 2004.[1] Due to its unique one-atom thickness, graphene exhibits extraordinary properties and is widely used in various fields, including thermal management, electronics, and engineering.[2-3] More recently, interest has expanded to other 2D materials beyond graphene, such as transition metal dichalcogenides (TMDs) with various band structures and insulating hexagonal boron nitride (h-BN).[4] Similar to graphene, these layered 2D materials can be isolated from their bulk counterparts, and new properties start to emerge as the thickness reaches the physical limit of a monolayer.[5] These layered 2D materials have strong intralayer chemical bonds and weak interlayer van der Waals (vdW) interactions, which provide a viable way to construct new artificial heterostructures with novel properties by easily stacking and assembling different 2D materials together via vdW interaction. Their intrinsic properties, such as ultrathin thickness, high transparency, and high flexibility, make layered 2D materials excellent candidates to meet the demanding needs of nanoscale high-performance next-generation electronic and optoelectronic devices.[6]

In this chapter, I will first introduce various kinds of 2D materials, covering their crystal structures and electronic/optoelectronic properties. Graphene is a conducting material with a unique zero-band gap structure, where the valence band and conduction band meet at the Dirac point. The low density of states near the Dirac point and the poor screening due to the ultrathin nature of graphene allow for effective

changes of carrier densities via doping and electric fields.[7] Monolayer TMDs, such as molybdenum disulphide (MoS_2) and tungsten disulphide (WS_2), are direct-band gap semiconductors in their monolayer form, exhibiting strong light-matter interactions due to their high absorption coefficients.[5,8,9] Hexagonal boron nitride (h-BN), which is atomically flat and chemically inert with a large band gap (~6 eV), serves as an ideal insulating material for tunnelling barriers or encapsulation.[10] While mechanical exfoliation can achieve high-quality layered materials and supports extensive fundamental research, its low production yield, wide thickness distribution, small domain size, and uncontrollable flake shape limits its industrial application.[11] In contrast, bottom-up methods, such as chemical vapor deposition (CVD), are more favourable for large-scale production. This chapter also provides an overview of the fundamentals of 2D heterostructures, including TMDs-based vdW heterojunctions and metal–semiconductor junctions. It focuses on graphene/TMDs stacks in both vertical and lateral configurations, where graphene serves as a good alternative for metal electrodes.[12] Additionally, this chapter covers recent advancements in heterojunction assembly, with a special focus on the aligned transfer method for layer-by-layer stacking of 2D materials. Since monolayer TMDs and TMDs stacks have unique band structures and highly efficient photon-to-charge conversion processes, the last part discusses the applications of TMDs in electronic and optoelectronic devices.[13,14]

2.2 Fundamentals of 2D Materials

This part focuses on the atomic structure and electronic properties of three extensively studied 2D materials: graphene, TMDs, and h-BN. Understanding these

properties is essential for further exploration of their applications in electronic and optoelectronic devices with heterostructures.

2.2.1 Graphene

Graphene is a 2D crystal lattice with a honeycomb structure that is only one atom thick, serving as the elemental building block of graphite, as shown in Figure 2.1.[3] It consists solely of carbon atoms that form strong bonds with their adjacent neighbours via sp^2 hybridization. The resulting σ bond, formed by the overlapping sp^2 orbitals, adopts a trigonal planar geometry, leading to the hexagonal planar structure of graphene. The C-C σ bond has a length of 1.42 Å. In addition to the three outer shell electrons that are σ-bonded with neighbouring atoms, the remaining electron in the p_z orbital, perpendicular to the graphene plane, forms a delocalized π orbital.[15]

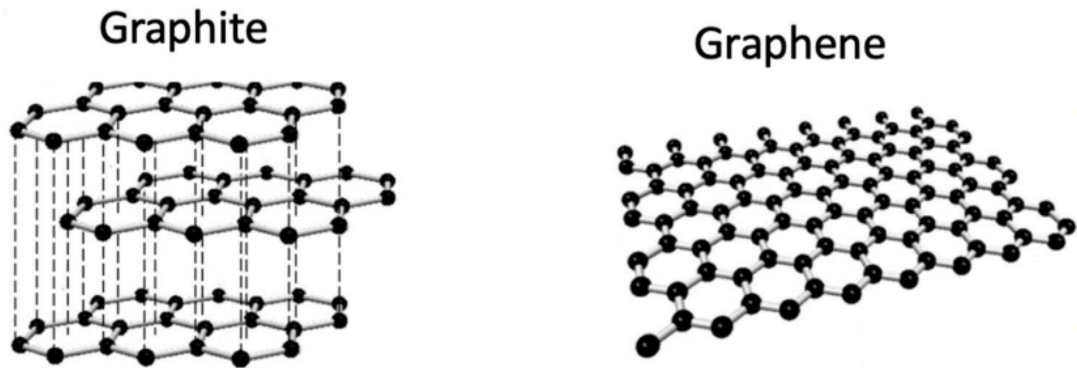

Figure 2.1 Graphene crystal lattice isolated from graphite.[16] Reproduced with permission.

Graphene is known as a zero-band gap semi-conductor because its conduction band and valence band connect with each other at six Dirac points located at the boundaries of the first Brillouin zone, known as Dirac points, as shown in Figure 2.2.[15] Electrons near the Dirac point (within 1 eV) have a linear dispersion relationship with a Fermi velocity of $v_F = 10^6\ m/s$, known as low-energy, massless Dirac Fermions. In graphene, Dirac fermions can tunnel through potential barriers of arbitrary height

and width, resulting in a transmission probability approaching 1 for some angles.[17,18] The unique crystal lattice and band structure of graphene endow it with many exceptional electronic properties. Electron mobility (μ) is a crucial parameter that describes the electronic properties of materials and is often limited by scatterings. In graphene, scattering can arise from multiple factors, including charged impurities, ripples/corrugations, defects, edges, strain, mid-gap states, surface-adsorbed atoms, electron-electron interaction and electron-phonon scattering.[19–23] The impurity-induced scatterings can be largely eliminated by current annealing of graphene samples.[24,25] For suspended monolayer graphene, μ can exceed 200,000 cm^2/Vs at low temperature (5K) and is predicted to be over 200,000 cm^2/Vs at room temperature when extrinsic disorders are eliminated. In this regime, the carriers approach near-ballistic transport.[24,26–28] For graphene supported by substrates, the presence of underlying substrates can lead to adsorbed contaminants, trapped states, and interfacial phonons, all of which can significantly reduce the mobility of graphene.[24] The mobility of graphene greatly reduces to 40,000 cm^2/Vs when an amorphous SiO_2 substrate is placed underneath it.[29] However, atomically flat and inert h-BN layers, which can be mechanically exfoliated from ultrapure h-BN single crystal synthesized by Watanabe and Taniguchi, serves as an exception among underlying substrates.[30,31] The standard deviation (σ) of the height distribution for monolayer graphene supported by h-BN can be reduced to 21 ± 2 pm, significantly lower than that observed underneath a SiO_2 substrate (σ = 154 pm).[32,33] This indicates that h-BN provides a much smoother surface compared to SiO_2. The mobility of mechanically exfoliated monolayer graphene on h-BN layers can be improved to 100,000 cm^2/Vs. To further enhance its properties, graphene can be encapsulated with top and bottom h-BN layers, which isolate it from

ambient scattering sources and make it less sensitive to the environment.[34,35] The carrier mobility of mechanically exfoliated graphene in h-BN/graphene/h-BN stacks can reach over 1,800,000 cm^2/Vs at low temperature (9K).[36] Similarly, for CVD-grown graphene at low temperature, the carrier mobility in h-BN/graphene/h-BN stacks can reach 320,000 cm^2/Vs.[37,38] However, the zero-band gap nature of graphene prevents it from achieving a low off-state current, which limits its application in digital logic transistors.[39,40] On the other hand, graphene's high transparency makes it suitable for use as a transparent electrode in optoelectronic devices.

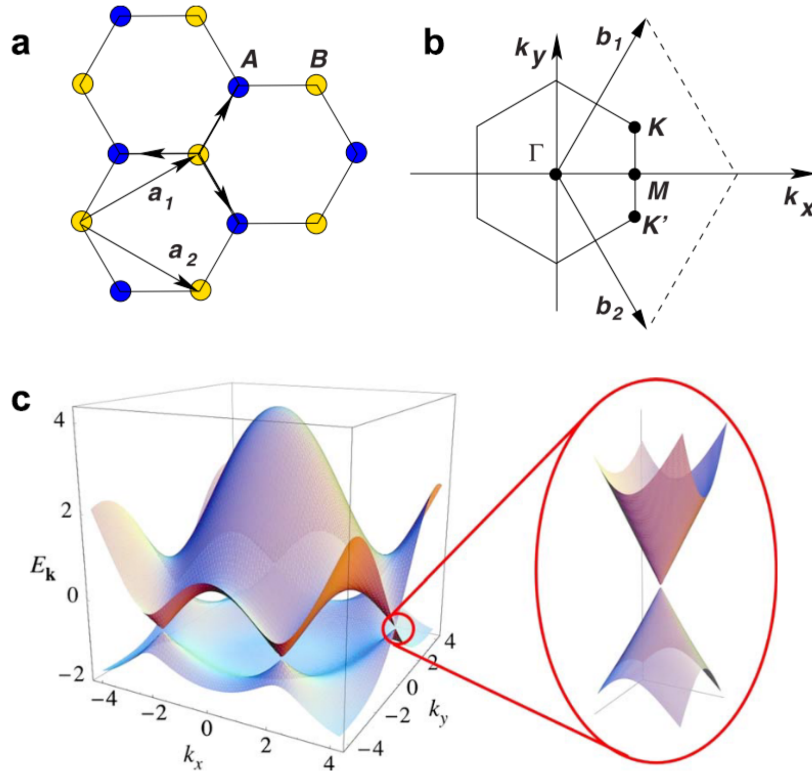

Figure 2.2 (a) Graphene crystal lattice (A and B are non-equivalent). $\boldsymbol{a_1}$ and $\boldsymbol{a_2}$ are the lattice unit vectors. (b) First Brillouin zone of graphene (K and K' are non-equivalent). $\boldsymbol{b_1}$ and $\boldsymbol{b_2}$ are the unit vectors in reciprocal lattice. (c) Electronic band structure of graphene. The conduction band and valence band are asymmetrical and meet each other at 6 Dirac points (as shown in the inset). This band structure was calculated under the tight-binding approximation.[15] Reproduced with permission.

2.2.2 TMDs

TMDs are represented in the form of MX_2, where M represents a transition metal atom (elements from group IV, V, VI, VII, IX, or X), and X represents a chalcogen atom (S, Se, Te), as shown in Figure 2.3a.[40] Transition metal atoms are covalently bonded with adjacent chalcogen atoms to form a sandwiched structure as shown in Figure 2.3b. TMDs layers are weakly stacked together via vdW interactions in various polymorphs, including 1T (trigonal), 2H (hexagonal), and 3R (rhombohedral). These numbers indicate the quantities of the X-M-X layers in a unit cell, forming the bulk counterpart of TMDs materials.[41] The electronic properties of TMDs vary from metallic to semiconducting, depending on their crystal structure and chemical compositions. For different combinations of M and X, both the 1T or 2H phase can be its thermodynamically stable phase, with the 1T phase exhibiting metallic behavior and the 2H phase exhibiting semiconducting behaviour in most cases. However, there are exceptions among MX_2 compounds with certain transition metals, such as Nb and Ta, where the 2H phase can exhibit metallic properties. Specifically, in the case of group VI TMDs (except for WTe_2), the semiconducting 2H phase is naturally thermodynamically stable, while the metallic 1T phase is metastable. [42,43] One of the most interesting properties of TMDs is their sizable bandgaps. The band structures vary with the number of layers, resulting in drastically different optoelectronic properties.[40]

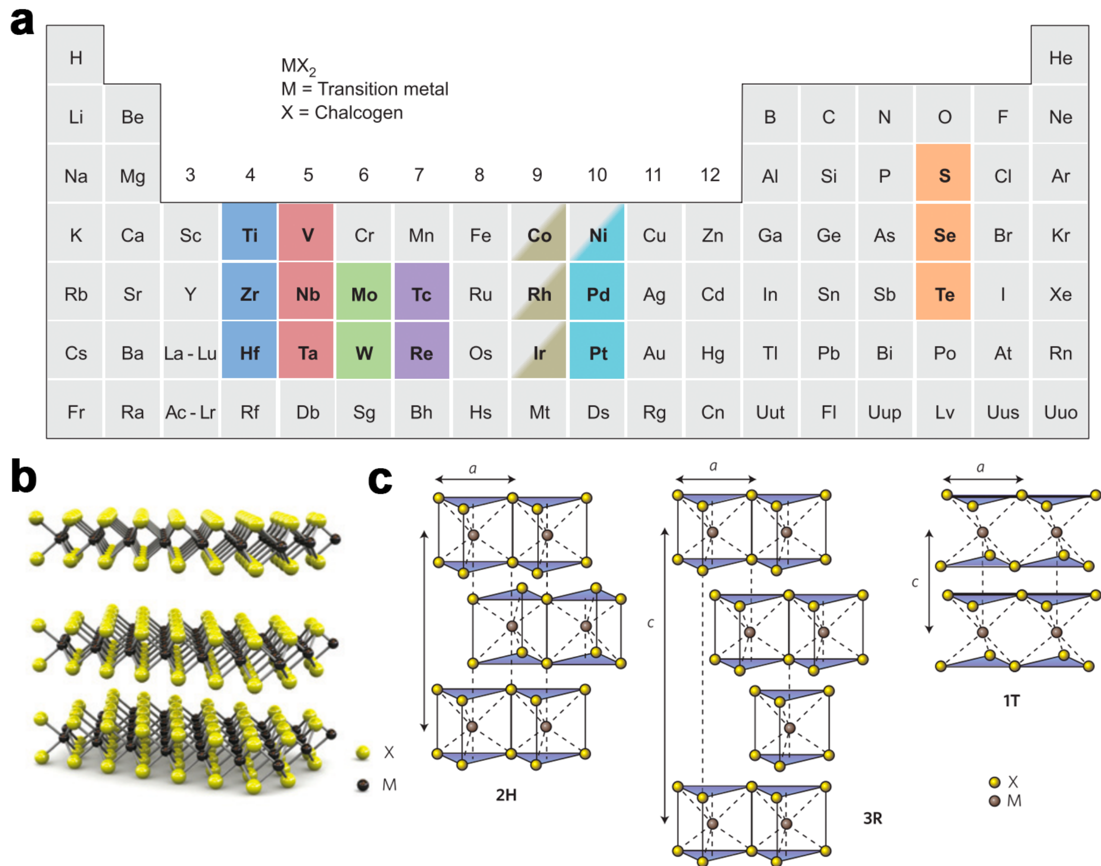

Figure 2.3 (a) The transition metal and chalcogen atoms are highlighted in the periodic table.[41] (b) Atomic structure of a typical TMDs, M is a transition metal atom and X is a chalcogen atom.[40] (c) Schematics of three polymorphs commonly encountered in TMDs: 2H, 3R, 1T.[40] Reproduced with permission.

Group VI TMDs

The band structures of group VI TMDs can be calculated using first-principles density functional theory and tight-binding approximation. These band structures can be further characterized through various spectroscopic analyses.[5,8,40,44,45] Figure 2.4a shows the calculated band structures for different layer numbers of MoS_2, where it undergoes a transition from an indirect-bandgap to a direct-bandgap as the layer number decreases from bulk to monolayer.[8] The band states at the K point remain almost unchanged with changing layer numbers while those around the Γ point shift a

lot, especially for those at the valence band.[41] The band states near the K point arise from the d orbitals (d_{z^2} $(l = 2, m = 0)$) of the Mo atoms. These states are not susceptible to interlayer coupling since the metal atoms are positioned in the middle of the S-Mo-S layered sandwich structure. On the other hand, the states near the Γ point are derived from the combination of the d orbitals ($d_{xy}, d_{x^2-y^2}$ $(l = 2, m = \pm 2)$) on the Mo atoms and the out-of-plane p_z orbitals on the S atoms located at the top and bottom of the layered structure. These states are highly sensitive to interlayer coupling.[5,46] When the layer number decreases from bulk to monolayer, the indirect gap undergoes a significant increase from 1.29 eV to over 1.90 eV, while the direct gap remains almost unchanged (only a 0.1 eV increase).[5] In monolayer MoS_2, the energy of the indirect transition around the Γ point is higher than that of the direct transition at the K point. As a result, the material undergoes a transformation into a direct-bandgap semiconductor. In a direct-bandgap material, the value of momentum at the bottom of the conduction band and that at the top of the valence band are the same. Therefore, a phonon is not required to interact with the electron to satisfy the momentum conservation law in band-to-band radiative recombination, where an excited electron in the conduction band recombines a hole in the valence band, emitting a photon to release the excess energy. On the other hand, in materials with an indirect bandgap, the conduction band minimum (CVM) and the valence band maximum (VBM) occur at different values of momentum. Therefore, in the case of radiative recombination in an indirect-bandgap material, three particles are involved: an electron, a hole, and a phonon. When an electron transitions from the conduction band to recombine with a hole from the valence band, it is necessary to interact with a phonon to ensure that the overall momentum is conserved in this process. [47] The

processes of radiative recombination compete with non-radiative recombination mechanisms, such as Auger recombination. In Auger recombination, an electron in the conduction band combines with a hole in the valence band, transferring the excess energy to another electron and exciting it to a higher excited state.[48] For indirect-bandgap materials, such as multilayer MoS_2, non-radiative recombination is the dominant process.

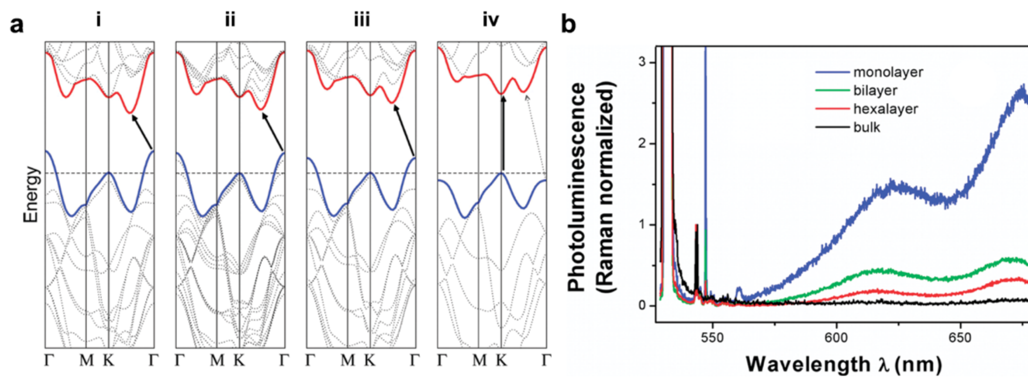

Figure 2.4 (a) The band structures of i) bulk, ii) four layers, iii) bilayers, iv) monolayer MoS_2 calculated from first-principles density functional theory (DFT).[8] (b) Normalized PL spectra for MoS_2 with different layer numbers (from monolayer to bulk). [8]

Photoluminescence (PL) spectroscopy can be used to characterize the radiative recombination of the electron–hole pair excited by the incident light with energy higher than the bandgap. The excited electron–hole pair is bound together by the electrostatic Coulombic interaction, forming an exciton that can be evaluated by its binding energy.[49] The binding energy of the monolayer TMDs is significantly higher than that of bulk semiconductors, primarily due to the quantum confinement effect and reduced dielectric screening.[49–51] The calculations indicate that the binding energy in monolayer MoS_2 is twice as much as that in bilayer MoS_2.[50] The strongly bounded excitons in monolayer TMDs are less inclined to dissociate into free charge carriers

than those in their multilayer and bulk counterparts. The quantum yield of PL relies on the possibility of radiative recombination. As shown in Figure 2.4b, monolayer MoS_2 with direct bandgap exhibits strong PL emission at 1.83 eV (~677 nm) and 1.97 eV (~627 nm). In contrast, no PL emission is observed in bulk MoS_2.[8] The two emission peaks, known as A and B direct exciton transitions, arise from the spin-orbital splitting of the valence band in monolayer 2H-MoS_2. This splitting energy is measured to be 0.14, which is attributed to the lack of inversion symmetry in the material.[52] The PL emission in monolayer MoS_2 exhibits a significant enhancement compared to its multilayer or bulk counterparts. This observation is consistent with the calculated results showing the evolution of their band structures from a direct to an indirect bandgap.

The negative (positive) trion, composed of an exciton and an excess electron (hole) and labelled as X^-(X^+), has lower energy than the exciton and causes a redshift in the position of the PL emission. The binding energy of trions is the energy required to dissociate a trion into an exciton and an electron at the Fermi level, within a range of 10 to 40 meV.[53,54] The emission peaks corresponding to trions and excitons can be extracted from the PL emission peak by using multi-peak fittings. Figure 2.5a shows a PL spectrum (A) of monolayer WS_2 multi-peak fitted by Lorentzian functions, with extracted charge-neutral exciton emission (X) and negative trion emission (X^-).[55] The spectral weight of trions can be modulated by gate bias, temperature and excitation power. [56–59] As shown in Figure 2.5b, the spectral weight of trions decreases with increasing temperature, which can be explained by the fact that the thermal energy at higher temperature is sufficient to dissociate the trions into excitons and electrons.[57] The redshift of PL peak positions shown in Figure 2.5c with increasing temperature is

due to the decrease in the bandgap size caused by the thermal expansion of the lattice.[60,61] The low-energy shoulder observed in the PL spectra at low temperatures (4 K and 30 K) in Figure 2.5b is attributed to the superposition of the defect-bound (X^D) and biexciton (XX) emissions.[57] The defect-bound emission occurs when an exciton is trapped at lattice defects and recombines radiatively, resulting in an emission energy lower than that of the exciton emission.[62,63] A biexciton is a four-body state formed when two excitons are bound together, and the biexciton emission occurs at high exciton density.[57,64,65]

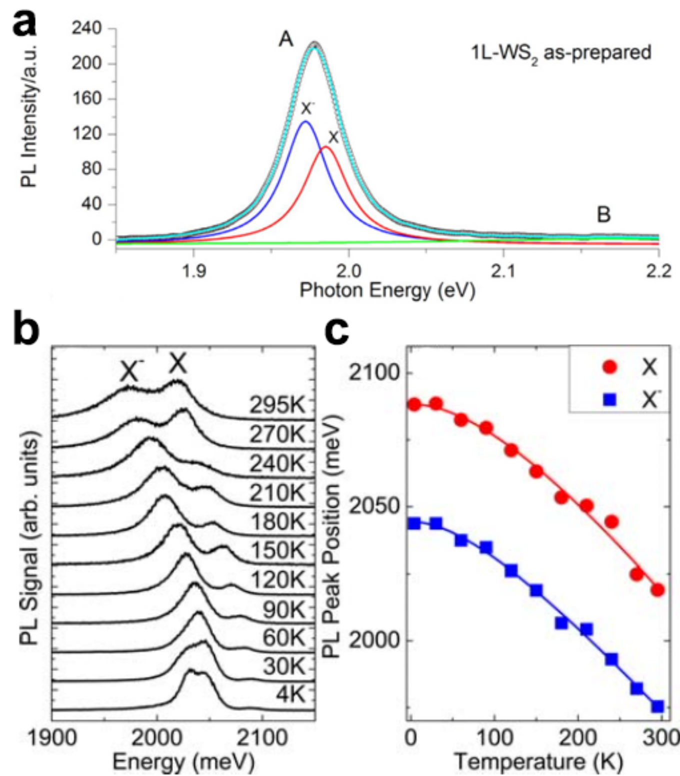

Figure 2.5 (a) A PL spectrum of monolayer WS_2 multi-peak fitted by Lorentzian functions, with extracted charge-neutral exciton emission (X) and negative trion emission (X^-). [55] (b) Normalized PL spectra of monolayer WS_2 at different temperatures.[57] (c) The redshift of peak positions of X and X^- with increasing temperature.[57] Reproduced with permission.

Group X TMDs

Unlike the direct-to-indirect bandgap transition observed in group VI TMDs, group X TMDs, such as $PtSe_2$ and $PdSe_2$, exhibit a semimetal-to-semiconductor evolution with decreasing thickness. For instance, monolayer $PtSe_2$ has an indirect bandgap of 1.17 eV,[66] with a predicted mobility as high as 4000 cm^2/Vs.[67] The monolayer to multi-layered $PtSe_2$ semiconductor, with a tunable bandgap ranging from 0 to 1.17 eV, is promising for electronic and optoelectronic devices.[68–71] Bulk $PtSe_2$ exhibits a slightly indirect overlap between the conduction band minimum (CBM) and the valance band maximum (VBM), which is a characteristic band structure of a semimetal.[66,72] The conductivity of bulk $PtSe_2$ with a thickness of 64 nm demonstrates a high conductivity, reaching 6.2×10^5 S/m at 50 K, which makes bulk $PtSe_2$ a promising material for 2D electrodes beyond graphene. [66]

2.2.3 h-BN

Monolayer h-BN, known as ‘white graphene’, has a similar layered crystal lattice with graphene.[73] In a single layer of h-BN, boron and nitrogen atoms are arranged alternatively in a hexagonal honeycomb lattice, without any additional dangling bonds.[74] The h-BN possesses a wide bandgap of 5.955 eV, exhibiting potential for ultraviolet emission at a wavelength of around 215 nm.[73,75] Moreover, h-BN is an insulating material that is chemically inert, resistant to oxidation, and exhibits high thermal stability, thermal conductivity, and mechanical strength.[76–78] These properties make h-BN essential for assembling van der Waals heterostructures, and hold promise for various applications in electronics. It can be utilized as an insulating layer or an encapsulation material, for example, as an ultrathin gate dielectric for transistors and

a defect-free dielectric for tunnelling devices.[30,79,80] Watanabe and Taniguchi successfully exfoliated high-quality h-BN layers with atomically flat surfaces from synthesized ultrapure h-BN single crystals.[30,31,81] By utilizing these exfoliated h-BN layers to encapsulate graphene, the root-mean-square roughness of the suspended sandwich stack can be reduced to 12 ± 5 pm.[32] In contrast, polycrystalline h-BN layers grown by CVD exhibit increased roughness and poor uniformity.[82,83]

2.3 Synthesis of 2D Materials

There are two mainstream strategies for synthesizing 2D materials: the top-down route (from bulk materials to its layered 2D counterparts) and the bottom-up route (from the molecular level to the final 2D crystal).

2.3.1 Top-down Route

The top-down synthesis approach is to peel off single- or multi-layered materials from their corresponding bulk crystals. One primary method is to mechanically exfoliate the bulk materials using adhesive tapes, as demonstrated by Geim *et al.* in the first isolation of graphene from highly oriented pyrolytic graphite.[1] Bulk materials can be obtained from naturally occurring minerals like graphite and molybdenite, as well as chemically synthesized crystals.[84]

As shown in Figure 2.6, the process of peeling off the material into nano-sheets involves applying normal force to the bulk materials by attaching Scotch tape directly to the surface and then peeling off thinner materials from the bulk crystal.[85]. Surface pre-treatment of the target substrate, such as oxygen plasma cleaning, can effectively remove the ambient absorbates. This process leads to better contact and adhesion between the substrate and materials, resulting in improved production yield of few-

layered flakes.[86] While mechanical exfoliation is capable of obtaining high-quality layered materials that are beneficial for fundamental research, it presents challenges for industrial applications due to its low production yield, wide thickness distribution, small domain size, and uncontrollable flake shape.[11]

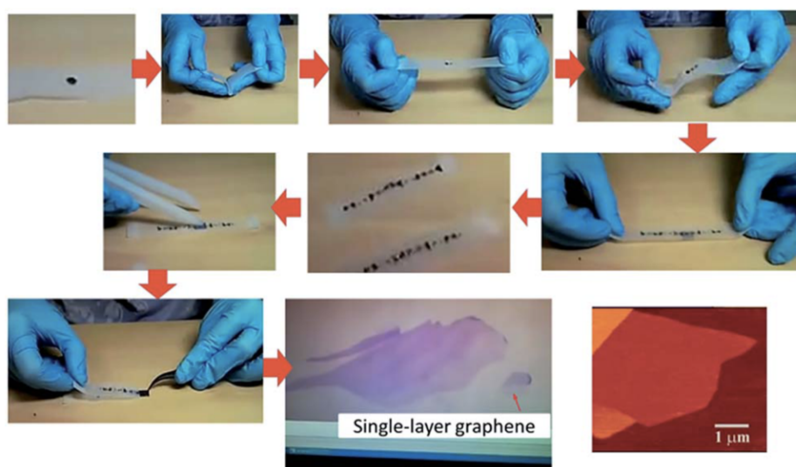

Figure 2.6 Schematics of the mechanical exfoliation process. [85] Reproduced with permission.

With the assistance of mechanical force, ion intercalation, or ion exchange, liquid exfoliation has been developed to increase the production yield and obtain free-standing samples.[87–90] In mechanical force-assisted liquid exfoliation, such as sonication and sheared force, it is crucial to select a compatible solvent to disperse the target materials. One advantage of this strategy is that the thickness and the lateral size of the final layered materials can be easily regulated by adjusting the sonication time, sonication power, or the addition of surfactants.[11] However, the disadvantages, including low monolayer production yield, relatively small lateral sizes, defects introduced during sonication, and residuals of surfactants on obtained nano-sheets, should not be ignored. The mechanism of ion-assisted liquid exfoliation is as follows: ions intercalate between adjacent layers or larger ions replace previous ions within the

layered crystals to enlarge the interlayer spacing and weaken vdW interactions, followed by agitation (such as sonication) of the solvent to separate each layer. Hydrogen gas generated during the reaction of the intercalated ion compound (such as organolithium, e.g., n-butyllithium) with the aqueous solvent accelerates the exfoliation process.[88,89] Zheng *et al.* reported a two-step liquid exfoliation method that achieves a high yield of monolayer MoS_2 (90%) and larger lateral size by pre-exfoliation with hydrazine (N_2H_4) before the intercalation of metal naphthalenide.[91] However, the long reaction time, the potential danger of organometal compounds, and the uncontrollable ion intercalation/exchange process limit the widespread application of this method.[11]

2.3.2 Bottom-up Route

Bottom-up methods involve the growth of layered materials from precursor feedstock, typically at high temperatures. Gaseous precursors can react on the surface of the substrates, enabling the growth of monolayer 2D materials with a large surface area and a high degree of control. One method commonly used for bottom-up growth is Molecular Beam Epitaxy (MBE), shown in Figure 2.7a. MBE utilizes an ultrahigh vacuum chamber and high-purity elemental source materials to grow 2D monolayer crystals.[92] Another widely employed technique is chemical vapour deposition (CVD), which offers a more robust and practical way to grow large-scale materials due to less required vacuum pressure and less complicated instrumentation. Both MBE and CVD have achieved wafer-scale synthesis of high-quality 2D materials.[43] As shown in Figure 2.7b, CVD relies on the chemical reaction of gaseous molecules in the vapour phase, which can either be deposited on a solid substrate or occur directly on a solid

substrate.[93,94] In CVD growth, various parameters, such as temperature and pressure of the chambers, concentration and types of the precursors, and the substrate, collectively play critical roles in the nucleation and growth of the 2D crystal. These parameters ultimately influence the thickness, shape, size, orientation, and doping level of the synthesized 2D crystal.[93]

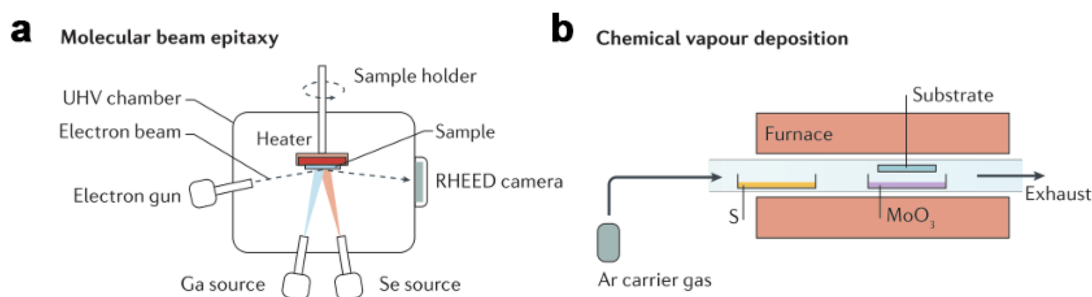

Figure 2.7 Schematics of setups for (a) Molecular Beam Epitaxy (MBE) and (b) Chemical Vapour Deposition (CVD)[43]. Reproduced with permission.

Figure 2.8a-b illustrates two main mechanisms of CVD growth of graphene: the segregation process and the surface absorption process, using Ni and Cu as growth substrates/catalysts, respectively. In the case of Ni substrates, carbon atoms are dissolved into Ni at high temperatures and then segregate from the Ni surface to form graphene during the cooling process. This is due to the high carbon solubility of Ni.[95] The cooling process influences the segregation behaviour and determines the thickness of graphene.[96] A fast cooling rate prevents carbon atoms from segregation, as the substrate is quickly quenched. A medium cooling rate allows for the proper segregation of carbon atoms. In a slow cooling process, carbon atoms have enough time to diffuse into the Ni body rather than segregating at the Ni surface. The microstructure of the Ni lattice, particularly the presence of grain boundaries, is also critical for the final morphology of graphene.[95] The grain boundaries present on the

polycrystalline Ni surface serve as nucleation sites for multilayer graphene. Therefore, Ni substrate is always first treated with thermal annealing by H_2 to enhance the quality of the graphene, as this process leads to an increased grain size and a flattened surface.[96–99] In this way, the uniformity of the graphene film is largely influenced by the grain size of polycrystalline Ni. Copper (Cu) substrates behave differently from Ni due to their low carbon solubility, resulting in most carbon atoms being adsorbed on the Cu surface and forming graphene. When the Cu surface is fully covered, the absence of a Cu catalyst hinders the decomposition of hydrocarbons, thereby limiting the growth of a second layer of graphene.[100] Cu substrates are widely used for monolayer graphene growth after it was first developed by Ruoff and his co-workers.[101]

Although the first CVD growth of TMDs thin films on various substrates can be attributed to Wolfgang K. Hofmann's work in 1988,[102] the successful synthesis of monolayer or few-layered 2D films or single crystal domains has only been achieved recently.[103–105]. In 2012, Li *et al.* synthesized large-area MoS_2 thin films with a thickness of only three layers using a two-step thermolysis process.[105] As shown in Figure 2.8c, the process involved dip-coating the insulating substrate with ammonium thiomolybdates ($(NH4)_2MoS_4$). The precursor then underwent a chemical change to MoS_3 during thermal annealing at 500 ℃, followed by transformation to MoS_2 with the addition of S under a second annealing step at 1000 ℃. The introduction of sulphur in the second step aimed to enhance the crystallinity of MoS_2, while the two-step process was developed to avoid the use of H_2 atmosphere, which can cause the decomposition of MoS_2 at high temperatures. These synthesized MoS_2 thin films possess good semiconductor electronic properties, with an ON/OFF ratio of ~ 10^5 and

an electron mobility of up to 6 cm^2/Vs. Another commonly used precursor for CVD growth TMDs is the transition metal oxide powders.[103,106,107] Pioneer work has been conducted by Lee and his co-workers on the synthesis of MoS_2 thin film using MoO_3 powders. In their study, MoO_3 powder exposed to sulphur vapor was reduced to gaseous MoO_{3-x}, which was then deposited onto the solid substrate followed by further sulfurization into a MoS_2 thin film.[106]

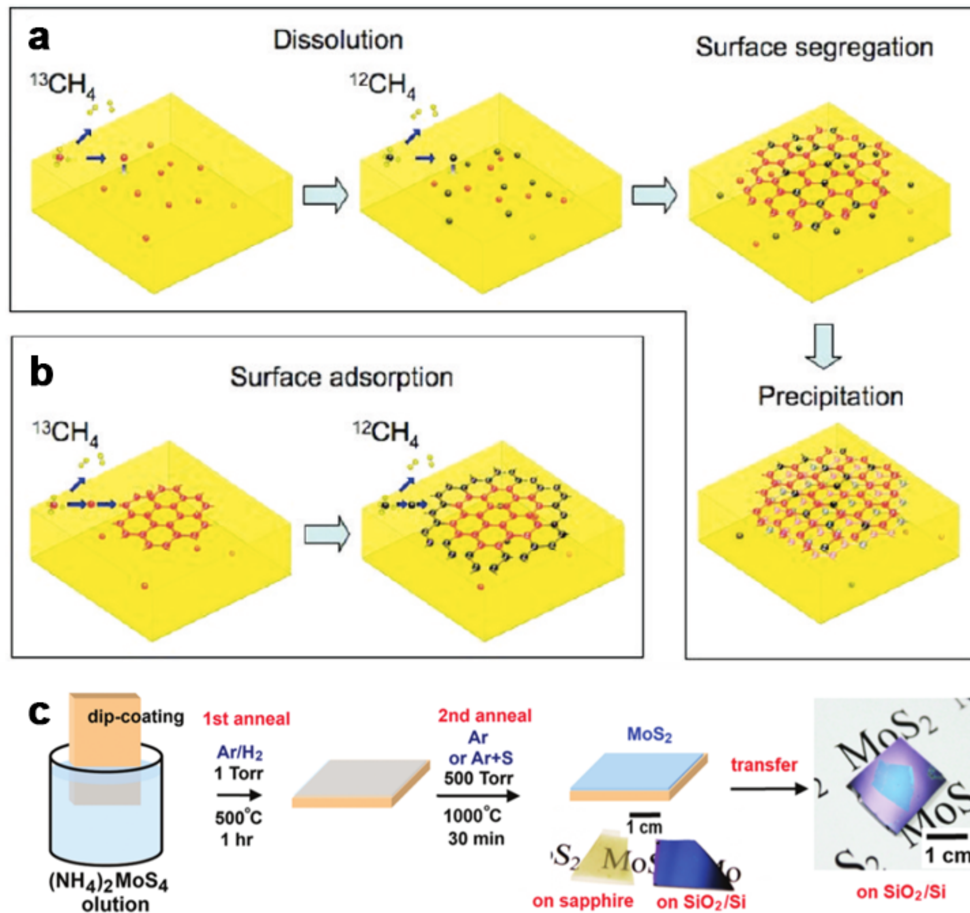

Figure 2.8 Schematics of two mechanisms for CVD growth graphene: (a) segregation process;[100] (b) surface adsorption process.[100] (c) Schematics of a two-step thermolysis process for synthesis of MoS_2 thin films.[105] Reproduced with permission.

The h-BN thin film can be synthesized by CVD on various catalytic metal substrates, such as Cu, Ni, and Pt.[10,74,108–110] Song *et al.* first reported a large-scale

growth of h-BN atomically thin film with 2~5 layers on copper foil in 2010.[108] By applying thermal annealing to polycrystalline metal substrates, the enlarged grain size of the metal decreases the nucleation density of h-BN and increases the h-BN grain size and surface flatness.[111] Wang *et al.* synthesized a monolayer h-BN film with a large grain size of 20 μm by annealing the copper foil before CVD growth at 1050 ℃ for 6h.[112] Another improvement made to increase the h-BN domain size is polishing the metal substrate.[83,113] Tay *et al.* reported h-BN single crystals with a grain size of 35 μm by using the electropolished copper substrate.[83] Precursors for h-BN growth can be both single and mixture components, such as diborane/ammonia (B_2H_6/NH_3), borazine ($B_3N_3H_6$), and ammonia borane (BNH_6).[109,114–116] Ammonia borane is a preferable single-component precursor due to its 1:1 B:N stoichiometry nature and stability in ambient conditions.[117] Ammonia borane is dehydrogenated to borazine ($B_3N_3H_6$) at a low-temperature range (< 135 ℃) and carried via gas flow to the substrate.[117] The BN nanoparticles formed during the transportation of borazine are deposited on the h-BN film, which is the main source of contaminants.[118]

Liu *et al.* reported an alternative method for growing h-BN using atmospheric pressure and high temperature (APHT).[119,120] In this method, high-purity elemental boron powder and flowing nitrogen gas serve as the sources of B and N, respectively, for the resulting single crystal of BN. A mixture of boron, nickel, and chromium powder is placed in an alumina crucible, which is then loaded into an alumina tube furnace. N_2 and H_2 gases flow through the tube at a pressure of 850 Torr, and the growth process takes place at 1550 ℃. After the cooling process, h-BN precipitates on the metal surface, and the crystals are exfoliated for subsequent use. The maximum crystal size can reach approximately 1 mm. The h-BN crystals synthesized using the

aforementioned method have a low defect density. The electronic transport properties of graphene encapsulated by APHT-grown h-BN are comparable to those encapsulated by h-BN exfoliated from ultrapure h-BN single crystals synthesized via high-pressure high-temperature (HPHT) methods, as provided by K. Watanabe and T. Taniguchi.[30,31]

As shown in Figure 2.9a-b, CVD,[121] chemical vapor transport (CVT)[66] can produce high-quality $PtSe_2$ but requires high growth temperatures and low-pressure vacuum conditions. CVT is a typical approach for synthesizing bulk crystals using non-volatile solids.[122] The non-volatile precursor is carried by a transport agent and deposited on the substrate.[123,124] The most significant difference between CVD and CVT is that the precursor is not volatile before the chemical reaction occurs during CVT. Thermally assisted selenization[70,125] and plasma-assisted selenization[126] are able to synthesize $PtSe_2$ thin films from monolayer to bulk at lower temperatures (usually < 400 °C), which can be used in applications with less strict requirements for crystal quality, as shown in Figure 2.11c-d. Monolayer $PtSe_2$ grown by thermally assisted selenization was first reported by Wang *et al.* in 2015.[125] It is described as a one-step precursor-free process, where the vaporized Se powder in a furnace tube (heated to 270 °C) reacts with pre-deposited Pt layer on a substrate to form $PtSe_2$ thin film. The thickness of $PtSe_2$ can be tuned by the thickness of the Pt layer, usually deposited by sputtering or evaporation.[127] Plasma-assisted selenization occurs at an even lower temperature of 100 °C. Similar with thermally assisted selenization, the Pt layer is first deposited onto a substrate, followed by a selenization process in a low-pressure chamber with a plasma power of 400 W.[126] The Se powder is individually heated to 250 °C in the tank placed above the chamber, and the vaporized Se was transported to

the substrate by N_2/H_2 flow. The thickness of the $PtSe_2$ layer can be controlled by plasma power and substrate temperature.

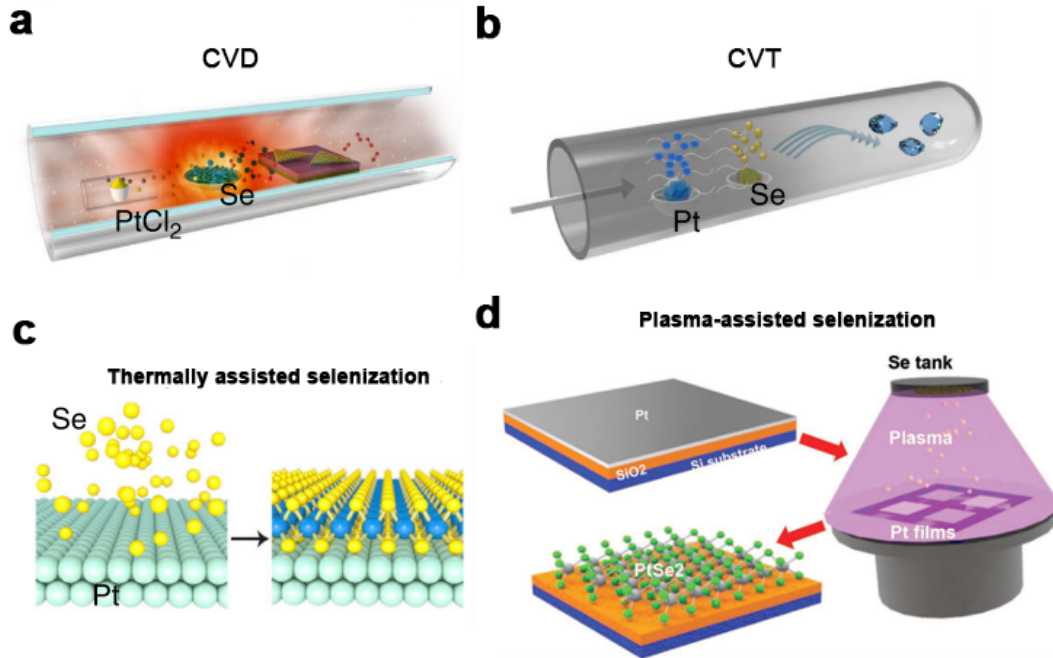

Figure 2.9 Bottom-up strategies to grow $PtSe_2$ thin film: (a) CVD;[128] (b) CVT;[128] (c)thermally assisted selenization;[128] (d) plasma-assisted selenization.[126] Reproduced with permission

2.4 Fundamentals of heterojunction

2.4.1 Van der Waals Heterostructures

Twisted stacks

As mentioned previously, layered 2D materials are free of dangling bonds and have weak interlayer van der Waals interactions. These features allow 2D materials to break the confinement of lattice matching and be freely stacked, enabling interlayer twists. Bilayer stacking can be achieved by CVD, yet this method yields a wide distribution of twist angles. Precisely controlling the twist angle through CVD still

remains a challenge.[129–131] In this way, mechanical stacking is a preferable approach to overcome this challenge. The 'tear and stack' technique has been developed to enable precise control of the twist angle. In this technique, half of the 2D flake is first torn off and picked up. Then, the remaining half of the 2D flake is rotated by a specific angle before being picked up and stacked with the first part.[129,132] A periodic moiré superlattice can be produced in a twisted bilayer graphene system.[133] At the magic angle of ~ 1.1 °, the twisted bilayer graphene shows flat bands with vanishing Fermi velocities. In this configuration, the valence band maximum and conduction band minimum approach a common energy throughout the Moiré superlattice Brillouin zone.[129] Magic-angle twisted bilayer graphene (MATBG) demonstrates superconductivity at extremely low temperatures by tuning the carrier density via gate bias.[134] Additionally, researchers have been conducted on other twisted systems. For example, Moiré excitons have been observed in twisted bilayer TMDs systems such as $MoSe_2/WSe_2$ and WSe_2/WS_2, which is also associated with the modulation of the electronic band structure by Moiré superlattice.[135,136]

h-BN Encapsulation

The performance of devices based on 2D materials can be influenced by their surroundings due to their ultrathin nature. This includes scatterings originating from the substrates or surface adsorbates. As mentioned previously, h-BN possessed properties such as being insulating, chemically inert, resistant to oxidation and exhibiting high thermal stability, thermal conductivity, and mechanical strength.[76–78] Therefore, it is promising to use h-BN thin films as encapsulation materials for isolating 2D materials from ambient scattering sources. Furthermore, they can protect

unstable materials that are sensitive to air or water from rapid degradation in ambient conditions. [30,79]

Substrates, such as Si/SiO_2, usually lower the carrier mobility of graphene due to substrate-induced doping and scatterings. However, encapsulating graphene with h-BN layers has proven to be an effective method to improve the carrier mobility of graphene. When exfoliated h-BN flakes from high-quality single crystals are used for the encapsulation, the carrier mobility of exfoliated monolayer graphene in h-BN/graphene/h-BN stacks can reach up to 180,000 cm^2/Vs at room temperature and 1,800,000 cm^2/Vs at low temperature (9 K).[36] Even for CVD-grown graphene, which is less pristine than exfoliated samples, the mobility can reach 320,000 cm^2/Vs at low temperature, exhibiting nearly a tenfold increase compared to graphene on a silicon substrate.[37] Furthermore, Cadiz *et al.* showed that encapsulating monolayer MoS_2 with h-BN results in a significant reduction in the line width (full width at half maximum, FWHM) of the PL spectrum, down to 2 meV at $T = 4\,K$.[137] This substantial improvement in narrowing line width, compared to the typical reported FWHM of MoS_2 without encapsulation at low temperature (~ 50 meV), indicates that h-BN encapsulation plays an important role in surface protection as well as preventing MoS_2 from surrounding disorders.[137] In addition to stable materials like graphene and MoS_2, h-BN encapsulation can also be used for unstable materials, such as black phosphorous (BP), indium selenium (InSe), and hafnium disulfide (HfS_2). The utilization of h-BN serves to isolate these materials from their surrounding environments and provide protection against degradations.[138–141]

Type II Heterojunction

The stacking of different 2D materials provides a practical way for bandgap engineering. Figure 2.10a shows the theoretical band structures of monolayer and bilayer MoS_2, WS_2, as well as MoS_2/WS_2 heterojunctions, calculated using the Vienna *ab initio* package (VASP).[46] At the MoS_2/WS_2 heterojunction, strong interlayer coupling occurs, resulting in a band structure that can be considered as the superposition of the individual monolayers. The conduction band minimum (CBM) and valence band maximum (VBM) of the heterojunction are located at the K point, originating from the MoS_2 and WS_2 monolayer, respectively, as shown in the panel of Figure 2.10a. Consequently, the MoS_2/WS_2 stack forms a type II band structure (staggered gap) with a direct bandgap, which is smaller than the bandgap of the individual photoactive monolayer TMDs. The interlayer coupling in TMDs stacks can be easily tuned by inserting different numbers of insulating h-BN layers ($n = 0\sim3$) between the two TMD layers.[142]

The band alignment of the type II heterojunction in a vertical stack of MoS_2/WS_2 is shown in Figure 2.10b.[143] Hong *et al.* first reported the observation of ultrafast charge transfer occurring in a stack of MoS_2/WS_2.[143] The hole transfer from the MoS_2 monolayer to the WS_2 monolayer occurs within 50 fs after photoexcitation.[143] Chen *et al.* suggested a two-step process for charge transfer in a van der Waals vertical heterostructure of MoS_2/WS_2, as shown in Figure 2.10c.[144] Under photoexcitation, electron–hole pairs are generated in each TMDs layer. In the first step, holes (electrons) transfer from MoS_2 (WS_2) to WS_2 (MoS_2) in less than 50 fs, forming interlayer hot excitons (intermediate states). The formation of interlayer hot exciton is much faster than that of the intralayer exciton. In the second step, the

hot excitons relax their excess energy to form tightly bound excitons with lower binding energy and larger electron–hole distance within approximately 800 fs.[144] Additionally, it has been reported that the exciton lifetime in $MoSe_2/WSe_2$ heterojunction is one order of magnitude longer than that in their monolayer individuals.[145] The fast charge transfer at the heterojunction and long interlayer excitonic lifetime are crucial for the electron–hole separation following photoexcitation, which influences the generation of photocurrent.[145,146] Therefore, these prominent optoelectronic properties make stacked TMDs a promising choice in the design of ultrathin light-harvesting devices.[147,148]

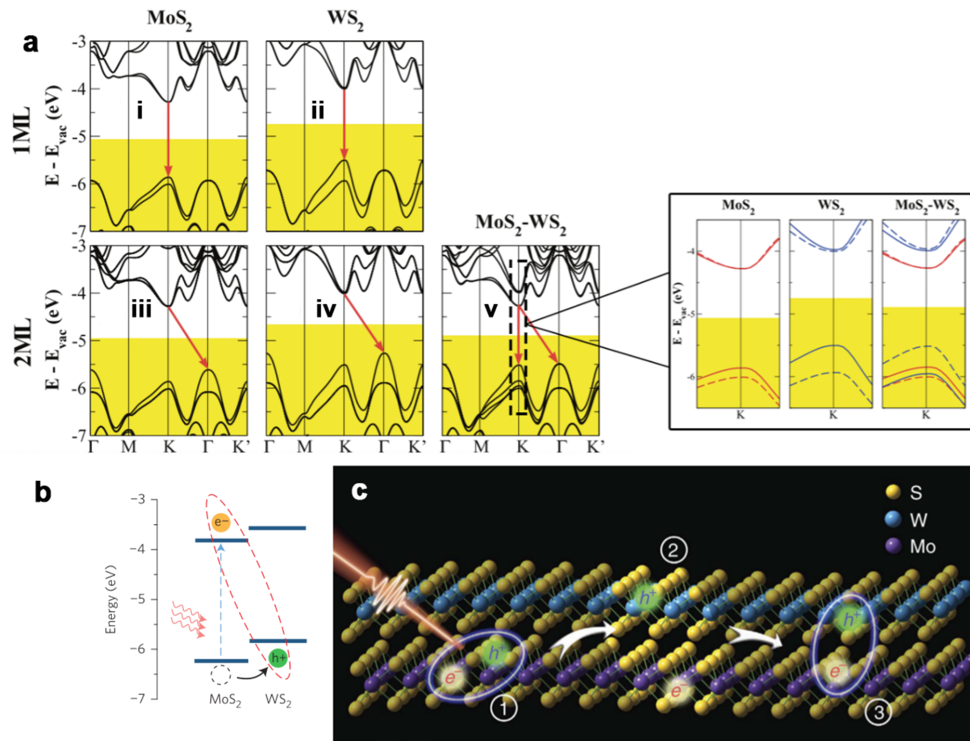

Figure 2.10 (a) Calculated band structures of monolayer (i) MoS_2, (ii) WS_2, bilayer (iii) MoS_2, (iv) WS_2, and (v) MoS_2/WS_2 heterojunction.[46] Panel: zoom of the band structures at the *K* point for monolayer MoS_2, monolayer WS_2, and MoS_2/WS_2 heterojunction. (b) The band alignment of a MoS_2/WS_2 type II heterojunction.[143] (c) Schematic of the charge separation process in MoS_2/WS_2 heterostructure (using the charge transfer process in MoS_2 layer as an example): (1) generated electron-hole pairs in MoS_2 layer after photoexcitation; (2) the formation of the interlayer hot excitons by transferring of holes from MoS_2 to WS_2; (3) the formation of tightly bound interlayer excitons by releasing excess energy of interlayer hot excitons.[144] Reproduced with permission.

Graphene Contact

Another important development in the research of vdW heterostructure is the TMDs/graphene stacks, where TMDs serve as the photoactive semiconducting material and graphene acts as the metallic electrode.[149–151] The vdW gap between the 2D materials and metal electrodes leads to large contact resistances (R_c) due to the absence of dangling bonds on the 2D materials for covalent bonding with the metal. Selecting specific metals (e.g., Ni for graphene[152], Ti for MoS_2[153]) to form hybridizations with the 2D materials can reduce the R_c. However, this approach requires breaking the covalent bond within the atomically thin layer of the 2D material, which can introduce defects and simultaneously lead to Fermi level pinning.[12] Furthermore, traditional metal deposition techniques like thermal evaporation, can lead to surface degradation of the 2D material during the deposition process. In contrast, graphene serves as a good alternative to traditional metal electrodes because its vdW interaction with semiconducting 2D materials does not introduce any damage.[150,151] Additionally, because of its unique band structure, the Fermi level of graphene can be easily tuned through gate bias[154] or extrinsic doping[149]. The tunable Fermi level, accompanied by graphene's chemical stability, transparency, and ultrathin nature, makes graphene a promising candidate for a versatile electrode in the fabrication of all-2D ultrathin electronic and optoelectronic devices.

The two most common configurations of graphene contacts with 2D materials, especially with TMDs, are coplanar lateral heterostructures[148,150,155,156] and vertical heterostructures[149,157–160], as shown in Figure 2.11a, c. The former configuration results in devices with an ultrathin nature but low device density when integrated on a chip. Moreover, the long carrier transport distance to the electrodes hinders the

recombination process.[161] For coplanar lateral heterostructures utilizing traditional metals as electrodes, the careful selection of metals with an appropriate work function to align the band structure of the semiconductor can significantly reduce the Schottky barrier height. Das *et al,* conducted a systematical study on the influence of metal contacts on the performance of MoS_2 transistors.[162] The Schottky barrier heights for Pt, Ni, Ti and Sc were extracted as 230, 150, 50, and 30 meV, respectively. Accordingly, the corresponding mobility was extracted as 21, 90, 125 and 184 cm^2/Vs, respectively.[162] This finding suggested that the choice of metal contact significantly influences the carrier transport of the semiconductor. The extracted mobility of the semiconductor can be underestimated due to the contact resistance of the metal, and using a metal contact with lower contact resistance can result in higher mobility. By utilizing graphene as a contact to substitute traditional metals in coplanar lateral heterostructures, the Schottky barrier between TMDs and graphene can be significantly reduced, and even brought to zero, by tuning the Fermi level of graphene via vertical gate voltage.[150] A transistor with a lateral heterostructure of graphene/$MoSe_2$ and a high-κ ion-gel gate dielectric exhibits ambipolar transport characteristics by tuning the Fermi level of graphene through gate bias.[163] The transfer curve of the graphene/$MoSe_2$ is shown in Figure 2.11b. This ambipolar behaviour can be explained by the gate modulation of the graphene Fermi level. With a gate bias $<$ 0.5 V, the Fermi level of graphene is closer to the valence band of $MoSe_2$ than the conduction band, making holes the major carriers. With the increase of gate bias, the graphene becomes more n-doped. The Fermi level is closer to the conduction band, and electrons become major carriers. While graphene demonstrates superior performance as a contact, the exploration of other 2D electrodes for coplanar lateral

structure, such as semi-metallic multilayer $PtSe_2$, remains an area of future investigation for optoelectronic device fabrication. In vertical heterostructures with semiconducting TMDs, a large junction area can be obtained compared to lateral devices, and the shorter charge extraction distance facilitates efficient light harvesting.[157–159] Gate modulation, chemical doping, or the initial doping difference of the two graphene electrodes, results in a difference in the top and bottom graphene electrode potentials, which creates a built-in potential within the stack. This built-in electric field improves the generated photocurrent, as shown in Figure 2.11d.[149,157,158]

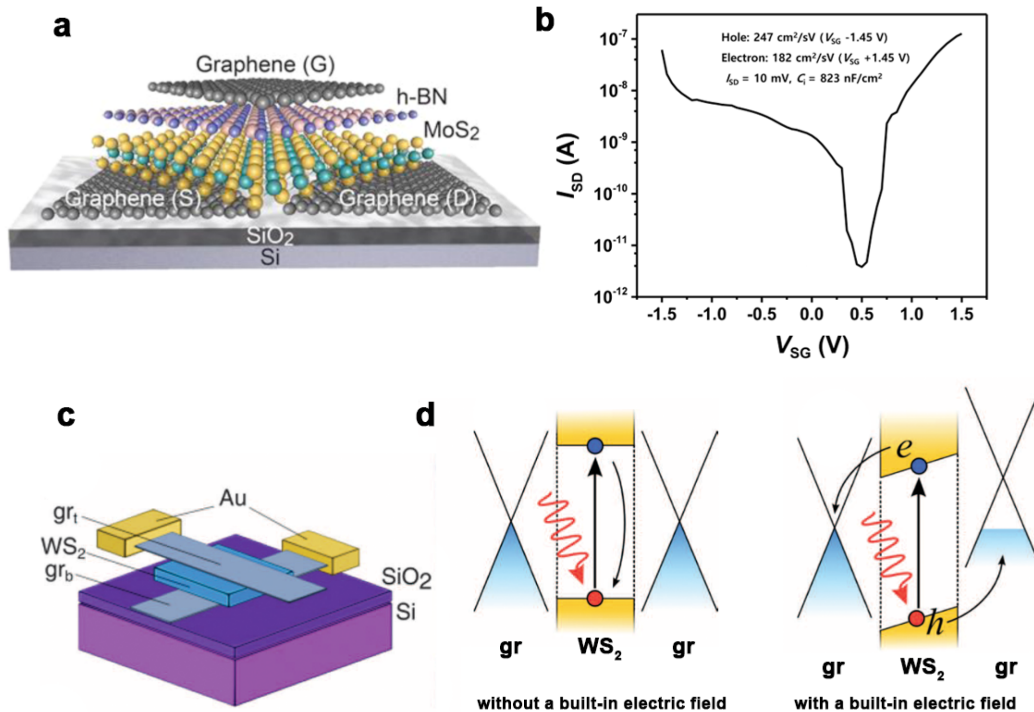

Figure 2.11 Two configurations of graphene contacts: (a) lateral heterostructure;[164] and (c) vertical heterostructures.[149] (b) The ambipolar transfer characteristics of the lateral structure of graphene/$MoSe_2$. I_{ds} was measured as a function of gate bias at a fixed V_{ds} of 10 mV.[163] (d) Band diagrams of a vertical heterostructure of graphene/WS_2/graphene with and without built-in electric field.[149] Reproduced with permission.

2.4.2 Metal-semiconductor Junction

Formation of the Schottky Barrier

A metal-semiconductor contact, also known as a Schottky diode, is formed when a metal is in close contact with a semiconductor. The barrier formed at the metal-semiconductor (M-SC) interface is called the Schottky barrier. The energy band diagram of a metal-semiconductor interface depends on the distance between the metal and the semiconductor, as shown in Figure 2.12.[165] The work function ($q\phi_M$) of metal is the energy difference between the vacuum level and its Fermi level. For a n-type semiconductor, the energy difference between the vacuum level and the Fermi level can be expressed as ($q\chi + q\phi_n$), where $q\chi$ is electron affinity of the semiconductor and $q\phi_n$ is the energy difference between CVM (E_c) and the Fermi level. When a metal is brought into contact with an n-type semiconductor, their Fermi levels tend to align. However, as the gap (δ) between them decreases, a built-in electric field starts to be formed between the metal and the semiconductor. This results in more electrons being accumulated on the metal surface and an equal number of holes migrating to the semiconductor depletion zone. In the limiting case when the metal touches the semiconductor or when the gap becomes negligible, the Schottky barrier height (SBH) (ϕ_{SB}) can be determined by $q\phi_M$ and $q\chi$ (Schottky-Mott rule):

$$q\phi_{SB} = q(\phi_M - \chi) \qquad 2\text{-}1$$

where q is the elementary electric charge. For a metal-p-type semiconductor interface, ϕ_{SB} is given by:

$$q\phi_{SB} = E_C - q(\phi_M - \chi) \qquad 2\text{-}2$$

However, in real conditions, the existence of surface states or non-ideal atomically closed contact between the metal and semiconductor can result in deviations from the ideal value of ϕ_{SB}.

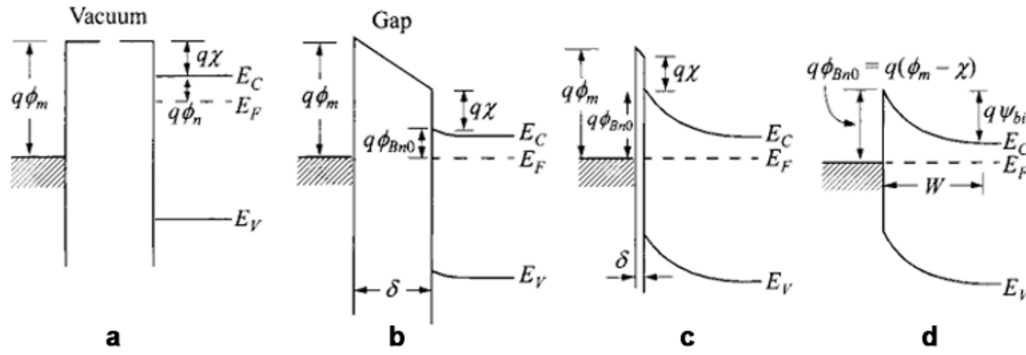

Figure 2.12 Energy band diagrams of a metal-semiconductor interface as the gap between the metal and semiconductor decreases: (a) not in contact; (b) close contact with a gap size of δ; (c) reducing δ; (d) $\delta = 0$.[165] Reproduced with permission.

Fermi Pinning

The charge neutrality level (CNL), denoted as ϕ_0, refers to the charge distribution at the surface region. When the Fermi level is above the CNL, the surface charges are negatively charged (electrons). This critical energy level associated with surface states is responsible for Fermi pinning at the semiconductor surface, and it is independent of the chosen metal.[166] In the limiting cases of the interface-trap density (D_{it}) $D_{it} = 0$ and $D_{it} \to \infty$, ϕ_{SB} is calculated as the following equations, respectively:[165]

$$q\phi_{SB} = q(\phi_m - \chi) \quad \text{2-3}$$

$$q\phi_{SB} = E_g - q\phi_0 \quad \text{2-4}$$

Eq. 2-3 is the ideal case of Schottky barrier height, as discussed previously in eq. 2-1. The latter equation demonstrates a scenario where the Fermi level at the interface is pinned due to the presence of surface states. In this situation, the Schottky barrier

height is only dependent on the band gap and charge neutral level of the semiconductor, and it is independent of the choice of the metal.

2.4.3 Heterostructure Assembly

Similar to the synthesis of 2D materials, the assembly of 2D heterostructure can also be classified into two approaches: top-down and bottom-up. Bottom-up strategies refer to the direct growth of 2D heterostructures. Directly grown heterostructures have atomically sharp and clean interfaces, leading to good interlayer couplings in certain TMDs stacks[167]. However, finding a universally applicable growth protocol for all heterostructures is challenging due to the different growth conditions required for each composition of 2D materials. Therefore, mixing and matching of different 2D materials and precise control of each layer number are ongoing challenges for bottom-up direct growth.[84] While some heterostructures have been successfully achieved through CVD-based growth, such as vertical MoS_2/h-BN[168], MoS_2/graphene[169], and lateral WS_2-WSe_2[170], it remains difficult to go beyond two different layer types. On the other hand, the top-down strategy refers to mechanically stacking various 2D materials layer by layer using transfer methods. This strategy provides more flexibility in assembling different materials, but it can result in weaker interlayer coupling due to interface contamination. However, thermal annealing can effectively remove interlayer contamination, reduce the distance between adjacent layers, and increase interlayer coupling.[142]

One of the most cutting-edge methods for realizing mechanical stacking is deterministic placement transfer, also known as aligned transfer. This method allows for the accurate alignment of each layer to the target substrate. Figure 2.13a-c are

images of setups for different aligned transfer systems. The common components of these setups include an objective lens with a long working distance and two moving stages for the micro-positioning of the top layer to be transferred and the bottom target layer, respectively.[171] The first step is to transfer the as-made 2D material to a solid substrate and coat it with a sacrificial polymer layer (e.g. poly(methyl methacrylate) PMMA[172], Elvacite 2550 acrylic resin[173]). This step can be accomplished using both dry transfer and wet transfer, as shown in Figure 2.13d. Subsequently, the polymer layer is attached to an elastopolymer stamp, typically made up of Poly(dimethyl siloxane) (PDMS). The PDMS stamp is supported by a glass slide for alignment and positioning. The top layer is then moved to the target position and slowly lowered down to establish contact between the layers. As shown in Figure 2.13e, there are three methods for the final treatment of the transferred sample with the sacrificial layer: dissolving the polymer in a chemical solvent; directly peeling off the polymer layer; and picking up the entire stack for the following transfer. Peel-off and pick-up are preferable in practice because wet chemical dissolving processes often leave more polymer residues between the layers.

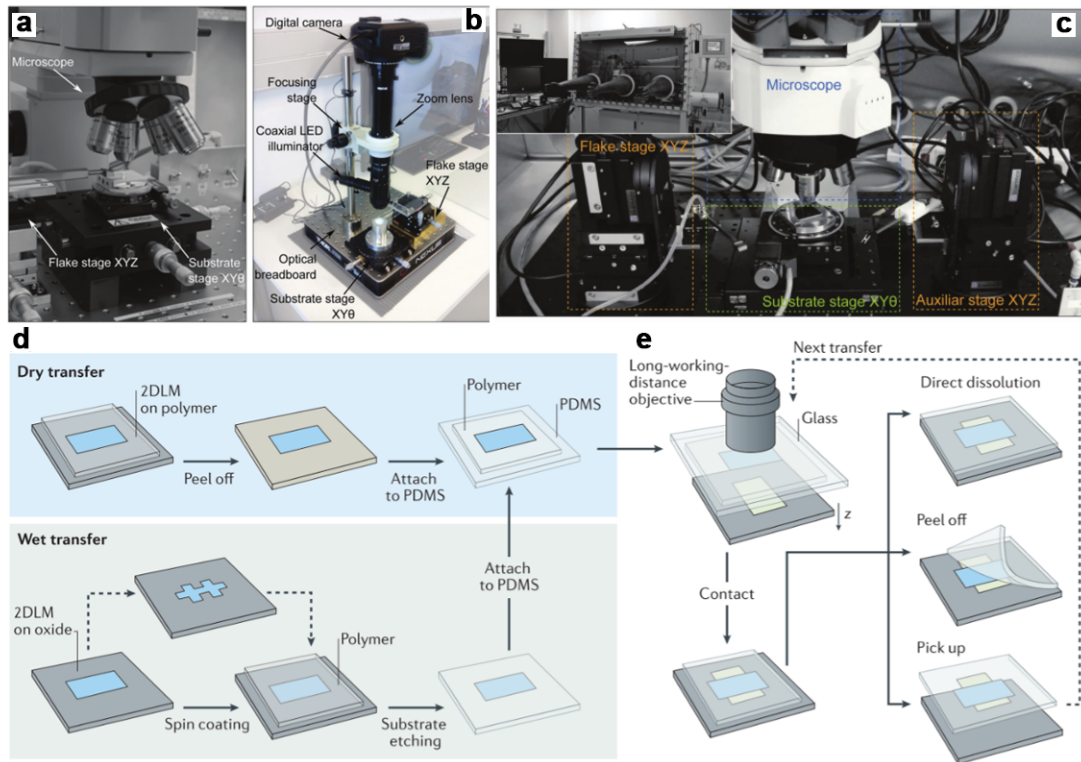

Figure 2.13 (a-c) Setups for some alignment transfer systems: (a) a system modified from a typical microscope; (b) replacing a microscope system with a zoom lens with coaxial illumination; (c) a system installed in a glovebox.[171] (d-e) Schematics of the aligned transfer process: (d) wet/dry transfer of 2D materials to PDMS stamp; (e) different surface treatments after contact.[84] Reproduced with permission.

The residues of the polymer induced during the mechanical transfer processes and surface adsorbates are the main sources of surface contaminants for 2D materials. Contaminants are often trapped between layers during fabrications of van der Waals heterostructure, resulting in the formation of localized blisters and wrinkles.[174] These blisters typically range in size from tens to hundreds of nanometers.[171] These defects weaken the interlayer couplings of the van der Waals layers and introduce strains and impurity scattering, which further degrade the performance of electronic devices based on vdW heterostructure.[36,171] For instance, Purdie *et al.* reported an average strain of 0.025% in the graphene encapsulated by h-BN layers, as determined by the position of the G peak from Raman mapping of the sample.[36] Efforts have been made to clean

the interfaces. Zhou *et al.* employed a combination of high pressure (0~1500 psi) and thermal annealing (250 ℃) to treat the as-assembled vdW stacks (graphene-WSe_2-graphene lateral heterostructure) to reduce the bubbles and wrinkles at the interface. This treatment significantly improved the hole mobility to 504.2 cm^2/Vs, exhibiting a ~356 × enhancement.[175] High pressure and thermal treatment can aggregate small bubbles into a large one and remove large bubbles at the edges, resulting in a larger and flatter interface.[175,176] Another improvement made during the assembly process is the pick-up technique.[177] In this technique, the sample is heated up to 110 ℃, and the surface contaminants diffuse out of the vdW stack during the slowly performed 'drop-down' process (lateral speeds < 1 μm/s), creating blister-free areas.[177] By using the hot pick-up technique, the mobility of bilayer/tri-layer graphene encapsulated by exfoliated h-BN flakes reached 37,000 and 23,000 cm^2/Vs, respectively.[177]

2.5 Device Applications of 2D materials

The exceptional properties of 2D materials and 2D material-based heterostructures provide foundations for the fabrication of various electronic and optoelectronic devices in the realm of 2D technology. This section focuses primarily on electronic and optoelectronic devices based on 2D semiconducting TMDs.

2.5.1 TMDs-based Field-effect Transistor

The traditional metal-oxide-semiconductor field effect transistor (MOS-FET) is one of the most important electronic devices. It consists of source, drain, and gate electrodes. As shown in Figure 2.14a, the gate electrode (metal) is separated from the source and drain electrode by a channel layer (semiconductor) and a dielectric layer

(oxide). This configuration can be considered as a combination of a parallel plate capacitor and a variable resistor. The current flowing through the source and drain electrodes can be modulated by the gate voltage. Figure 2.14b shows a typical transfer characteristic of an FET, showing the drain current (I_D) as a function of the gate voltage (V_{GS}). The threshold voltage (V_{Th}) is the minimum gate voltage needed required to turn the device from the OFF-state to the ON-state.[178] The ON/OFF ratio (I_{ON}/I_{OFF}) is defined as the ratio between the maximum ON-state current and the minimum OFF-state current.[178] The switching behaviour of an FET device can be measured by the subthreshold swing (S), which is defined as the inverse of the subthreshold slope (on a logarithmic scale): [178,179]

$$S = \frac{dV_{GS}}{d(logI_D)} \approx \frac{\Delta V_{GS}}{\Delta logI_D} \qquad 2\text{-}5$$

where V_{GS} is the gate voltage, and I_D is the drain current. S can be interpreted as the increment in V_{GS} required to raise the I_D by a factor of ten. A smaller S indicates a better switching ability, signifying a sharp transition between the ON and OFF states. For a MOS-FET to function as a logic transistor, it requires both an excellent switching capability and a high I_{ON}/I_{OFF}, typically ranging from 10^4 and 10^7.[179] Another important parameter is terminal transconductance (g_{mt}), which is defined as the slope of the transfer characteristic in the above-threshold region (on a linear scale):[178,179]

$$g_{mt} = \left.\frac{dI_D}{dV_{GS}}\right]_{V_D=constant} \qquad 2\text{-}6$$

The field effect mobility (μ_{FE}) is calculated from terminal transconductance (g_{mt}) as follows: [178,179]

$$\mu_{FE} = \frac{g_{mt}}{C_G V_{DS}\frac{W_{ch}}{L_{ch}}} \qquad 2\text{-}7$$

where C_G is the gate capacitance, V_{DS} is the source-drain voltage, W_{ch} is the channel width, and L_{ch} is the channel length.

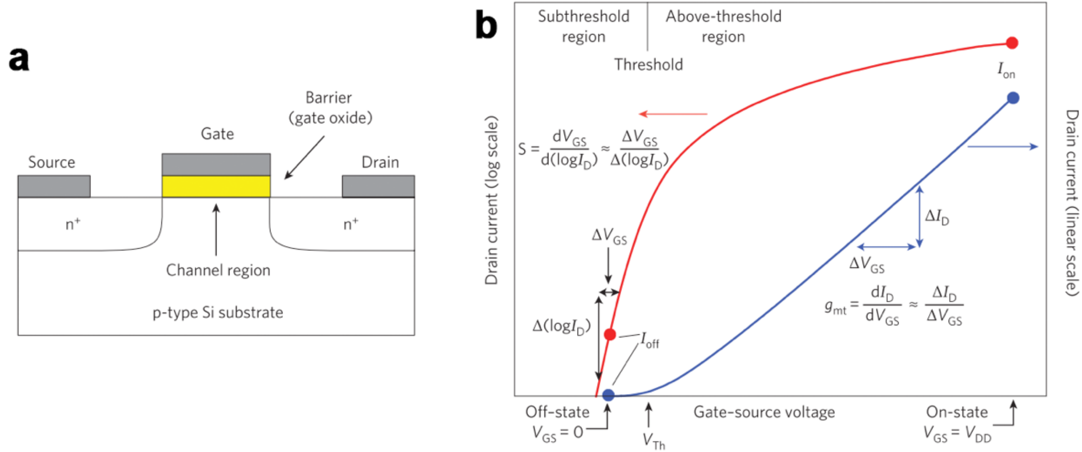

Figure 2.14 (a) Schematic of a typical n-channel Si MOS-FET. (b) A typical transfer characteristic of a FET: drain current (I_D) as a function of the gate voltage (V_{GS}).[179] Reproduced with permission.

The main charge injection mechanisms for MOS-FETs are thermionic emission (over the barrier) and tunnelling (across the barrier). The theory of the thermionic emission was developed by Bethe, based on the following assumptions: (1) the barrier height (ϕ_B) is much larger than κT; (2) thermal equilibrium is established at the interface; (3) the equilibrium is unaffected by the current flow.[165] The thermionic emission current (I_{TE}) can be expressed as follows: [165,180]

$$I_{TE} = ART^2 \exp\left(-\frac{q\varphi_B}{kT}\right)\left[\exp\left(\frac{qV}{kT}\right) - 1\right] \quad \text{2-8}$$

where A is the contact area, R is the Richardson constant, ϕ_B is the barrier height, κ is the Boltzmann constant, T is the temperature, V is the applied bias, and q is the elementary charge. Unlike thermionic emission, which requires carriers to overcome the barrier with excess energy, tunnelling is a quantum-mechanical phenomenon.[165] It occurs when the wavefunction can propagate through a thin barrier. Figure 2.15 shows the wavefunction of an electron tunnelling through a rectangular barrier from region

A to region B, where the wavefunction penetrates through the barrier instead of abruptly stopping at the barrier wall.[165] The tunneling probability (T_t) can be calculated from the wavefunction ψ, determined by the Schrödinger equation. For a simple rectangular barrier with a width of W and a height of U_0, T_t can be expressed as follows:[165]

$$T_t = \frac{|\psi_B|^2}{|\psi_A|^2} \approx \frac{16E(U_0 - E)}{{U_0}^2} exp\left(-2\sqrt{\frac{2m^*}{\hbar^2}[U_0 - E]}W\right) \qquad 2\text{-}9$$

where ψ_A and ψ_B are the wavefunctions before and after the tunneling (in regions A and B, respectively), E is the kinetic energy of the electron, m^* is effective electron mass, and $\hbar$ is the reduced Planck's constant. In a low-bias regime, the tunneling process is dominated by direct tunneling (DT), where the rectangular barrier does not deform significantly. Simmons derived a theory to describe the DT current (I_{DT}) as follows:[181,182]

$$I_{DT}(V) = \frac{A_{eff}\sqrt{m\varphi_B}q^2\mathrm{V}}{h^2 d} \exp\left[\frac{-4\pi\sqrt{m^*\varphi_B}d}{h}\right] \qquad 2\text{-}10$$

where A_{eff}, m, m^*, φ_B, q, V, h, d are the effective junction area, free electron mass, effective electron mass, barrier height, electron charge, applied bias, Planck's constant, and barrier width, respectively. In a high-bias regime, the barrier is deformed into a triangular shape, and the tunneling process is described as Fowler-Nordheim tunneling (FNT). The FNT current (I_{FNT}) is expressed as follows:[183,184]

$$I_{FNT}(V) = \frac{A_{eff}mq^3\mathrm{V}^2}{8\pi h\varphi_B d^2 m^*} \exp\left[\frac{-8\pi\sqrt{2m^*}\varphi_B^{\frac{3}{2}}d}{3hqV}\right] \qquad 2\text{-}11$$

From eq. 2-10 and 2-11, it can be observed that I_{DT} has a simple linear relationship with applied bias, whereas I_{FNT} increases monotonically and non-linearly with increasing bias.

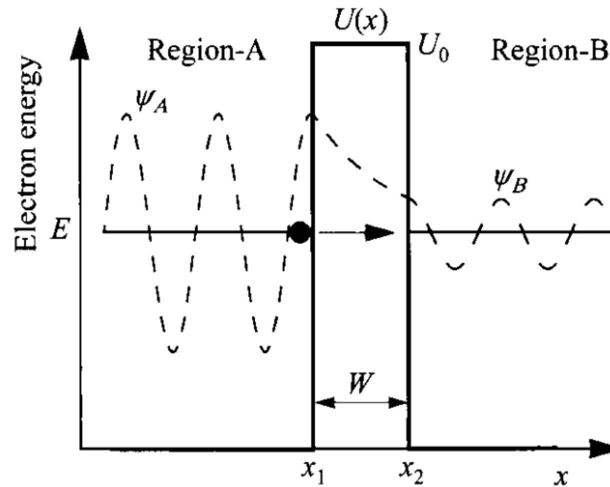

Figure 2.15 The wavefunction (ψ_A) of an electron tunnelling through a rectangular barrier with a barrier width of W and barrier height of U_0 from region A to region B.[165] Reproduced with permission.

In a thermionic transistor, thermionic emission is the main mechanism of charge injection. Radisavljevic *et al.* demonstrated a monolayer MoS_2 transistor using a 30 nm HfO_2 dielectric layer and a top-gated geometry, as shown in Figure 2.16a.[185] The device shows a mobility over 200 cm^2/Vs at room temperature, a subthreshold swing of 74 mV/decade, and an I_{ON}/I_{OFF} ratio of 1×10^8.[185] Liu *et al.* reported a TMDs-based thermionic FET with a coplanar lateral structure of graphene–MoS_2–graphene, as shown in Figure 2.16b.[150] Graphene was utilized as gate-tunable electrodes, while h-BN acts as an encapsulation material for MoS_2. Graphene, h-BN, and MoS_2 were obtained by mechanical exfoliation and assembled via a dry aligned transfer. As discussed in the previous section, the lateral configuration of graphene electrodes effectively reduces the SB between the TMDs semiconductor and the

electrode by gate modulation. Graphene forms an excellent barrier-free contact with MoS_2 by appropriate gate modulation, leading to an ohmic linear output curve.[150] The device shows a mobility of 1300 cm^2/Vs for a five-layer MoS_2 at low temperature (1.9 K).[150] Tang *et al.* reported a TMDs-based FET constructed with a lateral heterostructure of graphene–WSe_2–graphene, although the heterojunction was achieved by CVD growth, as shown in Figure 2.16c.[186] The I_{ON}/I_{OFF} is enhanced 1000 times to over 1×10^7 by reducing the barrier height via gate modulation of the graphene electrodes.[186]

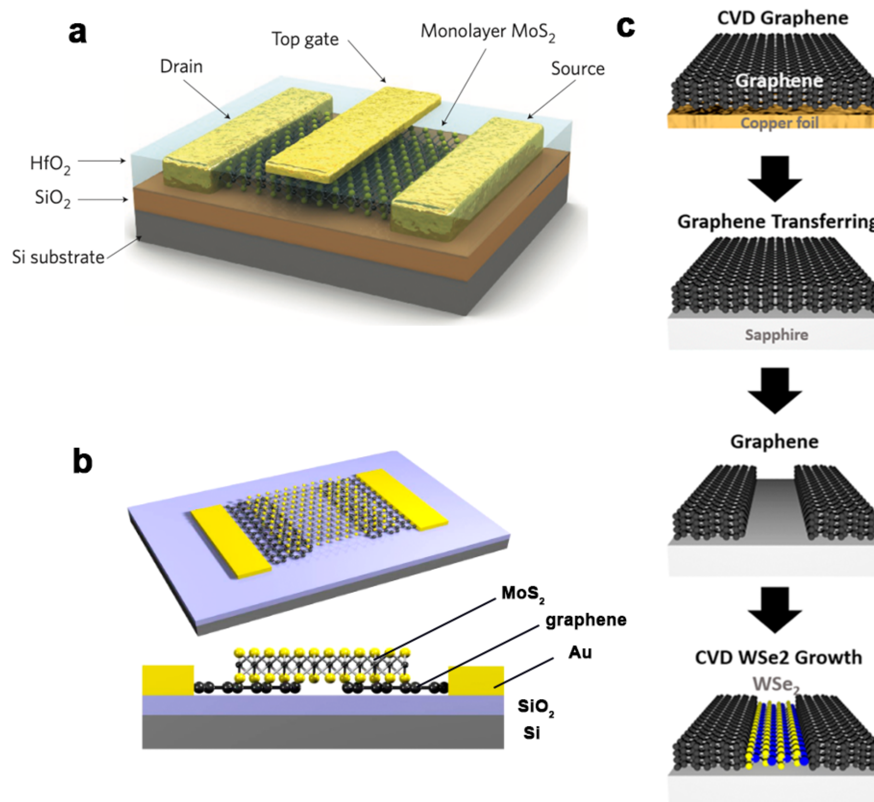

Figure 2.16 (a) Schematic of MoS_2 transistor with a HfO_2 dielectric layer and a top-gated geometry.[185] (b) Schematic of a TMDs-based FET with a coplanar lateral heterostructure of graphene–MoS_2–graphene.[150] (c) Schematic of the CVD growth of graphene–WSe_2–graphene lateral heterostructure.[186] Reproduced with permission.

In a tunnelling transistor, the main mechanism of charge injection is tunnelling. As shown in Figure 2.17a, in the vertical heterostructure of graphene/h-BN/graphene tunnelling transistors, the source and drain are formed by two graphene electrodes, while insulating h-BN layers act as the barrier material, separating the electrodes.[13] Due to the low density of states and poor screening of graphene, the Fermi level of both the top and bottom graphene electrodes can be easily tuned by applying a vertical electric field. When a positive gate voltage is applied, the Fermi level of electrodes is elevated due to the changes in the carrier concentration, as shown in Figure 2.17b-c. [15,187] This leads to a reduction of the barrier height for the tunnelling, resulting in changes in the current as a function of the gate voltage. The I_{ON}/I_{OFF} of the graphene/h-BN/graphene tunnelling transistor reaches 50, which is a significant improvement compared to the low I_{ON}/I_{OFF} ratios (usually < 10) observed in pure graphene transistors.[13,39,188] Substituting h-BN with WS_2 to separate the two graphene electrodes, as shown in Figure 2.17d, leads to an I_{ON}/I_{OFF} ratio exceeding 1×10^6, with a large ON-state current at room temperature.[189] The improvements in I_{ON}/I_{OFF} ratio can be explained as follows: The changes in the Fermi level of graphene are very small (usually < 0.5 eV) within the breakdown limit of the dielectric layer. In comparison, while insulating h-BN has a large band gap (> 5 eV), monolayer WS_2 has a smaller bandgap (~2.1 eV). Consequently, the changes in the Fermi level of graphene due to the gate modulation have a more significant impact on the barrier height of graphene/WS_2/graphene compared to graphene/h-BN/graphene.[189] The changes in the Fermi level of graphene are of the same order of magnitude as or larger than the barrier height of graphene/WS_2/graphene. As a result, the operation mechanism of

graphene/WS_2/graphene can be switched from pure tunnelling to a combination of tunnelling and thermionic emission through gate modulation.[189] As shown in Figure 2.17e-f, with a negative gate bias, the lowered Fermi levels of both the top and bottom graphene layer lead to a larger potential barrier, resulting in an OFF-state. Conversely, with a positive gate bias, the barrier height is reduced, and the Fermi levels of graphene enable thermionic emission through the device, resulting in an ON-state.[189]

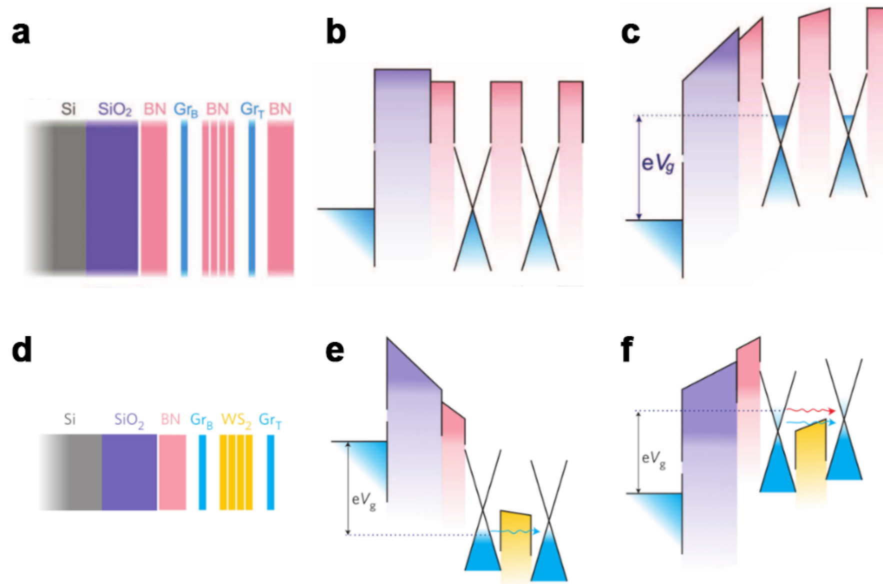

Figure 2.17 Schematics of (a) graphene/h-BN/graphene[13] and (d) graphene/TMDs/graphene vertical heterostructures.[189] (b) The band structure of graphene/h-BN/graphene without gate voltage.[13] (c) The band structure of graphene/h-BN/graphene with a positive gate voltage.[13] (e) The band structure of graphene/WS_2/graphene with a negative gate voltage.[189] (f) The band structure of graphene/WS_2/graphene with a positive gate voltage.[189] Blue and red arrows in (e-f) refer to tunnelling and thermionic emission, respectively.[189] Reproduced with permission.

2.5.2 TMDs-based Light Emitting Device (LED)

LEDs operate based on an electroluminescence (EL) process, wherein electrons and holes are injected from electrodes into the conduction and valence bands, respectively, and subsequently recombine radiatively to emit light. The efficiency of this charge-to-photon conversion process is quantified by a figure of merit known as

the quantum efficiency (QE).[93] The radioactive recombination processes of injected electrons and holes compete with non-radiative recombination processes. As a result, the recombination processes can be either radiative or non-radiative. Therefore, the internal quantum efficiency (IQE), which measures the efficiency of converting carriers to photons, is defined as follows:[165,190]

$$IQE = \frac{number\ of\ photons\ emitted\ internally}{number\ of\ carriers\ passing\ junction} \quad 2\text{-}12$$

It can also be expressed as the fraction of the radiative recombination to the total recombination rate, shown as follows:[165]

$$IQE = \frac{R_r}{R_r + R_{nr}} = \frac{\tau_{nr}}{\tau_{nr} + \tau_r} \quad 2\text{-}13$$

where R_r and R_{nr} are the radiative and non-radiative recombination rates, respectively; τ_r and τ_{nr} are the lifetimes of radiative and non-radiative recombination, respectively. When evaluating the performance of LEDs, the photons emitted from the junction are more important than the photons generated within the junction. Therefore, the external quantum efficiency (EQE), is defined as follows:[165]

$$EQE = \frac{number\ of\ photons\ emitted\ externally}{number\ of\ carriers\ passing\ junction} \quad 2\text{-}14$$

Optical efficiency (η_{op}) is a parameter that measures the efficiency of the photons getting out of the junction. It correlates the IQE and EQE as follows:[165]

$$EQE = IQE \times \eta_{op} \quad 2\text{-}15$$

Sundaram *et al.* first reported the EL phenomenon in single-layer MoS_2, paving the way for TMDs to act as light-emitting materials for LEDs.[191] EL devices utilizing TMDs semiconductors can be created in both lateral and vertical geometries, depending on the direction of carrier injection.[190] In lateral geometries, electrons and holes are laterally injected into a p–n junction and recombine radiatively to emit light.

Pioneering works on TMD-based LEDs focused on lateral p–n junction structure.[192–194] An EQE of 0.1 % was achieved for a lateral p-n junction of WSe_2, which was electrostatically doped via split gates, as shown in Figure 2.18a.[194] Dual-gating modification is a straightforward method to construct EL devices with p–n homojunctions, typically without the requirement for h-BN barrier layers. However, achieving effective doping control, especially to improve the hole density in p-type semiconductors to a comparable level with the electron density in n-type doping, remains a challenge.[191–195] Furthermore, the formation of a 1D junction at the metal-semiconductor contact region significantly limits the performance of TMDs-based LEDs due to the restricted depletion zone near the 2D interface.[84] Another issue with lateral geometries of EL devices using all 2D materials is that the injected electrons and holes from the electrodes can only migrate a short distance before dissipating their energy through non-radiative recombination processes. For atomically thin layers of TMDs, this migration distance is typically limited to several hundred nanometers.[196,197] Consequently, devices with semiconductor channel lengths longer than this have a low probability of injected electrons and holes recombining in the same spatial region, resulting in low-efficiency EL in large-area devices with long micron-scale channel lengths. Vertical geometries can overcome this limitation of charge carrier diffusion length because the distance from the electrode to the semiconductor is always small, enabling the creation of large-area devices.

In the vertical geometries, carriers are injected perpendicular to the photoactive layer, making it ideal for creating uniform planar emission over a large junction area. Various structures can achieve planar EL emission, including vertical p–n junctions,[198,199] quantum well (QW) structures,[14,200–207] and metal–insulator–

semiconductor (MIS) heterostructures[208,209]. Figure 2.18b shows an atomically sharp vertical p–n junction of WSe_2/MoS_2 reported by Cheng *et al.*, which achieved an EQE of 0.1~3%.[198] The emission mechanism for vertical p–n junctions is the same as that for lateral p–n junctions as shown in Figure 2.18a. However, vertical p–n junctions can achieve much higher EQE due to the larger emission area and shorter charge extraction distance. Withers and co-workers reported a multilayer vertical single QW (SQW) structure consisting of h-BN/graphene/h-BN/MoS_2/h-BN/graphene/h-BN, achieving an EQE of up to 1%, as shown in Figure 2.18c.[14] In this configuration, the top and bottom graphene layers act as electrodes for carrier injection, while the h-BN layers serve as tunnelling barriers, creating a QW composed of TMDs. The presence of h-BN layers increases the lifetime of injected electrons and holes within the TMDs layer by reducing the charge transfer probability from the TMDs to graphene. This increases the probability of radiative electron–hole recombination, resulting in significant EL. Without the insulating h-BN layers between the graphene and TMDs, electrons from one graphene electrode would rapidly transport to the other graphene electrode, leading to a reduced probability of radiative recombination and negligible EL. However, if the h-BN layer is too thick, the tunnel barrier width increases, significantly reducing the injection of charge carriers from graphene to the TMDs and resulting in minimal EL due to low carrier concentration in the TMDs layer.[201] Withers *et al.* demonstrated an ideal thickness of approximately 2-3 h-BN enables sufficient charge carrier injection by tunnelling and efficient electron–hole recombination within the TMD layer.[201] The observation that adding h-BN into graphene/TMD/graphene devices increases resistance and reduces current flowing through the semiconductor, while simultaneously increasing the observed EL signal indicates an improvement in

radiative recombination efficiency. These pioneering results highlight the effectiveness of h-BN as a tunnel barrier in facilitating efficient radiative recombination in 2D semiconductors. To further enhance the EQE, multiple SQWs can be stacked to form a multi-QW (MQW) structure, thereby increasing the number of injected carriers and recombination possibilities. The EQE of the MQW, consisting of 3-4 aforementioned SQWs, can reach up to 8.4%.[14] This MQW configuration allows for the utilization of various combinations of interlayer TMDs, enabling broad emission ranges. Wang *et al.* reported a metal-insulator-semiconductor (MIS) heterostructure of graphene/h-BN/WS_2 with high carrier-to-exciton conversion efficiency, as shown in Figure 2.18d. In this structure, graphene, h-BN, and WS_2 function as hole reservoirs, quasi-vacuum layer, and electron transport layer, respectively.[209] The device exhibits an extremely low current density of 4 pA/μm^2 to turn on the EL emission.[209] The author attributed the low turn-on current to the unipolar tunnelling across the h-BN layer.[209]

Table 2.1 summarizes the EQE and turn-on current for TMDs-based EL devices with different structures, along with commercial LEDs. High efficiency, compactness, material stability, and long operation lifetime are the minimum requirements for commercial LEDs.[210] Specifically, for LEDs used in display, the operational lifetime is expected to be at least several tens of thousands of hours.[211] Currently, the commercialization of 2D materials-based EL devices is limited by poor scalability, low EQE, small junction area, and short operation lifetime. However, the atomically thin nature, flexibility, and transparency of 2D materials continue to drive the exploration of novel architectures for EL devices.[212] In most studies, TMDs-based EL devices have been fabricated using mechanically exfoliated TMDs. As shown in

Table 2.1, the only exception is the QW structure reported by ref 207, where the TMDs were synthesized by CVD.[207] Mechanically exfoliated 2D materials are preferrable for proof-of-concept LEDs, whereas CVD offers a more suitable approach for industrial scale-up. While preliminary results have been published, there is still a need for further investigations to gain a deep understanding of the fundamental behaviour of these unique heterostructure systems and to facilitate the scale-up of the device fabrication process.

Table 2.1 Comparisons of TMDs-based EL devices with different structures and commercial LEDs.

Architecture	Material	EQE	Turn-on current	Ref
Lateral p-n diode	WSe_2	0.1%	< 50 nA	193
Lateral p-n diode	WSe_2	0.1%	200 pA	192
Lateral p-n diode	WSe_2	1%	-	194
Vertical p-n diode	WSe_2/MoS_2	0.1~3%	10 μA	198
Vertical SQW/MQW	gr/h-BN/MoS_2/h-BN/gr	1~8.4%	1.8 nA/μm^2	14
Vertical SQW	gr/h-BN/WSe_2/h-BN/gr	5%	0.5 μA/μm^2	201
Vertical SQW	gr/h-BN/WS_2/h-BN/Au	1.13~4.52%	-	207
MIS	WS_2/h-BN/gr	1%	4 pA/μm^2	209
p-i-n	ZnO-QD/WS_2/Poly-TPD	0.0001%	0.3 A/cm^2	204
Commercial LED	GaP	-	20 mA	212
Commercial LED	AlGaAs	-	50 mA	212

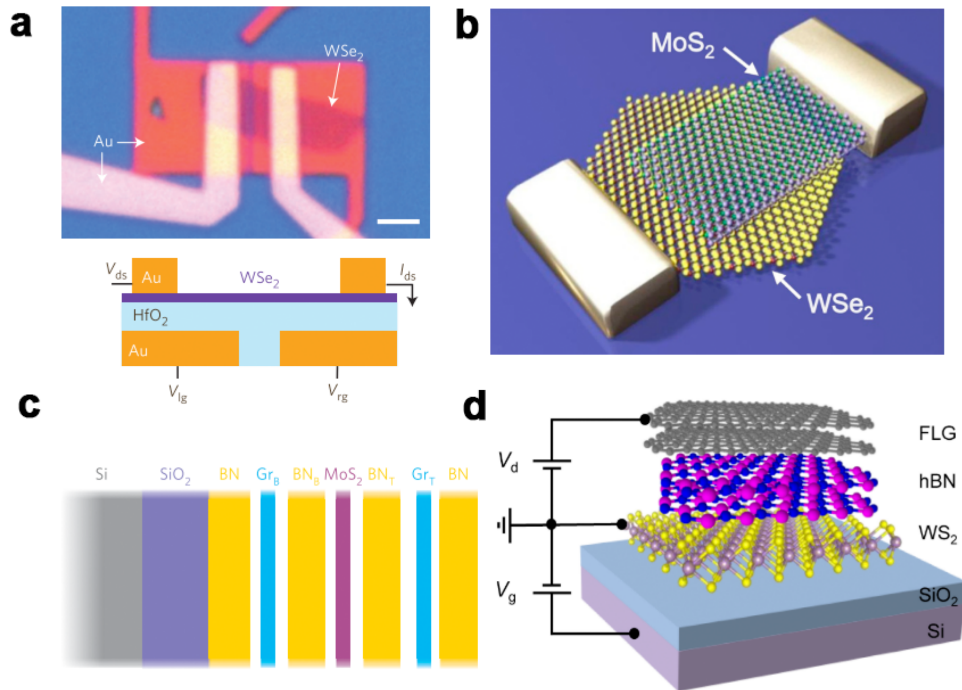

Figure 2.18 Schematics of EL devices with different heterostructures: (a) lateral p-n homojunction of WSe_2;[194] (b) vertical p-n junction of WSe_2/MoS_2;[198] (c) quantum well (QW) structure of h-BN/graphene/h-BN/MoS_2/h-BN/graphene/h-BN;[14] (d) metal-insulator-semiconductor (MIS) structure of WS_2/h-BN/graphene.[209] Reproduced with permission.

2.5.3 TMD-based Photodetector

A photodetector is a light-sensing device that converts incoming photons into electrical current. This conversion process typically involves the generation of electron–hole pairs through the interaction of photons with the photoactive material in the device under illumination. Subsequently, the electrons and holes are separated and migrate through the device, forming a photocurrent. There are three fundamental mechanisms for generating photocurrent: photovoltaic, photoconductivity, and photogating effects.[213] The photovoltaic effect is a process in which excited electron–hole pairs are separated by an electric field and migrate towards opposite electrodes, resulting in the generation of electric current. A built-in electric field can be

established in a Schottky barrier or a p–n junction, or by maintaining different potentials between electrodes, enabling the generation of photocurrent.[165] The photoconductivity effect occurs when the conductivity of the semiconductor increases under illumination due to the elevated carrier density. The photoexcited electron–hole pairs are then separated by the applied voltage (V_{DS}) to generate a photocurrent.[213] The photogating effect involves the trapping of photoinduced electrons or holes in the surface states of the semiconductor, while the opposite carriers circulate under an external electric field. The trapped carriers act as local gates, modulating the conductivity of the semiconductor.[214]

Photoresponsivity, photogain, and photodetectivity are three significant quantities used to evaluate the performance of a photodetector.[148,184] Similar to the definition of QE for EL emission, the quantum efficiency for the generation of photocurrent is defined as the number of carriers produced per photon:[165,198]

$$\eta = \frac{I_{ph}}{q\Phi} = \frac{I_{ph}}{q}\left(\frac{hv}{P_{opt}}\right) \quad 2\text{-}16$$

where I_{ph} is the photocurrent, q is the elementary charge, Φ is the photon flux ($= P_{opt}/hv$), h is the Planck's constant, v is the frequency of the incident light and the P_{opt} is the optical power. Ideally, η should be unity, yet factors such as photon recombination or insufficient absorption can result in a reduction of η in reality. Photoresponsivity (R) is a direct measurement of the current generated by the incident light, and is defined as the ratio of the generated photocurrent to the power of incident light:[165]

$$R = \frac{I_{ph}}{P_{opt}} \quad 2\text{-}17$$

Therefore, R and η can be correlated as follows:

$$R = \frac{\eta q}{h\nu} \tag{2-18}$$

Photogain measures the degree of multiplication caused by the different charge mobility of electrons and holes.[215] External photogain (G_{ext}) is expressed as the ratio of the number of electrons circulated in the circuit to the number of incident photons:[216,217]

$$G_{ext} = \frac{N_{electron\,circulated}}{N_{incident\,photon}} = \frac{I_{ph}/q}{P_{op}/h\nu} = \left(\frac{h\nu}{e}\right) R \tag{2-19}$$

The Specific detectivity (D^*) demonstrates the sensitivity of a device to detect weak signals and is defined as follows:[165,213,218]

$$D^* = \frac{(AB)^{\frac{1}{2}}}{NEP} \tag{2-20}$$

where A is the effective area of the photodetector, B is the bandwidth, NEP is noise-equivalent power. NEP refers to the minimum optical power required to achieve a signal-to-noise ratio (SNR) of 1 in a 1-Hz bandwidth. The noise current is mainly from three noise sources: shot noise, thermal noise, and $1/f$ noise.[218] A fast estimation can be made by assuming that the shot noise dominates. In this case, D^* can be expressed as follows:[155,213]

$$D^* \approx \frac{RA^{\frac{1}{2}}}{(2qI_{dark})^{\frac{1}{2}}} \tag{2-21}$$

where I_{dark} is the dark current.

Photodetectors can be broadly categorized into two types: phototransistor/photoconductor and photodiode.[165] Phototransistors are similar in construction to regular transistors, but utilize photoactive materials as the semiconductor, such as TMDs, and operate based on photoconductive or photogating

effects.[213] On the other hand, photodiodes are more complicated and can be realized using various heterostructures.

One commonly used construction for a photodiode is a vertical stacked metal/TMDs/metal heterostructure, which offers a large effective photoactive area and an atomically short charge extraction channel. To achieve high quantum efficiency, metal electrodes can be substituted with graphene to reduce contact resistance and minimize damage to the TMDs layer.[157] In vertical graphene/MoS_2/graphene structures, as shown in Figure 2.19a-b, the SB height between the MoS_2 and the bottom graphene is higher than that with the top graphene due to the stronger p-doping of the bottom graphene by the silicon substrate.[219] As a result, after photoexcitation and charge separation, the electrons in the CB of MoS_2 have a higher tendency to migrate towards the top graphene. This asymmetrical vertical structure is advantageous for generating a photocurrent. Different electrode designs, such as graphene/MoS_2/metal, can also be used to realize such asymmetrical structures.[157] Moreover, the addition of h-BN between graphene and the photoactive TMDs can effectively reduce the dark current tunnelling of the device.[184] In graphene/h-BN/MoS_2/metal vertical structures, as shown in Figure 2.19c, a photocurrent/dark current ratio exceeding 10^5, photoresponsivity of 180 A/W, and an ultrahigh photodetectivity of 2.6×10^{13} Jones can be achieved.[184]

Coplanar lateral graphene constructions can also be employed to lower the SB between graphene and TMDs. Tan *et al.* reported a lateral graphene-WS_2-graphene photodetector with a photoresponsivity of 3.5 A/W under an illumination power density of 2.5×10^7 mW/cm^2, EQE of 583% and photodetectivity of 9.9×10^{10} Jones.[155] His following work significantly improved the performance of the

photodetector with the same lateral structure by utilizing a WS_2/MoS_2 stack as the photoactive interlayer materials, as shown in Figure 2.19d. This type II band structure, with fast charge transfer and long lifetime excitons, exhibits a photoresponsivity of 103 A/W under an illumination power density of 1.7×10^2 mW/cm^2 and a large photogain of 3×10^4.[148] With a positive gate bias and illumination, holes move towards the sources electrode connected to ground while electrons move towards the drain electrode, resulting in a significant net photocurrent.

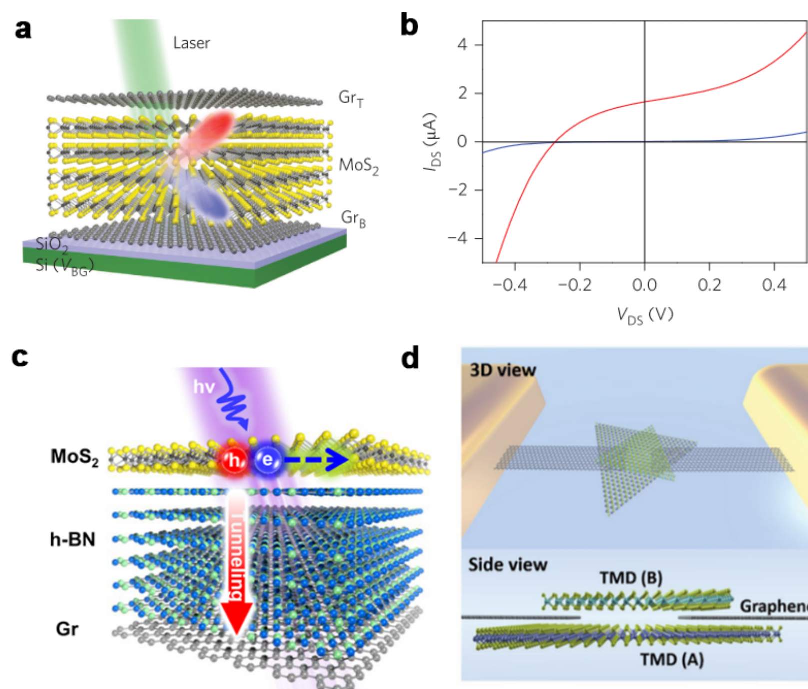

Figure 2.19 (a-b) Schematic of graphene/MoS_2/graphene with vertically stacked graphene electrodes and the output curves of the device with (black curve) and without illumination (red curve).[157] (c) Schematic of the graphene/h-BN/MoS_2 vertical heterostructure under illumination conditions.[184] (d) Schematic of the graphene/WS_2/MoS_2/graphene coplanar lateral heterostructure.[148] Reproduced with permission

Chapter 3: Methodology

3.1 Introduction

This chapter discusses the experimental methods and techniques used throughout the entire project. It covers the synthesis and transfer methods of 2D materials that are used as building blocks for heterostructures, the techniques used in device fabrication, and the characterization methods used to determine the 2D crystals and the device performance.

3.2 2D Material Synthesis

WS_2 single crystal, monolayer graphene, and few-layered h-BN were synthesized by CVD, while $PtSe_2$ thin film was synthesized by a thermally assisted selenization process. Previous group members developed the basic procedures for growing all the mentioned materials.[10,220,221] I optimized specific parameters during the growth process, such as growth temperature, growth time, and substrate pre-treatment, and successfully grew most of the materials used in my projects.

3.2.1 CVD Growth of WS_2

WS_2 single domains were grown on a silicon substrate (University Wafer, 300 nm SiO_2/p++ Si) by atmospheric pressure chemical vapor deposition (APCVD) in a double-furnace system. The silicon substrate was diced into 2 cm × 2cm pieces and cleaned by soaking and ultrasonicating in the DI water, acetone, and IPA in sequence for 10-15 min each. Sometimes, oxygen plasma etching was also applied for further

surface cleaning of the silicon substrate, with a power of 90 W and an etching time of 10 min. Sulfur powder (300 mg, purum grade > 99.5 %, Sigma-Aldrich) and WO_3 (200 mg, puriss grade > 99 %, Sigma-Aldrich) were separately loaded in an external (diameter: 22mm) and an internal quartz tube (diameter: 12 mm) to isolate each other. Each of them was placed in the middle position of two individual furnaces for the evaporation process: a low-temperature furnace for S and a high-temperature furnace for WO_3. The silicon substrate on an alumina crucible was placed in the external tuber downstream S and WO_3 and heated by the same furnace as WO_3. The system was sealed and purged with pure Ar (500 sccm) for at least 30 min to remove the air. After that, the growth started at the point when S and WO_3 reached 180 ℃ and 1145 ℃ together and lasted for 3 min, during which the Ar flow brought upstream S and WO_3 vapor to the silicon substrate. The system was then fast-cooled down to room temperature. Figure 3.1 shows the setup for WS_2 synthesis.

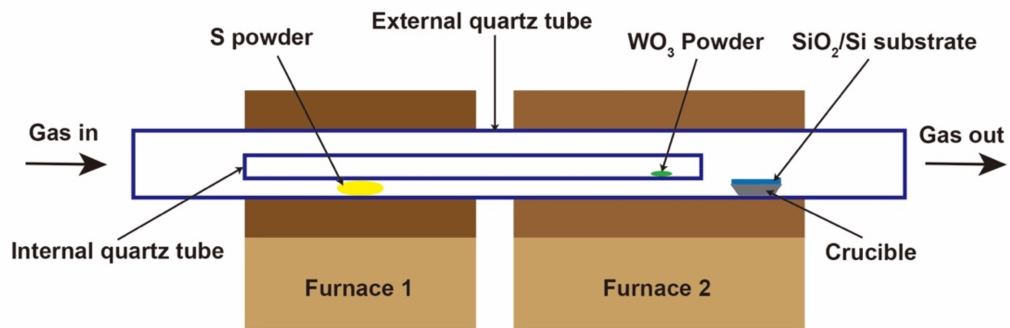

Figure 3.1 Schematic of the experimental setup for CVD synthesis of WS_2.

3.2.2 CVD Growth of Graphene

Graphene film was grown on a copper substrate (6.5 cm × 15 cm, 25 μm, 99.8 %, Alfa Aesar) by APCVD in a 4 in. quartz tube. The Copper substrate was first mechanically polished and sonicated in hydrochloric acid (HCl, 1 M), DI water,

acetone, and IPA, in sequence, for surface cleaning. The substrate was placed above a crucible in the middle of the furnace, and the tube was first purged with a gas mixture of argon (100%, BOC), hydrogen (25% H_2 and 75% Ar, BOC), and methane (1% CH_4 with 99% Ar, BOC) in a ratio of 20:5:1 for 30 min. The system was heated up to 1060 ℃ in the atmosphere of Ar and H_2 (4.17% H_2, 95.83% Ar) for 1 h to anneal the copper, followed by graphene growth at 1060 ℃ under the atmosphere of Ar, H_2, and CH_4 (0.01% CH_4, 4.13% H_2, 95.86% Ar) for another 1 h. Finally, the CH_4 was switched off and the system was fast-cooled to room temperature by sliding the furnace away under the atmosphere of Ar and H_2 (4.17% H_2, 95.83% Ar). Figure 3.2 shows the setup for CVD synthesis of graphene.

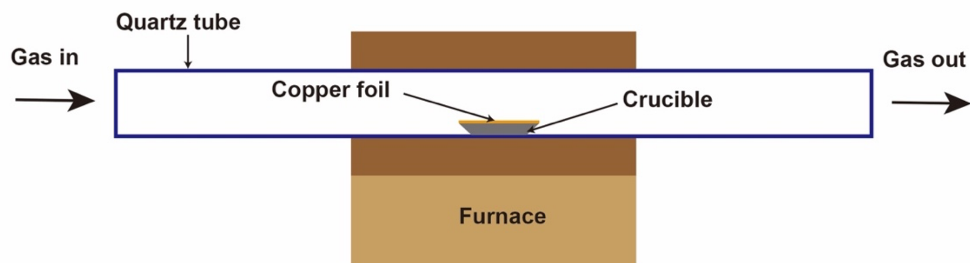

Figure 3.2 Schematic of the experimental setup for CVD synthesis of graphene.

3.2.3 CVD Grown of h-BN

h-BN film was grown on copper substrates (1 cm × 1 cm, 25 μm, 99.8%, Alfa Aesar) by APCVD in a 1 in. quartz tube. 5 pieces of copper foils were placed in a crucible boat in the middle of the tube after successive surface cleaning using HCl (1 M), DI water, acetone, and IPA in a sonicator. 15 g ammonia borane was placed in the middle of an isolated chamber with a valve connected to the front end of the tube, as shown in Figure 3.3. The system was first flushed with a mixture of Ar and H_2 (12.5 % H_2, 87.5% Ar) with the valve open, followed by an annealing process of the copper at

1070 °C under a gas mixture atmosphere (3.75 % H_2, 96.25% Ar) for 1 h with the valve closed. After that, the isolated chamber was heated up to 120 °C with the valve open to transport the precursor to the tube via a gas mixture (25 % H_2, 75% Ar). The growth of h-BN took place in the middle of the tube at 1070 °C for 30 min. Finally, both heating systems were switched off, and the whole system underwent a fast-cooling process by moving the furnace away.

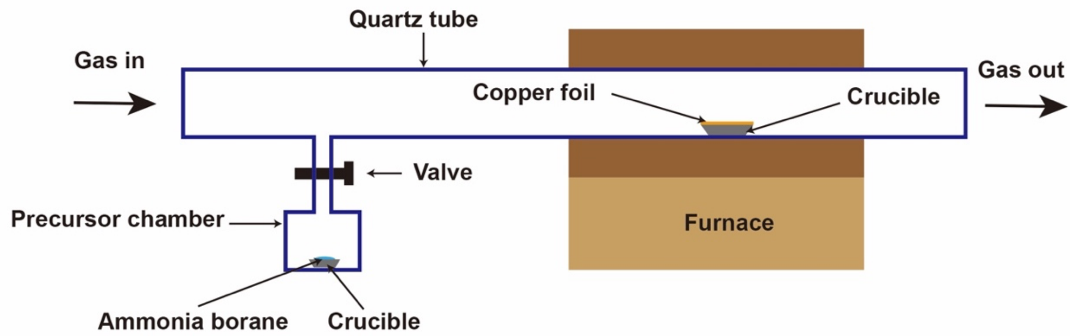

Figure 3.3 Schematic of the experimental setup for CVD synthesis of h-BN.

3.2.4 Direct Selenization of $PtSe_2$

A 2 nm Pt layer was first deposited on top of a SiO_2/Si substrate using electron-beam evaporation. Selenium powder (20 mg, ≥99.5%, Sigma-Aldrich) and the substrate uniformly coated Pt were loaded into a 2-in. diameter quartz tube. Two furnaces, a low-temperature (LT) furnace and a high-temperature (HT) furnace, were used to control the temperature of the Se powder and the Si substrate, respectively. The system was then sealed and flushed with pure Ar flow (500 sccm) for 30 min to remove reactive gases, such as oxygen. Subsequently, the Se and substrate were ramped up to 230 and 350 °C, respectively, to initiate the selenization process. During this process, an Ar flow (110 sccm) was utilized as the carrier gas to transport Se vapor downstream to the substrate surface. Specifically, the LT furnace and HT furnace were

first heated to 220 ℃ and 260 ℃, respectively, and before ramping them up to 230 ℃ and 350 ℃ to prevent temperature overshoot. To avoid undesired condensation of Se on the substrate, the HT furnace was usually started 20 s earlier than the LT furnace. The growth period lasted for 40 min to form a $PtSe_2$ thin film. Finally, the reaction was ended by slow-cooling of both the Se and the synthesized $PtSe_2$ using a pure Ar flow of 500 sccm.

3.3 Material Characterizations

3.3.1 Optical Microscopy

Optical microscopy is a fast and effective method for characterizing and examining 2D materials on a silicon substrate, as well as fabricated devices, on a large scale. In my project, silicon wafers with a SiO_2 thickness of 300 nm were used. 2D materials such as WS_2, graphene, and $PtSe_2$ exhibit clear contrast with silicon substrates, allowing them to be easily observed under an optical microscope. The changes in transmittance of these materials, which evolved with layer thickness, provide a possibility to roughly determine their thickness based on the contrast variations in different domains. I primarily utilized two custom-built optical microscopes in my project. One microscope had objective lenses ranging from 10 × to 50 × and was used for the preliminary examination of the quality of as-grown 2D materials and the completeness of transferred 2D materials. The other microscope had a 4× objective lens. Apart from its utility for rapid checks, this microscope with a long working distance can also be integrated with a rotational mount and a needle for aligned transfer.[222]

3.3.2 Scanning Electron Microscopy (SEM)

Scanning electron microscopy (SEM) is a fundamental imaging technique used to study the surface topography and composition of materials. The principle of SEM involves scanning a beam of electrons across the sample surface, which interacts with the sample to generate multiple signals for analysis. These signals include secondary electrons, backscattered electrons, and characteristic and Bremsstrahlung X-rays. Secondary electrons are electrons that are knocked out of their orbits by other electrons with higher energy and are collected by an Everhart-Thornley detector comprising a photomultiplier and a scintillator. Secondary electron imaging provides surface topography information and is typically conducted at a low accelerating voltage of around 2–3 kV. Backscattered electrons are high-energy electrons that escape the sample surface after undergoing multiple scattering events. Consequently, the backscattered electron yield is higher for heavy elements compared to light elements. Backscattered electron imaging contains both topographic and compositional information, with compositional contrast dominating the image. In my project, the Hitachi S-4300 SEM was intensively used for characterizing 2D materials and fabricated heterostructures, as shown in Figure 3.4. Most imaging of the 2D materials was performed using an accelerating voltage of 3 kV and a beam current of 11 μA, which produced secondary electron images with good contrast and minimized sample damage.

Figure 3.4 The Hitachi S-4300 SEM

3.3.4 The Raman & Photoluminescence (PL) Spectroscopy

Raman spectroscopy measures the coupling of light with vibration modes during scattering. It requires high-intensity laser input to observe the Raman spectrum. Each material has unique vibration modes of phonons that are specific to its elemental composition and crystal structure. As shown in Figure 3.5, the scattering of the incident light is composed of elastic Rayleigh scattering and inelastic Raman scattering.[223] Rayleigh scattering is a dominant scattering process with no energy change, while Raman scattering accounts for only a small proportion of scattering with energy changes. Raman scattering can be further divided into Stokes Raman scattering and anti-Stokes Raman scattering. Stokes Raman scattering describes the excitation of molecules to higher vibrational states from an initial ground vibrational state, while anti-Stokes Raman scattering follows the opposite pathway, from an excited vibrational state to the ground state. At room temperature, most molecules are in the ground states, resulting in a high occurrence of Stokes Raman scatterings compared to

anti-Stoke Raman scatterings. The basic principle of Raman spectroscopy is analysing Stokes Raman scattering of photons from a monochromatic laser interacting with the sample. The energy difference of the photon before and after Stokes Raman scattering leads to a shift in the spectrum. The characteristic peaks of the Raman shift (cm^{-1}) contain vibrational frequency information of the sample and can be considered as a fingerprint of the material.

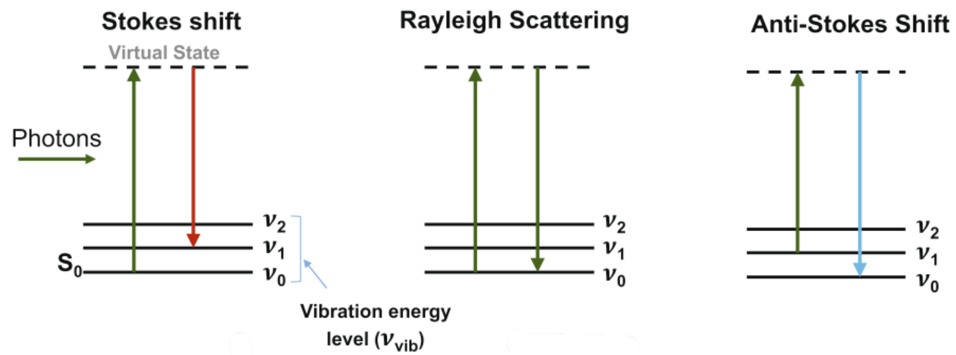

Figure 3.5 Schematics of three different scatterings: elastic Rayleigh scattering, inelastic Stokes Raman scattering, and inelastic anti-Stokes Raman scattering.[223] Reproduced with permission.

Raman spectroscopy has been intensively used to characterize graphene, containing loads of information such as thickness, defects, doping level, and strains.[224,225] Monolayer graphene has six phonon dispersion bands: iLO, iTO, oTO, iLA, iTA, and oTA, where A and O represent acoustic and optical branches; i and o represent in-plane and out-of-plane vibrations; L and T represent longitudinal or transverse modes.[226] The L and T modes describe the vibration of atoms in the direction parallel and perpendicular to the phonon wave vector, respectively.[227] As shown in Figure 3.6a, there are three most characteristic Raman peaks for graphene: the D band (~1350 cm^{-1}), the G band (~1580 cm^{-1}), and the 2D band (~2680 cm^{-1}) (also known as the G' band).[228] The G band is the only first-order Raman scattering

and related to doubly degenerate (iLO and iTO) phonon mode (E_{2g}) at Γ point, which is a feature for most graphitic materials.[226] The 2D and D bands are second-order scatterings. The 2D band is associated with two iTO phonons near K point while the D band comes from one iTO phonon and one defect near K point.[226] Other weak phonon-defect features and two phonon processes, such as the D' band (~ 1620 cm^{-1}), the D+D'' band (~2450 cm^{-1}), the D+D' band, and the 2D' band (~ 3200 cm^{-1}), are also identified in Figure 3.6a.[224,229] Figure 3.7 shows electron and phonon interactions that are responsible for some of the above-mentioned characteristic Raman peaks.[230] The G' band is sensitive to stacking and less prominent in graphite.[231] The D band reflects the induced defects, which are absent in graphite with high crystallinity. The intensity ratio of the D band to the G ($^{I_D}/_{I_G}$) band characterizes the defect level of graphene. The line shape of the G' band and the intensity ratio of the G' band to the G band ($^{I_{G'}}/_{I_G}$) are significant indicators of the layer numbers of graphene. Figure 3.6b shows the Raman spectra for exfoliated high-quality graphene with different layer numbers from 1 to 4.[232] Monolayer graphene shows symmetrical and sharp G' band (FWHM ~ 30 cm^{-1}) as well as high $^{I_{G'}}/_{I_G}$ ratio.[232] With the increase in thickness, the G' band becomes broader and less intense.

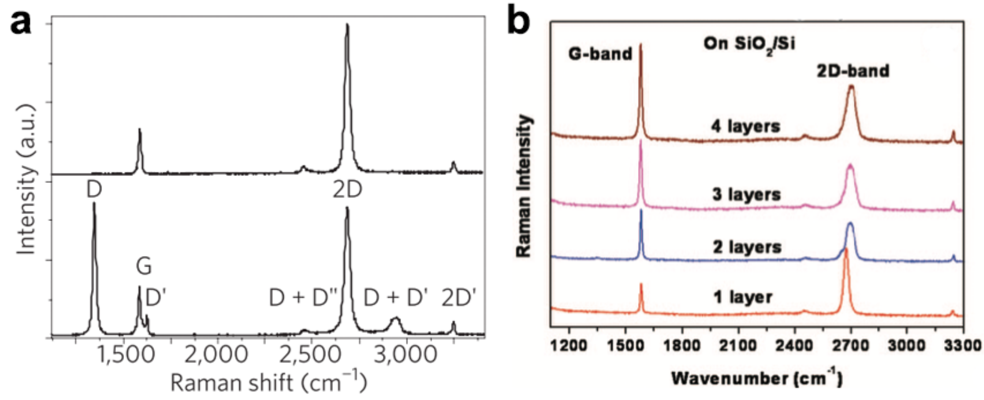

Figure 3.6 (a) Raman spectra of pristine (top) and defected graphene (bottom), with labeled characteristic peaks.[224] (b) Raman spectra of exfoliated graphene with different layer numbers from monolayer to four layers.[232] Reproduced with permission.

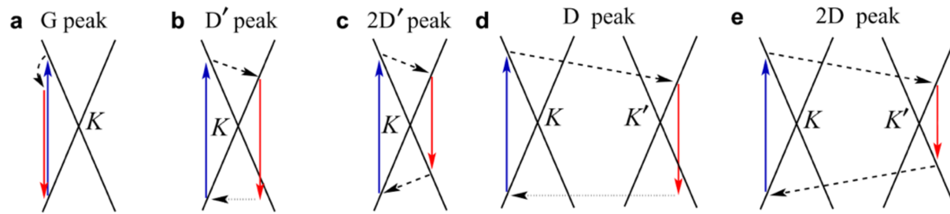

Figure 3.7 Electron and phonon interactions responsible for characteristic Raman peaks of graphene: (a) intravalley one-phonon G peak, (b) defect-assisted intravalley one-phonon D′ peak, (c) intravalley two-phonon 2D′ peak, (d) defect-assisted intervalley one-phonon D peak, (e) intervalley two-phonon 2D peak. Blue and red arrows represent photon absorption and emission; dashed and dotted arrows represent phonon emission and defect scattering.[230] Reproduced with permission.

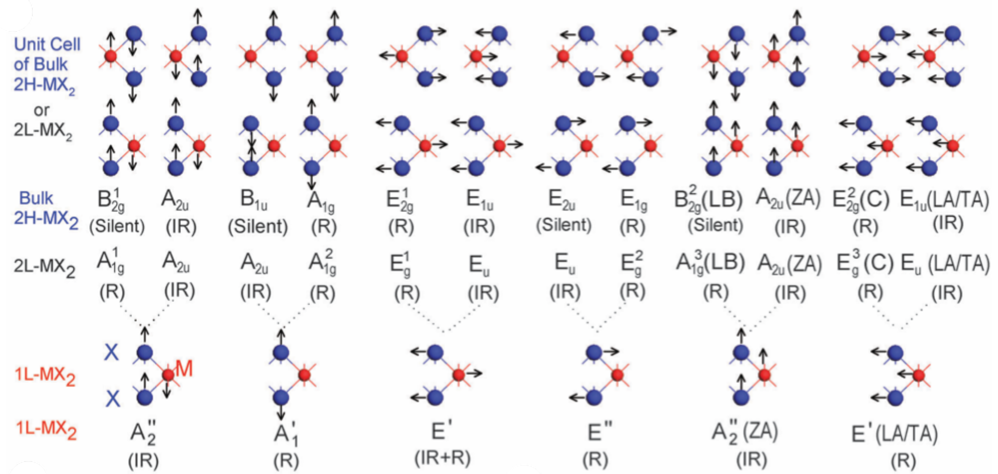

Figure 3.8 Various vibration modes for 2-H bulk MX_2, bilayer MX_2, and monolayer MX_2. R and IR refer to Raman mode and infrared-active mode, respectively. LA, TA, ZA, and LB refer to longitudinal acoustic, transverse acoustic, out-of-plane acoustic, and layer breathing modes, respectively. Each mode in monolayer MX_2 is split into two modes in its bilayer and bulk forms due to the presence of stacking order.[233] Reproduced with permission.

Raman spectroscopy has also been widely studied in characterizations of TMDs materials. Monolayer MX_2 and bilayer MX_2 belong to the categories of MX_2 with an odd number of layers (ONL- MX_2) and MX_2 with an even layer number (ENL- MX_2), respectively. The crystal lattice of 2H ENL- MX_2 has D_{3d} point group symmetry, which includes inversion symmetry. In contrast, ONL- MX_2 has D_{3h} point group symmetry, which does not possess inversion symmetry.[234,235] Figure 3.8 shows various vibration modes for 2H bulk MX_2, bilayer MX_2 and monolayer MX_2. At the Γ point (the center of the Brillouin zone), bilayer MX_2 exhibits vibration modes of $3A_{1g}$, $3A_{2u}$, $3E_g$, $3E_u$, while monolayer MX_2 (and) exhibits vibration modes of $2A_2''$, A_1'', $2E'$, and E''. The reduction in the number of vibration modes in monolayer MX_2 is due to the lack of stacking order.[233]

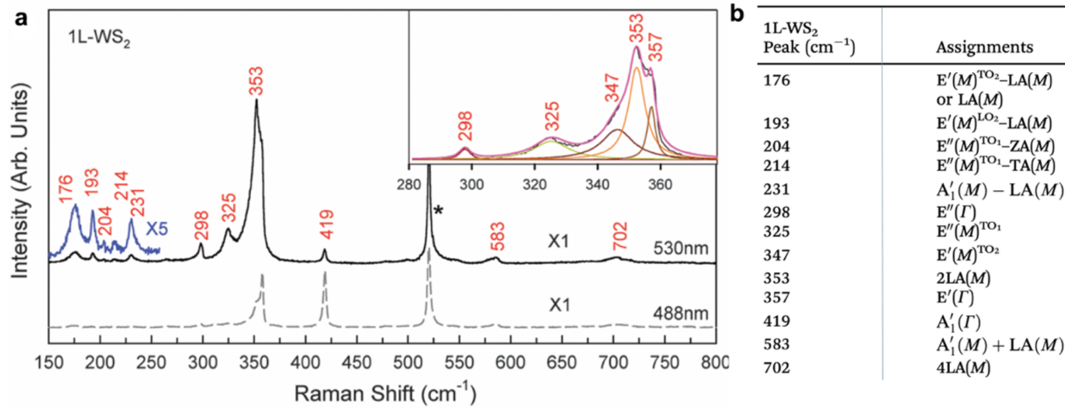

1L-WS$_2$ Peak (cm^{-1})	Assignments
176	$E'(M)^{TO_2}$–LA(M) or LA(M)
193	$E'(M)^{LO_2}$–LA(M)
204	$E''(M)^{TO_1}$–ZA(M)
214	$E''(M)^{TO_1}$–TA(M)
231	$A_1'(M) - LA(M)$
298	$E''(\Gamma)$
325	$E''(M)^{TO_1}$
347	$E'(M)^{TO_2}$
353	2LA(M)
357	$E'(\Gamma)$
419	$A_1'(\Gamma)$
583	$A_1'(M) + LA(M)$
702	4LA(M)

Figure 3.9 (a) Raman spectra of monolayer WS_2 at room temperature under illumination with the wavelength of 488 nm and 530 nm, respectively. Inset: Lorentzian multi-peak fitting is applied to fit different Raman modes. (b) Assignments of the main Raman modes for monolayer WS_2. LO_1 and LO_2 are two in-plane longitudinal optical phonon modes, while TO_1 and TO_2 are two in-plane transverse optical phonon dispersion. [233] Reproduced with permission.

Figure 3.9a shows a typical Raman spectrum of monolayer WS_2 at room temperature. The E'(M), 2LA, and E'(Γ) modes occur close to each other, resulting

in a convoluted peak. To distinguish them, Lorentzian curve fitting is employed, as shown in the inset of Figure 3.9a.[63,236–238] Figure 3.9b summarizes the assignments for each extracted peak. The $E'(\Gamma)$ corresponds to the in-plane vibration mode of sulfur atoms and the tungsten atoms moving in opposite directions at the Γ point. The $A_1'(\Gamma)$ refers to the out-of-plane vibration, where only the sulfur atoms move in opposite directions at Γ point. In the following discussions on the layer-dependent evolution of Raman modes, I adopt the commonly used terminology of A_{1g} and E_{2g}^1 from bulk MX_2 to refer to $A_1'(\Gamma)$ and $E'(\Gamma)$ in monolayer MX_2, respectively.[233] Similar to MoS_2, the A_{1g} mode in WS_2 experiences a stiffening (blue shift), while the E_{2g}^1 mode undergoes a softening (red shift) with increasing thickness.[234,239–241] Figure 3.10a shows the frequency of the A_{1g} and E_{2g}^1 modes, as well as the frequency difference between the two modes, as a function of film thickness in WS_2. The blueshift of the A_{1g} mode can be explained by higher force constants resulting from increased interlayer vdW force, which suppresses atom vibrations due to increased thickness.[240,242] However, instead of interlayer vdW interaction, the anomalous evolution of the E_{2g}^1 mode may be attributed to long-range Coulombic interaction between effective charges. With increasing thickness, the long-range Coulombic interaction decreases due to increased dielectric screening.[243] Figure 3.10b shows the Raman spectra of different monolayer WS_2 samples produced by low-pressure CVD (LPCVD), APCVD, and mechanical exfoliation. The spectra of the five samples appear similar, suggesting little dependence on the synthesis methods.[244,245] One notable difference between samples produced by APCVD and mechanical exfoliation is the emergence of a shoulder around 485 cm^{-1} (indicated by orange asterisks in Figure

3.10b), which has not been extensively addressed in the literature and requires further exploration.[63]

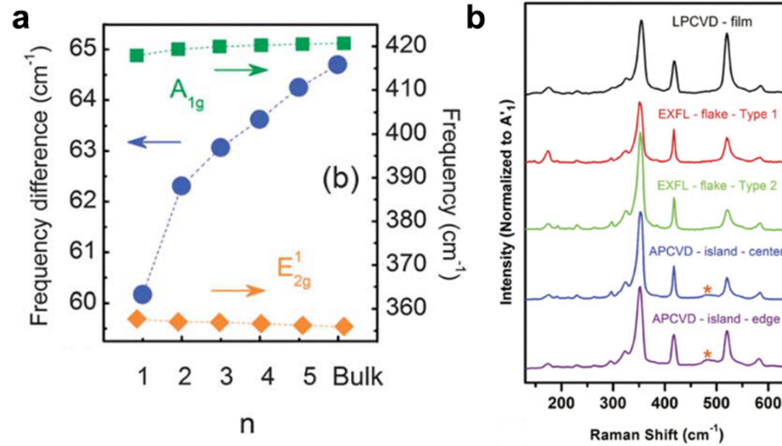

Figure 3.10 (a) The frequency of the A_{1g} mode (green) and E_{2g}^{1} mode (orange) and the frequency difference (blue) between the A_{1g} and E_{2g}^{1} modes as a function of layer number in WS_2.[245] (b) Raman spectra of monolayer WS_2 samples produced by different methods (LPCVD, APCVD, and mechanical exfoliation).[63] Reproduced with permission.

As discussed previously, PL is a radiative recombination process involving the emission of light when electron–hole pairs in a material radiatively recombine after being excited by incident photons. PL spectroscopy is commonly employed to characterize the bandgap energy of the material and is widely used in the study of monolayer TMDs like WS_2. The PL spectrum is typically measured in units of cm^{-1} (wavelength), but during data processing, it is often converted to units of eV (energy) using the Planck-Einstein relation: $E = hv = \frac{hc}{\lambda}$.

The Raman system used for my project is composed of a Raman spectrometer (LabRam Aramis Raman Spectrometer), a confocal microscope, and a laser source (532 nm doubled Nd:YAG). Figure 3.11 presents a typical optical pathway of a Raman spectrometer.[246] The laser is first filtered and then passed through the entrance slit to reach the sample surface. The scattered light is collected and focused by lenses to hit

the grating, which is used to separate the light into constituent wavelengths. Finally, the Raman signal is detected and recorded by a CCD camera to create a Raman spectrum.[247] The choice of the grating determines the resolution of the spectra, measured ingrooves per millimetre. The larger the grating, the higher the spectral resolution. For the Raman spectrum, a grating of 1800 g/mm was used, while a grating of 600 g/mm was applied for the PL spectrum. Table 3.1 shows the parameters used in Raman spectroscopy for different 2D materials. Table 3.2 shows the corresponding laser power with different objective lenses.

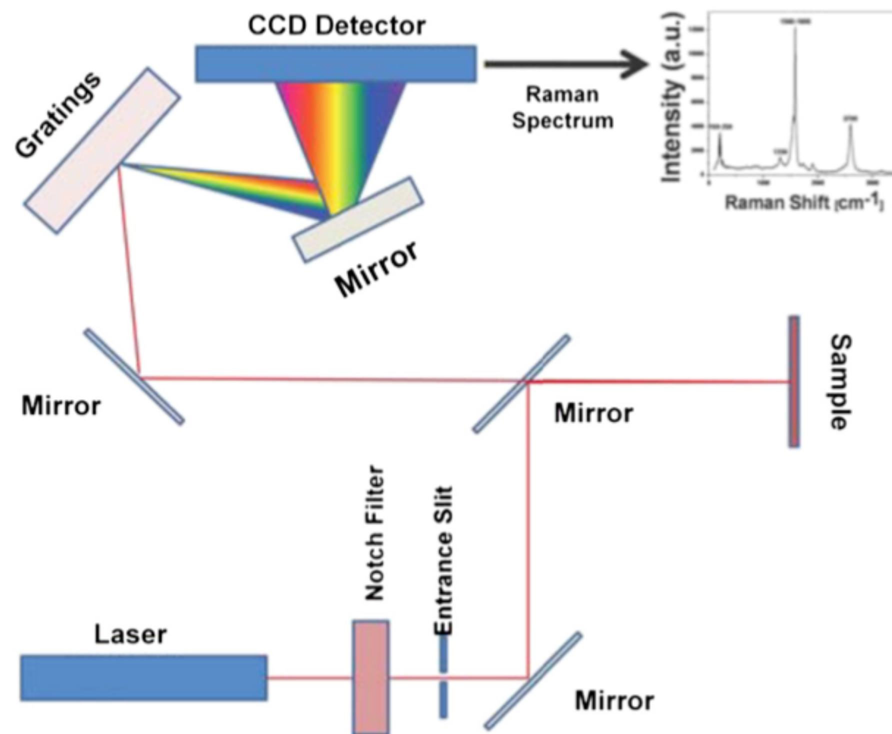

Figure 3.11 Schematic of an optical pathway of a Raman spectrometer.[246] Reproduced with permission.

Table 3.1 Parameters used in Raman characterization for different 2D materials

2D Materials	Lens (×)	Power (%)	Acq.time (s)	Accumulation	Range (cm^{-1})
Graphene	50	100	10	2	1200–3000
WS_2	50	25	10	2	200–600
h-BN	100	100	60	2	1200–1500
$PtSe_2$	50	25	1	5	100–300

Table 3.2 Laser power with different objective lens

Power (%) / Lens (×)	0.01	0.1	1	10	25	50
50	0.581	5.73	58.4	587	1600	3230
100	0.581	5.65	57.4	576	1562	3180

3.3.5 Atomic Force Microscopy (AFM)

AFM is a useful tool for surface analysis and is the most straightforward technique for determining the thickness of grown 2D materials. The basic principle of AFM is to image the surface topology by measuring the forces between the probe and the sample surface, which include the long-range attractive force (van der Waals force) and the short-range repulsive force.[248] Figure 3.12 shows the schematic of a basic AFM setup. A sharp probe, usually with a radius of 10~20 nm, is attached to the top of the cantilever with a reflective metal coating (gold or aluminium) on the backside.[249] A piezo crystal is used to mount the cantilever, allowing the probe to interact with the sample surface. The position displacement of the reflected laser is detected by a photodetector consisting of a segmented photodiode. The deflection of the laser beam can be interpreted as the bending of the cantilever and provides information about the sample surface. Due to its sensitivity to external vibrations, AFM is typically placed on an anti-vibration table or in an acoustic hood.

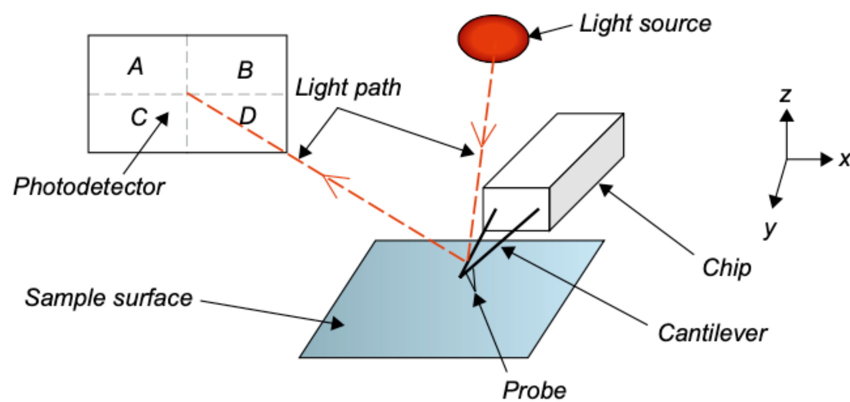

Figure 3.12 Schematic of a basic AFM setup: a cantilever with a probe on the top is mounted on a piezo crystal that allows the probe to move in x-, y-, and z- directions. The deflection of the reflected beam is detected by a photodetector and further interpreted to information about the sample surface.[250] Reproduced with permission.

There are two most commonly used imaging modes for AFM: contact mode and tapping mode.[250] In contact mode, the probe remains in very close contact with the sample surface. Contact mode operates in the repulsive regime, where the interactions between the surface and the probe repel the cantilever. Both constant height and constant force modes can be operated in contact mode. In constant height mode, the position of the cantilever along the z-axis remains the same. The bending of the cantilever results in the deflection of the laser beam, which is used to calibrate the height of the sample. In constant force mode, the deflection of the beam is set to a specific point, achieved by moving the piezo crystal along the z-axis via the feedback loop. The voltage applied to the piezo crystal is recorded to produce the topology of the sample surface. Contact mode is a simple and fast mode for samples with hard and flat surfaces. However, it has its drawbacks. The probe is easily damaged by large features on the surface, and vice versa. The strong capillary force caused by adsorbed water also decreases the resolution.

The tapping mode, also known as intermittent contact mode, is a dynamic mode where the cantilever oscillates close to its resonance frequency while the probe remains near the sample surface. Movements of the piezo crystal along the z-axis are controlled by a feedback loop to maintain the amplitude of the oscillation, which is dampened when the probe encounters features on the surface. Tapping mode significantly reduces lateral forces compared to contact mode, resulting in less damage during the operation, although it does increase the scanning. Therefore, for the soft 2D materials used in this project, tapping mode is preferable to contact mode for imaging the surface topology of the sample. The atomic force microscope used in this project was Asylum Research MEF-3D. The AFM probe used for the measurements was the Tap300-G, with a resonant frequency of 300 kHz and a force constant of 40 N/m. For example, for the measurement of the thickness of the $PtSe_2$ thin film, the parameters were as follows: the drive frequency was 280 Hz, the drive amplitude was 85 mV, the set point was 782.21 mV, and the scan speed was 10.02 μm/s.

3.4 Device Fabrication

3.4.1 Transfer Methods: DI Water/IPA/Aligned Transfer

The wet transfer was used for the transfer of 2D materials in my experiments. Figure 3.13 shows the schematics of different wet transfer methods for 2D materials grown on copper foil and silicon substrates. As-synthesized 2D materials were first coated with poly(methyl methacrylate) (PMMA) (495A8, MicroChem) by spinning at a speed of 4500 rpm for 60 s. The estimated thickness of the PMMA layer is 500 nm. PMMA was then cured on a hotplate at 180 ℃ for 90 seconds. Potassium hydroxide (KOH, 1 M, Sigma-Aldrich) and ammonium persulfate (APS, 0.2 M, Sigma-Aldrich)

were used as etchants for silicon (Si/SiO_2) substrate and copper foil, respectively. Notably, before the wet etching process, a diamond file was usually used to polish the edge of the silicon substrate covered with spare PMMA, which significantly hampers the etching rate of the silicon dioxide. The etching started from the edge and proceeded towards the center of the substrate. The copper foil was directly etched in APS, leaving the 2D material film floating on the surface of APS. However, the silicon substrate was detached from the film after the silicon dioxide was fully etched by KOH. During the late stage of the detaching process, if the net force of the gravity and buoyancy acting on the silicon substrate is greater than the surface tension, the film would be dragged from the surface and sink to the bottom of the container along with the silicon substrate. Therefore, a petri-dish was used for etching 2D materials with underlying silicon substrates to prevent the film from being dragged into the etchant during the detaching process. The 2D-material thin film with PMMA coating was scooped out and washed in the DI water to remove etchant residues for at least 3 times before being transferred to the target substrate, usually a silicon substrate. The PMMA coating was removed by soaking in acetone for 4 h after overnight natural evaporation and 15 min of baking at 180 °C on a hotplate. Specifically, to obtain a cleaner interface or prevent the monolayer TMDs from being washed away, an improved IPA-based transfer method was applied, as reported by a previous group member Dr. Yuewen Sheng.[251] In the IPA transfer process, the 2D-material thin film was first scooped out onto a cover glass before finally being transferred to the target substrate. Then, the IPA was dropped onto the cover glass to wash away the DI water and allow the thin film to float on the cover glass. Simultaneously, IPA drops were also dropped on the target substrate. Tweezers were used to drag the thin film from the cover glass to the target

substrate by tilting the cover glass to a certain angle and aligning it with the target substrate. After the natural evaporation of IPA underneath the thin film, the PMMA can be removed using the same procedure mentioned above. Compared with the traditional wet transfer method, the monolayer WS_2 transferred to graphene using the IPA transfer showed a stronger quenching effect on the PL signal, indicating a better interfacial coupling between graphene and WS_2.[251]

An optical microscope with a long working distance, a rotation mount, and a needle can be assembled into an aligned transfer system, as reported by my colleague Qianyang Zhang. In this system, the thin film is transferred to the target substrate fixed on the rotation mount using the IPA transfer method. The needle is used to drag and adjust the thin film to a specific position, while the optical microscope is employed for checking purposes.[222]

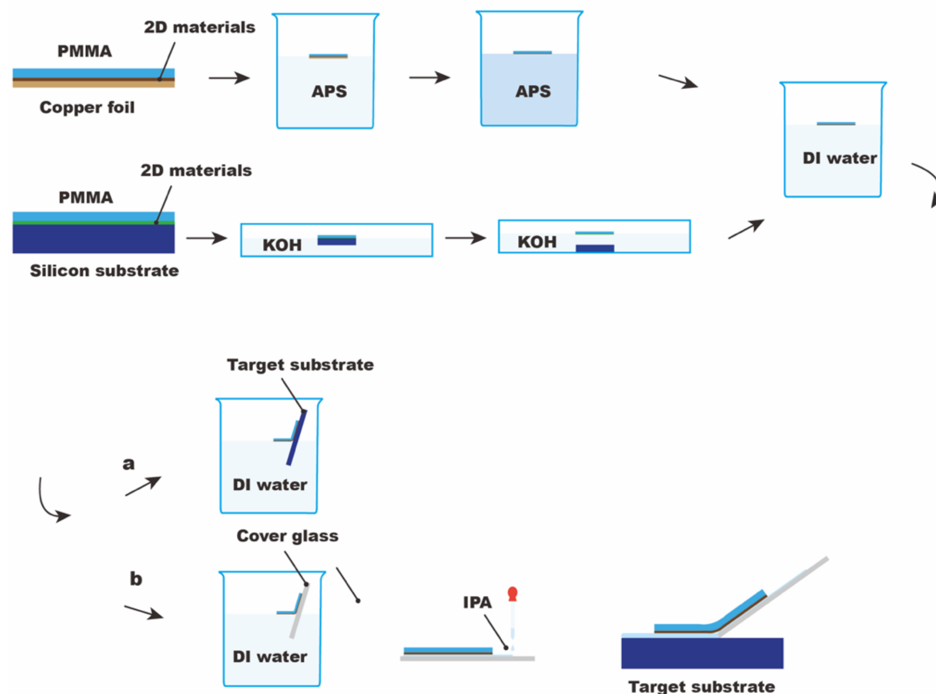

Figure 3.13 Schematics of wet transfer methods by using (a) the DI water and (b) IPA for 2D materials on copper foil and silicon substrates with a covered PMMA layer. Copper foil and silicon dioxide are etched by APS and KOH, respectively. 2D materials with PMMA coating on the top are washed in DI water for at least 3 times.

3.4.2 E-Beam Lithography (EBL) and Photolithography

Lithography is a process to create patterns on a wafer surface, and it is a conventional technique for nano-patterning. Two lithography methods used in my project are electron beam lithography (EBL) and photolithography. Photolithography is an optical method of lithography to transfer patterns from mask to wafer. This technique involves transferring a desired pattern to a substrate coated with a photoresist through a contact printing procedure. The apparatus used for photolithography is a mask aligner in the cleanroom, which utilizes UV light as the radiation source. The model of the mask aligner I used is Karl Suss MJB3, equipped with UV400 optics for 365nm and 405 nm exposure. EBL, on the other hand, is a maskless lithography approach that directly writes patterns on a substrate coated with resists using a focused electron beam. The primary electrons in the beam typically have an energy of 50 to 100+ keV to achieve the resolution.[252] I performed EBL using the JEOL 5500 FS, which has an accelerating voltage of 50 kV and a beam current of 10 nA. Figure 3.14 a-b show the EBL system and the mask aligner I used for the project in the cleanroom.

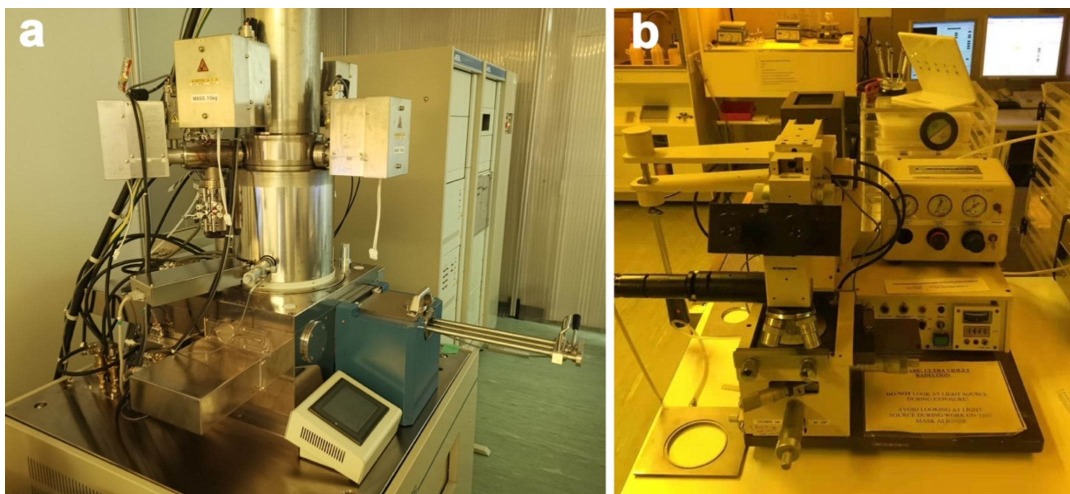

Figure 3.14 (a) The JEOL 5500 FS EBL system. (b) The mask aligner.

There are several steps involved in lithography: wafer cleaning (to enhance adhesion of the resist); resist spin coating; soft bake (to evaporate the solvent in the resist); alignment and exposure; development; and pattern check. The resist plays an important role in the lithography process. In positive resist, the area exposed to the radiation source is easily removed during the development process, while in negative resist, the exposed areas are cured and become insoluble.

Photolithography is fast and efficient for mass production, but its resolution is relatively poor. To address the issue of contamination on the mask resulting from direct contact between the wafer and mask, proximity printing was employed in lithography. Proximity printing involves creating a small gap, typically ranging from 5 to 30 μm, between the wafer and mask during the patterning process.[253] The resolution of the proximity printing is limited by the near-field (Fresnel) diffraction. It can be approximated by:[252]

$$R \approx \sqrt{\lambda L}$$

where λ is the wavelength of the light, and L is the gap between the wafer and mask. The resolution degrades as the gap distance increases, typically ranging from 2 to 3 μm.[253]

The resolution of Electron Beam Lithography (EBL) is primarily influenced by two factors: the point-spread function (PSF) of the exposing radiation (in this case, the electron beam) and the contrast of the development process.[254] Regarding the PSF, the width of the PSF is indeed influenced by the spot size of the electron beam and electron scattering within the resist. When high-energy electrons penetrate the resist layer and interact with the resist, electron scattering occurs. The broadening of the beam diameter is attributed to forward scattering, which arises from elastic collisions

between the incident electrons and the resist molecules. A high-energy electron beam or a thinner resist layer can be used to minimize this broadening effect.[254] Additionally, backscattered electrons, which bounce back through the resist upon reaching its bottom, unintentionally expose the resist and can spread over length scales of several microns. The contrast of the development process is influenced by resist swelling in the developer and the mechanical stability of the resist.[255,256] Resist swelling refers to the increase in resist volume when the developer penetrates the resist, leading to pattern distortion. Although resist contraction can occur during the rinsing process, it does not always compensate for the volume increase caused by swelling. Reducing the resist thickness can be effective in mitigating this limitation due to resist swelling. The feature size achieved through EBL can reach sub-10 nm.[254,256] Therefore, EBL is more suitable for fine features compared to photolithography. Another advantage of EBL is that it is mask-free. In photolithography, a mask must be prepared in advance, and once the mask is made, the pattern is fixed and unchangeable. AutoCAD was used to design patterns for EBL, allowing for flexible modifications before each patterning.

Various bilayer recipes were developed for different purposes, as shown in Table 3.3. It is important to note that the bilayer positive recipe for EBL was used to create an undercut structure for the following metal deposition process, while the bilayer negative recipes for EBL and bilayer positive recipe for photolithography aimed to reduce the residue of MaN-2403 and S1813. Figure 3.15 is the schematics of the fabrication process of graphene ribbons by using EBL with the bilayer negative recipe.

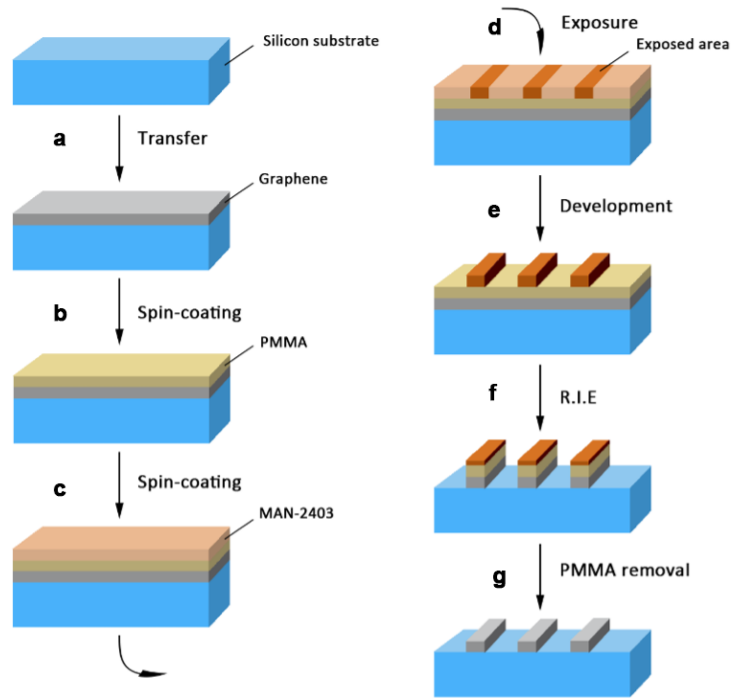

Figure 3.15 Schematics of the fabrication process of graphene ribbons: (a) transfer graphene film to a cleaned silicon wafer; (b) spin-coat a thin layer of PMMA on the graphene film; (c) spin-coat a thin layer of MAN-2403 on PMMA layer; (d) expose the specific area of the chip under E-beam; (e) develop the chip in MAD-525 to remove the negative resists on the unexposed area; (f) use reactive ion etching (R.I.E) or oxygen plasma to remove the positive resists and the graphene underneath the unexposed negative resists; (g) remove the rest positive resist underneath the exposed area in acetone.

Table 3.3 Bilayer recipes for the lithography

	EBL - Positive resist	**EBL - Negative resist**	**Photolithography - Positive resist**
Purpose	Au bondpads	Graphene ribbons	$PtSe_2$ ribbons
First layer	PMMA 495 A4	PMMA 495 A4	PMMA 495 A4
Spin-coating speed & time & resist thickness	4500 rpm / 60 s / 190 nm	4500 rpm / 60 s / 190 nm	4500 rpm / 60 s / 190 nm
Soft bake T &time	180 °C / 90 s	180 °C / 90 s	180 °C / 90 s
Second layer	PMMA 950 A4	MaN-2403	S1813
Spin-coating speed & time & resist thickness	4500 rpm/ 60 s/ 200 nm	3000 rpm / 30 s / 300 nm	2000 rpm / 1 min / 2000nm
Soft bake T & time	180 °C / 90 s	90 °C / 90 s	115 °C / 60 s
Dose/Mode/Aperture	650 μC/cm^2 / 2 / 1	180 μC/cm^2 / 2 / 1	45 mJ/cm^2 (UV)
Exposure time	\	\	18 s
Developer & time	MIBK: IPA = 1:3 / 45 s	ma-D525 /150 s	MF-319 / 30 s
Rinse & dry	IPA/ compressed nitrogen	DI water/ compressed nitrogen	DI water/ compressed nitrogen
Lift-off	Acetone overnight	Acetone overnight	Acetone overnight

3.4.3 Thermal Evaporation

Thermal evaporation is a physical vapor deposition process in which a target metal is evaporated by Joule heating and deposited onto a target substrate under vacuum conditions. The Edward 360 thermal evaporator in the cleanroom was used

for metal deposition in the devices of my project. After pattern writing by EBL or photolithography, the substrates were fixed on the holder by Kapton tape on two corners, and then the holder was placed back into the chamber. Once the base pressure stabilized at 2×10^{-6} mbar, the metal evaporation process began by gradually increasing the current through the metal source. The evaporation rate was carefully controlled within 0.1nm–0.2nm/s to achieve a compact and homogenous electrode. After metal deposition, acetone was used to lift off the unwanted area covered by PMMA. The electrodes of the devices were made of Au (50 nm), which has weak adhesion to the silicon substrate. Therefore, a layer of 5–10 nm Cr was usually deposited beforehand to improve the success rate of the lift-off process.

3.4.4 Patterning

Etching

Etching is a process that follows lithography to permanently transfer the mask pattern into the surface layer of the wafer. Both wet etching and dry etching can be used in this process. Wet etching involves using a liquid etchant to dissolve the materials on the surface, while dry etching involves using a gas-phase etchant in plasma to etch the material. Dry etching, such as reactive ion etching (R.I.E.) and oxygen plasma, is more suitable for small feature sizes compared to wet etching. In R.I.E., when an ion beam bombards the sample surface, it directly knocks atoms out of the surface and also triggers chemical reactions between the surface materials and the ion beam, resulting in a high etching rate. Oxygen plasma etching is another type of dry etching process that utilizes plasma generated under low pressure as the etching

species. Dry etching processes are used not only to remove graphene or h-BN grown on the backside of the copper foil but also to remove unwanted 2D materials that are not covered by PMMA after EBL/photolithography. For oxygen plasma etching, a power of 60 W is used. The chamber was first evacuated to 0.2 mbar, and then the chamber pressure was maintained at 0.4 mbar with an oxygen gas flow rate of 40 L_n/h during the etching process.

Direct Laser Patterning

Laser patterning is a process used to remove unwanted materials by exposing them to laser irradiation. The physics behind this is quite complex and primarily involves a thermal mechanism resulting from the absorption of laser energy on the surface of the materials. This thermal process can cause the material to melt, evaporate, or undergo lattice sublimation, ultimately forming narrow cutting kerfs in the material, as shown in Figure 3.16.[257,258]

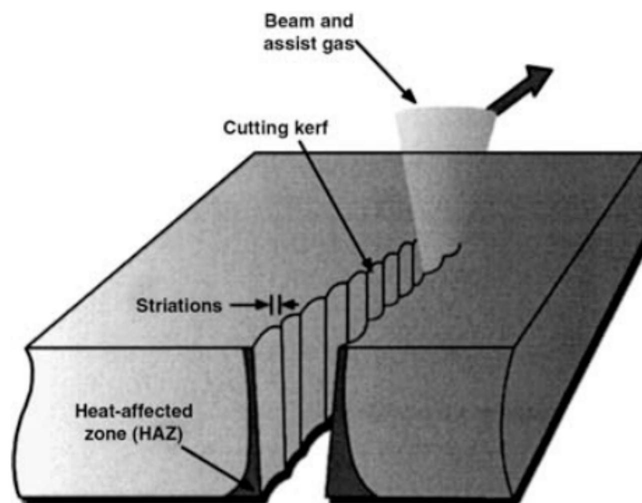

Figure 3.16 Schematic of laser cutting process.[257] Reproduced with permission.

LabRam Aramis Raman spectrometer system was also utilized for laser patterning, employing a laser with a wavelength of 532 nm. During the laser patterning process, a $PtSe_2$ ribbon was positioned laterally under the 100 × objective lens to reach a maximum laser power of 7.8 mW, with a spot size of 3 μm. The laser moved perpendicularly to cut the ribbon along a pre-drawn line. The spatial resolution of the line scanning is determined by both the spot size of the laser and the scan step. The scan steps, along with the corresponding channel widths and time required to cut a $PtSe_2$ ribbon with a width of 20 μm, are summarized in Table 3.4. By reducing the scan step, a channel with a smaller gap size can be achieved, although the overall cutting process would take a longer time.

Table 3.4 Summary of the scan steps, the corresponding channel widths, and time cost

Scan step	Time	Channel width
300 nm	1min 5s	1.5 μm
200 nm	2min 10s	1 μm
100 nm	4min 22s	0.8 μm

3.5 Electrical and Optoelectrical Measurements

All of the electrical and optoelectronic measurements in my project were conducted using a probe station coupled with a confocal microscope system. A 532 nm diode-pumped solid laser (Thorlabs, DJ523-40) and a 10× objective lens were employed to form a 2 μm spot on the sample. Electrical measurements were carried out using the Keithley 2400 source meter. EL spectra were collected using a custom-built microscope/spectrometer system. This system consisted of a spectrometer (SP-

2300 spectrometer, Princeton Instruments Acton), a CCD camera (PIXIS 100 CCD, Princeton Instruments Acton) attached to an optical microscope with a 10× objective lens, and a 532 nm diode-pumped solid laser (Thorlabs, DJ523-40).

Chapter 4 Photocurrent Direction Control and Increased Photovoltaic Effects in All-2D Ultrathin Vertical Heterostructures Using Asymmetric h-BN Tunnelling Barriers

4.1 Introduction

As discussed in Chapter 2, monolayer TMDs, such as MoS_2 and WS_2, have strong light-matter interactions due to their direct bandgap and high absorption coefficient.[5,8,9] Graphene is a very good alternative for a metal electrode since its Fermi level can be easily tuned by gate-voltage or extrinsic doping.[149,154] Insulating h-BN thin film is free of dangling bonds and has a large bandgap, making it widely used as a defect-free dielectric for tunnelling devices.[30,79,80,259] By using the aforementioned three building blocks, I demonstrated an asymmetrical vertical heterostructure of SiO_2/graphene/WS_2/ h-BN/graphene (Gr_B/WS_2/ h-BN/Gr_T), which is composed of all-2D materials grown by CVD. Here, WS_2 acts as an efficient photoactive material, graphene serves as a gate-tunable electrode, and h-BN works as a tunnelling barrier. Both asymmetrical vertical heterostructure (Gr_B/h-BN/WS_2/Gr_T and Gr_B/WS_2/h-BN/Gr_T) and symmetrical vertical heterostructure (Gr_B/WS_2/Gr_T) were fabricated for a systematic comparison study of their electronic properties and photovoltaic effect. Heterostructure of graphene coupled with TMDs[9,158] and TMDs-based p–n heterojunctions[160,161,170,260–262], in both vertical and lateral geometries, are widely reported to achieve an ultrathin all-2D solar cell. Most of the previous works have

focused on modulating the electron–hole separation process. In this study, an asymmetrical vertical heterostructure utilizing h-BN as an insulating layer was delicately designed to enhance the photovoltaic effect by controlling the tunnelling possibility of each electrode.

4.2 Results and Discussion

4.2.1 Characterizations of CVD-grown 2D Materials

Figure 4.1a shows the SEM image of CVD-grown continuous graphene on copper foil. Due to the different thermal expansion coefficients of copper foil and graphene, wrinkles start to appear on the continuous graphene film during the cooling process. Dark spots suggest the presence of multilayer graphene islands. As discussed in section 3.3.4, the intensity ratios of the 2D/G peak in the Raman spectrum shown in Figure 4.1b-c indicate that most of the region on the graphene electrode consists of continuous films, with some scattered multilayer islands.[101]

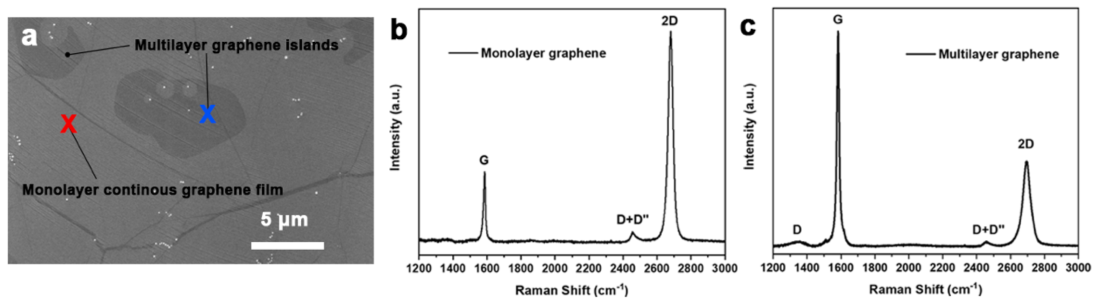

Figure 4.1 Characterizations of CVD-grown graphene. (a) SEM image of CVD-grown graphene continuous film on copper foil. (b) The Raman spectrum of graphene on the region of the red cross shown in (a). (c) The Raman spectrum of graphene on the region of the blue cross shown in (a).

The SEM image in Figure 4.2a shows a continuous h-BN film grown on copper foil. Similar to the scenario with the graphene film grown on copper foil, wrinkles can also be observed on the h-BN thin film. The Raman spectrum in Figure 4.2b exhibits the characteristic peak position of a few-layered h-BN at 1367 cm^{-1}. Figure 4.2d represents the corresponding height profile of the white line drawn on the AFM image of a transferred h-BN on a silicon substrate, as shown in Figure 4.2c. A vacuum annealing at 150 ℃ for 4 hours was performed on the h-BN continuous film to remove surface residues from PMMA coating.[263] The areas with sharp edges were delicately chosen for the AFM measurements. The clear bright line in the middle of the image is the edge of the h-BN thin film. This line split the whole image into two parts, with the h-BN film on the left-hand side and the silicon substrate on the right-hand side. Consistent with the SEM image, the paralleled lines close to the edge are wrinkles generated during the cooling process. The small white spots on h-BN films are speculated to be the BN nanoparticles formed during CVD growth.[118] The large bright spots are supposed to be dirt or other contaminants accumulated on the substrate. According to the height profile, the thickness of h-BN is 0.58 nm, corresponding to a layer number of 1–2 layers.[264]

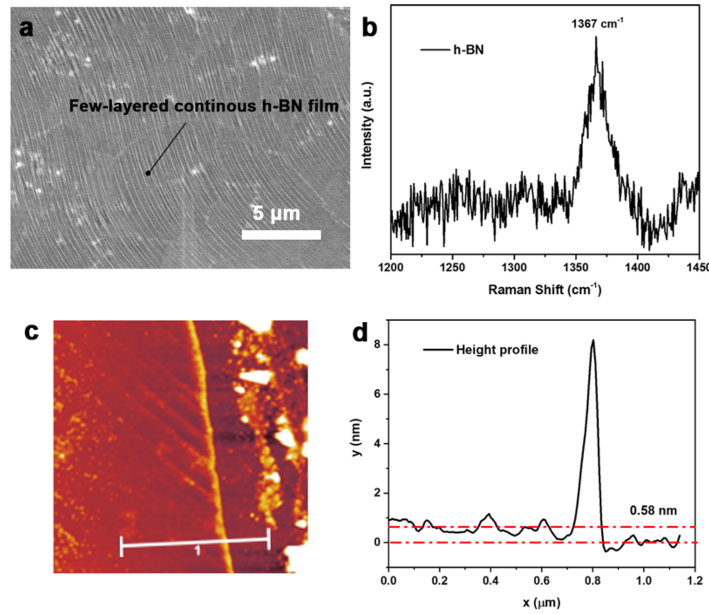

Figure 4.2 Characterizations of CVD-grown h-BN. (a) SEM image of CVD-grown few-layered continuous h-BN film on copper foil. (b) The Raman spectrum of continuous h-BN film. (c) AFM image of a transferred h-BN continuous film on a SiO_2/Si substrate. (d) The corresponding height profile for the white line drawn on (c).

As shown in Figure 4.3a-b, CVD-grown WS_2 is predominantly composed of isolated single-crystal domains, with an average flake size of 150 μm. Additionally, the CVD-grown WS_2 achieves large coverage and even distribution on the silicon wafer. The PL and Raman spectra, shown in Figure 4.3c-d, indicate that WS_2 is a monolayer. Voigt multi-peak fitting was used to extract the PL spectra of WS_2. A detailed discussion on the fitting process of the PL and Raman spectra is provided in Appendix A. Here, two extracted peaks X and X^- represent neutral exciton emission and negative trion emission, respectively, with peak position at 1.96 eV and 1.94 eV.[56] As discussed in Appendix A, the line width, represented by the full width at half maximum (FWHM), contains information on the crystal quality, disorders, strains, and the influence of the environments.[265–269] The FWHM of exciton emission is 71 meV,

which is relatively larger than that of exfoliated materials (~ 52 meV), suggesting that the CVD-grown WS_2 has more induced defects than exfoliated samples.[63] Gaussian multi-peak fitting was used to extract the Raman spectra of WS_2. In the Raman spectrum of WS_2, the E^1_{2g} peak is attributed to the in-plane vibration of W and S atoms towards opposite directions, while the A_{1g} peak results from the out-of-plane vibration of S atoms. The E^1_{2g} and A_{1g} modes are located in 356 cm^{-1} and 418 cm^{-1}, respectively, with a frequency difference of 62 cm^{-1}, which is in accordance with CVD-grown monolayer WS_2 in previous literature.[63,238,270]

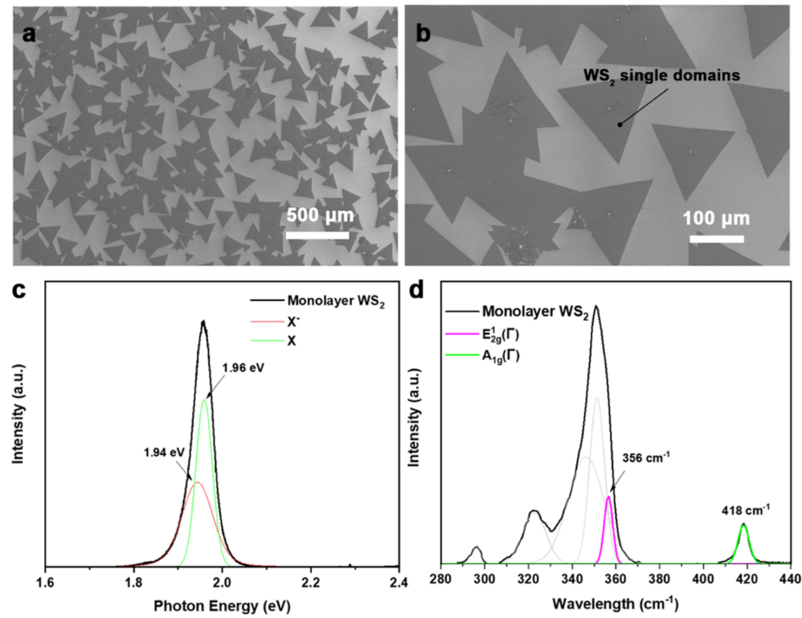

Figure 4.3 Characterizations of CVD-grown WS_2. (a-b) SEM images of CVD-grown WS_2 single domains on a SiO_2/Si substrate. (c) The PL spectrum of a WS_2 single domain. (d) The Raman spectrum of a WS_2 single domain.

4.2.2 Fabrication of the Gr_B/WS_2/h-BN/Gr_T Asymmetrical Vertical Heterostructure

Figure 4.4a illustrates the fabrication process of the Gr_B/WS_2/h-BN/Gr_T asymmetrical vertical heterostructure. First, bottom bond pads with markers were patterned on a silicon wafer using E-beam lithography (EBL), followed by the deposition of chromium/gold (Cr/Au) (75 µm squares) via thermal evaporation. Then, a continuous graphene film was transferred onto a silicon chip with bottom bond pads and patterned into 10 µm ribbons using EBL. During this process, markers were used to align the graphene ribbon to the middle of each bottom Cr/Au bond pad. After development, oxygen plasma was applied to etch the unwanted area of graphene, followed by the removal of resists to expose the patterned bottom graphene ribbons using acetone. Next, a film of WS_2 single-crystal domains and a continuous few-layered h-BN film were successively transferred onto the bottom graphene ribbons. Finally, another film of pre-patterned graphene ribbons was transferred onto WS_2, followed by the deposition of top Cr/Au bond pads onto it using EBL and thermal evaporation. The top graphene ribbons were perpendicular to the bottom graphene ribbons. Notably, after WS_2 was transferred onto the silicon chip, the 2D materials were supposed to be transferred using an IPA-based transfer technique.[251] The IPA-based transfer technique not only prevents WS_2 from being washed off but also increases the interlayer coupling.[251] Figure 4.4b shows an SEM image of fabricated device arrays on a single silicon chip. Figure 4.4c shows a SEM image of a typical device where there is a 90 ° rotation angle between the top and bottom graphene ribbons. This design creates a crossbar structure where the WS_2 single domain and continuous h-BN film are trapped between the top and bottom graphene electrodes. In

each crossbar, the layered vertical structure follows the sequence of Gr_B/WS_2/h-BN/Gr_T from bottom to top. Figure 4.4d shows the setup for the electrical measurements. Two probe tips were installed on two translation stages (x-axis, y-axis) and lowered down to make contact with the gold bond pads on both the top and bottom graphene electrodes as the source and drain. Therefore, electrons can directly flow vertically through the as-fabricated asymmetrical heterostructure. During the measurements, the top graphene electrodes were always grounded as the source.

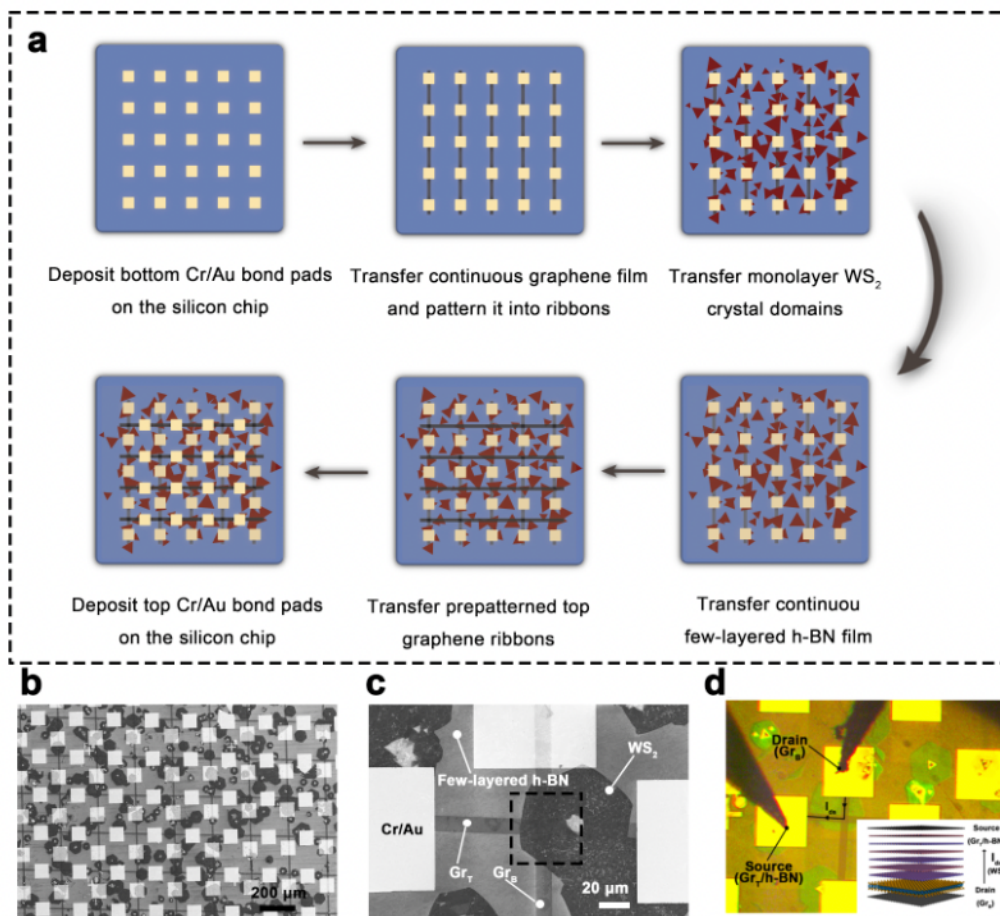

Figure 4.4 The fabrication process of asymmetrical Gr_B/WS_2/h-BN/Gr_T vertical heterostructure arrays. (a) Schematic illustration of the device fabrication: deposit bottom Cr/Au bond pads on a silicon substrate; transfer a continuous graphene film onto the silicon substrate with bond pads and pattern it into graphene ribbons; transfer a layer of WS_2 single-crystal domains onto it; transfer a continuous few-layered h-BN film onto it; transfer pre-patterned top graphene ribbons perpendicular to bottom graphene ribbons; deposit top Cr/Au bond pads. (b) SEM image of as-fabricated device arrays. (c) SEM image of a typical asymmetrical vertical device. (d) Setup for electrical measurements of a single device.

4.2.2 Comparison Study on the Symmetrical and Asymmetrical Vertical Heterostructures

To make a comparison, two other vertical heterostructures were also fabricated: one is the symmetrical heterostructure of $Gr_B/WS_2/Gr_T$, and the other is an asymmetrical heterostructure with h-BN intercalated in between the top graphene and WS_2 (Gr_B/WS_2/h-BN/Gr_T). Figure 4.5 illustrates the three configurations designed for the comparison study, where electrons tunnel through the barriers formed by both the vdW gap and the layer thickness of h-BN. As mentioned in section 2.5.1, the direct tunnelling current at the low voltage regime can be expressed as follows:[183]

$$I_{DT}(V) = \frac{A_{eff}\sqrt{m\varphi_B}q^2V_{ds}}{h^2d}\exp\left[\frac{-4\pi\sqrt{m\varphi_B}d}{h}\right] \qquad 4\text{-}1$$

where A_{eff}, m, φ_B, q, V_{ds}, h, d are the effective junction area, free electron mass, barrier height, the elementary charge, applied bias, Planck's constant, and barrier width, respectively.

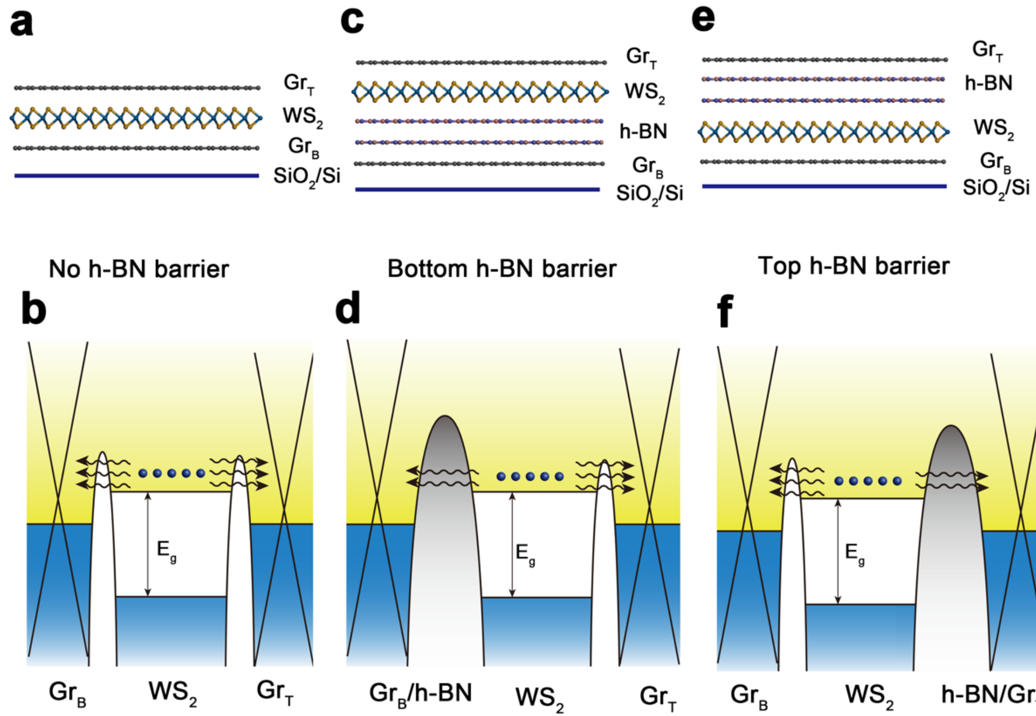

Figure 4.5 Configurations of the three vertical heterostructures with different barriers and their corresponding energy band diagrams. (a-b) $Gr_B/WS_2/Gr_T$; (c-d) Gr_B/h-BN/WS_2/Gr_T; (e-f) Gr_B/WS_2/h-BN/Gr_T. In the symmetrical configuration, (a) the barrier difference between the top graphene and bottom graphene is small, and the electrons on the conduction band of WS_2 have similar possibilities to transport to the top and bottom graphene. In asymmetrical configurations of (b) and (c), the introduced h-BN thin film largely increases the tunnelling barrier, so that the enlarged barrier difference can cause a one-way flow of electrons excited in WS_2.

In the symmetrical vertical structure of graphene/WS_2/graphene, the potential barrier widths on both sides are attributed to the vdW gap between graphene electrodes and WS_2, which is expected to be the same for both sides. The potential barrier heights on both sides are caused by the offset between graphene and WS_2. Therefore, the difference in potential barrier originates from the varying doping levels of the top and bottom graphene electrodes. From the transfer curves of the graphene electrodes, the Fermi levels of the top and bottom graphene can be roughly estimated, which are presented in the plot as the lowest point. As shown in Figure 4.6, the top graphene electrode is less p-doped compared to the bottom graphene electrode due to differences

in the dielectric environment and fabrication process.[158] Since the Fermi levels of the top and bottom graphene electrodes have only a slight difference, the excited electrons on the conduction band of WS_2 have similar possibilities to migrate to the top and bottom graphene electrodes. Therefore, the photovoltaic effect, which is the net current under exposure to light, would not be prominent.

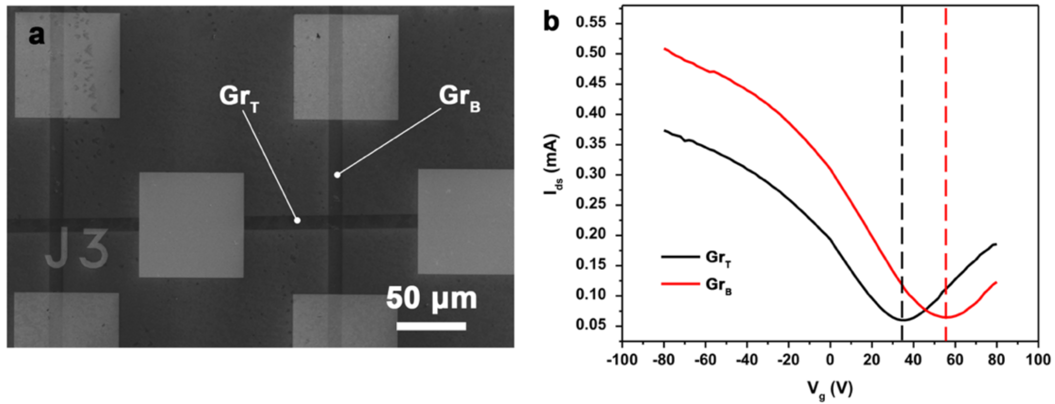

Figure 4.6 (a) SEM image of the top (Gr_T) and bottom (Gr_B) graphene field effect transistors (FET). (b) Back gate sweep (I_{ds}-V_g) of Gr_T and Gr_B graphene FET under a V_{ds} of 1 V.

In the asymmetrical vertical structure, with the introduction of the h-BN layer, the barrier width corresponds to the vdW gap and the thickness of h-BN, while the barrier height corresponds to the energy offset between the Fermi level of graphene and h-BN. In this configuration, the h-BN tunnelling barrier and vdW gap are combined together as one single potential barrier, as shown in the band diagram, which demonstrates a wider and higher barrier compared to the symmetrical vertical structure. In the Gr_B/h-BN/WS_2/Gr_T heterostructure, for example, both the barrier height and barrier width between WS_2 and the bottom graphene electrode are increased by the inserted h-BN layer. As a result, electrons excited on the conduction band of WS_2 are more likely to migrate towards the top graphene electrode rather than the bottom graphene electrode due to the enlarged barrier difference between the two sides. This

configuration exhibits a strong photovoltaic effect due to the large net current. A similar argument applies to the asymmetrical vertical heterostructure with the top barrier, Gr_B/WS_2/h-BN/Gr_T, where a reversed electron flow can be achieved by inserting the h-BN layer with a different sequence in the vertical stack.

PL mapping was used to demonstrate the influence of the introduced h-BN tunnelling barrier. Figure 4.7d-f show corresponding PL mappings of the crossbar area of the symmetrical vertical heterostructure, the asymmetrical vertical heterostructure with the top h-BN barrier, and the asymmetrical vertical heterostructure with the bottom h-BN barrier that are shown in Figure 4.7a-c, respectively, with the scale bar representing the integral intensity of PL. In a typical graphene/WS_2 heterostructure, the electrons excited in WS_2 under illumination tend to migrate to graphene and undergo non-radiative recombination due to the strong interlayer coupling, resulting in a quenching effect in the junction area of WS_2 and graphene.[271–273] In the symmetrical vertical heterostructure, both the bottom and top graphene electrodes have direct contact with WS_2, leading to a strong quenching effect in the overlapping area, as shown in Figure 4.7d. However, in the asymmetrical vertical structure, due to the presence of h-BN, only the graphene electrode with direct contact with WS_2 experiences a strong interlayer coupling effect and exhibits strong quenching in the PL mapping, as shown in Figure 4.7e-f. This observation confirms that the h-BN layer is successfully introduced in the vertical stacks and serves as an effective tunnelling barrier, hindering electron transportation from WS_2 to the graphene electrode.

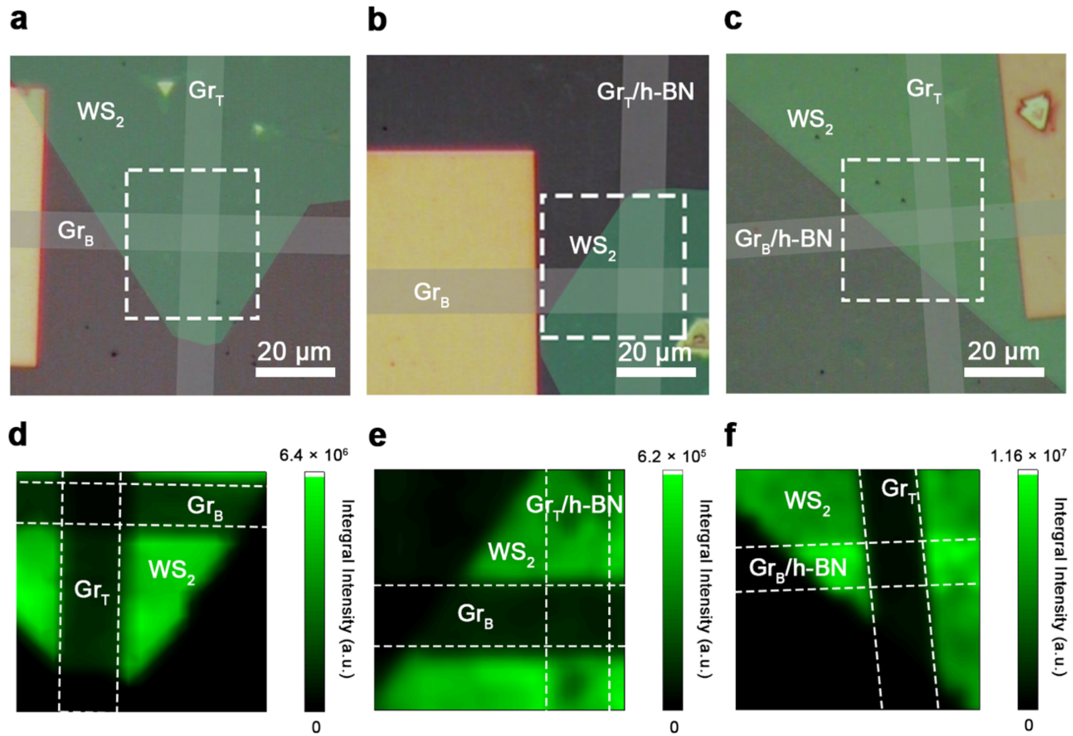

Figure 4.7 PL intensity mappings of three vertical heterostructures with different barriers. Spatial mappings (d-f) of the integrated PL intensity of crossbar structures in white dashed rectangles in optical images (a-c) of $Gr_B/WS_2/Gr_T$, Gr_B/WS_2/h-BN/Gr_T, and Gr_B/h-BN/WS_2/Gr_T. Colour masking indicates the different regions.

In the case of graphene ribbons patterned from a continuous graphene film, all devices with the crossbar structure are interconnected by these graphene ribbons. In other words, the graphene electrodes of the devices in the same row /column share the same graphene ribbon. If there are regions of the SiO_2 layer beneath a graphene ribbon that exhibit poor insulating properties, it is possible for the gate current, which is applied to the device with the graphene electrode sharing that particular ribbon, to leak from the gate to the source through that graphene ribbon. To prevent potential gate current leakage, it is necessary to isolate each device using probe tips before conducting electrical measurements. The devices were exposed to a green laser with a wavelength of 532 nm and a maximum power of 1.118 mW to investigate the influence of the h-BN tunnelling barrier on the photovoltaic effect in the vertical heterostructure.

I first studied the optical power dependence on both the asymmetrical vertical structure of Gr_B/WS_2/h-BN/Gr_T and the symmetrical vertical structure of $Gr_B/WS_2/Gr_T$. As shown in Figure 4.8a-b, the short-circuit current (I_{sc}) increases with an increase in power density for both configurations. This is because a larger power excites more electrons in WS_2, leading to an increase in the net photocurrent. Couples of devices were fabricated on each chip. The yield largely depends on the size and position distribution of the WS_2 single-crystal domains because only devices with the junction fully covered by WS_2 can be used for the measurements. Figure 4.8d shows the statistical results of the extracted I_{sc} from the I_{ds}–V_{ds} curve for both the asymmetrical vertical structure of Gr_B/WS_2/h-BN/Gr_T and the symmetrical vertical structure of $Gr_B/WS_2/Gr_T$ under different illumination conditions. As we can see, the photovoltaic effect of the asymmetrical vertical structure is around 7 times greater than that in the symmetrical structure without the h-BN layer under the same illumination condition of 1.118 mW. The significant improvement results from the enlarged potential barrier difference on the two sides of the vertical stack introduced by the asymmetrical h-BN tunnelling barrier, as shown in Figure 4.5b,d, which further increases the difference in tunnelling possibilities for the photoexcited electrons to both sides of the graphene electrodes. By changing the relative sequence of h-BN in a vertical stack, the photocurrent flow direction can also be changed, as shown in Figure 4.8b-c. This phenomenon also proves the effectiveness of the h-BN film acting as a tunnelling barrier in improving the photovoltaic effect in the vdW vertical heterostructure.

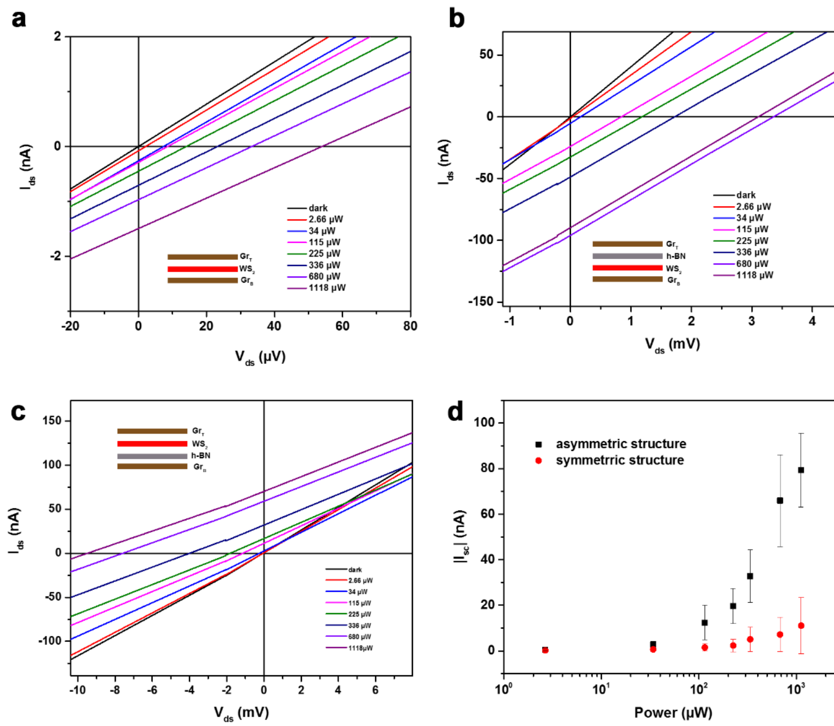

Figure 4.8 (a-c) Plots of I_{ds}–V_{ds} curves for vertical stacks of $Gr_B/WS_2/Gr_T$, Gr_B/WS_2/h-BN/Gr_T, and Gr_B/h-BN/WS_2/Gr_T under different illumination conditions. (d) Statistical results of the extracted short-circuit current from I_{ds}–V_{ds} curves of $Gr_B/WS_2/Gr_T$ and Gr_B/WS_2/h-BN/Gr_T under different illumination conditions.

4.3 Conclusion

In summary, my study focused on a high-performance asymmetrical vertical heterostructure of Gr_B/WS_2/h-BN/Gr_T, using all CVD-grown 2D materials. The introduction of the h-BN tunnelling barrier in the asymmetrical structure significantly improved the photovoltaic effect compared to the symmetrical structure without an h-BN layer. This improvement is attributed to the enlarged barrier difference between the top and bottom graphene electrodes and WS_2. Moreover, by altering the sequence of h-BN in the vertical structure, the direction of electron flow can also be precisely controlled. The use of CVD-grown 2D materials and carefully designed device array patterns enables statistically reliable measurements on each chip. These results demonstrate the effective influence of the h-BN tunnelling barrier in the asymmetrical

vertical heterostructure in the improvements on the photovoltaic effect, offering new insights for the design of ultrathin and flexible optoelectronic devices based on all-2D vertical heterostructure.

4.4 Contribution Statement

Qianyang Zhang provided WS_2 samples for the device fabrication. Dr. Yingqiu Zhou and Dr. Hefu Huang provided training in device fabrication and electrical measurements. Dr. Martin Tweedie provided training in the CVD growth of graphene and h-BN. Dr. Wenshuo Xu provided training in CVD growth of WS_2 and IPA transfer technique. Dr. Viktoryia Shautsova provided training in AFM measurements and offered useful discussions.

Chapter 5 Operational Limits and Failure Mechanisms in All-2D van der Waals Vertical Heterostructure Devices with Long-Lived Persistent Electroluminescence

5.1 Introduction

As discussed in Chapter 2, EL devices using TMD semiconductors can be created in both lateral and vertical geometries based on the carrier injection direction.[190] The vertical geometry, where carriers are injected perpendicular to the photoactive layer, offers a more desirable form factor for achieving uniform planar emission in a large junction area. Previous work on vertical layered heterostructure (VLH) EL devices has mainly been done with mechanically exfoliated materials, demonstrating the proof of concept but unable to provide statistical insights due to flake variation and facing challenges in fabricating numerous devices on a single chip.[14,191,198] While several different EL devices have been produced and investigated, most studies have focused on the EL wavelength and efficiency.[209,274] There is little information about the operation limits, lifetimes, and failure mechanisms of EL devices made using all-2D materials, particularly those using only CVD-grown materials. Understanding devices made using only CVD-grown materials is important as it represents the pathway for commercial implementation and scalable production of arrays. 2D materials, especially TMDs, are air sensitive, and the duration of VLH EL devices operating continuously under atmospheric conditions is an important question for their future development. Identifying the failure mechanism will also

enable future research to focus on addressing these issues and understanding the upper limits of light generation through electrical power.

Here, I created VLH EL devices on the silicon wafer with 300 nm oxide layers using 2D materials grown by CVD. The devices were designed with a graphene crossbar geometry to provide a large overlap area for EL. Tens of the devices have been successfully made. I demonstrated high-performance persistent red EL from these ultrathin 2D devices and explored their continual operation in atmospheric conditions, as well as the maximum bias before breakdown.

5.2 Result and Discussion

5.2.1 Fabrication of VLH EL Devices

Graphene continuous films,[221] WS_2 single domains,[220] and h-BN continuous films[10] used for device fabrication were all synthesized by CVD and transferred by a wet transfer method (DI water and IP-based[251]) as reported in the previous work from our group. Figure 5.1a illustrates a step-by-step fabrication process of the ultrathin crossbar all-2D EL device array, made using only CVD-grown materials. EBL and thermal evaporation were used to pattern and deposit Cr/Au (10 nm/60 nm) bond pads on a silicon chip (SiO_2/Si, with 300 nm thickness SiO_2). A graphene continuous film was transferred onto the silicon chip using a polymer-assisted water-based wet transfer. EBL was then used to pattern the bottom graphene ribbons in the middle, right above the Au bond pads, followed by oxygen plasma etching to achieve the bottom graphene electrodes. Next, a continuous few-layered h-BN film, WS_2 domains, and another h-BN film were successively transferred onto the silicon chip with bottom Au bond pads and bottom graphene electrodes. After WS_2 domains were transferred onto the vertical

stack, a polymer-assisted IPA-based wet transfer method was used to prevent monolayer WS_2 from being washed away.[251] PMMA was then coated to pre-patterned top graphene ribbons on a silicon chip, and KOH was used as an etchant to detach the graphene ribbons from the silicon chip. Top graphene ribbons were transferred onto the stack perpendicular to bottom graphene ribbons in between the middle of two neighbouring Au squares by an aligned transfer, followed by removing the PMMA in hot acetone.[222] Finally, top Cr/Au (10 nm/60 nm) bond pads were patterned and deposited onto the top graphene electrodes by EBL and thermal evaporation. Because of the usage of WS_2 domains, only devices with a crossbar that have single crystal domains, *i.e.*, triangles, fully sandwiched by top/bottom graphene, were selected for measurements. Failures in devices were mainly caused by the breakage of the narrow top graphene ribbons (10 μm) during the transfer process. Figure 5.1b shows a typical single EL device from the array of devices on a silicon chip. In each device, WS_2 and its h-BN tunnelling barriers are located between the top and bottom graphene electrodes in the junction area of the crossbar structure, providing a vertical interface for electroluminescence. The atomic model of the vertical stack in the junction area is shown in Figure 5.1c. During the optoelectrical measurements, two tungsten tips were brought into contact with the gold bond pads, serving as the source and drain for the top and bottom graphene electrodes, respectively. In this way, as shown in Figure 5.1d, the current could flow directly through the vertical stack to inject electrons and holes into a WS_2 monolayer semiconductor.

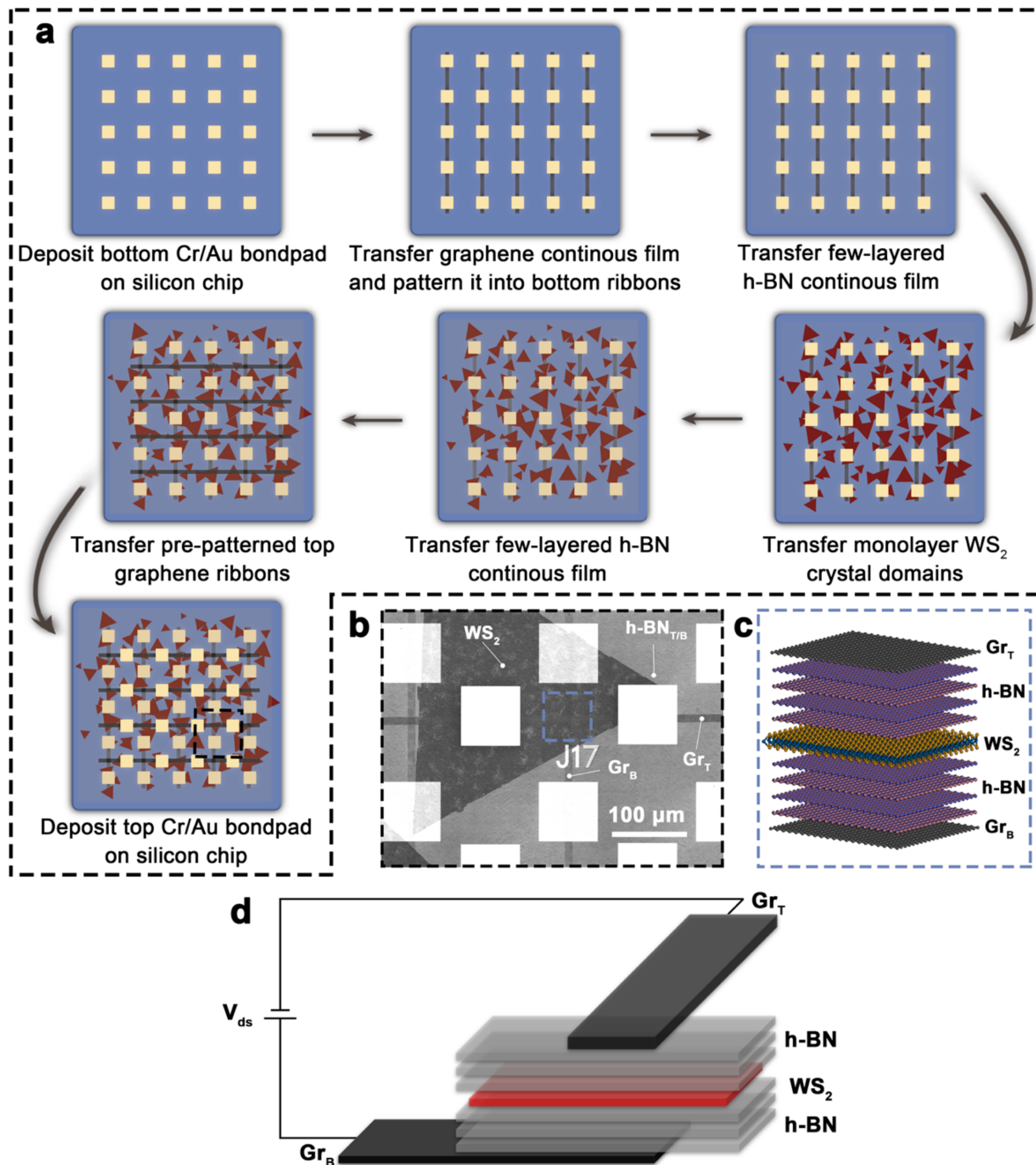

Figure 5.1 Fabrication process of EL devices with a vertical heterostructure of Gr_B/h-BN/WS_2/h-BN/Gr_T. (a) Schematic illustration of device fabrication: deposit bottom Cr/Au bond pads on a silicon wafer; transfer continuous graphene film onto bottom bond pads and pattern it into graphene ribbons right above Au bond pads; transfer continuous few-layered h-BN film; transfer a layer of WS_2 single-crystal domains; transfer another continuous few-layered h-BN film; transfer as-prepared top graphene ribbons perpendicular to the bottom graphene ribbons; deposit top Cr/Au bond pads on top graphene ribbons. (b) SEM image of the single EL device shown in the black dashed rectangle of (a). (c) Atomic model of the vertical structure of the crossbar in the blue dashed rectangle of b). d) Schematic of a typical device under operation.

5.2.2 Characterizations of 2D Materials and VHL EL Devices

Figure 5.2a shows the SEM image of CVD-grown h-BN on a copper foil substrate, with continuous and dense wrinkles on the h-BN film. Wrinkles result from different contraction rates between the copper substrate and the h-BN film during the cooling process of CVD growth, owing to the different thermal expansion coefficients of the two materials. This serves as an important indicator of film continuity. Figure 5.2b presents the Raman spectrum of an h-BN continuous film under a green laser with an excitation wavelength of 532 nm. The characteristic peak attributed to the E_{2g} phonon mode is observed at 1365.3 cm^{-1}, confirming that the h-BN is few-layered, consistent with previous reports.[264,275] The peak at 1450 cm^{-1} indicates third-order scattering from the silicon substrate.[74] AFM was employed to characterize the thickness of the h-BN in the vertical stack. First, the CVD-grown h-BN continuous film was transferred to a precleaned silicon chip, followed by a vacuum annealing for 4 h to remove polymer residues from the material surface. As shown in Figure 5.2c, the thickness of the h-BN film is estimated to be 3~5 layers. SEM and AFM characterizations demonstrate good continuity and homogeneity of the CVD-grown h-BN film. Figure 5.2d exhibits a well-patterned graphene ribbon on a silicon wafer, with a few multilayer islands dispersed on the monolayer graphene continuous film. The Raman spectra of graphene in Figure 5.2e-f show the 2D/G intensity ratios of 2.35 and 0.94, corresponding to the monolayer and multilayer graphene, respectively.[101,276] Figure 5.2g demonstrates high-density CVD-grown WS_2 single-crystal domains with grain sizes of approximately 150 μm. Figure 5.2h-i demonstrate the Raman and PL spectra of a WS_2 single-crystal domain. Lorentzian multipeak fitting was applied to the Raman spectrum to extract three vibration modes: the E_{2g}^1 peak denotes in-plane

vibrations, the A_{1g} peak represents out-of-plane vibrations, and the 2LA indicates the longitudinal acoustic mode. The E_{2g}^1 and A_{1g} peaks are observed at 347.8 cm^{-1} and 415.4 cm^{-1}, respectively, while the intensity ratio of the 2LA/A_{1g} is 3.1 (> 2), suggesting that the WS_2 is a monolayer.[234,238] Two peaks attributed to negatively charged trions (X^-) and neutral excitons (X) are extracted by Gaussian function to the PL spectrum of WS_2, as shown in Figure 5.2i, sitting at 1.96 eV and 1.99 eV, respectively.

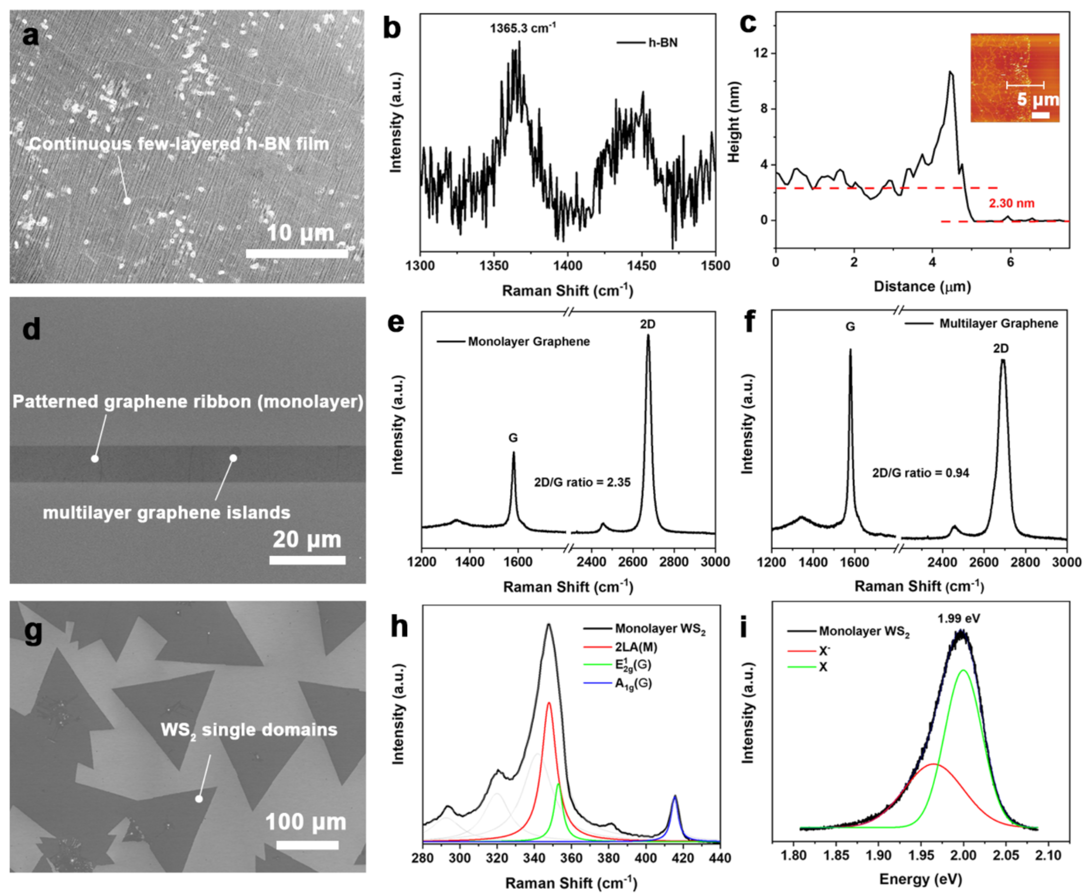

Figure 5.2 Characterizations of CVD-grown 2D materials and Gr_B/h-BN/WS_2/h-BN/Gr_T vertical heterostructure. (a) SEM image of continuous CVD-grown h-BN film on copper foil. b) AFM image of a transferred continuous h-BN film on a SiO_2/Si substrate and the corresponding height profile. (c) The Raman spectrum of a transferred h-BN film: the characteristic peak (1365.3 cm^{-1}) of h-BN and third-order phonon peak of Si. (d) SEM image of a patterned graphene ribbon, with a few multilayer islands dispersed on the monolayer continuous film. (e-f) The Raman spectra of multilayer and monolayer graphene. (g) SEM images of WS_2 single-crystal domains. (h-i) The Raman and PL spectra of a WS_2 single-crystal domain, fitted by Lorentzian and Gaussian multipeak fitting, respectively.

Figure 5.3b is the PL mapping of a device with a vertical heterostructure of Gr_B/h-BN/WS_2/h-BN/Gr_T. According to previous reports, the PL is significantly quenched when WS_2 is in direct contact with graphene.[272,273] However, no noticeable PL quenching of the WS_2 was observed in the areas where it overlays with the top and bottom graphene electrodes. This lack of quenching is attributed to the blocked photoexcited charge transfer due to the presence of h-BN barriers. The resistance is calculated to be 6 $K\Omega$ for a vertical structure without h-BN, while that is calculated as 13 $k\Omega$ for a vertical structure with inserted h-BN at 0.625 V. This indicates that h-BN provides a tunnelling barrier of 7 $k\Omega$ in this configuration. Both PL mapping and electrical measurements confirm the effectiveness of h-BN as a tunnelling barrier in a vertical stack.

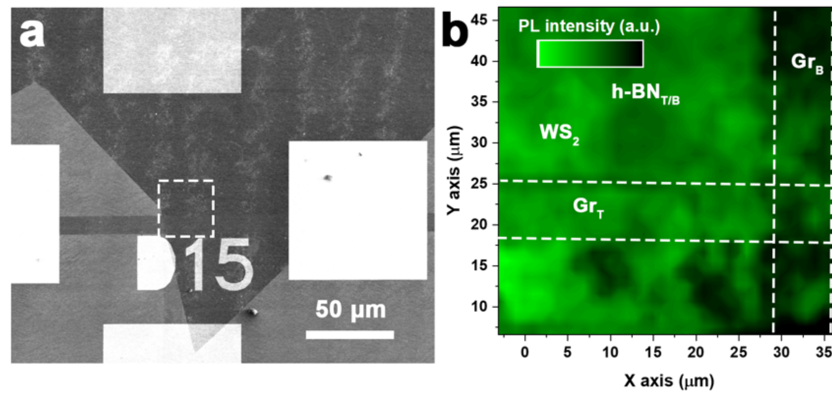

Figure 5.3 (a) SEM image of a typical EL device. (b) The mapping of the integrated PL intensity for the EL device shown in (a).

5.2.3 EL of the Gr_B/h-BN/WS_2/h-BN/Gr_T VLH

During the measurement, the as-fabricated chip was positioned at the focal plane of a homemade spectrometer system. A CCD camera was used to record the red EL emission, while a spectrometer was utilized to collect the EL signal. To prevent

current leakage, each device was isolated by the probe tip. For electrical operation, the source and drain outputs were connected to the top and bottom graphene electrodes, respectively, by penetrating probe tips into the gold bond pads, as shown in Figure 5.4a. This configuration facilitated the injection of holes and electrons from two graphene electrodes under an external electric field. Figure 5.4b illustrates a visible red EL dot located at the junction area, which was captured by the CCD camera under a certain bias, indicating that the EL signal of the device is strong enough to be observed. Magnified optical microscopic images of some EL emissions are shown in Figure 5.4c,e,g, demonstrating the variation in emission shape. The area of EL emission was estimated to be approximately 1/4 to 1/3 of the junction area. EL intensity profiles, as shown in Figure 5.4d,f,h, suggest that the emission is localized in the centre of the junction and can be roughly considered as a Gaussian distribution.

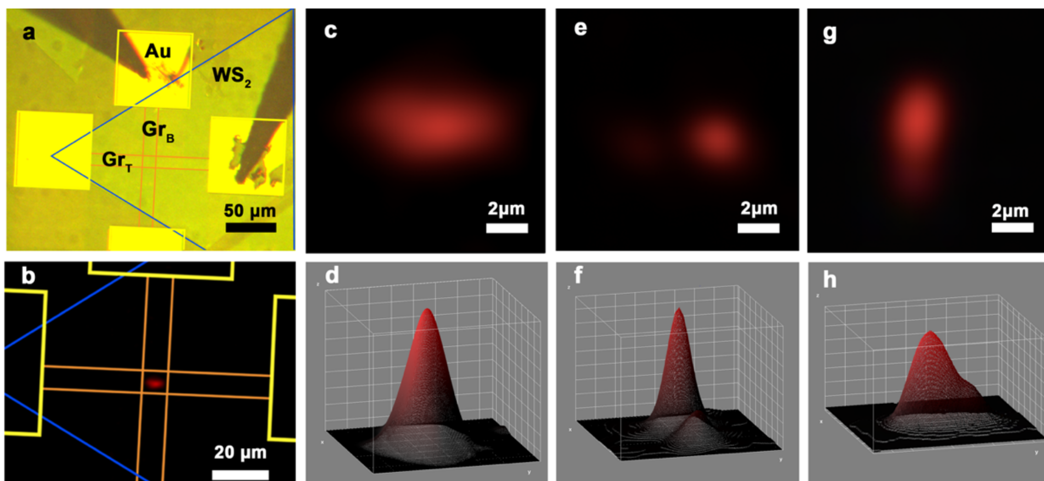

Figure 5.4 Visible EL signal from Gr_B/h-BN/WS_2/h-BN/Gr_T vertical heterostructure. (a) Optical microscopic image of a typical EL device under operation. (b) Observation of the bright red EL dot emitted in the junction area of vertical heterostructure under positive bias. (c,e,f) Magnified EL emissions. (d,f,h) The intensity profile for EL emissions in (c,e,f).

The mechanism of the emission process is explained through the band diagram, as shown in Figure 5.5. In the band diagram under no bias, as shown in Figure 5.5a,

the blue and yellow regions represent the band with a majority charge carrier of electrons and holes, respectively, while the purple rectangle represents the tunnelling barrier induced by the few-layered h-BN insulating thin film. When a positive bias is applied, both the h-BN tunnelling barrier and the band structure of WS_2 tilt at a certain angle, as shown in Figure 5.5b. Simultaneously, the Fermi level of the top graphene is elevated, and that of the bottom graphene electrode is lowered. As the positive bias increases and surpasses the threshold voltage, more electrons from the top graphene and more holes from the bottom graphene tunnel through the h-BN barrier into the conduction and valence bands of the WS_2 monolayer, respectively. These charge carriers then undergo radiative recombination, resulting in the emission of red light.

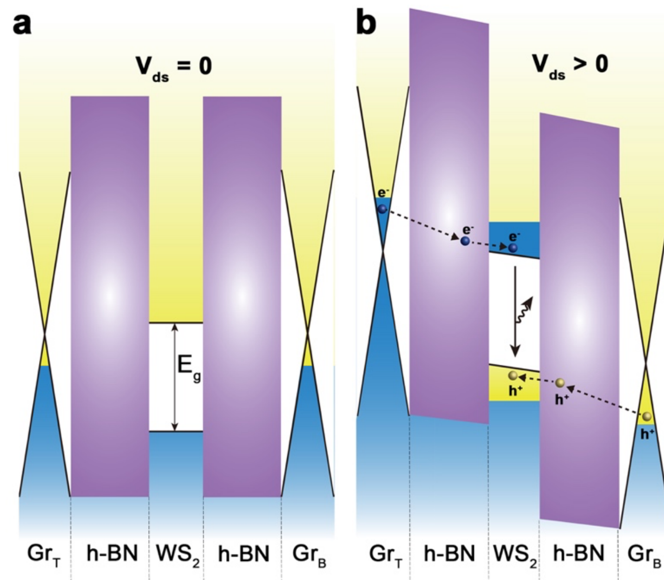

Figure 5.5 Band diagrams of the vertical heterostructure (a) without bias and (b) with positive bias.

Figure 5.6 shows the comparison of the EL signal under applied bias in a pure Gr/WS_2/Gr sandwich structure without h-BN and a Gr/h-BN/WS_2/h-BN/Gr heterostructure. It is evident that no EL signal can be detected in the Gr/WS_2/Gr heterostructure, providing evidence that the presence of the h-BN continuous film is

critical for EL emission. The h-BN layers increase the lifetime of injected electrons and holes within the TMDs layer by reducing the charge transfer probability from the TMDs to graphene. This, in turn, enhances the probability of radiative electron–hole recombination, resulting in significant EL. In the absence of the insulating h-BN layers between the graphene and TMDs, electrons from one graphene electrode will rapidly transport through to the other graphene electrode, reducing the probability of radiative electron–hole recombination and resulting in negligible EL.

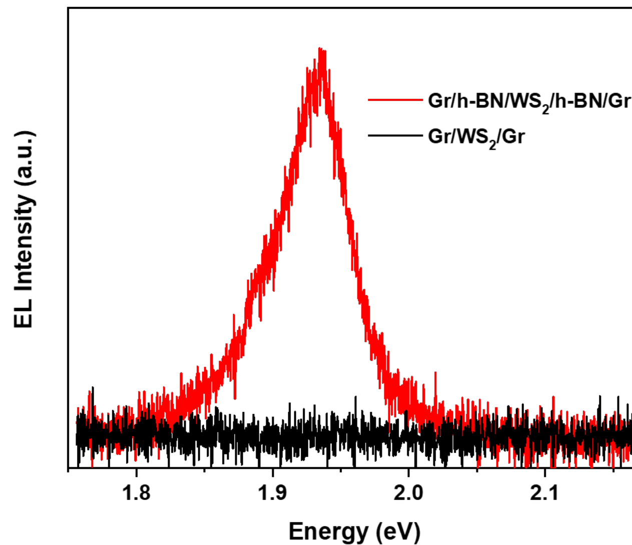

Figure 5.6 EL intensity of a typical device with vertical heterostructures of Gr/WS_2/Gr and Gr/h-BN/WS_2/h-BN/Gr under a bias of 30 V. Exposure time for both constructures is 30 seconds.

5.2.4 The Red Shift on the EL Mapping

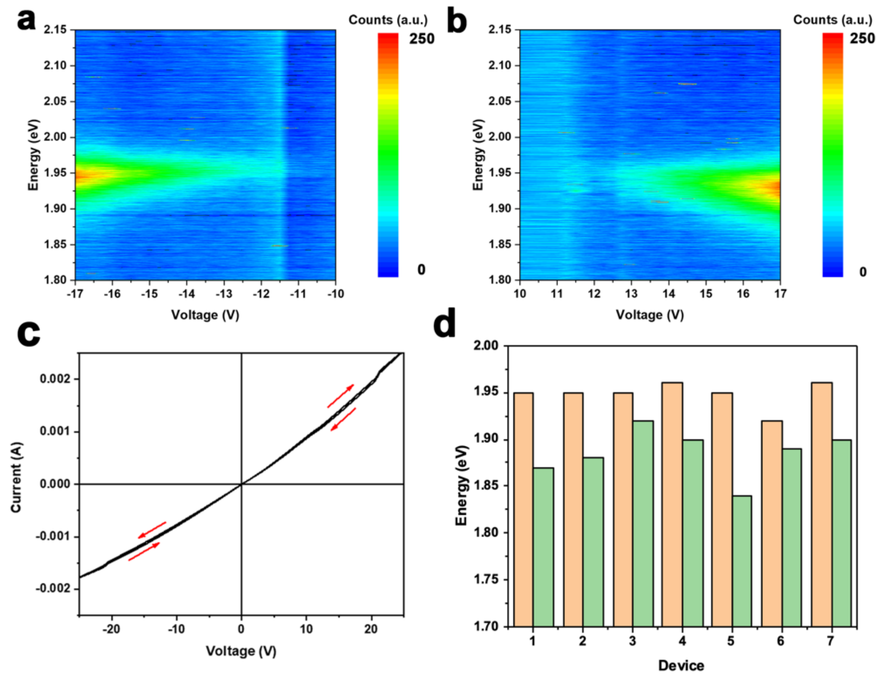

Figure 5.7 EL characterizations of a typical EL device. (a-b) The EL intensity mapping as a function of the applied bias (V_{ds}) in both positive and negative range. (c) I_{ds}–V_{ds} curves of a typical EL device under forward and backward sweeps. (d) Statistics of the red shift on EL devices with increasing bias: the emission shifts from orange bar to green bar.

To plot an EL mapping, it is necessary to capture the EL spectrum at each bias by ramping up the bias from low to high. In this case, the bias is ramped up in a step of 0.25 V, and the exposure time for each capture is set to 10 s. EL mappings of a typical device operated under both positive and negative bias are shown in Figure 5.7ab. It is evident that the EL intensity increases as the bias increases, and both negative and positive bias can drive the device to emit light in the symmetrical VLH. Figure 5.7c demonstrates that the drain current (I_{ds}) shows a non-linear increase with ramping drain-source voltage (V_{ds}) and during forward/backward sweeps. Throughout the measurements, the EL devices exhibit a noticeable red shift in the EL peak position as the V_{ds} is increased, as shown in Figure 5.7d.

Two factors that are likely to cause an energy shift during the device operation are the electric field (known as the Stark effect) and local heating.[204] The Stark effect is a phenomenon where the optical absorption or emission of a material can be manipulated by an external electric field.[277,278] The quantum confinement Stark effect (QCSE) is related to a quantum-well structure, in which a thin layer of semiconductor is sandwiched by barriers, such as the as-fabricated Gr/h-BN/WS_2/h-BN/Gr vertical heterostructure.[279–282] A quantum-well structure offers two preconditions for QCSE: the walls (h-BN layers) slow down the charge injection rate of the electrons and holes from the electrodes (graphene) to the well (WS_2); the well is narrow enough (< 10 nm) to ensure a close spatial separation of the electron and hole, facilitating a strong electron–hole interaction.[283] When an external electric field is applied perpendicular to the quantum-well structure, as in the case of the as-fabricated Gr/h-BN/WS_2/h-BN/Gr vertical heterostructure, the electrons and holes are pulled towards opposite sides of the layers. This results in an overall reduction in energy of the electron–hole pair and causes the Stark shift (red-shift) in the exciton emission.[14,204,283]

The Varshni equation, which is widely used to describe the temperature-dependent band gap size of various semiconductors,[61] is represented as follows:

$$E_g(T) = E_g(0) - \frac{\alpha T^2}{T + \beta}$$

where $E_g(T)$ is the band gap size at temperature T, $E_g(0)$ is the band gap size at 0 K, α and β are two fitting parameters. The temperature-dependent shift of the band gap energy is primarily influenced by changes in the crystal volume and lattice vibration with temperature.[284] In Figure 5.8a-e, Voigt multipeak fitting was applied to fit two characteristic peaks of X^- and X in the EL spectra obtained from an EL mapping under

different V_{ds}. The fitting parameters for the EL spectra are summarized in Appendix A. As shown in Figure 5.8f, the spectral weight of X^- decreases with increasing bias, suggesting that more electrons escape from their trions at higher bias. The detuning of X^- and X emission and the reduction in the spectral weight of X^- shown in Figure 5.6e-f align with studies on the temperature-dependent measurement of PL emission in TMDs as shown in Figure 2.5b-c. The drop in X^- is associated with partially dissociated trions with sufficient thermal energy.[57,285] The analysis implies that the red shift of the EL emission can be attributed to local heating caused by the applied bias.

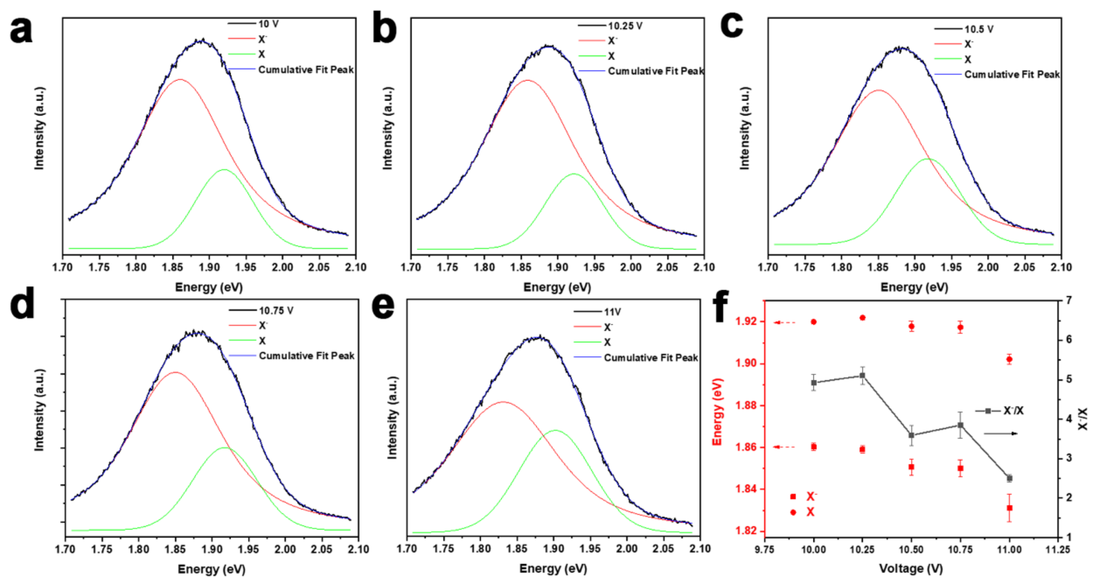

Figure 5.8 (a-e) The EL spectra of a device at different V_{ds}. Voigt multipeak fitting was used here to extract peaks attributed to X^- and X. With increasing V_{ds}, the spectral weight of X^- is decreasing. (e-f) The X^-/X ratio (area) and peak position of X^- and X as a function of V_{ds}.

5.2.4 Study on the Mechanism of the Failure and Operation Limits for the VLH EL

The emphasis was then placed on the operation stability, durability, and the maximum voltage that the EL devices can endure. The stability of the device was tested under a bias of 16 V, undergoing several ON/OFF cycles with a 1-min time

interval between each operation. The measurement starts from a 1 min OFF state. The EL spectrum was captured for a total of 1 min during each ON state. As shown in Figure 5.9a-b, the EL spectrum of the device exhibits negligible changes after five cycles, and the maximum EL intensity of the device at each ON state remains nearly constant. These results demonstrate the outstanding stability of the EL devices composed entirely of CVD-grown 2D materials under high bias.

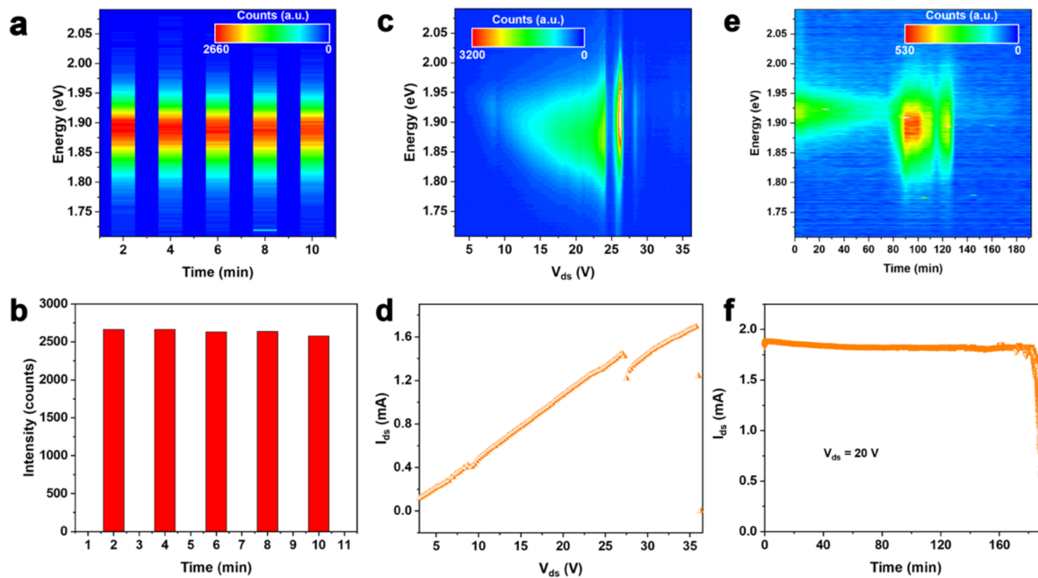

Figure 5.9 Fatigue, durability, and breakdown test of EL devices. (a) Cycling test of a typical EL device: variation of EL intensity when pulsed. (b) Maximum EL intensity of the device at each ON cycle. (c) The breakdown test for a typical EL device: the device stops working at a maximum V_{ds} of 36.25 V. d) Corresponding I_{ds}–V_{ds} curve of the device for the breakdown test. (e) Durability test for a typical EL device: EL intensity mapping *vs.* lifetime under a fixed bias of 20 V. (f) Corresponding I–t curve of the device for the durability test under a fixed bias of 20 V.

The breakdown test shown in Figure 5.9c was performed by gradually increasing V_{ds} to determine the operation limit. As the bias increases, the EL intensity initially experiences moderate growth until reaching a certain value, after which it gradually declines. The increasing EL intensity suggests an increased electron–hole recombination on the WS_2 layer, indicating a high number of injected carriers under

the rising bias. The decrease in intensity at high bias can be attributed to some electrons injected into the conduction band of WS_2 being pushed towards the other graphene electrode through the h-BN layer. As a result, less electron–hole recombination occurs on the WS_2 layer. In the first ascending stage, there is a sudden drop in intensity, which arises from the fluctuation of the emission area's spatial location outside the collection area of the microscope objective and the heat-induced changes in the contact resistance of the device.[286] The EL signal begins to emerge at 5 V and suddenly disappears at 36.5 V, coinciding with the I_{ds} dropping to zero at the same voltage. The corresponding I_{ds}–V_{ds} curve of the device, shown in Figure 5.9d, also indicates an open circuit when V_{ds} reached 36.25 V, signifying the breakage of the graphene ribbon caused by an accumulation of local heating.

As discussed in section 2.5.2, the external quantum efficiency (EQE) of EL devices can be defined using the following equation:[165]

$$EQE = \frac{Number\ of\ photons\ emitted\ externally}{Number\ of\ carriers\ passing\ junction} \quad 5\text{-}1$$

N_{photon} is the number of photons emitted per second in the EL device, and $N_{electron}$ is the number of electrons injected per second in the EL device under a certain bias. N_{photon} and $N_{electron}$ can be expressed as follows:[207]

$$N_{photon} = \frac{N_{photon\ collected-EL}}{\eta_{collection}} \quad 5\text{-}2$$

$$N_{electron} = \frac{I}{e} \quad 5\text{-}3$$

where $N_{photon\ collected-EL}$ is the number of photons collected by the detector of the spectrometer, $\eta_{collection}$ is the collection efficiency of the spectrometer, I is the current flowing through the EL device, and e is the elementary charge ($1.6 \times 10^{-19}\ C$).

By combining eq. 5-1, 5-2, and 5-3, the EQE of the EL device can be expressed as follows:

$$EQE = \frac{N_{photon}}{N_{electron}} = \frac{N_{photon\ collected-EL}/\eta_{collection}}{I/e} \qquad 5\text{-}4$$

Since both the PL and EL spectra were collected using the same custom-built spectrometer in the study, I used the PL spectrum to determine the $\eta_{collection}$.[207] The external quantum efficiency of PL (η_{PL}) is defined as follows:[287]

$$\eta_{PL} = \frac{Number\ of\ photons\ emitted\ externally}{Number\ of\ photons\ absorbed} \qquad 5\text{-}5$$

$N_{photon\ generated-PL}$ and $N_{photon\ injected-laser}$ are the emitted photons per second in PL emission and the injected photon per second under the laser power of P_{laser}, respectively. They can be expressed as the follows:[198,207]

$$N_{photon\ generated-PL} = \frac{N_{photon\ collected-PL}}{\eta_{collection}} \qquad 5\text{-}6$$

$$N_{photon\ generated-PL} = \frac{P_{laser}\lambda}{hc} \qquad 5\text{-}7$$

where $N_{photon\ collected-PL}$ is the number of photons collected per second by the detector of the spectrometer, λ is the wavelength of the incident laser, h is Planck's constant ($6.63 \times 10^{-34}\ J \cdot s$), and c is the speed of light ($3 \times 10^{8}\ m/s$). By combining eq. 5-5, 5-6, and 5-7, η_{PL} can be expressed as follows:

$$\eta_{PL} = \frac{N_{photon\ generated-PL}}{N_{photon\ injected-laser}} = \frac{N_{photon\ collected-PL}/\eta_{collection}}{P_{laser}\lambda/hc} \qquad 5\text{-}8$$

From eq. 5-4 and 5-8, the quantity of $\eta_{collection}$ can be eliminated, and the EQE can be expressed as follows:

$$EQE = \frac{N_{photon\ collected-EL}}{N_{photon\ collected-PL}} \times \frac{\eta_{PL} P_{laser}\lambda e}{Ihc} \qquad 5\text{-}9$$

The PL signal was collected under a laser power of 0.225 mW, with an exposure time of 1s. The integral of the PL peak was 52673/s. The largest EQE was observed in the

strongest EL emission under a bias of 26.5 in the device shown in Figure 5.9c, with an integral of the EL peak of 226878 counts under an exposure time of 10 s. This count was divided by 10 to obtain the EL peak integral in 1 s, which is 22688 counts/s. The PL quantum yield (η_{PL}) of monolayer WS_2 is reported to be between 0.1% and 6% with a reasonable defect density.[288,289] Therefore, the maximum EQE of the device is estimated is estimated to be 0.18 % with a maximum η_{PL} of 6%, as shown in Figure 5.10. This value is relatively lower compared to other reported vertical EL devices based on exfoliated TMD materials (ranging from 1 %~10 %).[14,209]

For the duration test, a fixed bias of 20 V was continuously applied to the device, and an EL spectrum was collected every 5 min with an exposure time of 10 s. Figure 5.9e shows the EL intensity mapping over time, demonstrating a continuous strong signal in the first 2 h, followed by a weak signal for another 1 h. Eventually, the EL signal abruptly drops to zero. Referring to the corresponding I–V curve in Figure 5.9f, the initial decrease in signal intensity is speculated to be the degradation of WS_2, while the sudden disappearance of the signal is caused by the electroburning of the graphene ribbons. To date, the lifetime of 2D-material-based EL devices has received little attention. Compared with a study on EL devices with an asymmetrical heterostructure of Gr/h-BN/WS_2/h-BN/Au,[207] where the EL device only lasts 4 min before collapsing, the symmetrical vertical structure with graphene serving as both the top and bottom electrodes for the carrier injection exhibits a significant improvement in the lifetime of EL devices. In the Gr/h-BN/WS_2/h-BN/Au heterostructure, when charge carriers are injected from the top Au electrode and bottom graphene electrode under bias, they undergo lateral diffusion and drifting in WS_2 before recombination occurs. The non-linear I–V curve also indicates a Schottky contact-like behaviour in

the Gr/h-BN/WS_2/h-BN/Au lateral heterostructure. This process accelerates the degradation of WS_2, resulting in an extremely short lifetime of EL emission. However, in the vertical heterostructure of Gr/h-BN/WS_2/h-BN/Gr, carriers are injected perpendicular to the WS_2 layer from the top and bottom graphene electrodes, leading to directly recombined on the WS_2 layer without lateral diffusion. This not only reduces the degradation of WS_2 but also allows for relatively large planar emission, ideally covering the entire junction area. Additionally, in the lateral structure with a metal electrode directly deposited on ultrathin 2D materials, more defects are introduced to both WS_2 and h-BN layers.[12] This destruction of 2D materials increases the risk of WS_2 degradation. On the contrary, graphene serves as a suitable alternative to metal electrodes because the vdW interaction between graphene and other 2D materials does not cause any interfacial damage. Furthermore, due to the voltage drop along the graphene ribbon electrodes, as discussed earlier, the actual voltage on the junction area in the symmetrical vertical heterostructure is much smaller than that in the lateral structure. This could be another reason for reduced WS_2 degradation.

In both the breakdown test and duration test, the sudden disappearance of the EL signal is accompanied by an abrupt drop of current. Upon examining several devices after breakdown, it was observed that cracks appeared on the top graphene electrodes rather than the bottom graphene electrodes. Figure 5.11a displays a typical SEM image of a top graphene electrode from a device after breakdown, clearly showing a crack in the middle of the ribbon. This finding confirms the earlier speculation that the circuit cut-off is related to the breakage of the graphene electrode. To investigate the different breakdown behaviour between the top and bottom graphene electrodes, I conducted separate biasing experiments by connecting probe

tips to the bond pads and applying a bias to one ribbon at a time. Measurements of the top and bottom graphene electrodes on different devices were performed to obtain statistically significant results for average breakdown voltage, as shown in Figure 5.11b-c. The statistical results shown in Figure 5.11d are derived from Figure 5.11b-c. It is observed that the average breakdown voltage of the bottom graphene electrodes is twice as large as that of the top graphene electrodes. This difference is speculated to be attributed to the different environments in which the top and bottom graphene electrodes are located. In the EL devices, the top graphene electrodes are in direct contact with insulating h-BN and exposed to air, while the bottom graphene electrodes are in direct contact with insulating h-BN and the silicon substrate. Passing huge currents through graphene constrictions and ribbons can cause localized degradation, which has been utilized to create controlled micro-gaps.[290–292] Although both air and the silicon substrate have poor thermal conductivity, the silicon substrate is 5 orders of magnitude larger than air. Consequently, the silicon substrate assists in heat dissipation from the bottom graphene, while the h-BN layer in contact with the bottom graphene helps protect against oxidation. On the other hand, the top graphene electrode is exposed to air and is more prone to oxidation, leading to its degradation and making it less robust than the bottom graphene electrode under the operational conditions of the devices. This analysis highlights the significant role of local heating in the failure mechanism of EL devices using all CVD-grown 2D materials.

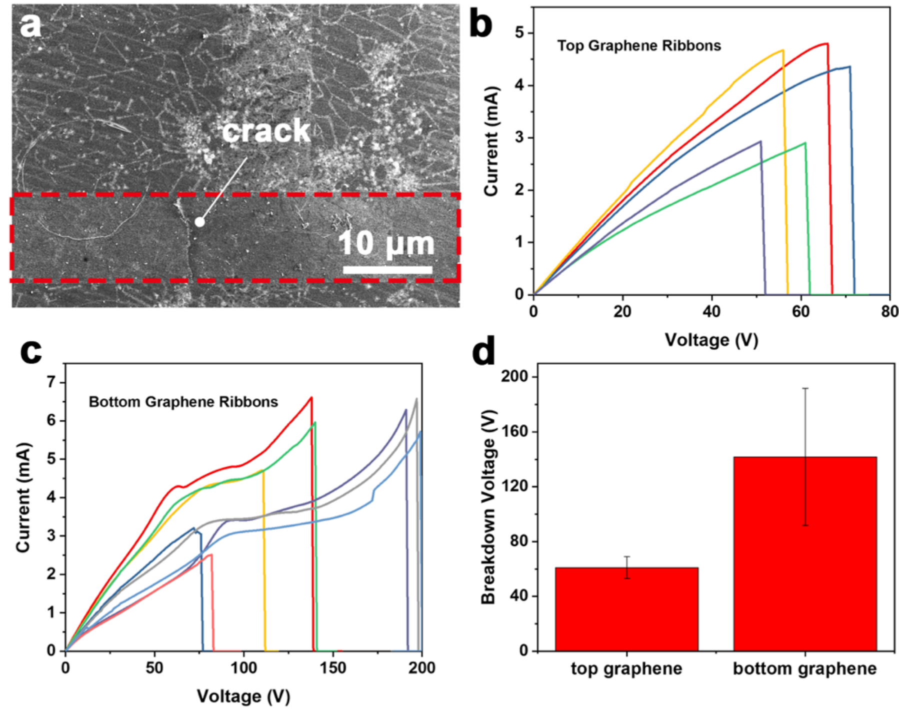

Figure 5.11 (a) SEM image of the top graphene electrode with a crack from a breakdown device. (b-c) I–V curves of top and bottom graphene electrodes, respectively, before breakdown. (d) Statistical results of the breakdown voltage for the top and bottom graphene electrodes.

5.3 Conclusion

In conclusion, I demonstrate high-performance EL devices based on a VLH of Gr/h-BN/WS_2/h-BN/Gr. Using all CVD-grown 2D materials and a crossbar-geometry design for the graphene electrode enabled the fabrication of multiple devices on a single chip, with a high success rate of devices to emit EL. The EL signal can be detected by the spectrometer across a wide range of operations, spanning approximately from 5 V to 35 V, with a visible and bright red spot emitted at the junction area. The red shift of the EL emission with positive bias ramping is primarily attributed to local heating. The stability and durability of the as-fabricated EL devices were excellent, as the position and intensity of the EL spectrum remained consistent over multiple ON/OFF switches under high bias, and the EL persisted for more than 2

h without noticeable degradation of WS_2. The electroburning of graphene electrodes, resulting from the accumulation of local heating, appears as a limiting factor for the operation of the devices in ambient air. Overall, this study provides valuable insights into the red shift of EL emission, failure mechanisms, and operation limits of EL devices using all CVD-grown 2D materials.

5.4 Contribution Statement

Qianyang Zhang provided h-BN and WS_2 samples for the device fabrication and helped me with the alignment transfer. Dr. Viktoryia Shautsova offered useful discussions.

Chapter 6 Ultrathin 2D Photodetectors using Transition Metal Dichalcogenides $PtSe_2$–WS_2–$PtSe_2$ by Direct Laser Patterning

6.1 Introduction

As discussed in Chapter 2, one of the most fascinating properties of TMDs is their band structure evolution with their thickness. Group VI TMDs, such as MoS_2 and WS_2, exhibit an indirect-to-direct bandgap transition when thinning down to a monolayer, resulting in strong light-matter interactions.[8,45,293,294] Monolayer group VI TMDs are widely utilized in optoelectronic applications, including photodetector, LEDs, and photovoltaic devices. In contrast, group X TMDs, exemplified by noble-metal TMDs $PtSe_2$, show a narrowing energy bandgap from 1.17 eV in monolayer to 0 eV in bulk form.[66,72,295–297] Bulk $PtSe_2$ exhibits a band structure in which the valence band maximum (VBM) is slightly higher than the conduction band minimum (CBM).[68] This slight indirect overlap between the conduction band and valence band is a characteristic feature of the band structure of a semimetal.[66,72,298] On the other hand, semiconducting monolayer $PtSe_2$ demonstrates high mobility and good air-stability, making it promising for photocatalysis, sensing, and optoelectronic applications.[70,71,299,300] On the other hand, the semimetal behaviour of $PtSe_2$ bulk material is less discussed but provides an alternative choice as a 2D material beyond graphene for metal contacts in electronic devices.

In device fabrication, direct laser patterning has emerged as a more approachable, time-efficient, and cost-effective technique. Traditional methods like EBL are known for their high-cost and time-consuming nature when used to create channels in electrodes with dimensions ranging from hundreds of nm to a few μm. However, recent discussions have focused on the laser thinning technique for tailoring TMDs, offering potential applications in TMDs-based device fabrication.[301–304] For example, controlled laser ablation has been used to ablate $PdSe_2$ thin films.[301] Compared to a graphene electrode, $PtSe_2$ electrodes can greatly reduce contact resistance in $PtSe_2$ homojunction, making the exploration of low-cost techniques for $PtSe_2$ electrode fabrication significant for future optoelectronic devices.[305]

Here, I demonstrate a lateral heterostructure of $PtSe_2$–WS_2–$PtSe_2$, where a multi-layered $PtSe_2$ thin-film acts as metal electrodes and monolayer WS_2 serves as the photoactive material. Such lateral structure can be considered as a metal–semiconductor–metal (MSM) configuration, which is a typical configuration for photodetector applications.[148,155,306] The device was fabricated using direct laser patterning, and the relevant optoelectronic properties were investigated, with $PtSe_2$ thin film synthesized by thermally assisted selenization.

6.2 Results and Discussion

6.2.1 Synthesis and Characterizations of $PtSe_2$ Thin Film

$PtSe_2$ was synthesized using a simple epitaxial method, which involved the pre-deposition of the platinum (Pt) layer followed by a direct selenization process under ambient pressure. Figure 6.1a schematically illustrates the growth of multi-layered

$PtSe_2$ thin film. Initially, a 2 nm thick platinum was deposited onto a silicon substrate (SiO_2/Si, with 300 nm thickness SiO_2) using electron-beam evaporation. The silicon substrate, with a pre-deposited Pt layer, exhibited a mirror-like silver surface. A double-furnace system was employed for the following selenization process. In Furnace 1, selenium (Se) powder was placed at the centre, while in Furnace 2, a silicon wafer uniformly coated with Pt was also placed at the centre. The temperature of Furnace 1 and Furnace 2 were ramped up to and stabilized at 230 ℃ and 350 ℃, respectively. Pure argon (Ar) was used to flush the system and carry the Se vapor downstream to the substrate. The entire selenization process lasted for 40 min to form the $PtSe_2$ thin film. The atomic model in Figure 6.1b shows the selenization process of the Pt substrate.

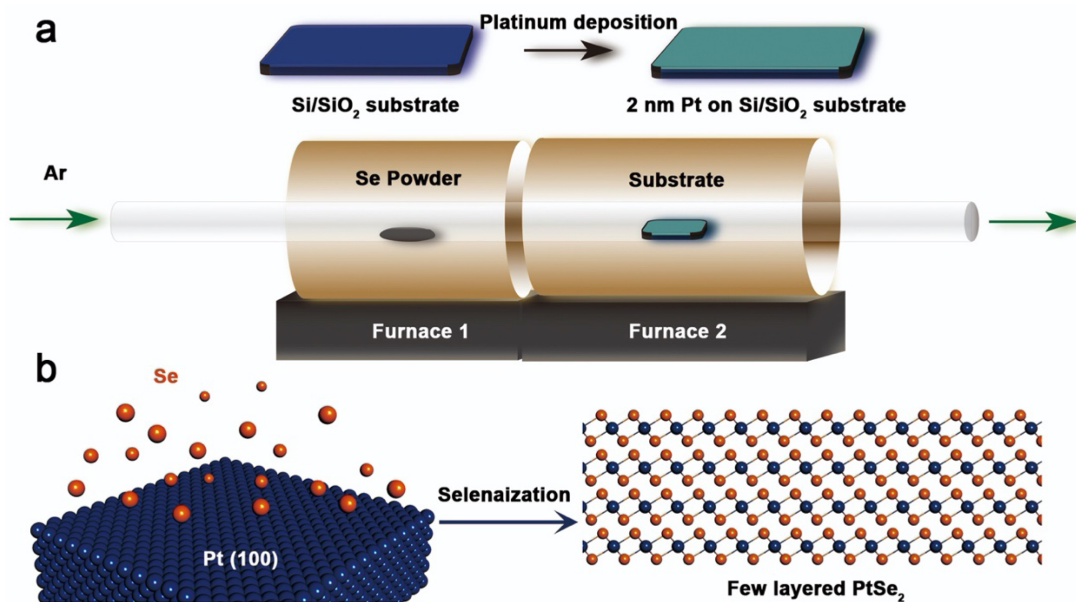

Figure 6.1 Synthesis of the $PtSe_2$ thin film. (a) Experimental setup for the synthesis of $PtSe_2$ thin film: direct selenization of a pre-deposited platinum layer on the silicon substrate. (b) Atomic model of the selenization process for multi-layered $PtSe_2$.

Figure 6.2a shows the SEM image of the as-synthesized $PtSe_2$ thin film. The SEM image demonstrates a fairly smooth surface with minimal accumulation of the

Se precursor. Figure 6.2b-c shows the TEM image of the $PtSe_2$ thin film and its corresponding fast Fourier transform (FFT) image. The FFT image indicates a d-spacing of 3.2 Å for the (100) crystallographic planes. Both the TEM and FFT images confirm the hexagonal lattice structure of $PtSe_2$, with a lattice constant $a = 3.7$ Å, consistent with the theoretical value of $PtSe_2$.[68] Figure 6.2d shows the Raman spectrum of the $PtSe_2$ film. The Raman spectrum shows two prominent Raman modes at 176.7 cm^{-1} and 205.4 cm^{-1}, assigned to the E_g mode and the A_{1g} mode, respectively. Additionally, a less intense feature at 230 cm^{-1} corresponds to the longitudinal optical (LO) mode.[66,307,308] The E_g and A_{1g} modes describe the in-plane and out-of-plane vibration of Se atoms moving in opposite directions, respectively.[66,307] The broad hump located at 330 cm^{-1} is attributed to a longitudinal optical (LO) mode, which is associated with the A_{2u} and E_u modes. The A_{2u} mode corresponds to the out-of-plane vibration of Pt atoms and S atoms moving away from each other, while the E_u mode relates to the in-plane vibration of Pt atoms and S atoms moving away from each other. Jiang *et al*. reported an increase in the intensity ratio of ${A_{1g}}/{E_g}$ from ~ 0.1 to 0.6 with an increase in the layer number from 1 to 22.[309] The increase in the peak ratio is consistent with the increase in van der Waals interactions. The intensity ratio of ${A_{1g}}/{E_g}$ for the as-synthesized $PtSe_2$ thin film is 0.66, indicating that it is multilayer. The LO mode exhibits the strongest intensity and splits into two separate peaks for monolayer $PtSe_2$, at around 230 and 237 cm^{-1}. However, it presents one broad and less intense shoulder with increasing thickness.[307] No literature has reported fittings for the overlapped A_{2u} and E_u mode for multilayer $PtSe_2$ thin film. Instead, this broad and less intense shoulder is an indicator of a $PtSe_2$ thin film with multilayer thickness. The

quality of the film can be evaluated by the line width of the characteristic peaks, indicated by the full width at half maximum (FWHM). The FWHM of the E_g mode for the reported $PtSe_2$ thin film ranges from approximately 4 to 11 cm^{-1}.[68] For the as-synthesized $PtSe_2$ thin film, the FWHM of the E_g mode is 8.5 cm^{-1}, indicating a good sample quality. The inset of Figure 6.2e shows the AFM image of the $PtSe_2$ film, where the sharp edge comes from a scratch made by a tungsten probe tip (the SEM image of this area is shown in Figure 6.2f). Figure 6.2e describes the height profile of line 1 drawn in the AFM image. The step height is estimated to be 11.2 nm, implying that the $PtSe_2$ thin film is multilayer. The thickness variation ranges from 10 to 12 nm. Considering that the interlayer distance of $PtSe_2$ is 5.08 Å, the estimated layer number is 20~22.[68]

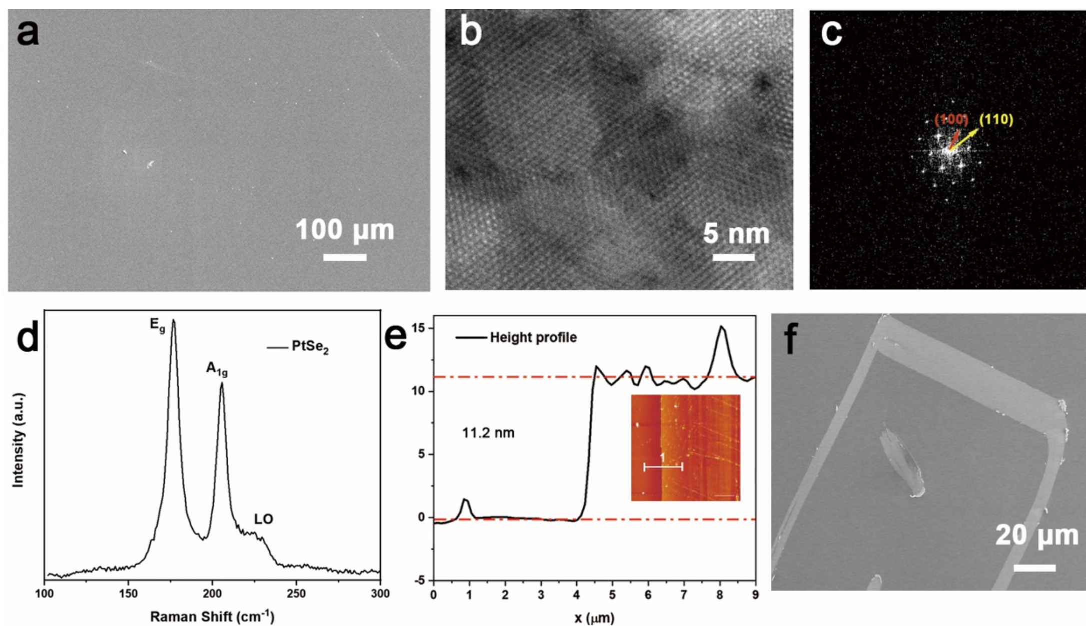

Figure 6.2 (a) SEM image of as-synthesized $PtSe_2$ thin film. (b) TEM image of as-synthesized $PtSe_2$ thin film. (c) Corresponding FFT image of (b). (d) Raman spectrum of as-synthesized $PtSe_2$ thin film. (e) Height profile of as-synthesized $PtSe_2$ thin film (inset: AFM image with a scanned line. (f) SEM image of the $PtSe_2$ film with sharp edges scratched made by a tungsten probe tip for AFM measurements.

6.2.2 Device Fabrication of $PtSe_2$–WS–$PtSe_2$ Photodetector

Figure 6.3a schematically illustrates the step-by-step fabrication process of the $PtSe_2$ contact. First, Cr/Au (5 nm/60 nm) bond pads ($150 \times 150\ \mu m^2$) were patterned and deposited on the silicon substrate using EBL and thermal evaporation. Next, $PtSe_2$ thin film was transferred onto the silicon substrate with gold bond pads using water-based wet transfer. Due to the thickness of the $PtSe_2$ thin film and the mass of Pt and Se elements, a long etching time using oxygen plasma was required to etch the unwanted area, indicating the need for a thicker resist. In this case, photolithography was employed to pattern $PtSe_2$ ribbons directly above the Au bond pad. S1813, a positive photoresist with higher resistance to oxygen plasma, allowed achieving a thickness of a few microns by adjusting the spinning speed. However, it should be noted that a buffering layer of PMMA 495 A4 (with a thickness of 190 nm) was necessary. Without the buffering layer, the MF-319 developer could react strongly with $PtSe_2$, causing the lift-off of the $PtSe_2$ film, as shown in Figure 6.4a. The bilayer recipe of PMMA/S1813 not only prevented the reaction between $PtSe_2$ and MF-319 developer but also resulted in a much cleaner surface. A comparison study between the single-layer recipe and the bilayer recipe is shown in Figure 6.4b-c. Removing PMMA residues from the $PtSe_2$ surface was much easier than removing S1813 using a hot acetone bath.

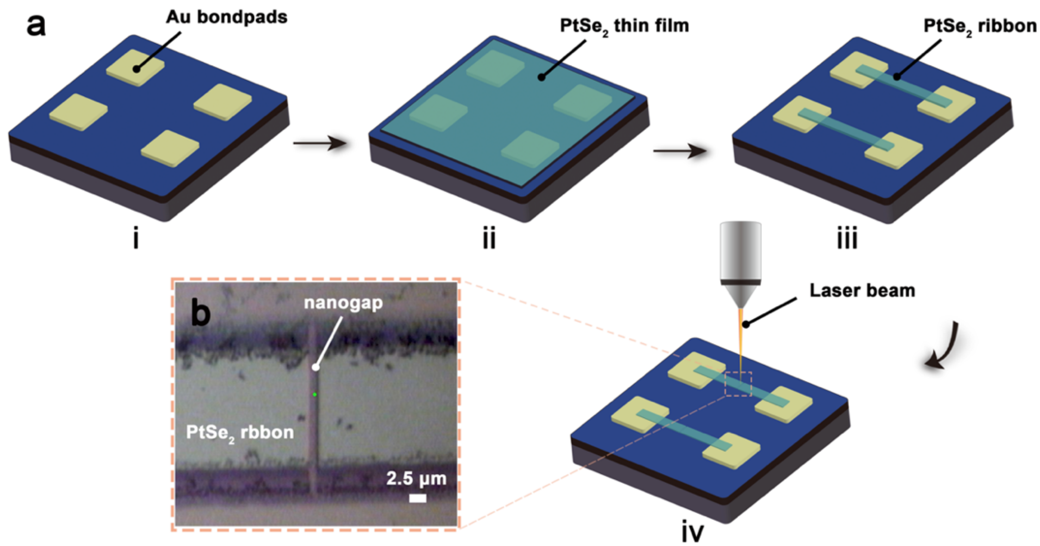

Figure 6.3 Fabrication process of $PtSe_2$ contacts. (a) Schematic illustration of the fabrication process for $PtSe_2$ ribbons with micro-gaps: i) deposit gold bond pads on a silicon substrate; ii) transfer $PtSe_2$ thin film to the silicon substrate; iii) pattern $PtSe_2$ ribbons using photolithography; iv) pattern micro-gaps on $PtSe_2$ ribbons using direct laser patterning. (b) Optical image of a typical $PtSe_2$ ribbon with a micro-gap.

In the fabrication process, laser patterning was applied to create micro-gaps on $PtSe_2$ ribbons. The $PtSe_2$ ribbon was positioned laterally under a 100 × objective lens to achieve a maximum laser power of 7.8 mW. The laser moved perpendicularly to cut the ribbon along the pre-drawn line. Figure 6.3b shows the optical image of a $PtSe_2$ ribbon with a laser-patterned micro-gap. The SEM image in Figure 6.4d is a $PtSe_2$ ribbon with a micro-gap patterned using a scan step size of 200 nm during the process. The materials remaining in the gap region after laser ablation appeared as particles rather than a continuous film. The corresponding grey value profile of the line drawn on the SEM image shows that the channel width can be estimated as 1 μm, as shown in Figure 6.4e. By modifying the scan step size of the laser beam, micro-gaps with different widths can be achieved. For instance, a channel width of 1.5 μm can be obtained using a scan step size of 300 nm. The *I*–*V* curves in Figure 6.4f present the

conductivity of the $PtSe_2$ ribbon and the $PtSe_2$ ribbon with the micro-gap. The conductivity of the $PtSe_2$ ribbon is calculated as $1.16 \times 10^3\ \mathrm{S/m}$, while the conductivity of the $PtSe_2$ ribbon with the micro-gap declines to zero, indicating the complete removal of $PtSe_2$ material from the channel.

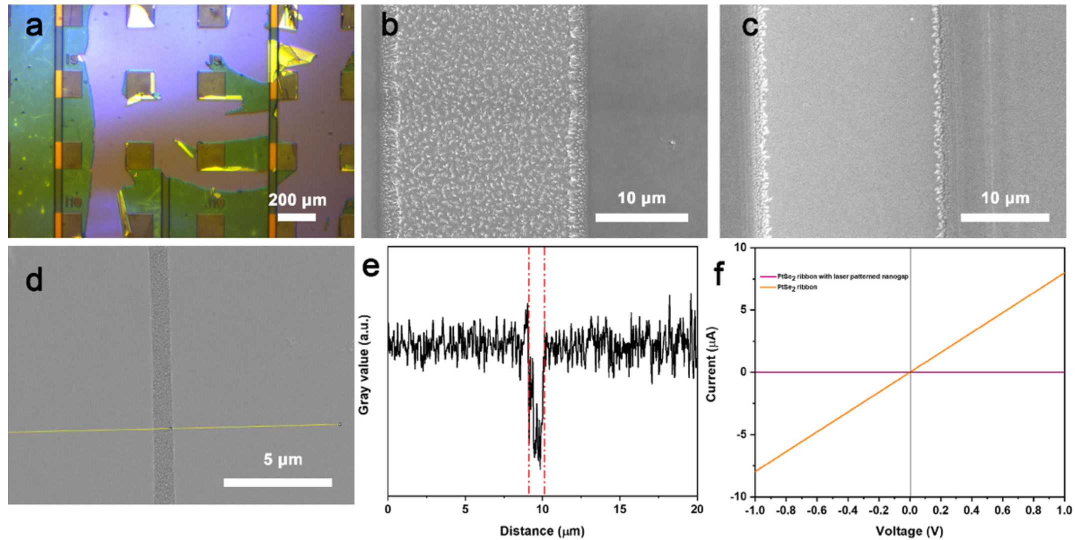

Figure 6.4 (a) The $PtSe_2$ film after being developed in the MF-319 developer for 30 s using the single-layer recipe (S1813). (b) SEM image of a $PtSe_2$ ribbon after development, oxygen plasma, and acetone lift-off using the single-layer recipe (S1813). (c) The surface of a patterned $PtSe_2$ ribbon using the bilayer recipe (PMMA/S1813). (d-e) Width measurement for a channel obtained using a scan step of 200 nm: (d) SEM image of the micro-gap; (e) corresponding grey value profile of the yellow line drawn in (c). (f) I–V curves of the $PtSe_2$ ribbon before and after laser patterning.

WS_2 was synthesized using APCVD in a double-furnace system.[310] Figure 6.5a shows CVD-grown WS_2 single-crystal domains, with an average domain size ranging from 100 to 150 µm. Figure 6.5b-c show the photoluminescence (PL) and Raman spectra of as-grown WS_2, confirming the presence of single-layered WS_2 reported.[238] To fabricate the lateral structure of $PtSe_2$–WS_2–$PtSe_2$, the final step involves covering the channel with WS_2 single-crystal domains. This was achieved through aligned transfer to ensure a high success rate of device fabrication, as shown in Figure 6.5d.[222]

Figure 6.5e shows the SEM image of an as-fabricated device with the lateral structure of $PtSe_2$–WS_2–$PtSe_2$.

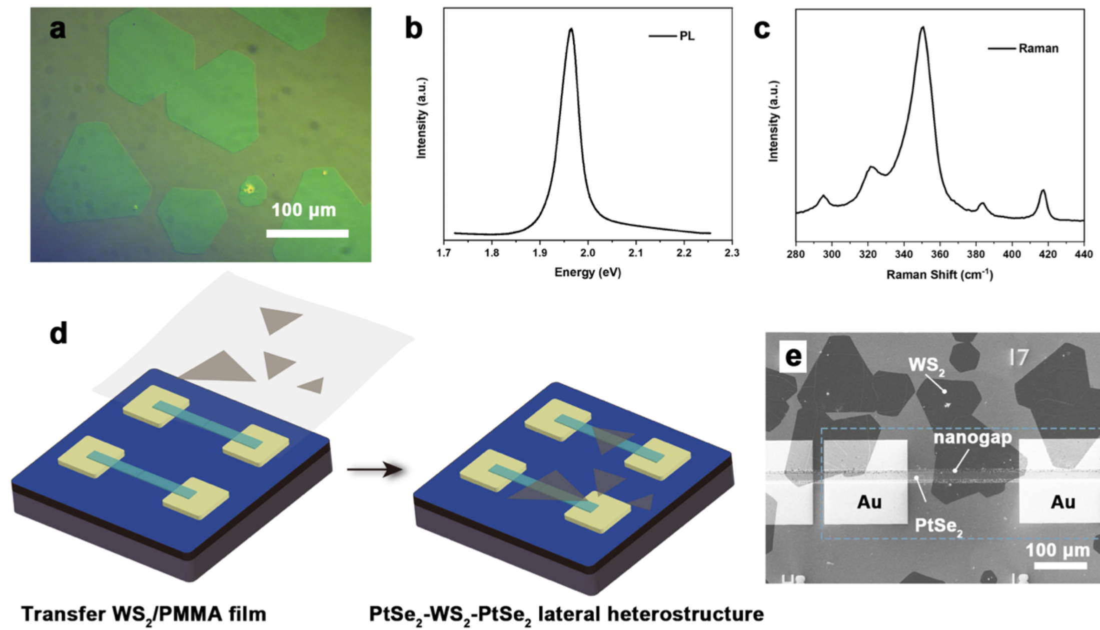

Figure 6.5 (a) Optical image of CVD-grown WS_2 single-crystal domains. The average grain size is estimated as 100~150 μm. (b-c) The PL and Raman spectra of CVD-grown WS_2. (d) Transfer of WS_2 single-crystal domains to $PtSe_2$ contacts. (e) SEM image of a typical device with the lateral structure of $PtSe_2$-WS_2-$PtSe_2$.

6.2.3 Optoelectronic Characterization $Ptse_2$–WS_2–$Ptse_2$ Photodetector

Figure 6.6a-b show the optical image and the side view schematic of a typical $PtSe_2$-WS_2-$PtSe_2$ device during operation. During device measurements, two tungsten tips were used to make contact with the gold bond pads, allowing the current to flow directly through the lateral stack of $PtSe_2$–WS_2–$PtSe_2$. To prevent degradation of WS_2 under high bias, the measurements were conducted within a range of – 5 to +5 V. Initially, I attempted to use a voltage range of -10 V to + 10 V, but it led to circuit breakdown during the laser power-dependent measurements. Therefore, the range was adjusted from -5 V to +5 V, where no circuit breakdown occurred. Figure 6.6c-d show

the output curves for devices with channel widths of 1 and 1.5 μm, respectively, under different illumination conditions from a green laser ($\lambda = 532$ nm). Both devices exhibit obvious photoresponse and non-linear *I*–*V* curves, indicating the presence of a Schottky contact at the $PtSe_2$-WS_2 interface. Figure 6.6e shows the time-resolved photoresponse for a device with a channel length of 1 μm under laser powers of 82 μW, 1.07 mW, and 1.24 mW, with an applied bias of +3 V. The ON/OFF cycles were performed with a time interval of 10 s. Our device shows remarkable ON/OFF ratios (I_{ON}/I_{OFF}) of 155, 822, and 1438, along with good reproducibility and a short response time. These quantities make the device a promising candidate for a photodetector with a highly sensible switch.

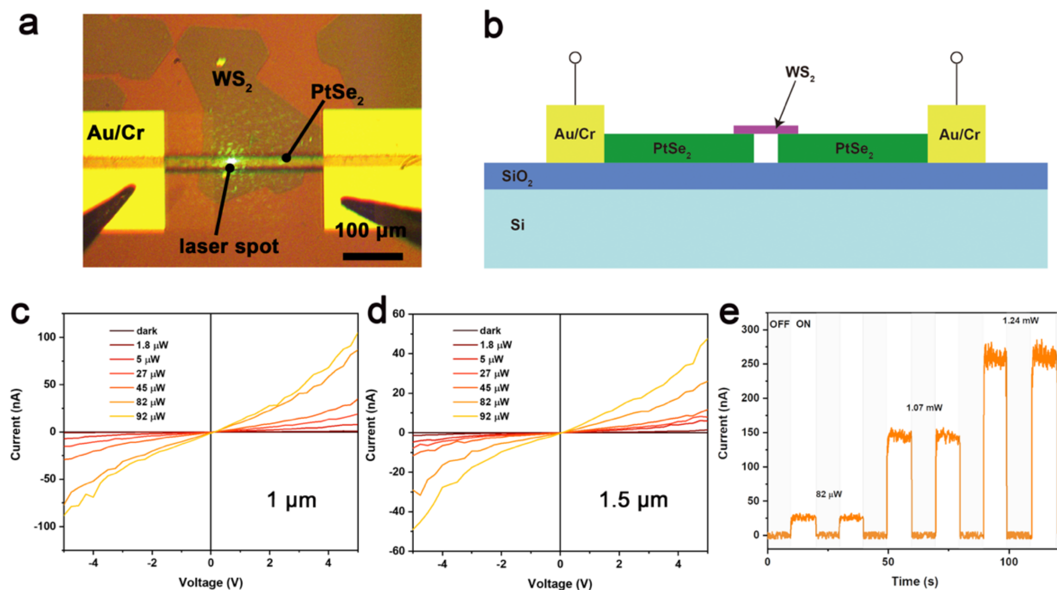

Figure 6.6 Opto-electrical measurements for a PtSe–WS_2–$PtSe_2$ photodetector. (a) Optical image of a typical $PtSe_2$-WS_2-$PtSe_2$ lateral heterostructure under illumination. (b) The side view schematic for a device under operation. (c-d) *I*–*V* curves of photodetectors with different channel widths (1 μm and 1.5 μm) under different illumination conditions. (e) The ON/OFF tests for the photodetector with a channel width of 1 μm under a bias of +3 V and laser powers of 82 μW, 1.07 mW, and 1.24 mW. The ON/OFF ratios are 155, 822, and 1438, respectively.

I then further investigated the mechanism of the photoresponse for the $PtSe_2$–WS_2–$PtSe_2$ lateral device. As previously mentioned, the non-linear *I–V* curves imply that the $PtSe_2$–WS_2 heterojunction can be considered a Schottky contact. Thus, the $PtSe_2$–WS_2–$PtSe_2$ lateral heterostructure can be regarded as a metal–semiconductor–metal (MSM) photodetector. A simplified back-to-back Schottky diode model was used here to describe the $PtSe_2$–WS_2–$PtSe_2$ lateral heterostructure, as shown in Figure 6.7a. This model consists of two $PtSe_2$–WS_2 Schottky diodes and a WS_2 resistor connected in series to form an electrical circuit. Figure 6.7b-c schematically illustrate the band diagrams of the lateral structure with and without bias, respectively.[311,312] In the absence of bias, under ideal conditions, it is assumed that the gap distance between $PtSe_2$ and WS_2 is on the atomic scale and transparent to electrons when $PtSe_2$ electrodes make contact with WS_2, establishing a single system in thermal equilibrium. V_{bi} represents the built-in electric field within the depletion layer in WS_2, induced by the accumulation of negative charges on the metal surface and the presence of positive charges on the WS_2 surface. When a positive bias is applied to the system, it acts as a forward bias for one $PtSe_2$–WS_2 diode and a reversed bias for the other one due to the intrinsic nature of the diode, as illustrated in Figure 6.7c. In the low-bias regime, the current in the circuit is predominantly determined by the diode under reversed bias, whereas in the high-bias regime, it is dominated by the diode under forward bias. The *I–V* curves presented in Figure 6.6c were fitted by using the back-to-back diode model.

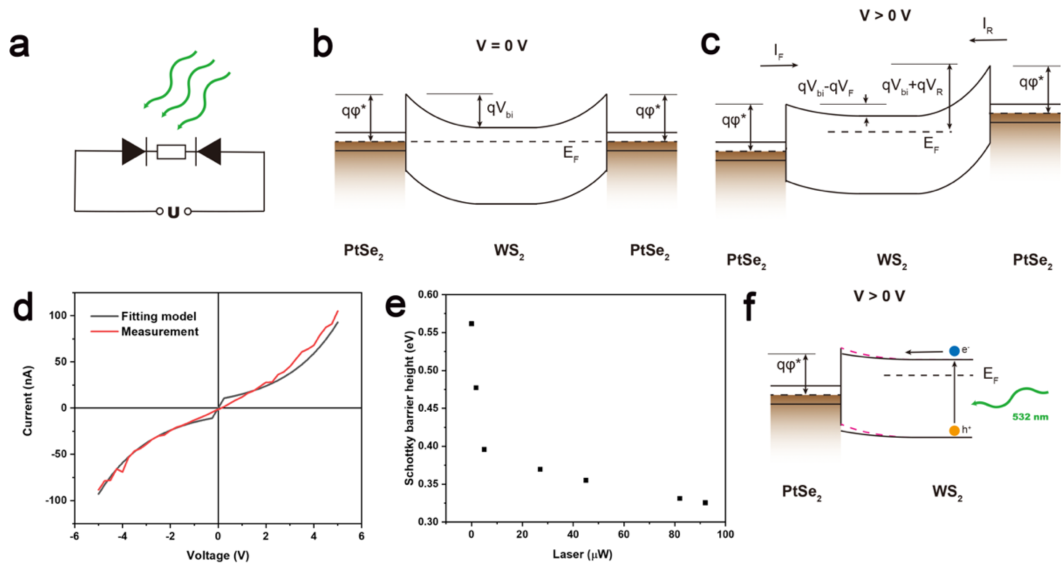

Figure 6.7 Calculation of the Schottky barrier height for the $PtSe_2$–WS_2 heterojunction. (a) The equivalent circuit diagram of the back-to-back Schottky diodes model. (b-c) Band diagrams for Schottky barriers on both sides of $PtSe_2$-WS_2-$PtSe_2$ heterojunction without bias and with positive bias, respectively. (d) Curve fitting of the *I*–*V* curve for $PtSe_2$–WS_2–$PtSe_2$ film by using the back-to-back Schottky diodes model. (e) Calculated Schottky barrier height as a function of incident laser power. (f) Band diagram for the $PtSe_2$–WS_2 heterojunction under illumination. The pink dashed lines exhibit the conduction band and valance band of WS_2 under dark conditions.

Here, numbers 1, 2, and 3 were used to consecutively label the three electric components shown in Figure 6.7a from left to right. For the system under bias, the major current transport process for a Schottky diode is the emission of electrons from the semiconductor to the metal, accompanied by other minor transport processes such as tunnelling, diffusion, and minority carrier injection.[165] In this study, a modified thermionic theory was utilized to describe the current flowing through each diode as follows:[12,313]

$$I = I_0 \exp\left[-\left(1-\frac{1}{n}\right)\frac{qV_F}{kT}\right]\left[\exp\left(\frac{qV_F}{kT}\right)-1\right] \quad \text{6-1}$$

$$I = {}^{V_s}/_{R_s} \quad \text{6-2}$$

$$I = -I_0 \exp\left[\left(1-\frac{1}{n}\right)\frac{qV_R}{kT}\right]\left[\exp\left(-\frac{qV_R}{kT}\right)-1\right] \quad \text{6-3}$$

$$V = V_F + V_S + V_R \quad 6\text{-}4$$

$$I_0 = wA^*T^{\alpha}\exp\left[-\frac{q\phi^*}{kT}\right] \quad 6\text{-}5$$

Where I is the output current, V is the output voltage, V_F, V_S, V_R are the voltage drops across component 1, 2, and 3, κ is the Boltzmann constant, T is the temperature, q is the elementary charge, n is the ideality factor describing barrier lowering by image force, w is the contact width of the metal and semiconductor ($w = 20\,um$ in the experiment), A^* is the effective Richardson constant (for 2D Schottky diode, $A^*_{2D} = 0.026\, A/_{mK^{2/3}}$), α is an exponent (for 2D Schottky diode, $\alpha = 3/2$) and ϕ^* is the effective Schottky barrier height. Another equation can be derived from eq.6-1~ 6-4 as follows:

$$I = wA^*T^{\alpha}\exp\left[-\frac{q\phi^*}{kT}\right]\left[\frac{\cosh\left(\frac{1}{2}(1-\frac{1}{n})\frac{q}{kT}(V-IR_S)\right)}{\cosh\left(\frac{1}{2n}\frac{q}{kT}(V-IR_S)\right)}\right]^{-(1-\frac{1}{n})}\cdot\frac{\sinh\left(\frac{1}{2}\frac{q}{kT}(V-IR_S)\right)}{\cosh\left(\frac{1}{2}\frac{q}{kT}(V-IR_S)\right)} \quad 6\text{-}6$$

In eq.6-6, the known quantities are the output voltage (V) and output current (I), and the unknowns are the Schottky barrier height ϕ^*, the resistance of the semiconductor R_S, and the ideality factor n.

Figure 6.7d presents an example of curve fitting using the back-to-back Schottky diode model, suggesting a good fit to the measured *I–V* curve. ϕ^* of the $PtSe_2$–WS_2 heterojunction was extracted under each illumination condition and plotted in Figure 6.7e. The work function of multilayer $PtSe_2$ (ϕ_{PtSe_2}) is 4.76 eV, and the electron affinity of WS_2 (χ_{WS_2}) is 4.0 eV.[314] According to the Schottky-Mott rule, the Schottky barrier (ϕ_{SB}) is expected to be $\phi_{SB} = \phi_{PtSe_2} - \chi_{WS_2} = 0.76$ eV. However, the calculated effective Schottky barrier height is 0.56 eV under dark conditions. This overestimation of the Schottky barrier height by the Schottky-Mott rule is mainly due

to the interface states located on WS_2. These trapped states caused a Fermi-pinning effect at the WS_2 interface and resulted in a lower effective Schottky barrier height. Another finding from Figure 6.7e is that the effective Schottky barrier height decreases with increasing laser power. The lowering of the Schottky barrier height can be explained by the increasing concentration of the photoinduced trapped state. As shown in Figure 6.7f, under the illumination of the incident light, the generated electron–hole pairs are separated into the conduction band and valence band, respectively. Electrons on the conduction band migrate to the $PtSe_2$ electrode, while holes on the valance band drift towards the WS_2 interface and become trapped at the surface. The increasing concentration of interface states leads to an accumulation of positive charge at the WS_2 interface, which lowers the local Fermi level of WS_2 and further reduces the effective Schottky barrier height.[315] In this process, the carriers in trapped states function as local gates and modulate the barrier height.[316–318] Similar cases of photogating/photoinduced lowering of the Schottky barrier height have been reported in Au–WS_2 and graphene–MoS_2 system.[306,319]

Photoresponsivity (R), external photogain (G_{ext}), and photodetectivity (D) are important figures of merit used to evaluate the performance of photodetectors. The definitions of R, G_{ext}, and specific photodetctivity (D^*) are provided in Chapter 2 (2.5.3). Figure 6.8a-b show the calculated photoresponsivity of devices with different channel widths as a function of laser power under a specific applied bias. Photoresponsivity increases with increasing bias, reaching maximum values of 1.6 and 1.2 mA/W for devices with channel widths of 1 and 1.5 μm, respectively. Both of these maximum values were measured under a maximum applied bias of 5 V and a laser power of 5 μW. It is noteworthy that the relationship between responsivity and

laser power is not simply monotonic. In low-illumination conditions, the increase of R is attributed to the significant decrease in the Schottky barrier height induced by the photogating effect, as shown in Figure 6.7e (1.8 and 5 μW). Subsequently, as the photogating effect reaches a relatively steady-state value and the trapped states become fully filled, the changes in the Schottky barrier height become minimal. At saturation, further increase in illumination do not result in higher currents, causing R to drop. However, with continuously increasing laser power, the photovoltaic signal starts to emerge from noise levels, contributing to the photocurrent and leading to a regrowth of the photoresponsivity at high powers. Figure 6.8c-d show the external photogain of devices with different channel widths as a function of laser power under a specific bias. The highest G_{ext} for both types of devices was also measured under the maximum applied bias of 5 V and a laser power of 5 μW, with values of 0.0037 and 0.0027 for channel widths of 1 and 1.5 μm, respectively. To refine the calculated results, the absorbance of WS_2 (8%) was taken into consideration, resulting in recalculated photogains of 0.046 and 0.033, respectively. The relatively long channel width leads to a large electron transit time, which may explain the small gain observed. Figure 6.8e-f show the specific detectivity for both devices under different illumination powers and biases. The maximum D^* value for devices with channel widths of 1 and 1.5 μm are 6.7×10^6 and 4.0×10^6 Jones, respectively, under an illumination power of 5 μW and an applied bias of 4 V. Despite of the high ON/OFF ratio, the devices show limited performance in photoresponsivity, photogain, and specific photodetectivity, compared to other reported WS_2-based MSM photodetectors.[155,320] One possible reason for this is the relatively low conductivity of the $PtSe_2$ electrodes (1.16×10^3 S/m) compared to other metal or graphene electrodes.[319] Another

potential reason is the accumulation of residues caused by laser ablation at the edge of the channel, which increases the contact resistance between $PtSe_2$ and WS_2.[321] In the comparison study of devices with different channel widths, the device with the shorter channel width demonstrates better performance in terms of photoresponsity, photogain, and specific detectivity. This can be attributed to a higher occurrence of electron–hole recombination in devices with longer channel widths.[306]

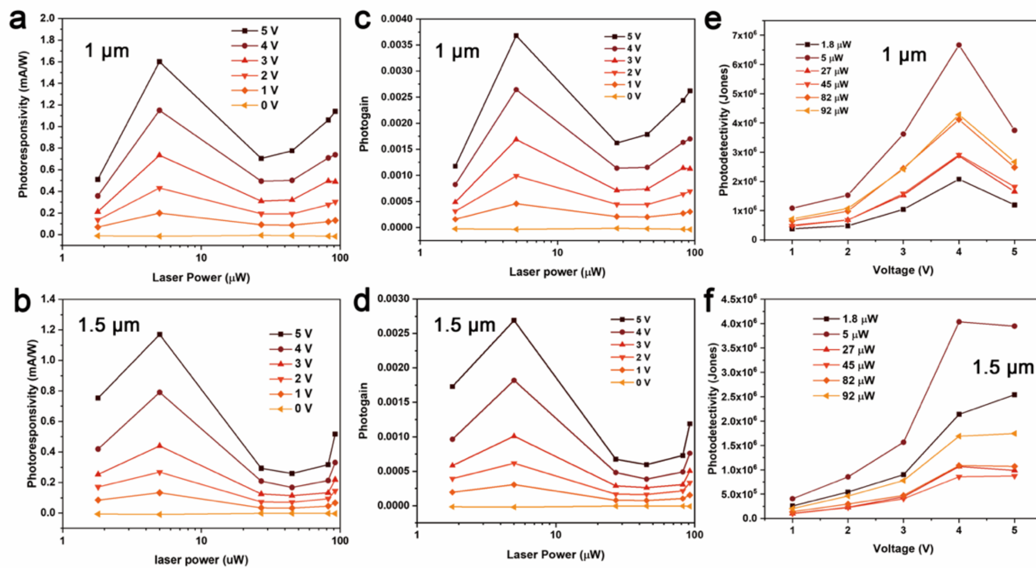

Figure 6.8 (a-b) Photoresponsivity and (c-d) Photogain of photodetectors with channel widths of 1 μm and 1.5 μm as a function of laser power. (e-f) Specific photodetectivity of two types of photodetectors as a function of applied bias.

6.3 Conclusion

In summary, this study demonstrated a photodetector with a lateral structure of $PtSe_2$–WS_2–$PtSe_2$, where multilayer $PtSe_2$ was used as a substitute for traditional metal electrodes, forming a typical MSM heterostructure. The $PtSe_2$ film was synthesized through a direct selenization process of a pre-coated Pt layer on a Si substrate in a double-furnace system under ambient pressure. The as-synthesized film exhibits homogeneity and a thickness of approximately 11.2 nm. A bilayer-photoresist recipe

was used to pattern $PtSe_2$ ribbons using photolithography. Direct laser patterning was employed to create micro-gaps on $PtSe_2$ ribbons. By modifying the scan steps during the laser patterning process, micro-gaps with different widths can be achieved. The $PtSe_2$–WS_2–$PtSe_2$ photodetector exhibits a remarkable $I_{\mathrm{ON}}/I_{\mathrm{OFF}}$ ratio of 155 under an illumination power of 82 μW. With its high $I_{\mathrm{ON}}/I_{\mathrm{OFF}}$ ratio, good reproducibility, and short response time, the device shows great potential as a candidate for photodetectors. However, the device shows lower photogain and photoresponsivity compared to other reported WS_2-based MSM photodetector, which could be attributed to factors such as long electron transit time, relatively low conductivity of the $PtSe_2$ electrodes, and residues generated by laser ablation. It is also observed that the device with a shorter channel width demonstrates better photoresponse due to reduced electron–hole recombination compared to the device with a longer width. The use of a back-to-back Schottky diodes model helped to estimate the barrier height of the $PtSe_2$–WS_2 heterojunction, which showed a decrease with increasing laser power, indicating a photoinduced lowering of the Schottky barrier height. This study highlights the potential of using 2D materials as electrodes and explores the feasibility of low-cost laser patterning for the fabrication of optoelectronic devices.

6.4 Contribution Statement

Qianyang Zhang helped me with the alignment transfer. Dr. Wenshuo Xu shared the recipe for the growth of $PtSe_2$ thin film, WS_2, and h-BN. Xuan Li and Yu Shu did the AFM measurements. Mr. Richard Makin from the Department of Physics did the Pt deposition by electron-beam evaporation. Dr. Ye Fan introduced the back-to-back diodes model for the calculation of Schottky barrier height.

Chapter 7 Conclusion and Future Outlook

This thesis covers the research conducted during my DPhil study, ranging from 2D materials synthesis to their applications in electronic and optoelectronic devices. The focus was on the fabrication of electronic and optoelectronic devices using grown 2D materials and the investigation of their properties. This section provides a summary of the key findings and results obtained from my research and presents an outlook for future research direction.

7.1 Thesis Summary

In Chapter 4, an asymmetrical vertical structure of graphene/WS_2/h-BN/graphene is demonstrated using all CVD-grown 2D materials. This structure uses three building blocks: conductive graphene as a good alternative for metal electrodes due to its tunable Fermi level and ultrathin nature, semiconducting TMDs as an ultrathin photoactive material, and insulating h-BN as a tunnelling barrier. The asymmetrical vertical structure exhibits a significantly stronger photovoltaic effect compared to a symmetrical one without the h-BN layer. By altering the sequence of h-BN within the vertical stack, the direction of electron flow can be precisely controlled. The enhanced photovoltaic effect is attributed to the different possibilities of excited electrons on the TMDs to migrate to the top and bottom graphene electrodes, which are caused by potential differences introduced by the insulating h-BN layer. This study demonstrates the effectiveness of few-layered h-BN thin films as tunnelling barriers

in vertical heterostructures, enabling improved photovoltaic effect and control over electron flow direction by tuning the tunnelling possibility at each electrode.

In Chapter 5, I demonstrate that all-2D VLH devices made using CVD-grown materials (Gr/h-BN/WS_2/h-BN/Gr) can generate strong red electroluminescence (EL). The success rate for EL emission in the devices is over 90%. EL is detected at a bias of approximately 5 V, with bright red emission localized at the crossbar intersection site, and the intensity increases with the applied bias. Furthermore, the devices exhibit long-lived persistent EL for more than 2 hours without significant degradation of WS_2 even under a high bias condition of 20 V. The ON/OFF cycling tests under high bias prove that the device has good stability and durability when pulsed. The device experiences breakdown is observed at a bias of around 35 V, leading to a reduction in current to zero and an abrupt stop of the EL emission. This breakdown is due to the failure of the top graphene electrode, which is associated with the accumulation of local heating. This study presents a promising approach for wafer-scale fabrication of high-performance 2D EL arrays for ultrathin optoelectronic devices using CVD-grown materials. Furthermore, it sheds light on the mechanisms underlying the failure and operation limits of EL devices using CVD-grown materials.

In Chapter 6, an MSM photodetector using only TMDs materials for both electrodes and photoactive materials was fabricated. Multi-layered $PtSe_2$ serves as metal electrodes, while monolayer WS_2 acts as photoactive material. $PtSe_2$ was synthesized through thermally assisted selenization, and the device was fabricated by using photolithography and direct laser patterning. By modifying the scan step during the laser patterning process, devices with various channel widths can be achieved. The as-fabricated devices exhibit a satisfactory ON/OFF ratio and decent photoresponse.

A comparison study reveals that the device with a shorter channel width demonstrates better photoresponsivity. The back-to-back Schottky diodes model well estimates the barrier height of the $PtSe_2$–WS_2 heterojunction. It is observed that the barrier height decreases with increasing laser power due to the photogating effect. This study expands the material choices for 2D electrodes and investigates the feasibility of low-cost laser patterning techniques for the fabrication of optoelectronic devices.

7.2 Future Outlook

Following the results from Chapter 5, some possible improvements can be made for future work on EL devices. Firstly, it is promising to encapsulate the devices with transparent dielectrics to reduce the top graphene degradation and enable longer persistent EL under higher biasing conditions. Secondly, a single EL device with a large emission area can be obtained by using our designed crossbar geometry and WS_2 single-crystal domains with larger grain size, or even better, WS_2 continuous film in mm scale. In addition, LED arrays can also be achieved by deterministically transferring patterned WS_2 squares from a WS_2 continuous film. Following this idea, full-colour LED arrays might be realized by vertically integrating the arrays of 2D EL devices with red/green/blue channel materials.

Following Chapter 6, instead of using oxygen plasma, SF6 is a suitable gas source for etching $PtSe_2$ without thinning down the photoresists such as PMMA. Therefore, the thickness of the resist is no longer a criterion for the choice of photoresists.[305,322] For example, PMMA can be used as a substitute for S1813. This approach eliminates the need for a buffering layer to prevent the reaction between the developer and the $PtSe_2$, simplifying the entire fabrication process. Inspired by

previous work on thinning down group VI TMDs to monolayer using direct laser ablation,[304] another alternative approach for photodetector fabrication can be explored: fabricating a lateral structure of bulk $PtSe_2$–monolayer $PtSe_2$–bulk $PtSe_2$ by using direct laser ablation to thin down the bulk $PtSe_2$ on the channel area to a monolayer semiconductor. This method offers the advantage of significantly reducing the contact resistance at the electrode–semiconductor interface. Additionally, the thickness of the $PtSe_2$ layer on the channel can be easily controlled by adjusting the parameters of the laser ablation, making the device a promising candidate for broadband photodetector.

Appendix A: Fitting procedures for PL and Raman spectra

In spectroscopy, Lorentzian and Gaussian distributions are assumed to be used to describe the homogeneous and inhomogeneous broadening of the line shapes that originate from the sum of all the individual transitions between energy levels (Raman, PL).[323,324] For example, Ajayi *et al.* adopted an approximation that the PL emission peak is subjected to the intrinsic Lorentzian line shape with the inhomogeneous broadening of Gaussian distribution due to defects and induced disorders.[323] More practically, from a graphical perspective, the Gaussian curve exhibits a smooth, bell-shaped symmetrical shape with a rapid decrease in intensity as you move away from the centre. In contrast, the Lorentzian curve is slightly narrower around its maximum intensity and decreases at a slower rate.[325,326] Since the observed line shape is the sum of scattering/absorbing events contributed by individual molecules, each peak should be positive. Therefore, fittings that result in peaks with negative areas should be avoided.

Various functions have been used for multi-peak fittings in PL and Raman analyses, such as the Lorentzian function (L), Gaussian function (G), or Voigt function (V, a convolution of L and G).[53,56,58,59,324,327–331] The fitting can be evaluated by R^2 values.[332] A R^2 value that is closer to 1 indicates a more precise fitting. The parameters involved in peak fittings are peak position, peak height, and line width. Peak position and peak height present the wavelength (energy) and intensity of the emission, respectively. The line width, represented by the full width at half maximum (FWHM), contains information on the crystal quality, disorders, strains, and the influence of the

environments.[265–269] Cadiz *et al.* showed that the FWHM of the PL of monolayer MoS_2 encapsulated by h-BN was down to 2 meV at $T = 4\ K$.[137] Compared with most reported FWHM of MoS_2 at low temperature (~ 50 meV), the large improvement on the narrowed line width indicates that the h-BN encapsulation plays an important role in surface protection and preventing the MoS_2 from surrounding disorders.[137] The broadening of the FWHM in the Raman spectrum of monolayer WS_2 is surmised to be associated with the grain boundaries, which distort the periodicity in the lattice.[331]

Here I take the PL and Raman spectrum of CVD-grown WS_2 used in Chapter 4 as examples to show a detailed procedure of the multi-curve fittings for PL and Raman, by comparing the fittings of the three different functions mentioned above and evaluating the fitting models by R^2 values. Figure A1 shows the multi-curve fittings of the PL and Raman spectrum by using the Lorentzian function (L), Gaussian function (G) or Voigt function (V), respectively. Table A1 summarizes the corresponding R_2 values of each fitting. As we can see from both Figure A1 and Table A1, Voigt fitting and Gaussian fitting have the best fitting for the PL and Raman spectrum, respectively, with R^2 values very close to 1 (three 9 after the decimal point).

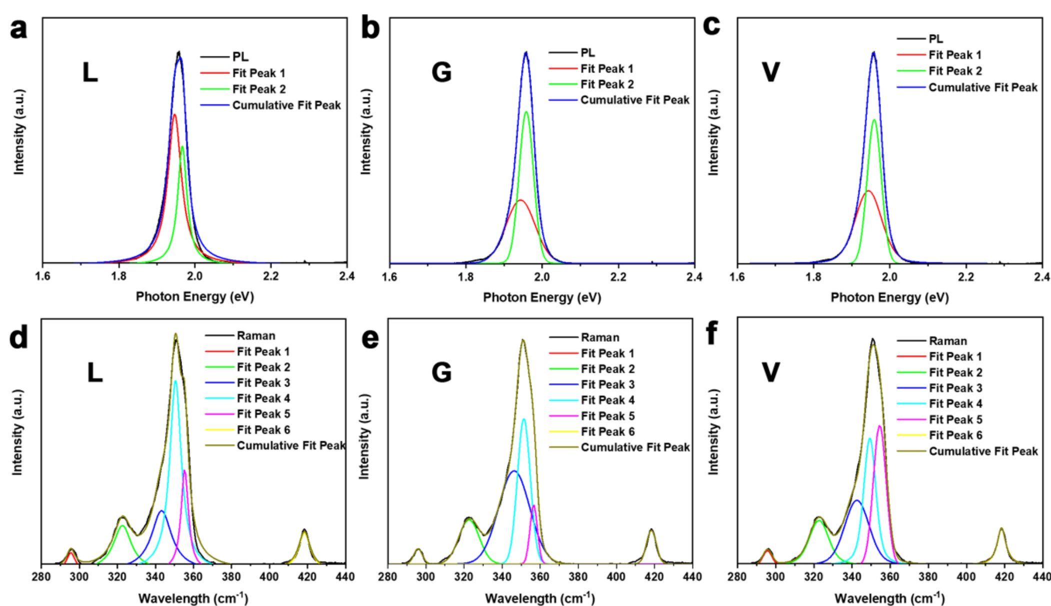

Figure A1. Multi-curve fittings of the PL (a-c) and Raman (d-f) spectrum by using Lorentzian function (L), Gaussian function (G) or Voigt function (V).

Table A1. Summary of R^2 values for the fittings from Figure A1.

R^2 values	Lorentzian function	Gaussian function	Voigt function
PL	0.99547	0.99934	**0.99947**
Raman	0.99380	**0.99925**	0.99832

Figure A2 shows the comparison of the peak positions by using different fitting methods. For the PL spectrum, G and V both have good R^2 values with three 9 after the decimal point, and L gives a less convincing fitting compared with G and V. From Figures A1a-c and A2a, the fitting results for G&V are very similar, according to both peak position and peak area, which is quite different with L fitting. For the Raman spectrum, only G fitting has R^2 values with three 9s after the decimal point, and the L&V functions lead to a relatively poor fitting. From Figure A1d-f and Figure A2b-c,

both the peak position and the peak area (peak height) are affected by the fitting method, especially for peak 3, 4, and 5, which are deconvoluted from one Raman peak.

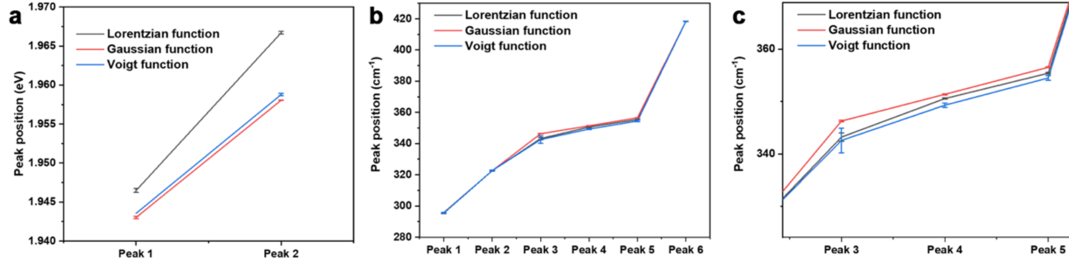

Figure A2. The comparisons of the peak positions by using different fitting methods for PL (a) and Raman (b-c). (c) The comparison of the peak positions of the peak 3, 4 and 5 which are deconvoluted from one Raman peak.

Therefore, I carefully chose the Voigt function for the PL spectrum of WS_2 and the Gaussian function for the Raman spectrum of WS_2. Here I summarized the peak position, peak area, FWHM, and corresponding error bar during the fitting process of deconvoluted peaks, as well as the corresponding assignments of the main Raman modes for Raman spectrum WS_2 in Table A2, the above-mentioned parameters and the assignments of the emission peaks for PL spectrum of WS_2 in Table A3.[233]

Table A2. Fitting parameters for PL spectrum by Voigt multi-curve fitting.

Plot	Negative Trion	Error bar	Exciton	Error bar
Peak position (eV)	1.94356	0.00015	1.95878	0.00004
Area (a.u.)	317.80673	2.42095	299.10516	2.08399
FWHM (G) (eV)	0.07111	0.00060	0.04355	0.00011
FWHM (L) (eV)	0.02051	0.00061	3.69×10^{-17}	0.00002

Table A3. Fitting parameters for Raman spectrum by Gaussian multi-curve fitting.

Plot	$E''(\Gamma)$	Error bar	$E''(\mathrm{M})$	Error bar	$E'(\mathrm{M})$	Error bar
Peak position (cm^{-1})	295.83718	0.14307	322.61987	0.10447	346.29068	0.15865
FWHM (cm^{-1})	4.47569	0.2935	10.72232	0.20819	16.34609	0.20529
Area (a.u.)	4484.61096	267.11415	31373.991	612.89921	101089.279	1807.32235
Plot	$2LA(\mathrm{M})$	Error bar	$E'(\Gamma)$	Error bar	$A_1'(\Gamma)$	Error bar
Peak position (cm^{-1})	351.37724	0.10464	356.53477	0.08984	418.31022	0.06824
FWHM (cm^{-1})	6.74657	0.20202	3.83754	0.1745	5.13031	0.1406
Area (a.u.)	64970.2351	3084.84742	15121.2412	1908.16366	11428.6767	286.54586

Parameters for fittings in Chapter 5 are shown as the following:

Table A4. Fitting parameters for Raman spectrum by using Lorentzian function in Figure 5.2h

Plot	$E''(\Gamma)$	Error bar	$E''(\mathrm{M})$	Error bar	$E'(\mathrm{M})$	Error bar
Peak position (cm^{-1})	293.6394	0.29212	320.2548	0.22626	340.9242	1.02004
FWHM (cm^{-1})	5.74465	0.92171	14.93949	0.79136	16.51912	1.35809
Area (a.u.)	9418.633	1200.493	69853.92	4395.84	138062.7	37197.56
Plot	$2LA(\mathrm{M})$	Error bar	$E'(\Gamma)$	Error bar	$A_1'(\Gamma)$	Error bar
Peak position (cm^{-1})	347.6562	0.16008	352.7747	0.21003	415.438	0.09078
FWHM (cm^{-1})	9.30627	1.31572	5.8537	0.74673	5.12662	0.29146
Area (a.u.)	147770.7	42279.96	41977.92	12464.76	25197.19	1147.944

Table A5. Fitting parameters for PL spectrum by using Gaussian function in Figure 5.2 i

Plot	Negative Trion	Error bar	Exciton	Error bar
Peak position (eV)	1.96489	0.00276	1.99983	0.00013
FWHM (G) (eV)	0.06948	0.00216	0.04407	0.00054
Area (a.u.)	54.0991	4.59264	85.07726	4.31586

Table A6. Fitting parameters for EL spectra by using Voigt function in Figure 5.8

11V	Negative Trion	Error bar	Exciton	Error bar
Peak position (eV)	1.83117	0.00649	1.90219	0.00248
Area (a.u.)	763.25656	100.10291	305.05121	51.71499
FWHM (G) (eV)	0.09691	0.01324	0.11659	0.00444
FWHM (L) (eV)	0.11778	0.01477	2.45×10^{-15}	0.00069

10.75 V	Negative Trion	Error bar	Exciton	Error bar
Peak position (eV)	1.85003	0.0041	1.91737	0.00283
Area (a.u.)	941.6924	87.96169	244.4609	43.93243
FWHM (G) (eV)	0.07265	0.00516	0.10317	0.00483
FWHM (L) (eV)	0.11704	0.00617	1.42×10^{-19}	0

10.5 V	Negative Trion	Error bar	Exciton	Error bar
Peak position (eV)	1.85067	0.00383	1.91784	0.00247
Area (a.u.)	922.6886	80.51772	257.0107	40.71158
FWHM (G) (eV)	0.07448	0.00472	0.10267	0.00419
FWHM (L) (eV)	0.11377	0.00574	1.95×10^{-20}	0

10.25	Negative Trion	Error bar	Exciton	Error bar
Peak position (eV)	1.85898	0.00177	1.92198	9.46E-04
Area (a.u.)	1108.75	54.26022	217.2657	20.18667
FWHM (G) (eV)	0.07274	0.00495	0.09186	0.00252
FWHM (L) (eV)	0.11772	0.0057	7.44×10^{-19}	0

10 V	Negative Trion	Error bar	Exciton	Error bar
Peak position (eV)	1.86026	0.00177	1.92001	0.00106
Area (a.u.)	1037.327	54.08355	210.5859	19.68916
FWHM (G) (eV)	0.06238	0.00589	0.09105	0.0027
FWHM (L) (eV)	0.12437	0.00588	3.22×10^{-20}	0

	11 V	10.75 V	10.5 V	10.25 V	10 V
R^2	0.99915	0.99932	0.99943	0.99942	0.99931

References

(1) Novoselov, K. S.; Geim, A. K.; Morozov, S. V.; Jiang, D.; Zhang, Y.; Dubonos, S. V.; Grigorieva, I. V.; Firsov, A. A. Electric Field in Atomically Thin Carbon Films. *Science* **2004**, *306*, 666–669.

(2) Cahill, D. G.; Ford, W. K.; Goodson, K. E.; Mahan, G. D.; Majumdar, A.; Maris, H. J.; Merlin, R.; Phillpot, S. R. Nanoscale Thermal Transport. *J. Appl. Phys.* **2003**, *93*, 793–818.

(3) Geim, A. K. Graphene: Status and Prospects. *Science* **2009,** *324*, 1530–1534.

(4) Das, S.; Robinson, J. A.; Dubey, M.; Terrones, H.; Terrones, M. Beyond Graphene: Progress in Novel Two-Dimensional Materials and van der Waals Solids. *Annu. Rev. Mater. Res.* **2015**, *45*, 1–27.

(5) Mak, K. F.; Lee, C.; Hone, J.; Shan, J.; Heinz, T. F. Atomically Thin MoS_2: A New Direct-Gap Semiconductor. *Phys. Rev. Lett.* **2010**, *105*, 136805.

(6) Moore, G. E. Cramming More Components onto Integrated Circuits. *Proc. IEEE* **1998**, *86*, 82–85.

(7) Lafkioti, M.; Krauss, B.; Lohmann, T.; Zschieschang, U.; Klauk, H.; Klitzing, K. V.; Smet, J. H. Graphene on a Hydrophobic Substrate: Doping Reduction and Hysteresis Suppression under Ambient Conditions. *Nano Lett.* **2010**, *10*, 1149–1153.

(8) Splendiani, A.; Sun, L.; Zhang, Y.; Li, T.; Kim, J.; Chim, C. Y.; Galli, G.; Wang, F. Emerging Photoluminescence in Monolayer MoS_2. *Nano Lett.* **2010**, *10*, 1271–1275.

(9) Bernardi, M.; Palummo, M.; Grossman, J. C. Extraordinary Sunlight Absorption and One Nanometer Thick Photovoltaics Using Two-Dimensional Monolayer Materials. *Nano Lett.* **2013**, *13*, 3664–3670.

(10) Wang, X.; Hooper, T. N.; Kumar, A.; Priest, I. K.; Sheng, Y.; Samuels, T. O. M.; Wang, S.; Robertson, A. W.; Pacios, M.; Bhaskaran, H.; et al. Oligomeric Aminoborane Precursors for the Chemical Vapour Deposition Growth of Few-Layer Hexagonal Boron Nitride. *CrystEngComm* **2017**, *19*, 285–294.

(11) Tan, C.; Cao, X.; Wu, X. J.; He, Q.; Yang, J.; Zhang, X.; Chen, J.; Zhao, W.; Han, S.; Nam, G. H.; et al. Recent Advances in Ultrathin Two-Dimensional Nanomaterials. *Chem. Rev.* **2017**, *117*, 6225–6331.

(12) Allain, A.; Kang, J.; Banerjee, K.; Kis, A. Electrical Contacts to Two-Dimensional Semiconductors. *Nat. Mater.* **2015**, *14*, 1195–1205.

(13) Britnell, L.; Gorbachev, R. V.; Jalil, R.; Belle, B. D.; Schedin, F.; Mishchenko, A.; Georgiou, T.; Katsnelson, M. I.; Eaves, L.; Morozov, S. V.; Peres, N. M. R.; Leist, J.; Geim, A. K.; Novoselov, K. S.; Ponomarenko, L. A. Field-Effect Tunneling Transistor Based on Vertical Graphene Heterostructures. *Science* **2012**, *335*, 947–950.

(14) Withers, F.; Del Pozo-Zamudio, O.; Mishchenko, A.; Rooney, A. P.; Gholinia, A.; Watanabe, K.; Taniguchi, T.; Haigh, S. J.; Geim, A. K.; Tartakovskii, A. I.; Novoselov, K. S. Light-Emitting Diodes by Band-Structure Engineering in van der Waals Heterostructures. *Nat. Mater.* **2015**, *14*, 301–306.

(15) Castro Neto, A. H.; Guinea, F.; Peres, N. M. R.; Novoselov, K. S.; Geim, A. K. The Electronic Properties of Graphene. *Rev. Mod. Phys.* **2009**, *81*, 109–162.

(16) Kitadai, H.; Yuan, M.; Ma, Y.; Ling, X. Graphene-Based Environmental Sensors: Electrical and Optical Devices. *Molecules* **2021**, *26*, 1-18.

(17) Katsnelson, M. I.; Novoselov, K. S.; Geim, A. K. Chiral Tunnelling and the Klein Paradox in Graphene. *Nat. Phys.* **2006**, *2*, 620–625.

(18) Stander, N.; Huard, B.; Goldhaber-Gordon, D. Evidence for Klein Tunneling in Graphene p-n Junctions. *Phys. Rev. Lett.* **2009**, *102*, 1-4.

(19) Katsnelson, M. I.; Geim, A. K. Electron Scattering on Microscopic Corrugations in Graphene. *Philos. Trans. R. Soc. A Math. Phys. Eng. Sci.* **2008**, *366*, 195–204.

(20) Meyer, J. C.; Geim, A. K.; Katsnelson, M. I.; Novoselov, K. S.; Booth, T. J.; Roth, S. The Structure of Suspended Graphene Sheets. *Nature* **2007**, *446*, 60–63.

(21) Chen, J. H.; Jang, C.; Adam, S.; Fuhrer, M. S.; Williams, E. D.; Ishigami, M. Charged-Impurity Scattering in Graphene. *Nat. Phys.* **2008**, *4*, 377–381.

(22) Jafri, S. H. M.; Carva, K.; Widenkvist, E.; Blom, T.; Sanyal, B.; Fransson, J.; Eriksson, O.; Jansson, U.; Grennberg, H.; Karis, O.; Quinlan, R. A.; Holloway, B. C.; Leifer, K. Conductivity Engineering of Graphene by Defect Formation. *J. Phys. D. Appl. Phys.* **2010**, *43*, 1-8.

(23) Kozikov, A. A.; Savchenko, A. K.; Narozhny, B. N.; Shytov, A. V. Electron-Electron Interactions in the Conductivity of Graphene. *Phys. Rev. B - Condens. Matter Mater. Phys.* **2010**, *82*, 1–5.

(24) Bolotin, K. I.; Sikes, K. J.; Jiang, Z.; Klima, M.; Fudenberg, G.; Hone, J.; Kim, P.; Stormer, H. L. Ultrahigh Electron Mobility in Suspended Graphene. *Solid State Commun.* **2008**, *146*, 351–355.

(25) Bolotin, K. I.; Sikes, K. J.; Hone, J.; Stormer, H. L.; Kim, P. Temperature-Dependent Transport in Suspended Graphene. *Phys. Rev. Lett.* **2008**, *101*, 1–4.

(26) Morozov, S. V.; Novoselov, K. S.; Katsnelson, M. I.; Schedin, F.; Elias, D. C.; Jaszczak, J. A.; Geim, A. K. Giant Intrinsic Carrier Mobilities in Graphene and Its Bilayer. *Phys. Rev. Lett.* **2008**, *100*, 1-4.

(27) Castro, E. V.; Ochoa, H.; Katsnelson, M. I.; Gorbachev, R. V.; Elias, D. C.; Novoselov, K. S.; Geim, A. K.; Guinea, F. Limits on Charge Carrier Mobility in Suspended Graphene Due to Flexural Phonons. *Phys. Rev. Lett.* **2010**, *105*, 16–18.

(28) Du, X.; Skachko, I.; Barker, A.; Andrei, E. Y. Approaching Ballistic Transport

in Suspended Graphene. *Nat. Nanotechnol.* **2008**, *3*, 491–495.

(29) Chen, J. H.; Jang, C.; Xiao, S.; Ishigami, M.; Fuhrer, M. S. Intrinsic and Extrinsic Performance Limits of Graphene Devices on SiO 2. *Nat. Nanotechnol.* **2008**, *3*, 206–209.

(30) Dean, C. R.; Young, A. F.; Meric, I.; Lee, C.; Wang, L.; Sorgenfrei, S.; Watanabe, K.; Taniguchi, T.; Kim, P.; Shepard, K. L.; Hone, J. Boron Nitride Substrates for High-Quality Graphene Electronics. *Nat. Nanotechnol.* **2010**, *5*, 722–726.

(31) Taniguchi, T.; Watanabe, K. Synthesis of High-Purity Boron Nitride Single Crystals under High Pressure by Using Ba-BN Solvent. *J. Cryst. Growth* **2007**, *303* (2), 525–529. https://doi.org/10.1016/j.jcrysgro.2006.12.061.

(32) Thomsen, J. D.; Gunst, T.; Gregersen, S. S.; Gammelgaard, L.; Jessen, B. S.; Mackenzie, D. M. A.; Watanabe, K.; Taniguchi, T.; Bøggild, P.; Booth, T. J. Suppression of Intrinsic Roughness in Encapsulated Graphene. *Phys. Rev. B* **2017**, *96*, 1–8.

(33) Lui, C. H.; Liu, L.; Mak, K. F.; Flynn, G. W.; Heinz, T. F. Ultraflat Graphene. *Nature* **2009**, *462*, 339–341.

(34) Haigh, S. J.; Gholinia, A.; Jalil, R.; Romani, S.; Britnell, L.; Elias, D. C.; Novoselov, K. S.; Ponomarenko, L. A.; Geim, A. K.; Gorbachev, R. Cross-Sectional Imaging of Individual Layers and Buried Interfaces of Graphene-Based Heterostructures and Superlattices. *Nat. Mater.* **2012**, *11*, 764–767.

(35) Wang, L.; Meric, I.; Huang, P. Y.; Gao, Q.; Gao, Y.; Tran, H.; Taniguchi, T.; Watanabe, K.; Campos, L. M.; Muller, D. A.; Guo, J.; Kim, P.; Hone, J.; Shepard, K. L.; Dean, C. R. One-Dimensional Electrical Contact to a Two-Dimensional Material. Science 2013, 342, 614–617.

(36) Purdie, D. G.; Pugno, N. M.; Taniguchi, T.; Watanabe, K.; Ferrari, A. C.; Lombardo, A. Cleaning Interfaces in Layered Materials Heterostructures. *Nat. Commun.* **2018**, *9*, 1–12.

(37) Banszerus, L.; Schmitz, M.; Engels, S.; Dauber, J.; Oellers, M.; Haupt, F.; Watanabe, K.; Taniguchi, T.; Beschoten, B.; Stampfer, C. Ultrahigh-Mobility Graphene Devices from Chemical Vapor Deposition on Reusable Copper. *Sci. Adv.* **2015**, *1*, 1–7.

(38) Banszerus, L.; Schmitz, M.; Engels, S.; Goldsche, M.; Watanabe, K.; Taniguchi, T.; Beschoten, B.; Stampfer, C. Ballistic Transport Exceeding 28 μm in CVD Grown Graphene. *Nano Lett.* **2016**, *16*, 1387–1391.

(39) Wu, Y.; Lin, Y. M.; Bol, A. A.; Jenkins, K. A.; Xia, F.; Farmer, D. B.; Zhu, Y.; Avouris, P. High-Frequency, Scaled Graphene Transistors on Diamond-like Carbon. *Nature* **2011**, *472*, 74–78.

(40) Wang, Q. H.; Kalantar-Zadeh, K.; Kis, A.; Coleman, J. N.; Strano, M. S. Electronics and Optoelectronics of Two-Dimensional Transition Metal Dichalcogenides. *Nat. Nanotechnol.* **2012**, *7*, 699–712.

(41) Chhowalla, M.; Shin, H. S.; Eda, G.; Li, L. J.; Loh, K. P.; Zhang, H. The Chemistry of Two-Dimensional Layered Transition Metal Dichalcogenide Nanosheets. *Nat. Chem.* **2013**, *5*, 263–275.

(42) Rafiq, Md. K. S. B.; Akhtaruzzaman, Md. Novel Chalcogenides and Their Fabrication Techniques. In *Comprehensive Guide on Organic and Inorganic Solar Cells*; Elsevier, **2022**, 171–185.

(43) Manzeli, S.; Ovchinnikov, D.; Pasquier, D.; Yazyev, O. V.; Kis, A. 2D Transition Metal Dichalcogenides. *Nature Reviews Materials*. **2017**, *2*, 17033.

(44) Kuc, A.; Zibouche, N.; Heine, T. Influence of Quantum Confinement on the Electronic Structure of the Transition Metal Sulfide TS2. *Phys. Rev. B - Condens. Matter Mater. Phys.* **2011**, *83*, 1–4.

(45) Gutiérrez, H. R.; Perea-López, N.; Elías, A. L.; Berkdemir, A.; Wang, B.; Lv, R.; López-Urías, F.; Crespi, V. H.; Terrones, H.; Terrones, M. Extraordinary Room-Temperature Photoluminescence in Triangular WS_2 Monolayers. *Nano Lett.* **2013**, *13*, 3447–3454..

(46) Koåmider, K.; Fernández-Rossier, J. Electronic Properties of the MoS2-WS2 Heterojunction. *Phys. Rev. B - Condens. Matter Mater. Phys.* **2013**, *87*, 075451.

(47) Kao, K. C. Optical and Electro-Optic Processes. *Dielectric Phenomena in Solids.*; Elsevier: Burlington, **2004**.

(48) Haug, A. Band-to-Band Auger Recombination in Semiconductors. *J. Phys. Chem. Solids* **1988**, *49*, 599–605.

(49) Raja, A.; Chaves, A.; Yu, J.; Arefe, G.; Hill, H. M.; Rigosi, A. F.; Berkelbach, T. C.; Nagler, P.; Schüller, C.; Korn, T.; Nuckolls, C.; Hone, J.; Brus, L. E.; Heinz, T. F.; Reichman, D. R.; Chernikov, A. Coulomb Engineering of the Bandgap and Excitons in Two-Dimensional Materials. *Nat. Commun.* **2017**, *8*, 1–7.

(50) Cheiwchanchamnangij, T.; Lambrecht, W. R. L. Quasiparticle Band Structure Calculation of Monolayer, Bilayer, and Bulk MoS_2. *Phys. Rev. B - Condens. Matter Mater. Phys.* **2012**, *85*, 205302.

(51) Ugeda, M. M.; Bradley, A. J.; Shi, S. F.; Da Jornada, F. H.; Zhang, Y.; Qiu, D. Y.; Ruan, W.; Mo, S. K.; Hussain, Z.; Shen, Z. X.; Wang, F.; Louie, S. G.; Crommie, M. F. Giant Bandgap Renormalization and Excitonic Effects in a Monolayer Transition Metal Dichalcogenide Semiconductor. *Nat. Mater.* **2014**, *13*, 1091–1095.

(52) Zhu, Z. Y.; Cheng, Y. C.; Schwingenschlögl, U. Giant Spin-Orbit-Induced Spin Splitting in Two-Dimensional Transition-Metal Dichalcogenide Semiconductors. *Phys. Rev. B - Condens. Matter Mater. Phys.* **2011**, *84*, 1–5.

(53) Mak, K. F.; He, K.; Lee, C.; Lee, G. H.; Hone, J.; Heinz, T. F.; Shan, J. Tightly Bound Trions in Monolayer MoS_2. *Nat. Mater.* **2013**, *12*, 207–211.

(54) Shang, J.; Shen, X.; Cong, C.; Peimyoo, N.; Cao, B.; Eginligil, M.; Yu, T. Observation of Excitonic Fine Structure in a 2D Transition-Metal

Dichalcogenide Semiconductor. *ACS Nano* **2015**, *9*, 647–655.

(55) Hu, P.; Ye, J.; He, X.; Du, K.; Zhang, K. K.; Wang, X.; Xiong, Q.; Liu, Z.; Jiang, H.; Kloc, C. Control of Radiative Exciton Recombination by Charge Transfer Induced Surface Dipoles in $MoS_2$and WS_2 Monolayers. *Sci. Rep.* **2016**, *6*, 24105.

(56) Mitioglu, A. A.; Plochocka, P.; Jadczak, J. N.; Escoffier, W.; Rikken, G. L. J. A.; Kulyuk, L.; Maude, D. K. Optical Manipulation of the Exciton Charge State in Single-Layer Tungsten Disulfide. *Phys. Rev. B - Condens. Matter Mater. Phys.* **2013**, *88*, 245403.

(57) Plechinger, G.; Nagler, P.; Kraus, J.; Paradiso, N.; Strunk, C.; Schüller, C.; Korn, T. Identification of Excitons, Trions and Biexcitons in Single-Layer WS_2. *Phys. Status Solidi - Rapid Res. Lett.* **2015**, *9*, 457–461.

(58) Golovynskyi, S.; Irfan, I.; Bosi, M.; Seravalli, L.; Datsenko, O. I.; Golovynska, I.; Li, B.; Lin, D.; Qu, J. Exciton and Trion in Few-Layer MoS_2: Thickness- and Temperature-Dependent Photoluminescence. *Appl. Surf. Sci.* **2020**, *515*, 146033.

(59) Zhu, B.; Chen, X.; Cui, X. Exciton Binding Energy of Monolayer WS_2. *Sci. Rep.* **2015**, *5*, 9218.

(60) Chen, Y.; Dumcenco, D. O.; Zhu, Y.; Zhang, X.; Mao, N. Temperature-Dependent Photoluminescence Emission and Raman Scattering from $Mo_{1-x}W_xS_2$ Monolayers. **2014**, *20*, 1–12.

(61) Varshni, Y. P. Temperature Dependence of the Energy Gap in Semiconductors. *Physica* **1967**, *34*, 149–154.

(62) Tongay, S.; Suh, J.; Ataca, C.; Fan, W.; Luce, A.; Kang, J. S.; Liu, J.; Ko, C.; Raghunathanan, R.; Zhou, J.; Ogletree, F.; Li, J.; Grossman, J. C.; Wu, J. Defects Activated Photoluminescence in Two-Dimensional Semiconductors: Interplay between Bound, Charged, and Free Excitons. *Sci. Rep.* **2013**, *3*, 2657.

(63) McCreary, A.; Berkdemir, A.; Wang, J.; Nguyen, M. A.; Elías, A. L.; Perea-López, N.; Fujisawa, K.; Kabius, B.; Carozo, V.; Cullen, D. A.; Mallouk, T. E.; Zhu, J.; Terrones, M. Distinct Photoluminescence and Raman Spectroscopy Signatures for Identifying Highly Crystalline WS_2 Monolayers Produced by Different Growth Methods. *J. Mater. Res.* **2016**, *31*, 931–944.

(64) You, Y.; Zhang, X. X.; Berkelbach, T. C.; Hybertsen, M. S.; Reichman, D. R.; Heinz, T. F. Observation of Biexcitons in Monolayer WSe_2. *Nat. Phys.* **2015**, *11*, 477–481.

(65) Kim, M. S.; Yun, S. J.; Lee, Y.; Seo, C.; Han, G. H.; Kim, K. K.; Lee, Y. H.; Kim, J. Biexciton Emission from Edges and Grain Boundaries of Triangular WS_2 Monolayers. *ACS Nano* **2016**, *10*, 2399–2405.

(66) Zhao, Y.; Qiao, J.; Yu, Z.; Yu, P.; Xu, K.; Lau, S. P.; Zhou, W.; Liu, Z.; Wang, X.; Ji, W.; Chai, Y. High-Electron-Mobility and Air-Stable 2D Layered $PtSe_2$ FETs. *Adv. Mater.* **2017**, *29*, 1604230.

(67) Huang, Z.; Zhang, W.; Zhang, W. Computational Search for Two-Dimensional

MX_2 Semiconductors with Possible High Electron Mobility at Room Temperature. *Materials* **2016**, *9*, 1–13.

(68) Jiang, W.; Wang, X.; Chen, Y.; Wu, G.; Ba, K.; Xuan, N.; Sun, Y.; Gong, P.; Bao, J.; Shen, H.; Lin, T.; Meng, X.; Wang, J.; Sun, Z. Large-area High Quality $PtSe_2$ Thin Film with Versatile Polarity. *InfoMat* **2019**, *1*, 260–267.

(69) Han, S. S.; Kim, J. H.; Noh, C.; Kim, J. H.; Ji, E.; Kwon, J.; Yu, S. M.; Ko, T. J.; Okogbue, E.; Oh, K. H.; Chung, H. S.; Jung, Y.; Lee, G. H.; Jung, Y. Horizontal-to-Vertical Transition of 2D Layer Orientation in Low-Temperature Chemical Vapor Deposition-Grown $PtSe_2$ and Its Influences on Electrical Properties and Device Applications. *ACS Appl. Mater. Interfaces* **2019**, *11*, 13598–13607.

(70) Yim, C.; Lee, K.; McEvoy, N.; O'Brien, M.; Riazimehr, S.; Berner, N. C.; Cullen, C. P.; Kotakoski, J.; Meyer, J. C.; Lemme, M. C.; Duesberg, G. S. High-Performance Hybrid Electronic Devices from Layered $PtSe_2$ Films Grown at Low Temperature. *ACS Nano* **2016**, *10*, 9550–9558.

(71) Sajjad, M.; Montes, E.; Singh, N.; Schwingenschlögl, U. Superior Gas Sensing Properties of Monolayer $PtSe_2$. *Adv. Mater. Interfaces* **2017**, *4*, 2–5.

(72) Guo, G. Y.; Liang, W. Y. The Electronic Structures of Platinum Dichalcogenides: PtS_2, $PtSe_2$ and $PtTe_2$. *J. Phys. C Solid State Phys.* **1986**, *19*, 995–1008.

(73) Cassabois, G.; Valvin, P.; Gil, B. Hexagonal Boron Nitride Is an Indirect Bandgap Semiconductor. *Nat. Photonics* **2016**, *10*, 262–266.

(74) Chang, R. J.; Wang, X.; Wang, S.; Sheng, Y.; Porter, B.; Bhaskaran, H.; Warner, J. H. Growth of Large Single-Crystalline Monolayer Hexagonal Boron Nitride by Oxide-Assisted Chemical Vapor Deposition. *Chem. Mater.* **2017**, *29*, 6252–6260.

(75) Watanabe, K.; Taniguchi, T.; Kanda, H. Direct-Bandgap Properties and Evidence for Ultraviolet Lasing of Hexagonal Boron Nitride Single Crystal. *Nat. Mater.* **2004**, *3*, 404–409.

(76) Ouyang, T.; Chen, Y.; Xie, Y.; Yang, K.; Bao, Z.; Zhong, J. Thermal Transport in Hexagonal Boron Nitride Nanoribbons. *Nanotechnology* **2010**, *21*, 245701.

(77) Peng, Q.; Ji, W.; De, S. Mechanical Properties of the Hexagonal Boron Nitride Monolayer: Ab Initio Study. *Comput. Mater. Sci.* **2012**, *56*, 11–17.

(78) Kumar, R.; Sahoo, S.; Joanni, E.; Singh, R. K.; Yadav, R. M.; Verma, R. K.; Singh, D. P.; Tan, W. K.; Pérez del Pino, A.; Moshkalev, S. A.; Matsuda, A. A Review on Synthesis of Graphene, h-BN and MoS_2 for Energy Storage Applications: Recent Progress and Perspectives. *Nano Res.* **2019**, *12*, 2655–2694.

(79) Mayorov, A. S.; Gorbachev, R. V.; Morozov, S. V.; Britnell, L.; Jalil, R.; Ponomarenko, L. A.; Blake, P.; Novoselov, K. S.; Watanabe, K.; Taniguchi, T.; Geim, A. K. Micrometer-Scale Ballistic Transport in Encapsulated Graphene at

Room Temperature. *Nano Lett.* **2011**, *11*, 2396–2399.

(80) Britnell, L.; Gorbachev, R. V.; Jalil, R.; Belle, B. D.; Schedin, F.; Katsnelson, M. I.; Eaves, L.; Morozov, S. V.; Mayorov, A. S.; Peres, N. M. R.; Castro Neto, A. H.; Leist, J.; Geim, A. K.; Ponomarenko, L. A.; Novoselov, K. S. Electron Tunneling through Ultrathin Boron Nitride Crystalline Barriers. *Nano Lett.* **2012**, *12*, 1707–1710.

(81) Divincenzo, D. P.; Duer, W.; Cirac, J. I.; Zoller, P.; Steel, D. G.; Rice, T. M.; Stahl, A.; Gotoh, H.; Temmyo, J.; Takagahara, T.; Ando, H.; Narozhny, N. B.; Eberly, J. H.; Grynberg, G.; Townes, C. H.; Chebotaev, V. P.; Hartmann, F.; Ezekiel, S.; Ducloy, M.; Mollow, B. R.; Macdonald, K. R.; Boyd, R. W.; Berman, P. R.; Snow, E. S.; Shanabrook, B. V; Katzer, D. S.; Park, D.; Zubairy, M. S. Deep Ultraviolet Light–Emitting Hexagonal Boron Nitride Synthesized at Atmospheric Pressure. *Science* **2007**, *317*, 932–935.

(82) Tay, R. Y.; Wang, X.; Tsang, S. H.; Loh, G. C.; Singh, R. S.; Li, H.; Mallick, G.; Tong Teo, E. H. A Systematic Study of the Atmospheric Pressure Growth of Large-Area Hexagonal Crystalline Boron Nitride Film. *J. Mater. Chem. C* **2014**, *2*, 1650–1657.

(83) Tay, R. Y.; Griep, M. H.; Mallick, G.; Tsang, S. H.; Singh, R. S.; Tumlin, T.; Teo, E. H. T.; Karna, S. P. Growth of Large Single-Crystalline Two-Dimensional Boron Nitride Hexagons on Electropolished Copper. *Nano Lett.* **2014**, *14*, 839–846.

(84) Liu, Y.; Weiss, N. O.; Duan, X.; Cheng, H. C.; Huang, Y.; Duan, X. Van der Waals Heterostructures and Devices. *Nature Reviews Materials*. **2016**, *1*, 16042.

(85) Yi, M.; Shen, Z. A Review on Mechanical Exfoliation for the Scalable Production of Graphene. *J. Mater. Chem. A* **2015**, *3*, 11700–11715.

(86) Huang, Y.; Sutter, E.; Shi, N. N.; Zheng, J.; Yang, T.; Englund, D.; Gao, H. J.; Sutter, P. Reliable Exfoliation of Large-Area High-Quality Flakes of Graphene and Other Two-Dimensional Materials. *ACS Nano* **2015**, *9*, 10612–10620.

(87) Hernandez, Y.; Nicolosi, V.; Lotya, M.; Blighe, F. M.; Sun, Z.; De, S.; McGovern, I. T.; Holland, B.; Byrne, M.; Gun'ko, Y. K.; Boland, J. J.; Niraj, P.; Duesberg, G.; Krishnamurthy, S.; Goodhue, R.; Hutchison, J.; Scardaci, V.; Ferrari, A. C.; Coleman, J. N. High-Yield Production of Graphene by Liquid-Phase Exfoliation of Graphite. *Nat. Nanotechnol.* **2008**, *3*, 563–568.

(88) Dines, M. B. Lithium Intercalation via N-Butyllithium of the Layered Transition Metal Dichalcogenides. *Mater. Res. Bull.* **1975**, *10*, 287–291.

(89) Joensen, P.; Frindt, R. F.; Morrison, S. R. Single-Layer MoS_2. *Mater. Res. Bull.* **1986**, *21*, 457–461.

(90) Coleman, J. N.; Lotya, M.; O'Neill, A.; Bergin, S. D.; King, P. J.; Khan, U.; Young, K.; Gaucher, A.; De, S.; Smith, R. J.; Shvets, I. V.; Arora, S. K.; Stanton, G.; Kim, H. Y.; Lee, K.; Kim, G. T.; Duesberg, G. S.; Hallam, T.; Boland, J. J.; Wang, J. J.; Donegan, J. F.; Grunlan, J. C.; Moriarty, G.; Shmeliov, A.; Nicholls, R. J.; Perkins, J. M.; Grieveson, E. M.; Theuwissen, K.; McComb, D. W.;

Nellist, P. D.; Nicolosi, V. Two-Dimensional Nanosheets Produced by Liquid Exfoliation of Layered Materials. *Science* **2011**, *331*, 568–571.

(91) Zheng, J.; Zhang, H.; Dong, S.; Liu, Y.; Tai Nai, C.; Suk Shin, H.; Young Jeong, H.; Liu, B.; Ping Loh, K. High Yield Exfoliation of Two-Dimensional Chalcogenides Using Sodium Naphthalenide. *Nat. Commun.* **2014**, *5*, 2995.

(92) Koma, A. Van der Waals Epitaxy for Highly Lattice-Mismatched Systems. *J. Cryst. Growth* **1999**, *201*, 236–241.

(93) Cai, Z.; Liu, B.; Zou, X.; Cheng, H. M. Chemical Vapor Deposition Growth and Applications of Two-Dimensional Materials and Their Heterostructures. *Chem Rev*. **2018**, *118*, 6091–6133.

(94) Schmidt, H.; Wang, S.; Chu, L.; Toh, M.; Kumar, R.; Zhao, W.; Castro Neto, A. H.; Martin, J.; Adam, S.; Özyilmaz, B.; Eda, G. Transport Properties of Monolayer MoS_2 Grown by Chemical Vapor Deposition. *Nano Lett.* **2014**, *14*, 1909–1913.

(95) Zhang, Y.; Zhang, L.; Zhou, C. Review of Chemical Vapor Deposition of Graphene and Related Applications. *Acc. Chem. Res.* **2013**, *46*, 2329–2339.

(96) Yu, Q.; Lian, J.; Siriponglert, S.; Li, H.; Chen, Y. P.; Pei, S. S. Graphene Segregated on Ni Surfaces and Transferred to Insulators. *Appl. Phys. Lett.* **2008**, *93*, 113103–121601.

(97) Gomez De Arco, L.; Zhang, Y.; Kumar, A.; Zhou, C. Synthesis, Transfer, and Devices of Single- and Few-Layer Graphene by Chemical Vapor Deposition. *IEEE Trans. Nanotechnol.* **2009**, *8*, 135–138.

(98) Reina, A.; Jia, X.; Ho, J.; Nezich, D.; Son, H.; Bulovic, V.; Dresselhaus, M. S.; Jing, K. Large Area, Few-Layer Graphene Films on Arbitrary Substrates by Chemical Vapor Deposition. *Nano Lett.* **2009**, *9*, 30–35.

(99) Akhtar, F.; Dabrowski, J.; Lisker, M.; Zaumseil, P.; Schulze, S.; Jouvray, A.; Caban, P.; Mai, A.; Wenger, C.; Lukosius, M. Large-Scale Chemical Vapor Deposition of Graphene on Polycrystalline Nickel Films: Effect of Annealing Conditions. *Thin Solid Films* **2019**, *690*, 137565.

(100) Li, X.; Cai, W.; Colombo, L.; Ruoff, R. S. Evolution of Graphene Growth on Ni and Cu by Carbon Isotope Labeling. *Nano Lett.* **2009**, *9*, 4268–4272.

(101) Li, X.; Cai, W.; An, J.; Kim, S.; Nah, J.; Yang, D.; Piner, R.; Velamakanni, A.; Jung, I.; Tutuc, E.; Banerjee, S. K.; Colombo, L.; Ruoff, R. S. Large-Area Synthesis of High-Quality and Uniform Graphene Films on Copper Foils. *Science*. **2009**, *324* (5932), 1312–1314.

(102) Hofmann, W. K. Thin Films of Molybdenum and Tungsten Disulphides by Metal Organic Chemical Vapour Deposition. *J. Mater. Sci.* **1988**, *23*, 3981–3986.

(103) Najmaei, S.; Liu, Z.; Zhou, W.; Zou, X.; Shi, G.; Lei, S.; Yakobson, B. I.; Idrobo, J. C.; Ajayan, P. M.; Lou, J. Vapour Phase Growth and Grain Boundary Structure of Molybdenum Disulphide Atomic Layers. *Nat. Mater.* **2013**, *12*,

754–759.

(104) Van Der Zande, A. M.; Huang, P. Y.; Chenet, D. A.; Berkelbach, T. C.; You, Y.; Lee, G. H.; Heinz, T. F.; Reichman, D. R.; Muller, D. A.; Hone, J. C. Grains and Grain Boundaries in Highly Crystalline Monolayer Molybdenum Disulphide. *Nat. Mater.* **2013**, *12*, 554–561.

(105) Liu, K. K.; Zhang, W.; Lee, Y. H.; Lin, Y. C.; Chang, M. T.; Su, C. Y.; Chang, C. S.; Li, H.; Shi, Y.; Zhang, H.; Lai, C. S.; Li, L. J. Growth of Large-Area and Highly Crystalline MoS_2 Thin Layers on Insulating Substrates. *Nano Lett.* **2012**, *12*, 1538–1544.

(106) Lee, Y. H.; Zhang, X. Q.; Zhang, W.; Chang, M. T.; Lin, C. Te; Chang, K. Di; Yu, Y. C.; Wang, J. T. W.; Chang, C. S.; Li, L. J.; Lin, T. W. Synthesis of Large-Area MoS_2 Atomic Layers with Chemical Vapor Deposition. *Adv. Mater.* **2012**, *24*, 2320–2325.

(107) Liu, B.; Chen, L.; Liu, G.; Abbas, A. N.; Fathi, M.; Zhou, C. High-Performance Chemical Sensing Using Schottky-Contacted Chemical Vapor Deposition Grown Monolayer MoS_2 Transistors. *ACS Nano* **2014**, *8*, 5304–5314.

(108) Song, L.; Ci, L.; Lu, H.; Sorokin, P. B.; Jin, C.; Ni, J.; Kvashnin, A. G.; Kvashnin, D. G.; Lou, J.; Yakobson, B. I.; Ajayan, P. M. Large Scale Growth and Characterization of Atomic Hexagonal Boron Nitride Layers. *Nano Lett.* **2010**, *10*, 3209–3215.

(109) Shi, Y.; Hamsen, C.; Jia, X.; Kim, K. K.; Reina, A.; Hofmann, M.; Hsu, A. L.; Zhang, K.; Li, H.; Juang, Z. Y.; Dresselhaus, M. S.; Li, L. J.; Kong, J. Synthesis of Few-Layer Hexagonal Boron Nitride Thin Film by Chemical Vapor Deposition. *Nano Lett.* **2010**, *10*, 4134–4139.

(110) Gao, Y.; Ren, W.; Ma, T.; Liu, Z.; Zhang, Y.; Liu, W. Bin; Ma, L. P.; Ma, X.; Cheng, H. M. Repeated and Controlled Growth of Monolayer, Bilayer and Few-Layer Hexagonal Boron Nitride on Pt Foils. *ACS Nano* **2013**, *7*, 5199–5206.

(111) Zhang, J.; Tan, B.; Zhang, X.; Gao, F.; Hu, Y.; Wang, L.; Duan, X.; Yang, Z.; Hu, P. A. Atomically Thin Hexagonal Boron Nitride and Its Heterostructures. *Adv. Mater.* **2021**, *33*, 1–28.

(112) Wang, L.; Wu, B.; Chen, J.; Liu, H.; Hu, P.; Liu, Y. Monolayer Hexagonal Boron Nitride Films with Large Domain Size and Clean Interface for Enhancing the Mobility of Graphene-Based Field-Effect Transistors. *Adv. Mater.* **2014**, *26*, 1559–1564.

(113) Lee, K. H.; Shin, H. J.; Lee, J.; Lee, I. Y.; Kim, G. H.; Choi, J. Y.; Kim, S. W. Large-Scale Synthesis of High-Quality Hexagonal Boron Nitride Nanosheets for Large-Area Graphene Electronics. *Nano Lett.* **2012**, *12*, 714–718.

(114) Whittell, G. R.; Manners, I. Advances with Ammonia-Borane: Improved Recycling and Use as a Precursor to Atomically Thin BN Films. *Angew. Chemie - Int. Ed.* **2011**, *50*, 10288–10289.

(115) Kim, K. K.; Hsu, A.; Jia, X.; Kim, S. M.; Shi, Y.; Hofmann, M.; Nezich, D.;

Rodriguez-Nieva, J. F.; Dresselhaus, M.; Palacios, T.; Kong, J. Synthesis of Monolayer Hexagonal Boron Nitride on Cu Foil Using Chemical Vapor Deposition. *Nano Lett.* **2012**, *12*, 161–166.

(116) Ismach, A.; Chou, H.; Ferrer, D. A.; Wu, Y.; McDonnell, S.; Floresca, H. C.; Covacevich, A.; Pope, C.; Piner, R.; Kim, M. J.; Wallace, R. M.; Colombo, L.; Ruoff, R. S. Toward the Controlled Synthesis of Hexagonal Boron Nitride Films. *ACS Nano* **2012**, *6*, 6378–6385.

(117) Wolf, G.; Baumann, J.; Baitalow, F.; Hoffmann, F. P. Calorimetric Process Monitoring of Thermal Decomposition of B-N-H Compounds. *Thermochim. Acta* **2000**, *343*, 19–25.

(118) Wang, Y.; Yamamoto, Y.; Kiyono, H.; Shimada, S. Effect of Ambient Gas and Temperature on Crystallization of Boron Nitride Spheres Prepared by Vapor Phase Pyrolysis of Ammonia Borane. *J. Am. Ceram. Soc.* **2009**, *92*, 787–792.

(119) Liu, S.; He, R.; Xue, L.; Li, J.; Liu, B.; Edgar, J. H. Single Crystal Growth of Millimeter-Sized Monoisotopic Hexagonal Boron Nitride. *Chem. Mater.* **2018**, *30*, 6222–6225.

(120) Sonntag, J.; Li, J.; Plaud, A.; Loiseau, A.; Barjon, J.; Edgar, J. H.; Stampfer, C. Excellent Electronic Transport in Heterostructures of Graphene and Monoisotopic Boron-Nitride Grown at Atmospheric Pressure. *2D Mater.* **2020**, *7*, 031009.

(121) Wang, Z.; Li, Q.; Besenbacher, F.; Dong, M. Facile Synthesis of Single Crystal $PtSe_2$ Nanosheets for Nanoscale Electronics. *Adv. Mater.* **2016**, *28*, 10224–10229.

(122) Zhao, S.; Weng, J.; Jin, S.; Lv, Y.; Ji, Z. Chemical Vapor Transport Deposition of Molybdenum Disulfide Layers Using H_2O Vapor as the Transport Agent. *Coatings* **2018**, *8*, 78.

(123) Och, M.; Martin, M. B.; Dlubak, B.; Seneor, P.; Mattevi, C. Synthesis of Emerging 2D Layered Magnetic Materials. *Nanoscale* **2021**, *13*, 2157–2180.

(124) Binnewies, M.; Glaum, R.; Schmidt, M.; Schmidt, P. Chemical Vapor Transport Reactions - A Historical Review. *Zeitschrift fur Anorg. und Allg. Chemie* **2013**, *639*, 219–229.

(125) Wang, Y.; Li, L.; Yao, W.; Song, S.; Sun, J. T.; Pan, J.; Ren, X.; Li, C.; Okunishi, E.; Wang, Y. Q.; Wang, E.; Shao, Y.; Zhang, Y. Y.; Yang, H. T.; Schwier, E. F.; Iwasawa, H.; Shimada, K.; Taniguchi, M.; Cheng, Z.; Zhou, S.; Du, S.; Pennycook, S. J.; Pantelides, S. T.; Gao, H. J. Monolayer $PtSe_2$, a New Semiconducting Transition-Metal-Dichalcogenide, Epitaxially Grown by Direct Selenization of Pt. *Nano Lett.* **2015**, *15*, 4013–4018.

(126) Su, T. Y.; Medina, H.; Chen, Y. Z.; Wang, S. W.; Lee, S. S.; Shih, Y. C.; Chen, C. W.; Kuo, H. C.; Chuang, F. C.; Chueh, Y. L. Phase-Engineered $PtSe_2$-Layered Films by a Plasma-Assisted Selenization Process toward All $PtSe_2$-Based Field Effect Transistor to Highly Sensitive, Flexible, and Wide-Spectrum Photoresponse Photodetectors. *Small* **2018**, *14*, 1800032.

(127) Wang, G.; Wang, Z.; McEvoy, N.; Fan, P.; Blau, W. J. Layered $PtSe_2$ for Sensing, Photonic, and (Opto-)Electronic Applications. *Adv. Mater.* **2021**, *33*, 1–23.

(128) Yu, X.; Yu, P.; Wu, D.; Singh, B.; Zeng, Q.; Lin, H.; Zhou, W.; Lin, J.; Suenaga, K.; Liu, Z.; Wang, Q. J. Atomically Thin Noble Metal Dichalcogenide: A Broadband Mid-Infrared Semiconductor. *Nat. Commun.* **2018**, *9*, 1–9.

(129) Andrei, E. Y.; MacDonald, A. H. Graphene Bilayers with a Twist. *Nat. Mater.* **2020**, *19*, 1265–1275.

(130) Sun, L.; Wang, Z.; Wang, Y.; Zhao, L.; Li, Y.; Chen, B.; Huang, S.; Zhang, S.; Wang, W.; Pei, D.; Fang, H.; Zhong, S.; Liu, H.; Zhang, J.; Tong, L.; Chen, Y.; Li, Z.; Rümmeli, M. H.; Novoselov, K. S.; Peng, H.; Lin, L.; Liu, Z. Hetero-Site Nucleation for Growing Twisted Bilayer Graphene with a Wide Range of Twist Angles. *Nat. Commun.* **2021**, *12*, 1–8.

(131) Chu, C. M.; Woon, W. Y. Growth of Twisted Bilayer Graphene through Two-Stage Chemical Vapor Deposition. *Nanotechnology* **2020**, *31*, 435603.

(132) Kim, K.; Yankowitz, M.; Fallahazad, B.; Kang, S.; Movva, H. C. P.; Huang, S.; Larentis, S.; Corbet, C. M.; Taniguchi, T.; Watanabe, K.; Banerjee, S. K.; Leroy, B. J.; Tutuc, E. Van der Waals Heterostructures with High Accuracy Rotational Alignment. *Nano Lett.* **2016**, *16*, 1989–1995.

(133) Bistritzer, R.; MacDonald, A. H. Moiré Bands in Twisted Double-Layer Graphene. *Proc. Natl. Acad. Sci. U. S. A.* **2011**, *108*, 12233–12237.

(134) Cao, Y.; Fatemi, V.; Fang, S.; Watanabe, K.; Taniguchi, T.; Kaxiras, E.; Jarillo-Herrero, P. Unconventional Superconductivity in Magic-Angle Graphene Superlattices. *Nature* **2018**, *556*, 43–50.

(135) Jin, C.; Regan, E. C.; Yan, A.; Iqbal Bakti Utama, M.; Wang, D.; Zhao, S.; Qin, Y.; Yang, S.; Zheng, Z.; Shi, S.; Watanabe, K.; Taniguchi, T.; Tongay, S.; Zettl, A.; Wang, F. Observation of Moiré Excitons in WSe_2/WS_2 Heterostructure Superlattices. *Nature* **2019**, *567*, 76–80.

(136) Tran, K.; Moody, G.; Wu, F.; Lu, X.; Choi, J.; Kim, K.; Rai, A.; Sanchez, D. A.; Quan, J.; Singh, A.; Embley, J.; Zepeda, A.; Campbell, M.; Autry, T.; Taniguchi, T.; Watanabe, K.; Lu, N.; Banerjee, S. K.; Silverman, K. L.; Kim, S.; Tutuc, E.; Yang, L.; MacDonald, A. H.; Li, X. Evidence for Moiré Excitons in van der Waals Heterostructures. *Nature* **2019**, *567*, 71–75.

(137) Cadiz, F.; Courtade, E.; Robert, C.; Wang, G.; Shen, Y.; Cai, H.; Taniguchi, T.; Watanabe, K.; Carrere, H.; Lagarde, D.; Manca, M.; Amand, T.; Renucci, P.; Tongay, S.; Marie, X.; Urbaszek, B. Excitonic Linewidth Approaching the Homogeneous Limit in MoS_2-Based van der Waals Heterostructures. *Phys. Rev. X* **2017**, *7*, 1–10.

(138) Ho, P. H.; Chang, Y. R.; Chu, Y. C.; Li, M. K.; Tsai, C. A.; Wang, W. H.; Ho, C. H.; Chen, C. W.; Chiu, P. W. High-Mobility InSe Transistors: The Role of Surface Oxides. *ACS Nano* **2017**, *11*, 7362–7370.

(139) Chae, S. H.; Jin, Y.; Kim, T. S.; Chung, D. S.; Na, H.; Nam, H.; Kim, H.; Perello, D. J.; Jeong, H. Y.; Ly, T. H.; Lee, Y. H. Oxidation Effect in Octahedral Hafnium Disulfide Thin Film. *ACS Nano* **2016**, *10*, 1309–1316.

(140) Doganov, R. A.; O'Farrell, E. C. T.; Koenig, S. P.; Yeo, Y.; Ziletti, A.; Carvalho, A.; Campbell, D. K.; Coker, D. F.; Watanabe, K.; Taniguchi, T.; Neto, A. H. C.; Özyilmaz, B. Transport Properties of Pristine Few-Layer Black Phosphorus by van der Waals Passivation in an Inert Atmosphere. *Nat. Commun.* **2015**, *6*, 6647.

(141) Avsar, A.; Vera-Marun, I. J.; Tan, J. Y.; Watanabe, K.; Taniguchi, T.; Castro Neto, A. H.; Özyilmaz, B. Air-Stable Transport in Graphene-Contacted, Fully Encapsulated Ultrathin Black Phosphorus-Based Field-Effect Transistors. *ACS Nano* **2015**, *9*, 4138–4145.

(142) Fang, H.; Battaglia, C.; Carraro, C.; Nemsak, S.; Ozdol, B.; Kang, J. S.; Bechtel, H. A.; Desai, S. B.; Kronast, F.; Unal, A. A.; Conti, G.; Conlon, C.; Palsson, G. K.; Martin, M. C.; Minor, A. M.; Fadley, C. S.; Yablonovitch, E.; Maboudian, R.; Javey, A. Strong Interlayer Coupling in van der Waals Heterostructures Built from Single-Layer Chalcogenides. *Proc. Natl. Acad. Sci. U. S. A.* **2014**, *111*, 6198–6202.

(143) Hong, X.; Kim, J.; Shi, S. F.; Zhang, Y.; Jin, C.; Sun, Y.; Tongay, S.; Wu, J.; Zhang, Y.; Wang, F. Ultrafast Charge Transfer in Atomically Thin MoS_2/WS_2 Heterostructures. *Nat. Nanotechnol.* **2014**, *9*, 682–686.

(144) Chen, H.; Wen, X.; Zhang, J.; Wu, T.; Gong, Y.; Zhang, X.; Yuan, J.; Yi, C.; Lou, J.; Ajayan, P. M.; Zhuang, W.; Zhang, G.; Zheng, J. Ultrafast Formation of Interlayer Hot Excitons in Atomically Thin MoS_2/WS_2 Heterostructures. *Nat. Commun.* **2016**, *7*, 12512.

(145) Rivera, P.; Schaibley, J. R.; Jones, A. M.; Ross, J. S.; Wu, S.; Aivazian, G.; Klement, P.; Seyler, K.; Clark, G.; Ghimire, N. J.; Yan, J.; Mandrus, D. G.; Yao, W.; Xu, X. Observation of Long-Lived Interlayer Excitons in Monolayer $MoSe_2$-WSe_2 Heterostructures. *Nat. Commun.* **2015**, *6*. 6242.

(146) Tongay, S.; Fan, W.; Kang, J.; Park, J.; Koldemir, U.; Suh, J.; Narang, D. S.; Liu, K.; Ji, J.; Li, J.; Sinclair, R.; Wu, J. Tuning Interlayer Coupling in Large-Area Heterostructures with CVD-Grown MoS_2 and WS_2 Monolayers. *Nano Lett.* **2014**, *14*, 3185–3190.

(147) Zhang, K.; Zhang, T.; Cheng, G.; Li, T.; Wang, S.; Wei, W.; Zhou, X.; Yu, W.; Sun, Y.; Wang, P.; Zhang, D.; Zeng, C.; Wang, X.; Hu, W.; Fan, H. J.; Shen, G.; Chen, X.; Duan, X.; Chang, K.; Dai, N. Interlayer Transition and Infrared Photodetection in Atomically Thin Type-II $MoTe_2/MoS_2$ van der Waals Heterostructures. *ACS Nano* **2016**, *10*, 3852–3858.

(148) Tan, H.; Xu, W.; Sheng, Y.; Lau, C. S.; Fan, Y.; Chen, Q.; Tweedie, M.; Wang, X.; Zhou, Y.; Warner, J. H. Lateral Graphene-Contacted Vertically Stacked WS_2/MoS_2 Hybrid Photodetectors with Large Gain. *Adv. Mater.* **2017**, *29*, 1–8.

(149) Britnell, L.; Ribeiro, R. M.; Eckmann, A.; Jalil, R.; Belle, B. D.; Mishchenko, A.; Kim, Y. J.; Gorbachev, R. V.; Georgiou, T.; Morozov, S. V.; Grigorenko,

A. N.; Geim, A. K.; Casiraghi, C.; Castro Neto, A. H.; Novoselov, K. S. Strong Light-Matter Interactions in Heterostructures of Atomically Thin Films. *Science* **2013**, *340*, 1311–1314.

(150) Liu, Y.; Wu, H.; Cheng, H. C.; Yang, S.; Zhu, E.; He, Q.; Ding, M.; Li, D.; Guo, J.; Weiss, N. O.; Huang, Y.; Duan, X. Toward Barrier Free Contact to Molybdenum Disulfide Using Graphene Electrodes. *Nano Lett.* **2015**, *15*, 3030–3034.

(151) Cui, X.; Lee, G. H.; Kim, Y. D.; Arefe, G.; Huang, P. Y.; Lee, C. H.; Chenet, D. A.; Zhang, X.; Wang, L.; Ye, F.; Pizzocchero, F.; Jessen, B. S.; Watanabe, K.; Taniguchi, T.; Muller, D. A.; Low, T.; Kim, P.; Hone, J. Multi-Terminal Transport Measurements of MoS_2 Using a van der Waals Heterostructure Device Platform. *Nat. Nanotechnol.* **2015**, *10*, 534–540.

(152) Yu, W. J.; Liu, Y.; Zhou, H.; Yin, A.; Li, Z.; Huang, Y.; Duan, X. Highly Efficient Gate-Tunable Photocurrent Generation in Vertical Heterostructures of Layered Materials. *Nat. Nanotechnol.* **2013**, *8*, 952–958.

(153) Yu, W. J.; Liu, Y.; Zhou, H.; Yin, A.; Li, Z.; Huang, Y.; Duan, X. Highly Efficient Gate-Tunable Photocurrent Generation in Vertical Heterostructures of Layered Materials. *Nat. Nanotechnol.* **2013**, *8*, 952–958.

(154) Yu, Y. J.; Zhao, Y.; Ryu, S.; Brus, L. E.; Kim, K. S.; Kim, P. Tuning the Graphene Work Function by Electric Field Effect. *Nano Lett.* **2009**, *9*, 3430–3434.

(155) Tan, H.; Fan, Y.; Zhou, Y.; Chen, Q.; Xu, W.; Warner, J. H. Ultrathin 2D Photodetectors Utilizing Chemical Vapor Deposition Grown WS_2 with Graphene Electrodes. *ACS Nano* **2016**, *10*, 7866–7873.

(156) Chen, T.; Sheng, Y.; Zhou, Y.; Chang, R. J.; Wang, X.; Huang, H.; Zhang, Q.; Hou, L.; Warner, J. H. High Photoresponsivity in Ultrathin 2D Lateral Graphene:WS_2:Graphene Photodetectors Using Direct CVD Growth. *ACS Appl. Mater. Interfaces* **2019**, *11*, 6421–6430.

(157) Yu, W. J.; Liu, Y.; Zhou, H.; Yin, A.; Li, Z.; Huang, Y.; Duan, X. Highly Efficient Gate-Tunable Photocurrent Generation in Vertical Heterostructures of Layered Materials. *Nat. Nanotechnol.* **2013**, *8*, 952–958.

(158) Zhou, Y.; Tan, H.; Sheng, Y.; Fan, Y.; Xu, W.; Warner, J. H. Utilizing Interlayer Excitons in Bilayer WS_2 for Increased Photovoltaic Response in Ultrathin Graphene Vertical Cross-Bar Photodetecting Tunneling Transistors. *ACS Nano* **2018**, *12*, 4669–4677.

(159) Massicotte, M.; Schmidt, P.; Vialla, F.; Schädler, K. G.; Reserbat-Plantey, A.; Watanabe, K.; Taniguchi, T.; Tielrooij, K. J.; Koppens, F. H. L. Picosecond Photoresponse in van der Waals Heterostructures. *Nat. Nanotechnol.* **2016**, *11*, 42–46.

(160) Lee, C. H.; Lee, G. H.; Van Der Zande, A. M.; Chen, W.; Li, Y.; Han, M.; Cui, X.; Arefe, G.; Nuckolls, C.; Heinz, T. F.; Guo, J.; Hone, J.; Kim, P. Atomically Thin p–n Junctions with van der Waals Heterointerfaces. *Nat. Nanotechnol.*

2014, *9*, 676–681.

(161) Zhou, Y.; Xu, W.; Sheng, Y.; Huang, H.; Zhang, Q.; Hou, L.; Shautsova, V.; Warner, J. H. Symmetry-Controlled Reversible Photovoltaic Current Flow in Ultrathin All 2D Vertically Stacked Graphene/MoS_2/WS_2/Graphene Devices. *ACS Appl. Mater. Interfaces* **2019**, *11*, 2234–2242.

(162) Das, S.; Chen, H. Y.; Penumatcha, A. V.; Appenzeller, J. High Performance Multilayer MoS_2 Transistors with Scandium Contacts. *Nano Lett.* **2013**, *13*, 100–105.

(163) Oh, G.; Jeon, J. H.; Kim, Y. C.; Ahn, Y. H.; Park, B. H. Gate-Tunable Photodetector and Ambipolar Transistor Implemented Using a Graphene/$MoSe_2$ Barristor. *NPG Asia Mater.* **2021**, *13*, 10.

(164) Roy, T.; Tosun, M.; Kang, J. S.; Sachid, A. B.; Desai, S. B.; Hettick, M.; Hu, C. C.; Javey, A. Field-Effect Transistors Built from All Two-Dimensional Material Components. *ACS Nano* **2014**, *8*, 6259–6264.

(165) Sze, S. M.; Ng, K. K. *Physics of Semiconductor Devices*, 1st ed.; Wiley, **2006**.

(166) Bardeen, J. Surface States and Rectification at a Metal Semi-Conductor Contact. *Phys. Rev.* **1947**, *71*, 717–727.

(167) Zhang, J.; Wang, J. H.; Chen, P.; Sun, Y.; Wu, S.; Jia, Z. Y.; Lu, X. B.; Yu, H.; Chen, W.; Zhu, J. Q.; Xie, G. B.; Yang, R.; Shi, D. X.; Xu, X. L.; Xiang, J. Y.; Liu, K. H.; Zhang, G. Y. Observation of Strong Interlayer Coupling in MoS_2/WS_2 Heterostructures. *Adv. Mater.* **2016**, *28*, 1950–1956.

(168) Fu, L.; Fu, L.; Sun, Y.; Wu, N.; Mendes, R. G.; Chen, L.; Xu, Z.; Zhang, T.; Rümmeli, M. H.; Rellinghaus, B.; Pohl, D.; Zhuang, L. Direct Growth of MoS_2/h-BN Heterostructures via a Sulfide-Resistant Alloy. *ACS Nano* **2016**, *10*, 2063–2070.

(169) Zhang, Y.; Shi, J.; Liu, M.; Wen, J.; Ren, X.; Zhou, X.; Ji, Q.; Ma, D.; Zhang, Y.; Jin, C.; Chen, H.; Deng, S.; Xu, N.; Liu, Z. All Chemical Vapor Deposition Synthesis and Intrinsic Bandgap Observation of MoS_2/Graphene Heterostructures. *Adv. Mater.* **2015**, *27*, 7086–7092.

(170) Duan, X.; Wang, C.; Shaw, J. C.; Cheng, R.; Chen, Y.; Li, H.; Wu, X.; Tang, Y.; Zhang, Q.; Pan, A.; Jiang, J.; Yu, R.; Huang, Y.; Duan, X. Lateral Epitaxial Growth of Two-Dimensional Layered Semiconductor Heterojunctions. *Nat. Nanotechnol.* **2014**, *9*, 1024–1030.

(171) Frisenda, R.; Navarro-Moratalla, E.; Gant, P.; Pérez De Lara, D.; Jarillo-Herrero, P.; Gorbachev, R. V.; Castellanos-Gomez, A. Recent Progress in the Assembly of Nanodevices and van der Waals Heterostructures by Deterministic Placement of 2D Materials. *Chemical Society Reviews*. **2018**, *47*, 53–68.

(172) Tien, D. H.; Park, J. Y.; Kim, K. B.; Lee, N.; Seo, Y. Characterization of Graphene-Based FET Fabricated Using a Shadow Mask. *Sci. Rep.* **2016**, *6*, 25050.

(173) Zomer, P. J.; Dash, S. P.; Tombros, N.; Van Wees, B. J. A Transfer Technique

for High Mobility Graphene Devices on Commercially Available Hexagonal Boron Nitride. *Appl. Phys. Lett.* **2011**, *99*, 232104.

(174) Khestanova, E.; Guinea, F.; Fumagalli, L.; Geim, A. K.; Grigorieva, I. V. Universal Shape and Pressure inside Bubbles Appearing in van der Waals Heterostructures. *Nat. Commun.* **2016**, *7*, 1–10.

(175) Zhou, L.; Ge, C.; Yang, H.; Sun, Y.; Zhang, J. A High-Pressure Enhanced Coupling Effect between Graphene Electrical Contacts and Two-Dimensional Materials Thereby Improving the Performance of Their Constituent FET Devices. *J. Mater. Chem. C* **2019**, *7*, 15171–15178.

(176) Uwanno, T.; Hattori, Y.; Taniguchi, T.; Watanabe, K.; Nagashio, K. Fully Dry PMMA Transfer of Graphene on H-BN Using a Heating/Cooling System. *2D Mater.* **2015**, *2*, 041002.

(177) Pizzocchero, F.; Gammelgaard, L.; Jessen, B. S.; Caridad, J. M.; Wang, L.; Hone, J.; Bøggild, P.; Booth, T. J. The Hot Pick-up Technique for Batch Assembly of van der Waals Heterostructures. *Nat. Commun.* **2016**, *7*, 11894.

(178) Kumaresan, Y.; G. R., N.; Poola, P. K. Flexible and Stretchable Indium-Fallium-Zinc Oxide-Based Electronic Devices for Sweat pH Sensor Application. In *Flexible and Stretchable Indium-Fallium-Zinc Oxide-Based Electronic Devices for Sweat PH Sensor Application*; INC, **2021**; 525-543.

(179) Schwierz, F. Graphene Transistors. *Nat. Nanotechnol.* **2010**, *5*, 487–496.

(180) Lee, S. P. Electrode Materials and Electrode-Oxide Interfaces in Semiconductor Gas Sensors. In *Semiconductor Gas Sensors*; Elsevier, **2013**; 64–113.

(181) Simmons, J. G. Generalized Formula for the Electric Tunnel Effect between Similar Electrodes Separated by a Thin Insulating Film. *J. Appl. Phys.* **1963**, *34*, 1793–1803.

(182) Yu, W. J.; Vu, Q. A.; Oh, H.; Nam, H. G.; Zhou, H.; Cha, S.; Kim, J. Y.; Carvalho, A.; Jeong, M.; Choi, H.; Castro Neto, A. H.; Lee, Y. H.; Duan, X. Unusually Efficient Photocurrent Extraction in Monolayer van der Waals Heterostructure by Tunnelling through Discretized Barriers. *Nat. Commun.* **2016**, *7*, 13278.

(183) Lee, G. H.; Yu, Y. J.; Lee, C.; Dean, C.; Shepard, K. L.; Kim, P.; Hone, J. Electron Tunneling through Atomically Flat and Ultrathin Hexagonal Boron Nitride. *Appl. Phys. Lett.* **2011**, *99*, 243114.

(184) Vu, Q. A.; Lee, J. H.; Nguyen, V. L.; Shin, Y. S.; Lim, S. C.; Lee, K.; Heo, J.; Park, S.; Kim, K.; Lee, Y. H.; Yu, W. J. Tuning Carrier Tunneling in van der Waals Heterostructures for Ultrahigh Detectivity. *Nano Lett.* **2017**, *17*, 453–459.

(185) Radisavljevic, B.; Radenovic, A.; Brivio, J.; Giacometti, V.; Kis, A. Single-Layer MoS_2 Transistors. *Nat. Nanotechnol.* **2011**, *6*, 147–150.

(186) Tang, H. L.; Chiu, M. H.; Tseng, C. C.; Yang, S. H.; Hou, K. J.; Wei, S. Y.; Huang, J. K.; Lin, Y. F.; Lien, C. H.; Li, L. J. Multilayer Graphene-WSe2 Heterostructures for WSe_2 Transistors. *ACS Nano* **2017**, *11*, 12817–12823.

(187) Ando, T. Screening Effect and Impurity Scattering in Monolayer Graphene. *J. Phys. Soc. Japan* **2006**, *75*, 074716.

(188) Avouris, P.; Chen, Z.; Perebeinos, V. Carbon-Based Electronics. *Nature Nanotechnology*. 2007, *2*, 605–615.

(189) Georgiou, T.; Jalil, R.; Belle, B. D.; Britnell, L.; Gorbachev, R. V.; Morozov, S. V.; Kim, Y. J.; Gholinia, A.; Haigh, S. J.; Makarovsky, O.; Eaves, L.; Ponomarenko, L. A.; Geim, A. K.; Novoselov, K. S.; Mishchenko, A. Vertical Field-Effect Transistor Based on Graphene-WS_2 Heterostructures for Flexible and Transparent Electronics. *Nat. Nanotechnol.* **2013**, *8*, 100–103.

(190) Wang, J.; Verzhbitskiy, I.; Eda, G. Electroluminescent Devices Based on 2D Semiconducting Transition Metal Dichalcogenides. *Adv. Mater.* **2018**, *30*, 1802687.

(191) Sundaram, R. S.; Engel, M.; Lombardo, A.; Krupke, R.; Ferrari, A. C.; Avouris, P.; Steiner, M. Electroluminescence in Single Layer MoS_2. *Nano Lett.* **2013**, *13*, 1416–1421.

(192) Ross, J. S.; Klement, P.; Jones, A. M.; Ghimire, N. J.; Yan, J.; Mandrus, D. G.; Taniguchi, T.; Watanabe, K.; Kitamura, K.; Yao, W.; Cobden, D. H.; Xu, X. Electrically Tunable Excitonic Light-Emitting Diodes Based on Monolayer WSe_2 p–n Junctions. *Nat. Nanotechnol.* **2014**, *9*, 268–272.

(193) Pospischil, A.; Furchi, M. M.; Mueller, T. Solar-Energy Conversion and Light Emission in an Atomic Monolayer p–n Diode. *Nat. Nanotechnol.* **2014**, *9*, 257–261.

(194) Baugher, B. W. H.; Churchill, H. O. H.; Yang, Y.; Jarillo-Herrero, P. Optoelectronic Devices Based on Electrically Tunable p–n Diodes in a Monolayer Dichalcogenide. *Nat. Nanotechnol.* **2014**, *9*, 262–267.

(195) Ye, Y.; Ye, Z.; Gharghi, M.; Zhu, H.; Zhao, M.; Wang, Y.; Yin, X.; Zhang, X. Exciton-Dominant Electroluminescence from a Diode of Monolayer MoS_2. *Appl. Phys. Lett.* **2014**, *104*, 193508.

(196) Zhao, Y.; Ouyang, G. Thickness-Dependent Photoelectric Properties of MoS_2/Si Heterostructure Solar Cells. *Sci. Rep.* **2019**, *9*, 1–11.

(197) Quereda, J.; Castellanos-Gomez, A. Excitons Surf the Waves. *Nat. Photonics* **2022**, *16*, 179–180.

(198) Cheng, R.; Li, D.; Zhou, H.; Wang, C.; Yin, A.; Jiang, S.; Liu, Y.; Chen, Y.; Huang, Y.; Duan, X. Electroluminescence and Photocurrent Generation from Atomically Sharp WSe_2/MoS_2 Heterojunction p–n Diodes. *Nano Lett.* **2014**, *14*, 5590–5597.

(199) Andrzejewski, D.; Hopmann, E.; John, M.; Kümmell, T.; Bacher, G. WS_2 Monolayer-Based Light-Emitting Devices in a Vertical p–n Architecture. *Nanoscale* **2019**, *11*, 8372–8379.

(200) Liu, C. H.; Clark, G.; Fryett, T.; Wu, S.; Zheng, J.; Hatami, F.; Xu, X.; Majumdar, A. Nanocavity Integrated van der Waals Heterostructure Light-

Emitting Tunneling Diode. *Nano Lett.* **2017**, *17*, 200–205.

(201) Withers, F.; Del Pozo-Zamudio, O.; Schwarz, S.; Dufferwiel, S.; Walker, P. M.; Godde, T.; Rooney, A. P.; Gholinia, A.; Woods, C. R.; Blake, P.; Haigh, S. J.; Watanabe, K.; Taniguchi, T.; Aleiner, I. L.; Geim, A. K.; Fal'Ko, V. I.; Tartakovskii, A. I.; Novoselov, K. S. WSe_2 Light-Emitting Tunneling Transistors with Enhanced Brightness at Room Temperature. *Nano Lett.* **2015**, *15*, 8223–8228.

(202) Binder, J.; Howarth, J.; Withers, F.; Molas, M. R.; Taniguchi, T.; Watanabe, K.; Faugeras, C.; Wysmolek, A.; Danovich, M.; Fal'ko, V. I.; Geim, A. K.; Novoselov, K. S.; Potemski, M.; Kozikov, A. Upconverted Electroluminescence via Auger Scattering of Interlayer Excitons in van der Waals Heterostructures. *Nat. Commun.* **2019**, *10*, 2335.

(203) Gu, J.; Chakraborty, B.; Khatoniar, M.; Menon, V. M. A Room-Temperature Polariton Light-Emitting Diode Based on Monolayer WS_2. *Nat. Nanotechnol.* **2019**, *14*, 1024–1028.

(204) Andrzejewski, D.; Myja, H.; Heuken, M.; Grundmann, A.; Kalisch, H.; Vescan, A.; Kümmell, T.; Bacher, G. Scalable Large-Area p–i–n Light-Emitting Diodes Based on WS_2 Monolayers Grown via MOCVD. *ACS Photonics* **2019**, *6*, 1832–1839.

(205) Clark, G.; Schaibley, J. R.; Ross, J.; Taniguchi, T.; Watanabe, K.; Hendrickson, J. R.; Mou, S.; Yao, W.; Xu, X. Single Defect Light-Emitting Diode in a van der Waals Heterostructure. *Nano Lett.* **2016**, *16*, 3944–3948.

(206) He, Z.; Liu, Y.; Yang, Z.; Li, J.; Cui, J.; Chen, D.; Fang, Z.; He, H.; Ye, Z.; Zhu, H.; Wang, N.; Wang, J.; Jin, Y. High-Efficiency Red Light-Emitting Diodes Based on Multiple Quantum Wells of Phenylbutylammonium-Cesium Lead Iodide Perovskites. *ACS Photonics* **2019**, *6*, 587–594.

(207) Sheng, Y.; Chen, T.; Lu, Y.; Chang, R. J.; Sinha, S.; Warner, J. H. High-Performance WS_2 Monolayer Light-Emitting Tunneling Devices Using 2D Materials Grown by Chemical Vapor Deposition. *ACS Nano* **2019**, *13*, 4530–4537.

(208) Palacios-Berraquero, C.; Barbone, M.; Kara, D. M.; Chen, X.; Goykhman, I.; Yoon, D.; Ott, A. K.; Beitner, J.; Watanabe, K.; Taniguchi, T.; Ferrari, A. C.; Atatüre, M. Atomically Thin Quantum Light-Emitting Diodes. *Nat. Commun.* **2016**, *7*, 12978.

(209) Wang, S.; Wang, J.; Zhao, W.; Giustiniano, F.; Chu, L.; Verzhbitskiy, I.; Zhou Yong, J.; Eda, G. Efficient Carrier-to-Exciton Conversion in Field Emission Tunnel Diodes Based on MIS-Type van der Waals Heterostack. *Nano Lett.* **2017**, *17*, 5156–5162.

(210) Dwivedi, J.; Kumar, P.; Kumar, A.; Sudama; Singh, V. N.; Singh, B. P.; Dhawan, S. K.; Shanker, V.; Gupta, B. K. A Commercial Approach for the Fabrication of Bulk and Nano Phosphors Converted into Highly Efficient White LEDs. *RSC Adv.* **2014**, *4*, 54936–54947.

(211) Woo, S. J.; Kim, J. S.; Lee, T. W. Characterization of Stability and Challenges to Improve Lifetime in Perovskite LEDs. *Nat. Photonics* **2021**, *15*, 630–634.

(212) Thakar, K.; Lodha, S. Optoelectronic and Photonic Devices Based on Transition Metal Dichalcogenides. *Mater. Res. Express* **2019**, *7*, 014002.

(213) Xie, C.; Mak, C.; Tao, X.; Yan, F. Photodetectors Based on Two-Dimensional Layered Materials Beyond Graphene. *Adv. Funct. Mater.* **2017**, *27*, 1603886.

(214) Konstantatos, G.; Sargent, E. H. Nanostructured Materials for Photon Detection. *Nat. Nanotechnol.* **2010**, *5*, 391–400.

(215) Tsai, D. S.; Liu, K. K.; Lien, D. H.; Tsai, M. L.; Kang, C. F.; Lin, C. A.; Li, L. J.; He, J. H. Few-Layer MoS_2 with High Broadband Photogain and Fast Optical Switching for Use in Harsh Environments. *ACS Nano* **2013**, *7*, 3905–3911.

(216) Borelli, C.; Bosio, A.; Parisini, A.; Pavesi, M.; Vantaggio, S.; Fornari, R. Electronic Properties and Photo-Gain of UV-C Photodetectors Based on High-Resistivity Orthorhombic κ-Ga_2O_3 Epilayers. *Mater. Sci. Eng. B Solid-State Mater. Adv. Technol.* **2022**, *286*, 116056.

(217) Wang, Q.; Guo, J.; Ding, Z.; Qi, D.; Jiang, J.; Wang, Z.; Chen, W.; Xiang, Y.; Zhang, W.; Wee, A. T. S. Fabry-Perot Cavity-Enhanced Optical Absorption in Ultrasensitive Tunable Photodiodes Based on Hybrid 2D Materials. *Nano Lett.* **2017**, *17*, 7593–7598.

(218) Tkachenko, N. V. Optical Measurements. In *Opt. Spectroscopy*; Elsevier, **2006**; 61–87.

(219) Ryu, S.; Liu, L.; Berciaud, S.; Yu, Y. J.; Liu, H.; Kim, P.; Flynn, G. W.; Brus, L. E. Atmospheric Oxygen Binding and Hole Doping in Deformed Graphene on a SiO_2 Substrate. *Nano Lett.* **2010**, *10*, 4944–4951.

(220) Rong, Y.; Fan, Y.; Leen Koh, A.; Robertson, A. W.; He, K.; Wang, S.; Tan, H.; Sinclair, R.; Warner, J. H. Controlling Sulphur Precursor Addition for Large Single Crystal Domains of WS_2. *Nanoscale* **2014**, *6*, 12096–12103.

(221) Sheng, Y.; Rong, Y.; He, Z.; Fan, Y.; Warner, J. H. Uniformity of Large-Area Bilayer Graphene Grown by Chemical Vapor Deposition. *Nanotechnology* **2015**, *26*, 395601.

(222) Zhang, Q.; Hou, L.; Lu, Y.; Chen, J.; Zhou, Y.; Shautsova, V.; Warner, J. H. Large-Scale Uniform-Patterned Arrays of Ultrathin All-2D Vertical Stacked Photodetector Devices. *ACS Appl. Mater. Interfaces* **2021**, *13*, 34696–34704.

(223) Cho, Y. C.; Ahn, S. I. Fabricating a Raman Spectrometer Using an Optical Pickup Unit and Pulsed Power. *Sci. Reports* **2020**, *10*, 1–8.

(224) Ferrari, A. C.; Basko, D. M. Raman Spectroscopy as a Versatile Tool for Studying the Properties of Graphene. *Nat. Nanotechnol.* **2013**, *8*, 235–246.

(225) Ferralis, N. Probing Mechanical Properties of Graphene with Raman Spectroscopy. *J. Mater. Sci.* **2010**, *45*, 5135–5149.

(226) Malard, L. M.; Pimenta, M. A.; Dresselhaus, G.; Dresselhaus, M. S. Raman Spectroscopy in Graphene. *Phys. Rep.* **2009**, *473*, 51–87.

(227) Kittel, C. *Introduction to Solid State Physics*, 8th ed.; Wiley: Hoboken, NJ, **2005**.

(228) Cooper, D. R.; D'Anjou, B.; Ghattamaneni, N.; Harack, B.; Hilke, M.; Horth, A.; Majlis, N.; Massicotte, M.; Vandsburger, L.; Whiteway, E.; Yu, V. Experimental Review of Graphene. *ISRN Condens. Matter Phys.* **2012**, *2012*, 1–56.

(229) Venezuela, P.; Lazzeri, M.; Mauri, F. Theory of Double-Resonant Raman Spectra in Graphene: Intensity and Line Shape of Defect-Induced and Two-Phonon Bands. *Phys. Rev. B - Condens. Matter Mater. Phys.* **2011**, *84*, 1–25.

(230) Basko, D. M.; Piscanec, S.; Ferrari, A. C. Electron-Electron Interactions and Doping Dependence of the Two-Phonon Raman Intensity in Graphene. *Phys. Rev. B* **2009**, *80*, 165413.

(231) Pimenta, M. A.; Dresselhaus, G.; Dresselhaus, M. S.; Cançado, L. G.; Jorio, A.; Saito, R. Studying Disorder in Graphite-Based Systems by Raman Spectroscopy. *Phys. Chem. Chem. Phys.* **2007**, *9*, 1276–1291.

(232) Wang, Y. Y.; Ni, Z. H.; Yu, T.; Shen, Z. X.; Wang, H. M.; Wu, Y. H.; Chen, W.; Wee, A. T. S. Raman Studies of Monolayer Graphene: The Substrate Effect. *J. Phys. Chem. C* **2008**, *112*, 10637–10640.

(233) Zhang, X.; Qiao, X. F.; Shi, W.; Wu, J. Bin; Jiang, D. S.; Tan, P. H. Phonon and Raman Scattering of Two-Dimensional Transition Metal Dichalcogenides from Monolayer, Multilayer to Bulk Material. *Chem. Soc. Rev.* **2015**, *44* (9), 2757–2785.

(234) Zeng, H.; Liu, G. Bin; Dai, J.; Yan, Y.; Zhu, B.; He, R.; Xie, L.; Xu, S.; Chen, X.; Yao, W.; Cui, X. Optical Signature of Symmetry Variations and Spin-Valley Coupling in Atomically Thin Tungsten Dichalcogenides. *Sci. Rep.* **2013**, *3*, 1608.

(235) Liang, F.; Xu, H.; Wu, X.; Wang, C.; Luo, C.; Zhang, J. Raman Spectroscopy Characterization of Two-Dimensional Materials. *Chinese Phys. B* **2018**, *27*, 037802.

(236) Xu, X.; Li, L.; Yang, M.; Guo, Q.; Wang, Y.; Li, X.; Zhuang, X.; Liang, B. Localized State Effect and Exciton Dynamics for Monolayer WS_2. *Opt. Express* **2021**, *29*, 5856.

(237) He, Z.; Xu, W.; Zhou, Y.; Wang, X.; Sheng, Y.; Rong, Y.; Guo, S.; Zhang, J.; Smith, J. M.; Warner, J. H. Biexciton Formation in Bilayer Tungsten Disulfide. *ACS Nano* **2016**, *10*, 2176–2183.

(238) Berkdemir, A.; Gutiérrez, H. R.; Botello-Méndez, A. R.; Perea-López, N.; Elías, A. L.; Chia, C. I.; Wang, B.; Crespi, V. H.; López-Urías, F.; Charlier, J. C.; Terrones, H.; Terrones, M. Identification of Individual and Few Layers of WS_2 Using Raman Spectroscopy. *Sci. Rep.* **2013**, *3*, 1755.

(239) Lee, C.; Yan, H.; Brus, L. E.; Heinz, T. F.; Hone, J.; Ryu, S. Anomalous Lattice Vibrations of Single- and Few-Layer MoS_2. *ACS Nano* **2010**, *4* (5), 2695–2700.

(240) Li, H.; Zhang, Q.; Yap, C. C. R.; Tay, B. K.; Edwin, T. H. T.; Olivier, A.; Baillargeat, D. From Bulk to Monolayer MoS_2: Evolution of Raman Scattering. *Adv. Funct. Mater.* **2012**, *22*, 1385–1390.

(241) Mitioglu, A. A.; Plochocka, P.; Deligeorgis, G.; Anghel, S.; Kulyuk, L.; Maude, D. K. Second-Order Resonant Raman Scattering in Single-Layer Tungsten Disulfide WS_2. *Phys. Rev. B - Condens. Matter Mater. Phys.* **2014**, *89*, 1–5.

(242) Bagnall, A. G.; Liang, W. Y.; Marseglia, E. A.; Welber, B. Raman Studies of MoS_2 at High Pressure. *Phys. B+C* **1980**, *99*, 343–346.

(243) Molina-Sánchez, A.; Wirtz, L. Phonons in Single-Layer and Few-Layer MoS_2 and WS_2. *Phys. Rev. B - Condens. Matter Mater. Phys.* **2011**, *84*, 1–8.

(244) Liu, J.; Lo, T. W.; Sun, J.; Yip, C. T.; Lam, C. H.; Lei, D. Y. A Comprehensive Comparison Study on the Vibrational and Optical Properties of CVD-Grown and Mechanically Exfoliated Few-Layered WS_2. *J. Mater. Chem. C* **2017**, *5*, 11239–11245.

(245) Zhao, W.; Ghorannevis, Z.; Amara, K. K.; Pang, J. R.; Toh, M.; Zhang, X.; Kloc, C.; Tan, P. H.; Eda, G. Lattice Dynamics in Mono- and Few-Layer Sheets of WS_2 and WSe_2. *Nanoscale* **2013**, *5*, 9677–9683.

(246) John, N.; George, S. Raman Spectroscopy. In *Spectroscopic Methods for Nanomaterials Characterization*; Elsevier, **2017**; 95–127.

(247) Jones, R. R.; Hooper, D. C.; Zhang, L.; Wolverson, D.; Valev, V. K. Raman Techniques: Fundamentals and Frontiers. *Nanoscale Res. Lett.* **2019**, *14*, 231.

(248) Voigtländer, B. Forces Between Tip and Sample. In *Atomic Force Microscopy*; Springer International Publishing: Cham, **2019**; 161–176.

(249) Sinha Ray, S. Structure and Morphology Characterization Techniques. In *Clay-Containing Polymer Nanocomposites*; Elsevier, **2013**; 39–66.

(250) Johnson, D.; Hilal, N.; Bowen, W. R. Basic Principles of Atomic Force Microscopy. In *Atomic Force Microscopy in Process Engineering*; Elsevier, **2009**; 1–30.

(251) Sheng, Y.; Xu, W.; Wang, X.; He, Z.; Rong, Y.; Warner, J. H. Mixed Multilayered Vertical Heterostructures Utilizing Strained Monolayer WS_2. *Nanoscale* **2016**, *8*, 2639–2647..

(252) Lawson, R. A.; Robinson, A. P. G. Overview of Materials and Processes for Lithography. In *Frontiers of Nanoscience*; Elsevier, **2016**; 1–90.

(253) Jones, S. W. *Photolithography*; IC Knowledge LLC, **2008**.

(254) Cord, B.; Yang, J.; Duan, H.; Joy, D. C.; Klingfus, J.; Berggren, K. K. Limiting Factors in Sub-10 nm Scanning-Electron-Beam Lithography. *J. Vac. Sci. Technol. B Microelectron. Nanom. Struct.* **2009**, *27*, 2616.

(255) Andok, R.; Vutova, K.; Bencurova, A.; Kostic, I.; Koleva, E. Study and Comparison of Resist Characteristics for Different Negative Tone Electron Beam Resists. *J. Phys. Conf. Ser.* **2023**, *2443*, 012006.

(256) Manfrinato, V. R.; Zhang, L.; Su, D.; Duan, H.; Hobbs, R. G.; Stach, E. A.; Berggren, K. K. Resolution Limits of Electron-Beam Lithography toward the Atomic Scale. *Nano Lett.* **2013**, *13*, 1555–1558.

(257) Molpeceres, C.; Lauzurica, S.; Porro, J.; Ocana, J. Metrologic Assessment of High Power Laser Generated Surface Roughness by Confocal Laser Scanning Microscopy. In *Recent Advances in Multidisciplinary Applied Physics*; Elsevier, **2005**; 133–140.

(258) Lin, L.; Li, J.; Li, W.; Yogeesh, M. N.; Shi, J.; Peng, X.; Liu, Y.; Rajeeva, B. B.; Becker, M. F.; Liu, Y.; Akinwande, D.; Zheng, Y. Optothermoplasmonic Nanolithography for On-Demand Patterning of 2D Materials. *Adv. Funct. Mater.* **2018**, *28*, 1803990.

(259) Lin, J.; Tay, R. Y.; Li, H.; Jing, L.; Tsang, S. H.; Wang, H.; Zhu, M.; McCulloch, D. G.; Teo, E. H. T. Smoothening of Wrinkles in CVD-Grown Hexagonal Boron Nitride Films. *Nanoscale* **2018**, *10*, 16243–16251.

(260) Tsai, M. L.; Su, S. H.; Chang, J. K.; Tsai, D. S.; Chen, C. H.; Wu, C. I.; Li, L. J.; Chen, L. J.; He, J. H. Monolayer MoS_2 Heterojunction Solar Cells. *ACS Nano* **2014**, *8*, 8317–8322.

(261) Wi, S.; Kim, H.; Chen, M.; Nam, H.; Guo, L. J.; Meyhofer, E.; Liang, X. Enhancement of Photovoltaic Response in Multilayer MoS_2 Induced by Plasma Doping. *ACS Nano* **2014**, *8*, 5270–5281.

(262) Gong, Y.; Lin, J.; Wang, X.; Shi, G.; Lei, S.; Lin, Z.; Zou, X.; Ye, G.; Vajtai, R.; Yakobson, B. I.; Terrones, H.; Terrones, M.; Tay, B. K.; Lou, J.; Pantelides, S. T.; Liu, Z.; Zhou, W.; Ajayan, P. M. Vertical and In-Plane Heterostructures from WS_2/MoS_2 Monolayers. *Nat. Mater.* **2014**, *13*, 1135–1142.

(263) Lin, Y. C.; Lu, C. C.; Yeh, C. H.; Jin, C.; Suenaga, K.; Chiu, P. W. Graphene Annealing: How Clean Can It Be? *Nano Lett.* **2012**, *12*, 414–419.

(264) Gorbachev, R. V.; Riaz, I.; Nair, R. R.; Jalil, R.; Britnell, L.; Belle, B. D.; Hill, E. W.; Novoselov, K. S.; Watanabe, K.; Taniguchi, T.; Geim, A. K.; Blake, P. Hunting for Monolayer Boron Nitride: Optical and Raman Signatures. *Small* **2011**, *7*, 465–468.

(265) Tongay, S.; Zhou, J.; Ataca, C.; Liu, J.; Kang, J. S.; Matthews, T. S.; You, L.; Li, J.; Grossman, J. C.; Wu, J. Broad-Range Modulation of Light Emission in Two-Dimensional Semiconductors by Molecular Physisorption Gating. *Nano Lett.* **2013**, *13*, 2831–2836.

(266) Han, T.; Liu, H.; Wang, S.; Chen, S.; Yang, K. Research on the Preparation and Spectral Characteristics of Graphene/TMDs Hetero-Structures. *Nanoscale Res. Lett.* **2020**, *15*, 1–14.

(267) Wang, S.; Rong, Y.; Fan, Y.; Pacios, M.; Bhaskaran, H.; He, K.; Warner, J. H.

Shape Evolution of Monolayer MoS_2 Crystals Grown by Chemical Vapor Deposition. *Chem. Mater.* **2014**, *26*, 6371–6379.

(268) Park, H.; Kang, J.; Kim, M.; Seo, J.; Kim, J.; Moon, J. S.; Lee, J.; Kim, J. H. High-Crystalline Monolayer Transition Metal Dichalcogenides Films for Wafer-Scale Electronics. *ACS Nano* **2021**, *15*, 3038–3046.

(269) Tanoh, A. O. A.; Alexander-Webber, J.; Fan, Y.; Gauriot, N.; Xiao, J.; Pandya, R.; Li, Z.; Hofmann, S.; Rao, A. Giant Photoluminescence Enhancement in $MoSe_2$ Monolayers Treated with Oleic Acid Ligands. *Nanoscale Adv.* **2021**, *3*, 4216–4225.

(270) Elías, A. L.; Perea-López, N.; Castro-Beltrán, A.; Berkdemir, A.; Lv, R.; Feng, S.; Long, A. D.; Hayashi, T.; Kim, Y. A.; Endo, M.; Gutiérrez, H. R.; Pradhan, N. R.; Balicas, L.; Mallouk, T. E.; López-Urías, F.; Terrones, H.; Terrones, M. Controlled Synthesis and Transfer of Large-Area WS_2 Sheets: From Single Layer to Few Layers. *ACS Nano* **2013**, *7*, 5235–5242.

(271) Huo, N.; Wei, Z.; Meng, X.; Kang, J.; Wu, F.; Li, S. S.; Wei, S. H.; Li, J. Interlayer Coupling and Optoelectronic Properties of Ultrathin Two-Dimensional Heterostructures Based on Graphene, MoS_2 and WS_2. *J. Mater. Chem. C* **2015**, *3*, 5467–5473.

(272) Tan, H.; Fan, Y.; Rong, Y.; Porter, B.; Lau, C. S.; Zhou, Y.; He, Z.; Wang, S.; Bhaskaran, H.; Warner, J. H. Doping Graphene Transistors Using Vertical Stacked Monolayer WS_2 Heterostructures Grown by Chemical Vapor Deposition. *ACS Appl. Mater. Interfaces* **2016**, *8*, 1644–1652.

(273) Bhanu, U.; Islam, M. R.; Tetard, L.; Khondaker, S. I. Photoluminescence Quenching in Gold-MoS_2 Hybrid Nanoflakes. *Sci. Rep.* **2014**, *4*, 1–5.

(274) Nikam, R. D.; Sonawane, P. A.; Sankar, R.; Chen, Y. T. Epitaxial Growth of Vertically Stacked p-MoS_2/n-MoS_2 Heterostructures by Chemical Vapor Deposition for Light Emitting Devices. *Nano Energy* **2017**, *32*, 454–462.

(275) Kim, G.; Jang, A. R.; Jeong, H. Y.; Lee, Z.; Kang, D. J.; Shin, H. S. Growth of High-Crystalline, Single-Layer Hexagonal Boron Nitride on Recyclable Platinum Foil. *Nano Lett.* **2013**, *13*, 1834–1839.

(276) Ferrari, A. C.; Meyer, J. C.; Scardaci, V.; Casiraghi, C.; Lazzeri, M.; Mauri, F.; Piscanec, S.; Jiang, D.; Novoselov, K. S.; Roth, S.; Geim, A. K. Raman Spectrum of Graphene and Graphene Layers. *Phys. Rev. Lett.* **2006**, *97*, 187401.

(277) Xia, Y.; Li, Q.; Kim, J.; Bao, W.; Gong, C.; Yang, S.; Wang, Y.; Zhang, X. Room-Temperature Giant Stark Effect of Single Photon Emitter in van der Waals Material. *Nano Lett.* **2019**, *19*, 7100–7105.

(278) Noh, G.; Choi, D.; Kim, J. H.; Im, D. G.; Kim, Y. H.; Seo, H.; Lee, J. Stark Tuning of Single-Photon Emitters in Hexagonal Boron Nitride. *Nano Lett.* **2018**, *18*, 4710–4715.

(279) Chakraborty, C.; Goodfellow, K. M.; Dhara, S.; Yoshimura, A.; Meunier, V.; Vamivakas, A. N. Quantum-Confined Stark Effect of Individual Defects in a

van der Waals Heterostructure. *Nano Lett.* **2017**, *17*, 2253–2258.

(280) Kuo, Y. H.; Lee, Y. K.; Ge, Y.; Ren, S.; Roth, J. E.; Kamins, T. I.; Miller, D. A. B.; Harris, J. S. Strong Quantum-Confined Stark Effect in Germanium Quantum-Well Structures on Silicon. *Nature* **2005**, *437*, 1334–1336.

(281) Liu, Y.; Qiu, Z.; Carvalho, A.; Bao, Y.; Xu, H.; Tan, S. J. R.; Liu, W.; Castro Neto, A. H.; Loh, K. P.; Lu, J. Gate-Tunable Giant Stark Effect in Few-Layer Black Phosphorus. *Nano Lett.* **2017**, *17*, 1970–1977.

(282) Klein, J.; Wierzbowski, J.; Regler, A.; Becker, J.; Heimbach, F.; Müller, K.; Kaniber, M.; Finley, J. J. Stark Effect Spectroscopy of Mono- and Few-Layer MoS_2. *Nano Lett.* **2016**, *16*, 1554–1559.

(283) Miller, D. A. B.; Chemla, D. S.; Damen, T. C.; Gossard, A. C.; Wiegmann, W.; Wood, T. H.; Burrus, C. A. Band-Edge Electroabsorption in Quantum Well Structures: The Quantum-Confined Stark Effect. *Phys. Rev. Lett.* **1984**, *53*, 2173–2176.

(284) Fan, H. Y. Temperature Dependence of the Energy Gap in Monatomic Semiconductors. *Phys. Rev.* **1950**, *78*, 808–809.

(285) Ross, J. S.; Wu, S.; Yu, H.; Ghimire, N. J.; Jones, A. M.; Aivazian, G.; Yan, J.; Mandrus, D. G.; Xiao, D.; Yao, W.; Xu, X. Electrical Control of Neutral and Charged Excitons in a Monolayer Semiconductor. *Nat. Commun.* **2013**, *4*, 1474.

(286) Jo, S.; Ubrig, N.; Berger, H.; Kuzmenko, A. B.; Morpurgo, A. F. Mono- and Bilayer WS_2 Light-Emitting Transistors. *Nano Lett.* **2014**, *14*, 2019–2025.

(287) De Mello, J. C.; Wittmann, H. F.; Friend, R. H. An Improved Experimental Determination of External Photoluminescence Quantum Efficiency. *Advanced Materials* **1997**, *9*, 230–232.

(288) Yuan, L.; Huang, L. Exciton Dynamics and Annihilation in WS_2 2D Semiconductors. *Nanoscale* **2015**, *7*, 7402–7408.

(289) Rosenberger, M. R.; Chuang, H. J.; McCreary, K. M.; Li, C. H.; Jonker, B. T. Electrical Characterization of Discrete Defects and Impact of Defect Density on Photoluminescence in Monolayer WS_2. *ACS Nano* **2018**, *12*, 1793–1800.

(290) Sadeghi, H.; Mol, J. A.; Lau, C. S.; Briggs, G. A. D.; Warner, J.; Lambert, C. J. Conductance Enlargement in Picoscale Electroburnt Graphene Nanojunctions. *Proc. Natl. Acad. Sci. U. S. A.* **2015**, *112*, 2658–2663.

(291) Mol, J. A.; Lau, C. S.; Lewis, W. J. M.; Sadeghi, H.; Roche, C.; Cnossen, A.; Warner, J. H.; Lambert, C. J.; Anderson, H. L.; Briggs, G. A. D. Graphene-Porphyrin Single-Molecule Transistors. *Nanoscale* **2015**, *7*, 13181–13185.

(292) Lau, C. S.; Mol, J. A.; Warner, J. H.; Briggs, G. A. D. Nanoscale Control of Graphene Electrodes. *Phys. Chem. Chem. Phys.* **2014**, *16*, 20398–20401.

(293) Ovchinnikov, D.; Allain, A.; Huang, Y. S.; Dumcenco, D.; Kis, A. Electrical Transport Properties of Single-Layer WS_2. *ACS Nano* **2014**, *8*, 8174–8181.

(294) Zhao, W.; Ghorannevis, Z.; Chu, L.; Toh, M.; Kloc, C.; Tan, P. H.; Eda, G. Evolution of Electronic Structure in Atomically Thin Sheets of WS_2 and WSe_2. *ACS Nano* **2013**, *7*, 791–797.

(295) Zibouche, N.; Kuc, A.; Miró, P.; Heine, T. Noble-Metal Chalcogenide Nanotubes. *Inorganics* **2014**, *2*, 556–564.

(296) Villaos, R. A. B.; Crisostomo, C. P.; Huang, Z. Q.; Huang, S. M.; Padama, A. A. B.; Albao, M. A.; Lin, H.; Chuang, F. C. Thickness Dependent Electronic Properties of Pt Dichalcogenides. *npj 2D Mater. Appl.* **2019**, *3*, 1–8.

(297) Chen, E.; Xu, W.; Chen, J.; Warner, J. H. 2D Layered Noble Metal Dichalcogenides (Pt, Pd, Se, S) for Electronics and Energy Applications. *Materials Today Advances* **2020**, *7*, 100076.

(298) Pawar, M. S.; Late, D. J. Temperature-Dependent Raman Spectroscopy and Sensor Applications of $PtSe_2$ Nanosheets Synthesized by Wet Chemistry. *Beilstein J. Nanotechnol.* **2019**, *10*, 467–474.

(299) Singh, A. K.; Mathew, K.; Zhuang, H. L.; Hennig, R. G. Computational Screening of 2D Materials for Photocatalysis. *J. Phys. Chem. Lett.* **2015**, *6*, 1087–1098.

(300) Wang, Y.; Yu, Z.; Tong, Y.; Sun, B.; Zhang, Z.; Xu, J. Bin; Sun, X.; Tsang, H. K. High-Speed Infrared Two-Dimensional Platinum Diselenide Photodetectors. *Appl. Phys. Lett.* **2020**, *116*, 211101.

(301) Shautsova, V.; Sinha, S.; Hou, L.; Zhang, Q.; Tweedie, M.; Lu, Y.; Sheng, Y.; Porter, B. F.; Bhaskaran, H.; Warner, J. H. Direct Laser Patterning and Phase Transformation of 2D $PdSe_2$ Films for On-Demand Device Fabrication. *ACS Nano* **2019**, *13*, 14162–14171.

(302) Nagamine, Y.; Sato, J.; Qian, Y.; Inoue, T.; Nakamura, T.; Maruyama, S.; Katsumoto, S.; Haruyama, J. Optoelectronic Properties of Laser-Beam-Patterned Few-Layer Lateral MoS_2 Schottky Junctions. *Appl. Phys. Lett.* **2020**, *117*, 043101.

(303) Mine, H.; Kobayashi, A.; Nakamura, T.; Inoue, T.; Pakdel, S.; Marian, D.; Gonzalez-Marin, E.; Maruyama, S.; Katsumoto, S.; Fortunelli, A.; Palacios, J. J.; Haruyama, J. Laser-Beam-Patterned Topological Insulating States on Thin Semiconducting MoS_2. *Phys. Rev. Lett.* **2019**, *123*, 146803.

(304) Castellanos-Gomez, A.; Barkelid, M.; Goossens, A. M.; Calado, V. E.; Van Der Zant, H. S. J.; Steele, G. A. Laser-Thinning of MoS_2: On Demand Generation of a Single-Layer Semiconductor. *Nano Lett.* **2012**, *12*, 3187–3192.

(305) Yang, Y.; Jang, S. K.; Choi, H.; Xu, J.; Lee, S. Homogeneous Platinum Diselenide Metal/Semiconductor Coplanar Structure Fabricated by Selective Thickness Control. *Nanoscale* **2019**, *11*, 21068–21073.

(306) Fan, Y.; Zhou, Y.; Wang, X.; Tan, H.; Rong, Y.; Warner, J. H. Photoinduced Schottky Barrier Lowering in 2D Monolayer WS_2 Photodetectors. *Advanced Optical Materials* **2016**, *4*, 1573–1581.

(307) O'Brien, M.; McEvoy, N.; Motta, C.; Zheng, J. Y.; Berner, N. C.; Kotakoski, J.; Elibol, K.; Pennycook, T. J.; Meyer, J. C.; Yim, C.; Abid, M.; Hallam, T.; Donegan, J. F.; Sanvito, S.; Duesberg, G. S. Raman Characterization of Platinum Diselenide Thin Films. *2D Mater.* **2016**, *3*, 021004.

(308) Lin, S.; Liu, Y.; Hu, Z.; Lu, W.; Mak, C. H.; Zeng, L.; Zhao, J.; Li, Y.; Yan, F.; Tsang, Y. H.; Zhang, X.; Lau, S. P. Tunable Active Edge Sites in $PtSe_2$ Films towards Hydrogen Evolution Reaction. *Nano Energy* **2017**, *42*, 26–33.

(309) Yan, M.; Wang, E.; Zhou, X.; Zhang, G.; Zhang, H.; Zhang, K.; Yao, W.; Lu, N.; Yang, S.; Wu, S.; Yoshikawa, T.; Miyamoto, K.; Okuda, T.; Wu, Y.; Yu, P.; Duan, W.; Zhou, S. High Quality Atomically Thin $PtSe_2$ Films Grown by Molecular Beam Epitaxy . *2D Mater.* **2017**, *4*, 045015.

(310) Rong, Y.; Sheng, Y.; Pacios, M.; Wang, X.; He, Z.; Bhaskaran, H.; Warner, J. H. Electroluminescence Dynamics across Grain Boundary Regions of Monolayer Tungsten Disulfide. *ACS Nano* **2016**, *10*, 1093–1100.

(311) Ohta, Y.; Kubozono, Y.; Fujiwara, A. Transport Properties in C_{60} Field-Effect Transistor with a Single Schottky Barrier. *Appl. Phys. Lett.* **2008**, *92*, 1–4.

(312) Nagano, T.; Tsutsui, M.; Nouchi, R.; Kawasaki, N.; Ohta, Y.; Kubozono, Y.; Takahashi, N.; Fujiwara, A. Output Properties of C60 Field-Effect Transistors with Au Electrodes Modified by 1-Alkanethiols. *J. Phys. Chem. C* **2007**, *111*, 7211–7217.

(313) Chiquito, A. J.; Amorim, C. A.; Berengue, O. M.; Araujo, L. S.; Bernardo, E. P.; Leite, E. R. Back-to-Back Schottky Diodes: The Generalization of the Diode Theory in Analysis and Extraction of Electrical Parameters of Nanodevices. *J. Phys. Condens. Matter* **2012**, *24*, 7.

(314) Kandemir, A.; Akbali, B.; Kahraman, Z.; Badalov, S. V.; Ozcan, M.; Iyikanat, F.; Sahin, H. Structural, Electronic and Phononic Properties of $PtSe_2$: From Monolayer to Bulk. *Semicond. Sci. Technol.* **2018**, *33*, 085002.

(315) Nicholls, J. R.; Dimitrijev, S.; Tanner, P.; Han, J. The Role of Near-Interface Traps in Modulating the Barrier Height of SiC Schottky Diodes. *IEEE Trans. Electron Devices* **2019**, *66*, 1675–1680.

(316) Newton, M. C.; Warburton, P. A.; Firth, S. Ultraviolet Photoresponse of ZnO Tetrapod Nanocrystal Schottky Diodes. *2006 6th IEEE Conf. Nanotechnology, IEEE-NANO* **2006**, *2*, 453–456.

(317) Keem, K.; Kim, H.; Kim, G. T.; Lee, J. S.; Min, B.; Cho, K.; Sung, M. Y.; Kim, S. Photocurrent in ZnO Nanowires Grown from Au Electrodes. *Appl. Phys. Lett.* **2004**, *84*, 4376–4378.

(318) Chen, H. M.; Chang, T. C.; Liao, P. Y.; Chiang, H. C.; Chen, C. E.; Chen, B. W.; Pan, C. H.; Hung, Y. J. Identical Off-State Current Raise Induced by Photo-Induced Schottky Barrier Lowering in a-$InGaZnO_4$ Thin Film Transistors. *16th Int. Conf. Nanotechnol. - IEEE NANO* **2016**, 783–786.

(319) Zhang, W.; Chuu, C. P.; Huang, J. K.; Chen, C. H.; Tsai, M. L.; Chang, Y. H.;

Liang, C. Te; Chen, Y. Z.; Chueh, Y. L.; He, J. H.; Chou, M. Y.; Li, L. J. Ultrahigh-Gain Photodetectors Based on Atomically Thin Graphene-MoS_2 Heterostructures. *Sci. Rep.* **2015**, *4*, 3826.

(320) Lan, C.; Li, C.; Yin, Y.; Liu, Y. Large-Area Synthesis of Monolayer WS_2 and Its Ambient-Sensitive Photo-Detecting Performance. *Nanoscale* **2015**, *7*, 5974–5980.

(321) Račiukaitis, G.; Brikas, M.; Gedvilas, M.; Rakickas, T. Patterning of Indium-Tin Oxide on Glass with Picosecond Lasers. *Appl. Surf. Sci.* **2007**, *253*, 6570–6574.

(322) Zanini, S.; Papagni, A.; Vaghi, L.; Thatti, B. K.; Barton, S.; Williams, N.; Shokri, N.; Riccardi, C. Sulfur Hexafluoride (SF6) Plasma Treatment of Medical Grade Poly(Methyl Methacrylate). *Coatings* **2020**, *10*, 1–14.

(323) Ajayi, O. A.; Ardelean, J. V; Shepard, G. D.; Wang, J.; Antony, A.; Taniguchi, T.; Watanabe, K.; Heinz, T. F.; Strauf, S.; Hone, J. C. Approaching the Intrinsic Photoluminescence Linewidth in Transition Metal Dichalcogenide Monolayers. *2D Mater.* **2017**, *4*, 1–16.

(324) Cheng, G.; Li, B.; Zhao, C.; Yan, X.; Wang, H.; Lau, K. M.; Wang, J. Interfacially Bound Exciton State in a Hybrid Structure of Monolayer WS_2 and InGaN Quantum Dots. *Nano Lett.* **2018**, *18*, 5640–5645.

(325) Jain, V.; Biesinger, M. C.; Linford, M. R. The Gaussian-Lorentzian Sum, Product, and Convolution (Voigt) Functions in the Context of Peak Fitting X-Ray Photoelectron Spectroscopy (XPS) Narrow Scans. *Appl. Surf. Sci.* **2018**, *447*, 548–553.

(326) Bradley, M. Curve Fitting in Raman and IR Spectroscopy : Basic Theory of Line Shapes and Applications. *Thermo Fish. Sci. Appl. Note* **2007**, AN50733.

(327) Karmakar, S.; Chatterjee, U.; Kumbhakar, P. Transition from Saturable Absorption to Reverse Saturable Absorption in Multi-Layered WS_2 Nanosheets. *Optics & Laser Technology* **2021**, *136*, 106696.

(328) Uifsnbm, J. O.; Pg, D.; Dbvtfe, N.; Jo, E.; Tdjfodf, N.; Jdsp, B. O. E.; Fdibojdbm, M. Reduction in Thermal Conductivity of Monolayer WS_2 Caused by Substrate Effect. *Nano Res.* **2022**, *15*, 9578–9587.

(329) Liu, H.; Wang, C.; Zuo, Z.; Liu, D.; Luo, J. Direct Visualization of Exciton Transport in Defective Few-Layer WS_2 by Ultrafast Microscopy. *Adv. Mater.* **2020**, *32*, 1906540.

(330) Groven, B.; Claes, D.; Nalin Mehta, A.; Bender, H.; Vandervorst, W.; Heyns, M.; Caymax, M.; Radu, I.; Delabie, A. Chemical Vapor Deposition of Monolayer-Thin WS_2 Crystals from the WF_6 and H_2S Precursors at Low Deposition Temperature. *J. Chem. Phys.* **2019**, *150*, 104703.

(331) Groven, B.; Nalin Mehta, A.; Bender, H.; Meersschaut, J.; Nuytten, T.; Verdonck, P.; Conard, T.; Smets, Q.; Schram, T.; Schoenaers, B.; Stesmans, A.; Afanas'Ev, V.; Vandervorst, W.; Heyns, M.; Caymax, M.; Radu, I.; Delabie, A.

Two-Dimensional Crystal Grain Size Tuning in WS_2 Atomic Layer Deposition: An Insight in the Nucleation Mechanism. *Chem. Mater.* **2018**, *30*, 7648–7663..

(332) Wu, T.; Lu, C.; Sun, T.; Li, Y. Study on Raman Multi-Peak Fitting and Structure Quantitative Analysis of PAN-Based Carbon Fibers. *J. Mater. Sci.* **2022**, *57*, 15385–15412.